



UNIVERSITAT DE  
BARCELONA

# Quantitative methods for electron energy loss spectroscopy

Alberto Eljarrat Ascunce



Aquesta tesi doctoral està subjecta a la llicència [Reconeixement- CompartIgual 3.0. Espanya de Creative Commons](#).

Esta tesis doctoral está sujeta a la licencia [Reconocimiento - CompartirIgual 3.0. España de Creative Commons](#).

This doctoral thesis is licensed under the [Creative Commons Attribution-ShareAlike 3.0. Spain License](#).

# **Quantitative methods for electron energy loss spectroscopy**

**Alberto Eljarrat Ascunce**

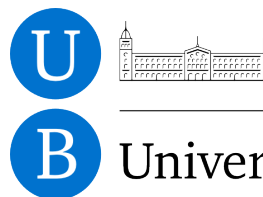
Tesi presentada per a optar al títol de  
Doctor per la Universitat de Barcelona,  
en el marc del Programa de Nanociències

Directores de la Tesis:

Dr. Francesca Peiró Martínez

Dr. Sònia Estradé Albiol

LENS-MIND-IN2UB Departament d'Electrònica





**Dr. Francesca Peiró Martínez,**

Professor Titular del Departament d'Electrònica i

**Dr. Sònia Estradé Albiol,**

Professor Lector del Departament d'Electrònica

certifiquen que la tesi “**Quantitative methods for electron energy loss spectroscopy**”, que presenta **Alberto Eljarrat Asuncion** per a optar al títol de Doctor per la Universitat de Barcelona, en el marc del Programa de Nanociències, ha estat realitzada sota la seva direcció.

A Barcelona, 1 de Juliol 2015.

Les directores:

Dr. Francesca Peiró Martínez

Dr. Sònia Estradé Albiol



# Agradecimientos

“Life, uh, finds a way.”

---

Jeff Goldblum as some mathematician guy, *Jurassic Park*.

Es un hecho que para la realización de esta tesis ha sido necesario contar muchísimos electrones. Ésta es una tarea agotadora, en la cual se pierde mucha energía durante múltiples interacciones. Sin la atención debida, puede ser que estas pérdidas se hagan mayores de lo soportable; cuando las pérdidas pasan de bajas a altas, podemos quedar tocados en lo mas profundo. Ha sido mi interés en esta tesis mantener las pérdidas bajas, para, al menos, estar seguro de no afectar mucho el núcleo. La ayuda de muchas personas ha hecho posible llevar esta empresa a buen puerto, y es por tanto justo y necesario tomar unos instantes para nombrarlos. Reciban ahora mi agradecimiento estas gentes, porque ayudaron a mejorar o hacer más sencillo este trabajo, y en no pocos casos (aun sin saberlo ellos), sin su participación esta tesis no habría sido igual, incluso digamos, nada de esto habría sido posible <sup>i</sup>.

Començaré mencionant el grup en el qual he desenvolupat gairebé tota la feina associada a aquesta tesi, Micro-nanotecnologies i nanoscòpies per dispositius electrònics i fotònics (MIND) del Departament d'Electrònica, encapçalat pel Prof Albert Cornet. Moltes gràcies a tots els membres d'aquest grup i del Departament, no sols per l'ajuda prestada, si no també per les bones estones, picatrònics i calçotades, entre altres coses. Una salutació especial al Prof. Blas Garrido, i als Drs Sergi Hernández, Albert Cirera, Albert Romano i Daniel Prades, amb els quals he pogut col·laborar més estretament i que han sigut de gran ajuda en certs moments claus.

Als meus companys MINDundis del passat, present i futur: començant pels meus compatriotes del Depatx Patera superior (H23); Dr Julià López, Oriol Blázquez, Adrià Huguet i Martí Busquets, per mantenir el meu elevat nivel de cafeïna en sang. També vull mencionar els habitants del Despatx Patera inferior (PL1); Oriol Monereo, Giovanni Vescio, els Drs Núria García, Sergio Illera, Olga Casals, antics compatriotes,

---

<sup>i</sup>En un pintoresco ataque de originalidad, estos agradecimientos han sido escritos en varias lenguas como pequeño homenaje al carácter universal del mundo de la investigación.

i "noves" incorporacions; Beatriz Medina, Xavier Arrese, els Drs Elena Xuriguera i Aïda Varea. Finalment, als Drs Yonder Berencén i Joan Manel Ramírez, que escolten les nostres converses a través de les primes parets.

Als meus companys del Laboratori de NanoScopies Electròniques (LENS); Josep Rebled, al qual vaig dir moltes vagades que no defensaria la meva tesi abans que ell; Dr Lluís Yedra, amb el qual vaig anar d'alpinisme en texans i vaig sobreuirer; Lluís López, que ja ha trobat tots els errors ortogràfics i gramaticals d'aquest text; Gemma Martín, que compagina el doctorat amb la fidelitat màxima a les hores de break; Pau Torruella, al qual no hi ha barrera que se li resisteixi; Catalina Coll i Laura Gómez, noves i prometedores incorporacions al grup. També als antics companys del LENS, Dr Sònia Conesa, Dr Marie Hélène Chambrier, Dr Yuanbin Qin i Xavier Sastre.

A tots els profes de l'assignatura d'Informàtica, encapçalats per el Dr. José María Gómez. Una salutació als meus companys a les aules, Dr. Ricardo Mayol i Daniel Alsina. També voldria agrair al Prof. Francesc Salvat, que ens va donar valuosos consells i eines de càlcul i simulació.

To all my friends at the Ernst Ruska-Centre (ER-C) in Jülich, Germany, which hosted me for three months; for allowing me full access to their cutting edge electron microscopy facilities and great scientific advice. Starting by my stage supervisors, Prof Rafal Dunin-Borkowski and Dr Martial Duchamp, thank you for your time and kindness, specially Martial, we spent many hours together in the microscope and FIB, sometimes in suffering because the samples were destroyed, but also performing great experiment and having a beer and many good times.

Also from ER-C, Prof Karsten Tillman and my office mate Prof Giulio Pozzi, for good memories and a most marvellous photo session at the microscope. And to Drs Chris Boothroyd, Amir Tavabi, Vadim Mingunov, Daniel Stroppa, Justinas Palisaitis, Sheri Chang, Chris Dwyer and András Kóvacs; so many good memories, such as visiting (probably) all the bars in Jülich, which by the way is not so difficult, visiting many more bars in Köln and driving a huge van full of valuable belongings in the autobahn! ... Apart from having a great time, these people have to be acknowledged for the great scientific insight they provided, always discussing new experiments and possibilities, sharing ideas and advice about the use of the instruments and fruitful scientific discussions!

To our our collaborators, that exemplify the virtues of scientific partnership. Big thanks to: Drs César Magén and Raúl Arenal from LMA-INA and Universidad de Zaragoza; Prof Ernesto Calleja and Drs Žarco Gačević and Sergio Fernández-Garrido from ISOM, Universidad Politécnica de Madrid. Dr Francisco de la Peña from University of Cambridge, also deserves an acknowledgment, for much useful advice and teaching me to use the HyperSpy software. Finally, many thanks to all the people involved in the national electron microscopy project IMAGINE, Materials at the sub-Ångstrom Resolution, from multiple Universities in Spain.

---

En el terreno profesional mis agradecimientos mas especiales van dedicados a las Drs Francesca Peiró y Sònia Estradé, directoras de esta tesis doctoral. Gracias por haberme brindado un apoyo constante, con un trato siempre excelente, y, en definitiva, por haberme dado la oportunidad de realizar un trabajo del que estoy orgulloso. Espero que mantengamos el contacto a través de la colaboración científica y si algún día dejo de mirar electrones, siempre nos quedará el Pollo Rico.

Tampoco habría sido posible llevar esta empresa a buen puerto sin la gente que es capaz de aportar una solución a los problemas cuando todas las otra cosas fallan. Gracias a mis amigos en Barcelona: de la casa del puma y el grupo de Borras, Jordi Samà, Manuel Villa, José Luis Cárdenas, Carme Gómez, Miquel Martí, Lucasz Grisales. A los amigos del Master de Biofísica, Melchor Sánchez (y Marce), Max von Vopelius, Cristina Sans, Guillermo Rodríguez, David Palau, Cristian Esplugas, Sara Teller, David Frigola...

A tódala familia dos Harmónicos Esféricos, Dr Ricardo Escudero, Bieito Fernández, Xesus Luís González, María Fuciños, Lorena Nieves y Dios, Maribel Verdú y La Cerveza. Un saúdo pra xente que daquela andaba pola USC, en particular, Dr Raquel Eirey, Antón Fente, Rosalía Rodríguez, Pablo Argüeso e o auténtico Nacho Vidal. Os amigos de sempre en Vigo, Daniel Torrado, Adrián Cortizo (& family), Lino Rodriguez, Omar Torrado, Jorge y Dan Castro, Nano Bravo... polos tempos de basuring na Cruz! Gracias polas infalibles xuntanzas e por lembrar ás historias de cando éramos más nenos.

A mi Familia, que hacen que me sienta como en casa esté en Barcelona o en Madrid. A mi abuelo Paco y mi abuela Inés. A mi Hermano, Daniel, que ha tenido fácil ser mejor persona y guitarrista que yo.

A mis Padres, Pilar e Isaac, sin ellos, estrictamente hablando, nada de esto habría ocurrido. En este momento y por brevedad, quizá lo que tenga mayor sentido es agradecerlos la educación que me habeis dado.

Y a mi compañera Anna, que renueva a cada momento mi ilusión y ganas de continuar caminando por todos los senderos de esta vida.

Barcelona, Julio 2015.



# Contents

<b>Agradecimientos</b>	<b>i</b>
<b>1 Introduction</b>	<b>3</b>
1.1 Why STEM-EELS? . . . . .	3
1.1.1 Scope of this thesis . . . . .	5
1.2 Fundamentals of EELS . . . . .	6
1.2.1 Electron imaging and spectroscopy . . . . .	6
1.2.2 Electron scattering . . . . .	11
1.2.3 Low-loss and core-loss . . . . .	16
1.2.4 Single, plural and multiple scattering . . . . .	22
1.2.5 Resolution limits . . . . .	23
1.3 Physical elements for low-loss EELS . . . . .	28
1.3.1 Dielectric model for material media . . . . .	28
1.3.2 Dielectric formulation of low-loss EELS . . . . .	38
<b>2 Methods</b>	<b>51</b>
2.1 Analytical tools for low-loss EELS . . . . .	51
2.1.1 Calibration and deconvolution . . . . .	53
2.1.2 Kramers-Kronig analysis . . . . .	60
2.1.3 Bethe f-sum . . . . .	64
2.2 Hyperspectral analysis . . . . .	67
2.2.1 Multivariate analysis . . . . .	67
2.3 Ab-initio simulation tools . . . . .	71
2.3.1 DFT simulations with Wien2k . . . . .	72
<b>3 DFT modeling of wurtzite III-nitride ternary alloys</b>	<b>81</b>
3.1 Introduction . . . . .	82
3.1.1 Band structure based calculations . . . . .	83
3.1.2 Modeling the dielectric response . . . . .	83
3.2 Simulation of the binary compounds . . . . .	84

3.2.1	Initial set-up of the structures . . . . .	84
3.2.2	Band structure and density of states . . . . .	87
3.2.3	Complex dielectric and energy-loss functions . . . . .	89
3.3	Simulation of the ternary alloys . . . . .	90
3.3.1	Super-cell approach . . . . .	90
3.3.2	Band gap . . . . .	91
3.3.3	Plasmon energy . . . . .	92
3.3.4	CDF zero-cut energy . . . . .	94
3.4	Conclusions . . . . .	95
<b>4</b>	<b>AlN/GaN and InAlN/GaN DBRs</b>	<b>103</b>
4.1	Introduction . . . . .	104
4.2	System I: AlN / GaN DBR . . . . .	106
4.2.1	Sample details and previous characterization . . . . .	106
4.2.2	Characterization through plasmon peak position . . . . .	107
4.2.3	Anomalous segregation regions . . . . .	111
4.3	System II: InAlN / GaN DBR . . . . .	115
4.3.1	Sample details and previous characterization . . . . .	116
4.3.2	Low-loss EELS data treatment . . . . .	117
4.3.3	Composition and bowing parameter from Vegard law . . . . .	120
4.3.4	Optoelectronic and structural properties . . . . .	122
4.3.5	Assesing the impact of retardation losses . . . . .	126
4.4	Conclusions . . . . .	128
<b>5</b>	<b>Multiple InGaN QW heterostructure</b>	<b>137</b>
5.1	Introduction . . . . .	138
5.1.1	Structure growth and previous experiments . . . . .	138
5.2	High resolution HAADF image analysis . . . . .	140
5.3	Band gap and plasmon analysis . . . . .	143
5.3.1	Low-loss EELS in nanometer-sized structures . . . . .	144
5.3.2	Band gap energy . . . . .	144
5.3.3	Plasmon analysis . . . . .	147
5.4	KKA and electronic properties . . . . .	149
5.4.1	Zero-cut energy . . . . .	150
5.4.2	Electron effective mass . . . . .	151
5.4.3	Ga 3d intensity . . . . .	152
5.5	Conclusions . . . . .	154

<b>6 Er-doped Si-nc/SiO<sub>2</sub> multilayer</b>	<b>163</b>
6.1 Introduction . . . . .	164
6.1.1 Sample details and preliminary examination . . . . .	165
6.2 HAADF and relative thickness analysis . . . . .	167
6.3 Measuring the Si-ncs plasmon energy . . . . .	169
6.3.1 Double plasmon fit . . . . .	170
6.3.2 Discussion . . . . .	174
6.4 Conclusions . . . . .	175
<b>7 Si-NCs embedded in dielectric matrices</b>	<b>179</b>
7.1 Introduction . . . . .	180
7.1.1 Sample details and preliminary examinations . . . . .	180
7.2 Phase identification and MVA analysis . . . . .	183
7.2.1 Analytical methodology . . . . .	183
7.2.2 System I: silicon oxide barriers . . . . .	188
7.2.3 System II: silicon carbide barriers . . . . .	191
7.2.4 System III: silicon nitride barriers . . . . .	193
7.2.5 Discussion and remarks . . . . .	195
7.3 Optoelectronic properties of the Si-NCs . . . . .	196
7.3.1 KKA in the Si-NCs and dielectric regions . . . . .	198
7.3.2 Band gap measurements . . . . .	198
7.3.3 Electron effective mass . . . . .	201
7.4 Conclusions . . . . .	202
<b>8 Conclusions</b>	<b>211</b>
8.1 Simulation of group-III ternary compounds . . . . .	212
8.2 Group-III ternary compound-based structures . . . . .	213
8.3 Silicon-based structures . . . . .	216
<b>A Sample growth, preparation procedures and instrumentation</b>	<b>221</b>
<b>B Resumen en Español</b>	<b>225</b>
<b>C Scientific Curriculum</b>	<b>233</b>







# Chapter 1

## Introduction

“(...) All collected data had come to a final end. Nothing was left to be collected. But all collected data had yet to be completely correlated and put together in all possible relationships. A timeless interval was spent in doing that. And it came to pass that AC learned how to reverse the direction of entropy. But there was now no man to whom AC might give the answer of the last question. No matter. The answer – by demonstration – would take care of that, too. For another timeless interval, AC thought how best to do this. Carefully, AC organized the program. The consciousness of AC encompassed all of what had once been a Universe and brooded over what was now Chaos. Step by step, it must be done.

And AC said, "LET THERE BE LIGHT!"  
And there was light—”

---

Isaac Asimov, *The last question*

### 1.1 Why STEM-EELS?

Microscopy has evolved from the rudimentary optical instruments of the 17<sup>th</sup> century to a multidisciplinary science that connects many different technological branches and knowledge fields. Seemingly disparate applications of life and material sciences are now related by similar imaging and spectroscopic characterization solutions. Electron microscopy is an example of this advance and diversification process, offering both imaging and spectroscopic techniques capable of exploring materials at the nanometer level and beyond.

The invention of electron microscopy took place at the beginning of the 20<sup>th</sup> century. As the understanding of the physical laws was quickly increasing, new

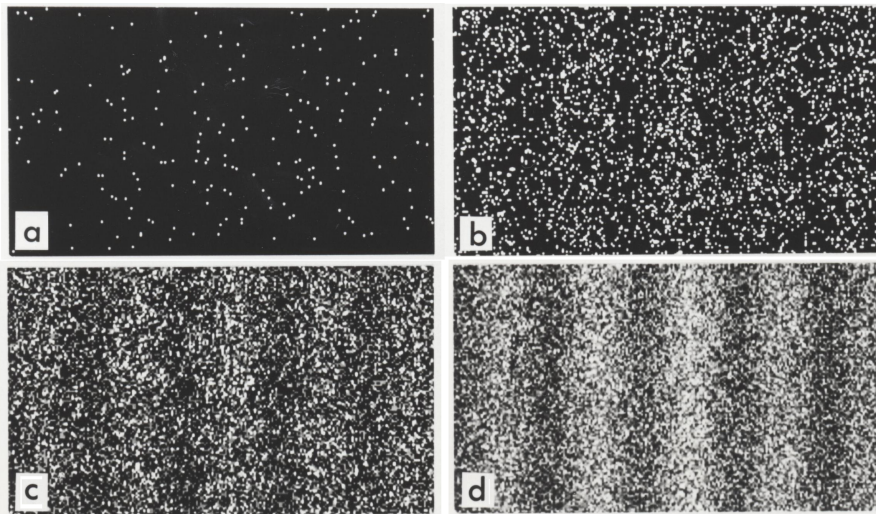


**Fig. 1.1** Results of a double-slit-experiment performed by Dr. Tanamura showing the build-up of an interference pattern of single electrons. Numbers of electrons are 200 (a), 6000 (b), 40000 (c), 140000 (d). Adapted from Ref. 3.

possible experiments and techniques appeared. Before that, only optical instruments existed, with their spatial resolution constrained by the wavelength of visible light. Then, in 1925, in order to fix inconsistencies in the emerging field of quantum physics, Louis de Broglie theorized that the electron could sometimes behave as a wave, and sometimes as a particle. The wave-particle duality theory was confirmed by experiments as soon as two years later. The first magnetic lenses were devised by Busch that same year<sup>1</sup>. This event opened the gates for the construction of the first electron microscope, culminated in 1932 with the instrument of Knoll and Ruska<sup>2</sup>. Only 7 years had passed since it was first realized that fast electrons have a wavelength in the order of the picometer and interact strongly with matter, and they were starting to be used for imaging and spectroscopic purposes.

Richard Feynman, at his famous lectures<sup>4</sup>, thought of a time when electron microscopy would be able to directly resolve crystalline structures and chemical compounds at the atomic level. At that time (1970s), electron optics in transmission electron microscopy (TEM) suffered from incorrigible aberrations. The unleashing of electron resolution then seemed a hopeless case, aberrations arresting the dawn of this new era.

Nowadays, thanks to the generalization of aberration correction, modern TEMs feature powerful electron optics that produce probes with sizes below the

nanometer. Additionally, modern instruments are versatile tools that allow for many different possibilities of operation. There are different modes for electron optics to be configured, e.g. the scanning TEM (STEM) mode to raster a very small probe along given areas in order to form a pixel-by-pixel map. There are also many complementary characterization techniques that can be performed using specific detectors attached to the TEM column. One of these techniques, and the *raison d'être* of the present work, is electron energy loss spectroscopy (EELS).

Although it is presented as a TEM-related technique, EELS can be viewed as a fundamental spectroscopic technique. It is based on a rather simple experiment. EELS measures the energy lost by a beam of electrons upon transmission through a thin film sample. The recorded spectrum, an energy-loss distribution, is characteristic of the chemical and electronic properties of the material probed by the electron beam. In this way, EELS represents a valuable source of information capable of retrieving many material properties, most of them inaccessible to other TEM methods, and within the small volumes defined by the electron-matter interaction.

The resolution limits of electron spectroscopy techniques in the TEM have also been greatly improved in the recent past. We owe this improvement to the generalization of electron beam monochromation. Modern systems feature energy resolutions well below the electron-volt range. Interesting material properties, *e.g.* related to the material valence band structure, can be measured directly in spectra acquired at great spatial resolution. In the last few years, extremely powerful STEM-EELS instruments have appeared, capable of measuring spectra at the atomic level, with an energy resolution in the meV range. In future years the power of the TEM to resolve even smaller structures will further increase, hopefully beyond our imagination. Ground breaking applications in the field of solid-state physics and optics have already been devised for these ultimate resolution experiments.

### 1.1.1 Scope of this thesis

In this work, we examine structures of interest in the semiconductor materials field that demand characterization solutions at the higher resolution available. The examined semiconductor materials are based on silicon or III-V nitrides, among the more important of their kind for industrial applications. The analyzed samples contain structures, from thin deposited layers to quantum well and dot structures, in the nanometer size range. Our tool of choice, the aberration-corrected and beam-monochromated STEM, gives us the opportunity to push the resolution barrier close to the atomic level. Our aim is to explore the analytical capabilities of the EELS technique in these interesting materials and using the

most advanced tools.

The following sections in this chapter give an overview of the theoretical foundations of the EELS technique. The low-loss part of the EEL spectrum will be our main analysis tool, so a special focus is put on its main features; the link of the spectral features with theoretical properties of materials and the limitations of the technique. A following chapter describes the analytical and theoretical Methods that are used to treat the experimental data and to simulate spectral shapes. Indeed, this thesis includes results from both analytical and theoretical work. The simulation results are first presented in the third chapter, and after that, several more chapters deal with different analytical works. These chapters serve to introduce the more specific techniques that have been developed for the preparation of this research work. These results are aimed at the better understanding of the EELS spectrum, overcoming some of the limitations of the technique and revealing some interesting properties of the examined materials and structures.

## 1.2 Fundamentals of EELS

The following sections introduce the EELS technique as performed in modern STEM instruments. First, some general concepts regarding TEM and related spectroscopies are reviewed. Then, the scattering processes that occur in the interaction of the electron beam with the sample are introduced. Finally, some physical limitations to the EELS spatial and energy resolution are explained.

### 1.2.1 Electron imaging and spectroscopy

All electron microscopes, for imaging and/or spectroscopic purposes, use an accelerated electron beam as an illumination source. In any TEM system, the electron beam is focused onto a thin film sample through which it is transmitted. The resulting exit-wave distribution is projected into a viewing screen or charge-coupled device (CCD) detector. The EELS experiment consists in measuring the energy-loss distribution of the electrons in this exit-wave (or outgoing beam).

The accelerating voltages typically used in TEM systems determine the initial electron speed,  $v$ , or in other words its initial kinetic energy,  $E_0$ . Any energy spread in the beam is disregarded in the following description. In other words, we assume that the incident electrons have nearly equal  $E_0$  before interacting with the thin film sample. In general applications, these energies are fairly large, typically between tens of keV and a few MeV. Hence, relativistic kinematics have to be used in order to calculate accurately the electron speeds, *e.g* using the following formula,

$$\frac{v^2}{c^2} = \frac{E_0(E_0 + 2m_0c^2)}{(E_0 + m_0c^2)^2} \quad (1.1)$$

where  $m_0$  is the electron rest mass, given by  $m_0c^2 \sim 511$  keV. To grasp the magnitude of the involved speeds, consider that electrons accelerated at  $E_0$  in the range of 80 – 300 keV travel at  $v$  between 0.50 – 0.78  $c$ . In a typical experiment, the great kinetic energy of the electrons means that they travel so *fast* that even at the highest intensities used in the microscope only one electron is *being* transmitted through the sample at a given time.

More importantly, these speeds are also huge when compared to the mean orbital speed of atomic or molecular electrons in their shells. For instance, in the Bohr model, the mean  $v/c$  value for the first circular orbit is given by the fine structure constant,  $\alpha(\alpha^{-1} \sim 137)$ , well below the speed of a typical TEM electron beam. In solids, another measure of the electron mean orbital speed, the Fermi velocity, is also typically below the electron beam speed. This feature of the beam has allowed theoretical physicists to treat the interaction of the fast electrons with matter in terms of perturbation theory<sup>5</sup>, as explained ahead in this text.

The ability to curve, focus and shape an electron beam is determined by the electron-optics (see Fig. 1.2), composed of round magnetic lenses, interchangeable apertures, and sometimes other elements. Modern TEM configurations mostly comprise common, similar elements. The illumination system is composed of an electron gun and condenser lens(es). In conventional TEM, the electron beam is focused onto the sample to achieve near-parallel illumination. When in STEM mode, the illumination system forms the smallest possible electron probe onto the sample. The image forming system is composed of the objective, intermediate and

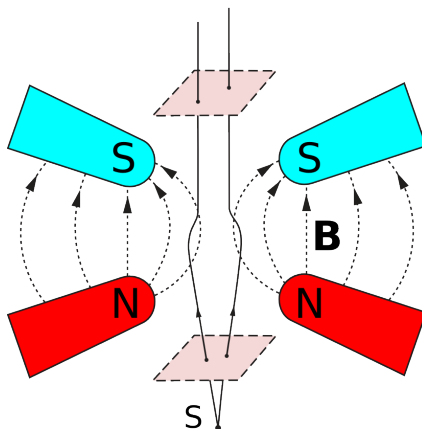


**Fig. 1.2** Electron beam focusing ability through the magnetic field created by a magnetic lens, represented here in a schematic way. Adapted from Ref. 4.

projective lenses. Images or diffraction patterns are formed with the objective lens, closest to the sample, and selected by the intermediate lens(es). Finally, magnification is chosen by means of the projective lens.

The study of the energy-loss distribution of the outgoing electrons is equivalent to the study of the distribution of speeds. One way of measuring the velocity distribution in practice is by using a homogeneous magnetic field<sup>6</sup>, in a device called a magnetic prism spectrometer, depicted schematically in Fig. 1.3. The effect of the magnetic field in this device is to bend the electron beam to a circular trajectory. Electrons traveling at different speeds will have a different radius, that is also a function of the strength of the magnetic field. A dispersion of these trajectories is observed when electrons travel at different speeds in a beam. This dispersion is what allows us to measure the energy loss. We will not go into more detail about the design of such devices, which is very complex. For instance, magnification of the dispersion plane is achieved by additional electron optics, specifically designed to obtain the correct focusing properties. See Ref. 7 and references within for a detailed account on the design of magnetic prisms for EELS applications.

Different spectrometer models exist for different applications. A popular one is the parallel recording spectrometer<sup>8</sup>, preferred for producing single spectra. Another typical configuration, the image filter<sup>9</sup>, is preferred for energy-filtered TEM (EFTEM) imaging applications. Most modern TEMs, that also have the capability to operate in STEM mode, are equipped with some model of Gatan imaging filter (GIF). This is a family of post-column image filters that double as

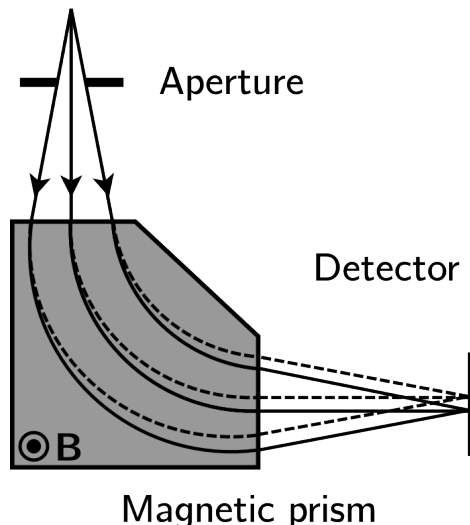


**Fig. 1.3** Operation principle of the EELS spectrometer: electrons follow circular trajectories in a magnetic field, with a radius that depends on their speed. The field is generated in a magnetic prism. Two different speeds are depicted here, solid and dashed lines, the solid one being faster and, thus, having a bigger radius.

a parallel recording spectrometer.

The configuration of the elements in the microscope is of major relevance for any EELS experiment performed in a STEM system. For the sake of simplicity, it is useful to describe very schematically this configuration, as depicted in Fig. 1.4. In a STEM experiment the illumination system of the microscope is in charge of producing a very small probe, as already mentioned. We need to consider the size of this probe, or spot size, and the angular spread of the incident beam,  $\alpha$ , the convergence angle. For most applications we choose spot sizes in the order of the nm or less, and convergence angles of a few mrad. Once the beam is transmitted through the sample and projected by the post-specimen lenses, only a fraction enters the EELS spectrometer. A collection angle is then defined, considering the angular aperture and camera length of the projector/spectrometer system.

As a first approach to theoretical resolution, the diffraction-limited resolution of any imaging system can be approximated using the Rayleigh criterion<sup>10</sup>. In this approach, the radius of the Airy disc formed by an incoherent source is related to the wavelength of the radiation and the angle-limiting aperture of the system. Some values of the Airy disc radius as a function of collection angle and electron wavelength are included in Fig. 1.5. This figure also shows the inverse dependence of the electron wavelength with the voltage being used in the microscope. Although this criterion alone should not be used to calculate the resolution of a real system (see section 1.2.5), it illustrates an important point in electron microscopy: higher voltages are desirable when possible, as they will

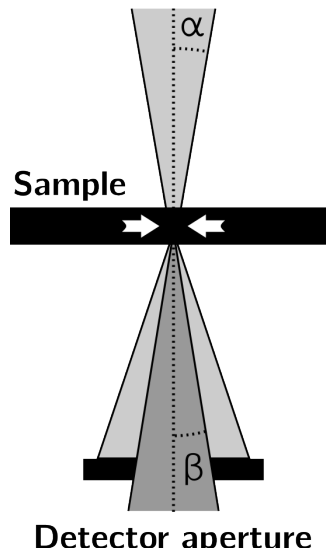


**Fig. 1.4** The schematic description of the EELS experiment attending only to the convergence and collection (semi) angles. The convergence angle,  $\alpha$ , is depicted at the top of the image. The collection angle,  $\beta$ , appears below, limited by the aperture of the detector. The finite size of the beam over the sample is also qualitatively indicated using two white lines.

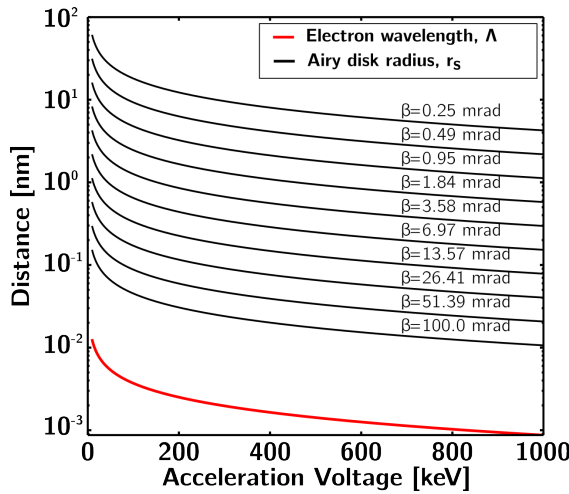


**Fig. 1.5** In black lines, Airy disc radius,  $r_s$ , for a series of apertures,  $\beta$ , and electron wavelengths,  $\Lambda$ . The Airy disc radius,  $r_s = 1.22\Lambda\beta^{-1}$ , gives the diffraction-limited resolution in the Rayleigh criterion. A red line is used to depict the dependence of the electron wavelength with energy.

give higher resolutions. However, the caveat is that the processes of electron scattering and diffraction as well as beam induced damage (the interaction of the electrons with the sample) are also affected by the energy of the impinging electrons. In fact, much effort is spent through this text addressing some of these relationships. Modern instruments are capable of revealing detail well below the nanometer range, thanks to the generalization of aberration correction (more in Sec. 1.2.5).

Following the given definitions for the STEM-EELS experiments, we see that the object of study here is the momentum distribution of the electron exit-wave from a small probe-volume. Actually, this is just one of the characteristic radiations that can be studied when the high energy electrons are transmitted through a sample. A variety of interaction processes involve the emission of photons and electrons which can be detected and analyzed. For instance, an example of a technique exploiting photon radiation in the TEM in the form of X-ray emission is energy dispersive spectroscopy (EDS). The process behind X-ray emission is the relaxation of atomic core electrons that have been excited by a fast electron from the beam. The atomic species in the sample are identified by a characteristic EDS energy.

It turns out that a mode analogous to EDS exists in the EELS technique. EELS measures the energy lost by the transmitted electrons when they interact *inelastically* with the sample. Among these electrons, those that excited *core* levels of atoms in a process analogous to XES may be measured. However, there is a vast array of other possible interactions of electrons with material media. Moreover, experimental spectra are constituted by mixed signals related to some

of these possible interactions. This fact increases perhaps the complexity of the analysis of EELS data, when the different contributions to our experimental spectra have to be identified. It is thus necessary to start a classification of the different processes that affect the fast electron interaction with a specimen, and may be behind an energy-loss spectrum.

Before that, the acquisition modes in each experiment present additional differences that need to be addressed. In some experiments, multiple spectra are acquired successively to characterize spatial variations in the sample. In this acquisition modes, equally spaced spectra are collected along a line or inside an area as the STEM probe rasters the specimen. Such *hyperspectral* acquisition modes have some analytical advantages, as they allow to monitor changes in localized regions of the sample. In EELS jargon, these modes are typically called spectrum lines or spectrum images (SL or SI), for the 1- or 2-dimensional acquisitions, respectively.

### 1.2.2 Electron scattering

In a scattering process, a form of radiation is deviated from its initial trajectory due to the interaction with a medium through which it passes. There is a close relationship between the fast development of quantum theory and beam scattering experiments. A well known example is the devising of the first atomic model by Rutherford, after a series of  $\alpha$  particle scattering experiments by Geiger and Marsden<sup>11</sup>. Similarly, in EELS one studies the scattering of fast electrons by material media. More precisely, these fast electrons change their momentum and kinetic energy upon interaction with the constituents of the sample.

A first general classification of the electron interaction processes can be made attending solely to the existence of an energy exchange. In this energy-wise sense, classification of scattering involves the distinction between elastic and inelastic processes. It is said that pure elastic processes are those that involve no energy change whatsoever for the scattered particle. In turn, an inelastic process involves some energy exchange between the scattered particle and the medium. This energy exchange is governed by the usual laws for the conservation of energy and momentum. In electron spectroscopy some interaction processes, involve an energy exchange so small that it is negligible. These processes are also termed elastic scattering, as there is practically no measured energy-loss. In order to better understand this subject it is useful to introduce some concepts about the kinematics of scattering processes.

#### Kinematics of scattering

In this section, the relativistic kinematics of the scattering process are reviewed taking only into account the projectile, a fast electron. The description takes

into account the initial and final state of this particle. Let us start with the initial momentum and total energy of the incident electron, which are set from the beginning of the experiment. If we call the initial momentum  $\mathbf{p}$ ,

$$\mathbf{p} = \gamma m_0 \mathbf{v} = \mathbf{k}_0 \hbar \quad (1.2)$$

where  $\mathbf{v}$  is the electron initial velocity and  $m_0$  its rest mass. Notice that the right-hand term of this equation expresses the initial momentum in units of  $\hbar$ , as a wave-vector,  $\mathbf{k}_0$ . This notation will be useful later on, in the quantization of the electromagnetic field. The Lorentz factor present in this equation,  $\gamma$ , is also equivalent to the total energy of the incident electron expressed in units of the electron rest energy  $m_0 c^2$ . This value of the total energy can also be obtained from the relativistic speed of the electron as,

$$\gamma = \sqrt{1 - (v/c)^2} \quad (1.3)$$

Another way of defining the electron total energy is in natural units for energy, *e.g.* eV, using its kinetic energy  $E_0$ , set by the accelerating voltage. If we call this total energy,  $W_0$ , then it is defined as,

$$W_0 = \gamma m_0 c^2 = E_0 + m_0 c^2 \quad (1.4)$$

Total electron energy after interaction is obtained through conservation of energy  $W_1 = W_0 - E$ . Since  $E$  is the energy loss which is measured in EELS, this quantity is typically known. Electron momentum after interaction  $\mathbf{k}_1$ , is defined through conservation of momentum, see Fig. 1.6. This conservation law requires the introduction of a momentum transfer,  $\mathbf{q}$ . It turns out that momentum transfer is unknown, but we can use conservation of energy to express  $k_1$ , the modulus of the final momentum, as a function of the known variables,

$$k_1^2 = k_0^2 - 2\gamma m_0 E / \hbar^2 + E^2 / (\hbar c)^2 \quad (1.5)$$

Both conservation laws for energy and momentum can be used together to obtain an expression for the magnitude of the momentum transfer as a function of energy loss and scattering angle, *i.e.*  $q = q(\theta, E)$ . The scattering angle,  $\theta$ , is the angle through which the electron is deflected. This relationship for the momentum transfer is rather long and cumbersome<sup>7</sup>, and will not be reproduced here. Nevertheless, we will give some definitions that stem from that equation, in a small scattering angle approximation. The first one concerns the minimum attainable momentum transfer,  $q(\theta = 0, E) = q_{min}(E) \approx k_0 \theta_E$ . Where,

$$\theta_E = \frac{E}{\gamma m_0 v^2} \quad (1.6)$$

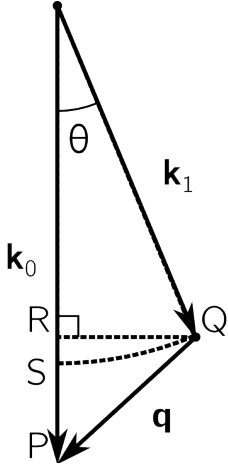


**Fig. 1.6** Vector diagram for the conservation of momentum, as given in the text,  $\mathbf{q} = \mathbf{k}_1 - \mathbf{k}_0$ . The dashed circle defines different values of  $q$  and  $\theta$  for a given  $\mathbf{k}_1$ , see Eq. (1.5). For small  $\theta$ ,  $RP \sim SP \sim k_0\theta_E$  and  $RQ \sim k_1\theta \sim k_0\theta$ , leading to the approximate solution in Eq. (1.7). The original diagram is included in Ref. 7.

$\theta_E$  is called the characteristic scattering angle, which becomes relevant in the description of inelastic scattering at low angles (see Sec. 1.2.3 and beyond). In fact, this definition allows to find a shorter expression for the momentum transfer in the case  $E \ll E_0$ ,

$$q^2 = q_{min} + 4k_0k_1 \sin^2(\theta/2) \approx k_0^2(\theta^2 + \theta_E^2) \quad (1.7)$$

The right-hand side approximation holds for scattering angles much smaller than 1 rad. In other words, for  $\theta \ll 1$  rad, the momentum transfer can be approximated using the quadratic sum of the characteristic and actual scattering angle, in units of the initial momentum. This approximation generally holds and is used since the convergence and collection angles in STEM experiments are in the order of 10 mrad.

### Elastic scattering processes

In a purely elastic scattering event  $k_0 = k_1$  and  $E = 0$ ; the incident and final momenta have the same magnitude and there is no energy loss. By solving Eq. (1.7) with these conditions, momentum transfer is shown to be a function solely of the scattering angle and the incident momentum,

$$q = 2k_0 \sin(\theta/2) \quad (1.8)$$

In a transmission experiment, some of the electrons in the beam do not interact with the specimen in any way. By this definition, a fraction of the total outgoing intensity is termed direct beam. Since in TEM analysis the sample is

typically very thin, it is usually among the more intense parts of the total signal. These electrons travel with the same velocity as the incident beam, they have emerged from the sample literally unscathed. These exit trajectories are expected inside a cone centered around the optical axis, with a diameter determined by the incidence angle. As introduced above, in a STEM set-up the maximum incidence angle is given by the probe convergence angle,  $\alpha$ . As a consequence, in the back focal plane, the direct beam is a central spot with a diameter proportional to  $2\alpha$ , as seen in convergent beam electron diffraction (CBED)<sup>10</sup>.

A fraction of the electrons interact with the electrostatic field of the atomic nuclei in the sample. To the negatively-charged fast electron this field is attractive, because it is generated by the positive nucleus and the partial screening of the atomic electrons. This interaction is termed elastic scattering because of the huge difference between the mass of the atomic nucleus and the fast electron. Hence, the trajectory of this fast electron is deflected with a negligible associated energy-loss, by a scattering angle close to the above defined  $\theta$ . This insignificant energy-loss is equal to the recoil energy associated with the momentum transfer of the fast electron to the atomic nucleus mass. Typical recoil energies in TEM experiments are  $< 0.1$  eV<sup>7</sup>, not even measurable for the typical EELS spectrometers.

In scattering experiments it is instructive to define the probability of scattering per unit solid angle,  $\Omega$ , called the differential cross section (DCS). Using our definition of momentum transfer and taking the Fourier transform of the atomic potential,  $V(r)$ , to be proportional to an elastic form factor,  $F(q)$ , the elastic DCS for a single atomic species takes the following general form:

$$\frac{d\sigma}{d\Omega} = \frac{4\gamma^2}{a_0^2 q^4} |F(q)|^2 \quad (1.9)$$

Here  $a_0$  is the first Bohr radius. Within some general approximations and including a model for screening, analytical formulas for the elastic scattering DCS can be obtained. A notable method is the semi-classical Lenz model, that incorporates screening through the Wentzel-Yukawa potential,

$$\frac{d\sigma}{d\Omega} = \frac{4\gamma^2}{a_0^2} \left( \frac{Z}{q^2 + r_0^{-2}} \right)^2 \sim \frac{4\gamma^2 Z^2}{a_0^2 k_0^4} \frac{1}{(\theta^2 + \theta_0^2)^2} \quad (1.10)$$

where  $Z$  is the atomic number,  $r_0$  is the potential screening radius and  $\theta_0$  is a characteristic angle of elastic scattering such that  $\theta_0 = (k_0 r_0)^{-1}$  (see Fig. 1.6). Additionally, this model gives an estimate of the screening radius, as  $r_0 = a_0 Z^{-1/3}$ . This relatively simple model provides an estimate of the atomic DCS. More refined methods for the calculation of atomic DCS exist, such as full-relativistic Mott cross sections.

The single-atom elastic DCS are only useful for gases and amorphous materials; the theory needs to be extended to the case of crystalline specimens. In a crystalline material atoms are regularly arranged forming a lattice and the electron wave scattered from each atom in the lattice interferes with itself. In this case, atomic electron scattering is modulated by a structure factor,  $F(\theta)$ , again related with the Fourier transform of the lattice. Without further detail, the direct consequence of this formulation is the well known Bragg equation for the reflection maxima<sup>12</sup>. This equation states that for an incident electron wavelength  $\Lambda$ , a family of atomic planes with spacing  $d$  modulates the atomic scattering with a maximum at the characteristic Bragg angle  $\theta_B$ :

$$\Lambda = 2d \sin \theta_B \quad (1.11)$$

In a diffraction pattern, this means that bright spots appear where Bragg conditions are fulfilled, surrounding the direct beam. An alternative point of view is that these spots are the constructive interference of the exit electron waves.

This formulation is at the basis of the formation of diffraction patterns and images in TEM, but is of no less importance for EELS. This is because, in practice, the most common configuration for the acquisition of spatially resolved energy-loss spectra from crystalline specimens places the aperture of the detector over the central spot of the diffraction pattern (see  $\beta$  in Fig. 1.4). Of course, this central spot is composed of the direct beam and elastically and inelastically scattered electrons. In fact, a small collection angle configuration is preferred since most inelastic scattering is contained in a narrow cone surrounding the optical axis. As long as a small angle configuration is set-up, the intensity from this central spot dominates for a crystalline sample (see  $2\theta_B$  in Eq. (1.11)). In other words, most of the Bragg scattered electrons are left outside the energy-loss spectra. Conversely, atomic elastic scattering is axially symmetric and dominant for amorphous materials. The intensity entering the detector is much reduced in relation to the total elastic scattering intensity (see  $2\theta_0$  in Eq. (1.10)). The importance of this fact will become apparent in the following section.

### The zero-loss peak

In general, all electrons which have undergone elastic scattering processes, or no scattering at all, once collected in the spectrometer, are focused to the same point. This is translated into an intense peak in the energy-loss spectrum at  $E = 0$ , the zero-loss peak (ZLP).

Figure 1.7 portrays an idealized EELS spectrum, containing the ZLP and other peaks, such as the plasmon excitation peak and a core-loss edge. The study of these features, associated to inelastic scattering, is the aim of any EELS

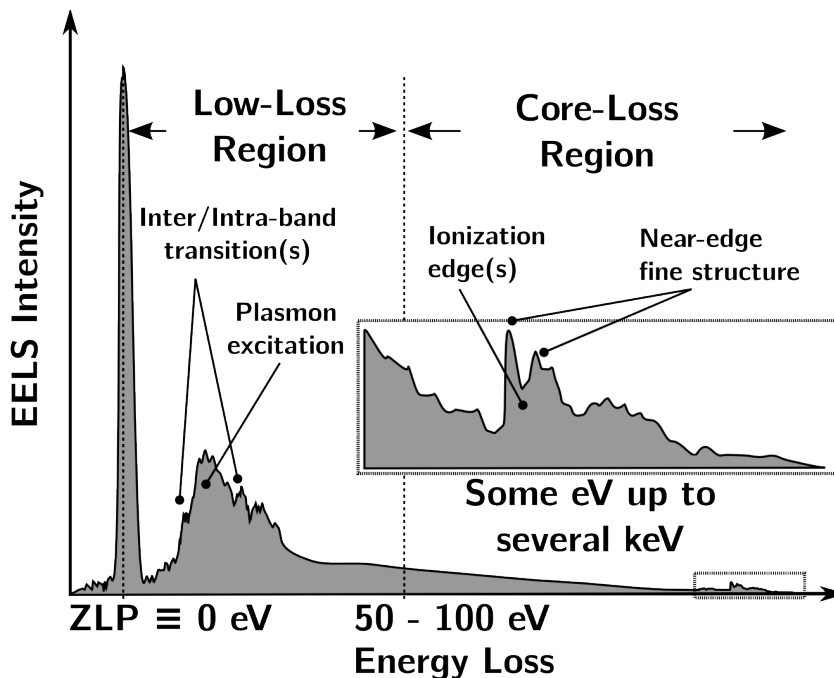


**Fig. 1.7** Idealization of a typical energy-loss spectrum, showing the zero-loss peak (ZLP) and low- and core-loss regions. The ZLP is always located at 0 eV, because it is associated with elastic scattering processes. The low- and core-loss regions contain inelastically scattered electrons.

experiment. Typically, EELS acquisition is difficult by the large intensity differences between the peaks. For thin-film analysis, the ZLP is almost always the most intense feature of an EELS spectrum. Depending on the energy dispersion of the beam, it will extend its tail into the low-loss region, beyond several eV. This poses a threat to the analysis of the inelastic signal at low energies. Apart from this fact, the ZLP is important because it can provide with an estimate of the sample thickness, as shown in Sec. 1.2.4.

### 1.2.3 Low-loss and core-loss

So far, elastic processes have been described, in which the interaction of the fast electron with the atoms in the specimen is mainly defined by the screened field of the atomic nucleus. In this picture, there is a large mass difference between the projectile and the target. Because of this difference, most elastic scattering at

small angles does not present an appreciable energy-loss. In inelastic processes this picture no longer holds because a given fast electron also interacts with atomic electrons; thus, the mass difference is small. This fact has two interesting consequences. First, the energy loss in this processes is not negligible; on the contrary, it can be in the order of a few keV. Second, the process of inelastic scattering is characteristic of the electronic configuration. However, it is necessary to develop a theoretical framework to conceptualize and take advantage of this fact.

Equivalent electron energy-loss processes have two radically different outcomes depending on the nature of the atomic electrons involved in it. According to this, two major regions may be distinguished in almost every energy-loss spectrum from a material medium: the low- and the core-loss region. The low-loss region is defined as the energy-loss range in which we expect to find those electrons that have interacted with the outermost electronic shells of a material. This energy region starts at zero energy-loss and goes up to several tens of eV, depending on the material. Conversely, the electrons above this energy-loss range have interacted with the innermost shells.

The difference in energy-loss ranges can be explained by a simple single-atom model. Outermost shells are relatively loosely bound to the atomic nucleus. They may absorb a small amount of energy and jump to an excited state. These energies are typically below some tens of eV. Conversely, innermost shells are more tightly bound to the atomic nucleus by a strong Coulomb field. Hence, these electronic states lie in orbitals closer to the nucleus and it may take a large amount of energy to excite one of them to an unoccupied orbital. These energies range from a few to thousands of eV. To improve the description of the fast electron interaction with the atom, let us take a closer look at the quantum-mechanical implications of this model.

### Bethe theory

In the single-atom view, the quantum mechanical problem of electronic scattering is approached using perturbation theory. This is just natural considering that the field of the incident electron is much smaller than the field of the target atom. For electrons with energies  $\sim 10$  keV and above, their velocity is large compared with the mean orbital velocity of the atomic electrons (see Sec. 1.2.1). Thus, they represent a sudden and small perturbation, and may be treated within the first order Born approximation framework. Additionally, we will consider the  $E \ll E_0$  case, that allows to use a plane-wave description for the incident and exit wave. Under this assumptions, Bethe developed a quantum-mechanical theory of inelastic scattering<sup>5,13</sup>. As in the elastic scattering case, the magnitude of interest is the differential cross section (DCS), the probability of an electron being inelastically scattered per unit solid angle. The first Born approximation

for a transition from an initial state  $\psi_0$  to a final state  $\psi_n$  reads,

$$\frac{d\sigma_n}{d\Omega} = \left( \frac{m_0}{2\pi\hbar^2} \right)^2 \frac{k_1}{k_0} \left| \int V(r) \psi_0 \psi_n^* e^{i\mathbf{q}\cdot\mathbf{r}} d\tau \right|^2 \quad (1.12)$$

This relationship gives the inelastic DCS, but models are still needed for the atomic wave-functions and the interaction potential (energy),  $-V(r)$ , for a fast electron at coordinate  $r$ . For high projectile energies, a full relativistic description of the interaction potential, including retardation effects is required<sup>7,14</sup>. This description is simplified for incident electrons with an energy below  $\sim 300$  keV, and the potential is written as,

$$V(r) = \frac{Ze^2}{4\pi\epsilon_0 r} - \frac{1}{4\pi\epsilon_0} \sum_{j=1}^Z \frac{e^2}{|\mathbf{r} - \mathbf{r}_j|} \quad (1.13)$$

Where the first term is the Coulomb attraction by the nucleus and the second one is the repulsion by each atomic electron. When evaluating the integral in Eq. (1.12) using this  $V(r)$ , the nuclear term adds to zero, because of the orthogonality of the wave-functions (also, nuclear positions are considered fixed). Thus, only the electronic terms matter for the inelastic DCS, reflecting its origin from electron-electron events. By rearranging these elements we have,

$$\frac{d\sigma_n}{d\Omega} = \left( \frac{2\gamma}{a_0 q^2} \right)^2 \frac{k_1}{k_0} \langle \psi_n | \sum_j e^{i\mathbf{q}\cdot\mathbf{r}_j} | \psi_0 \rangle^2 \equiv \left( \frac{2\gamma}{q} \right)^2 \frac{k_1}{k_0} \frac{R}{E_n} f_n(q) \quad (1.14)$$

Where  $f_n(q)$  is the generalized oscillator strength (GOS) of the target atom for the transition with an associated energy change  $E_n$ . Notice that  $R$  is the Rydberg energy,  $R = 13.6$  eV. Notice also that the GOS depends on a momentum matrix element, here presented in bra-ket notation, that contains the electronic state wave-functions. This formulation can be generalized to ionization transitions to a continuum of states, to explore the angular and energy dependence of inelastic scattering,

$$\frac{d^2\sigma}{d\Omega dE} = \left( \frac{2\gamma}{q} \right)^2 \frac{k_1}{k_0} \frac{R}{E_n} \frac{df}{dE}(q, E) \quad (1.15)$$

The angular dependence of this equation in the small angle limit can be examined by using the approximate kinematic relationship, Eq. (1.7). Notice also that the  $k_1/k_0$  factor tends to 1 as the momentum transfer is small. This approximation yields a Lorentzian dependence for inelastic scattering, with a characteristic scattering angle,  $\theta_E$ ,

$$\frac{d^2\sigma}{d\Omega dE} \approx \left(\frac{2\gamma}{k_0}\right)^2 \frac{R}{E} \left(\frac{1}{\theta^2 + \theta_E^2}\right) \frac{df}{dE}(q, E) \quad (1.16)$$

The meaning of  $\theta_E$  is of a half-width at half maximum (HWHM) of the distribution of scattering, which is more intense at small angles. The range of application for this approximation is also called dipole region. In this region of small scattering angle and relatively low energy loss the GOS is equivalent to a dipole oscillator strength;  $f(q, E) \rightarrow f(0, E)$ . This function is related with the optical absorption of an atom, *i.e.* its response to incident photons.

Bethe theory generally expresses the DCS as a product of two factors. One is related with the kinematics of the incident particle only. The other one is related with the quantum-mechanical description of the target atom only. This term is the GOS, which in Eq. (1.14) is explicitly shown to isolate the transition matrix element, also known as dynamic structure factor. This formalism can be generalized for material media, restricting the movement of the fast electron to a single axis. Then, the double-differential cross section (per atom) is related to the stopping power of the medium,

$$\frac{dE}{dx} = \int \int n_a E \frac{d^2\sigma}{d\Omega dE} d\Omega dE \quad (1.17)$$

where  $n_a$  is the number of atoms per unit volume of the medium, and  $x$  is an arbitrary axis. The importance of this equation and the concept of stopping power becomes apparent in the following sections, where the dielectric model is presented. In this sense, a model of the GOS will not be useful for the study of the features in low-loss EELS, but it is at the core of the analysis of the features at higher energies. In order to obtain a model of the GOS, an electronic

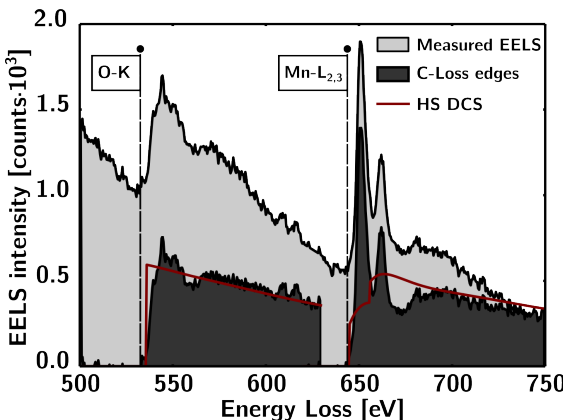


**Fig. 1.8** Experimental energy-loss spectrum from a  $La_{1/2}Sn_{1/2}MnO_3$  crystal, showing the O-K and Mn-L<sub>2,3</sub> core-loss edges. The edges have been striped from their background intensity using a model fit. The DCS used for quantification in the commercial software DigitalMicrograph are also portrayed, in red lines. They are obtained from a Hartree-Slater atomic calculation<sup>7</sup>.

structure model is needed. Simple models can be calculated for this purpose, such as the Hydrogenic model. In this model, the Schrödinger equation is solved using an effective nuclear charge and only one atomic electron. More complex models include self-consistent field calculations, such as, for example, Hartree-Slater calculations (see Fig. 1.8). Again, these equations are derived from a single-atom view and apply directly only to isolated atom situations, like low-density gases.

## Material media

Bethe theory constitutes the starting point for the analysis of core-shell excitations in material media, both crystalline and amorphous. This is so because the wavefunctions of the inner shells in the solid state material can be approximated by the single-atom ones. Nevertheless, in material media many atoms are present, producing a multiplicity of electronic energies that are represented, in solid state physics, by a continuous density of states (DOS). For a visual example, see Fig. 1.9.

Generally, it is the initial state of a tightly bound atomic electron involved in an inelastic scattering event that describes a core-loss process. The initial state gives its name to the characteristic energy-loss distribution: the core-loss edge (*e.g.* Carbon  $K_a$  edge). For different media composed of the same atomic species, but in a different structure or with a different stoichiometry, similar core-loss edges are expected. Yet, fine-structure modifications due to the solid state properties of the material media are also expected: this is the so-called energy-loss near edge structure (ELNES).

In the solid-state interpretation, the Fermi golden rule states that a DOS weights the transition matrix. This DOS is determined by the transition initial core level and final state (joint DOS). These states are in turn given by the local band structure at the excited atom site (local DOS). Of course, only transitions to unoccupied states above the Fermi level are permitted. Additionally, the strength of the transition is related to the dipole selection rule. When these considerations are examined in detail, it becomes clear that the characteristic ELNES modulations are related to local bonding effects, both chemical and structural properties of the material. Further effects are also to be expected in solid-state physics, like the core-hole effect or non-dipole effects, or the extended energy-loss fine structure (EXELFS) from multiple scattering.

Nevertheless, quantification based on atomic core-shell modeling is a most powerful EELS tool and analysis of the ELNES is also routinely performed. Ab initio calculations of the ELNES are also available, *e.g.* via density functional theory (DFT) software that is capable of obtaining the detailed band structure of many systems.

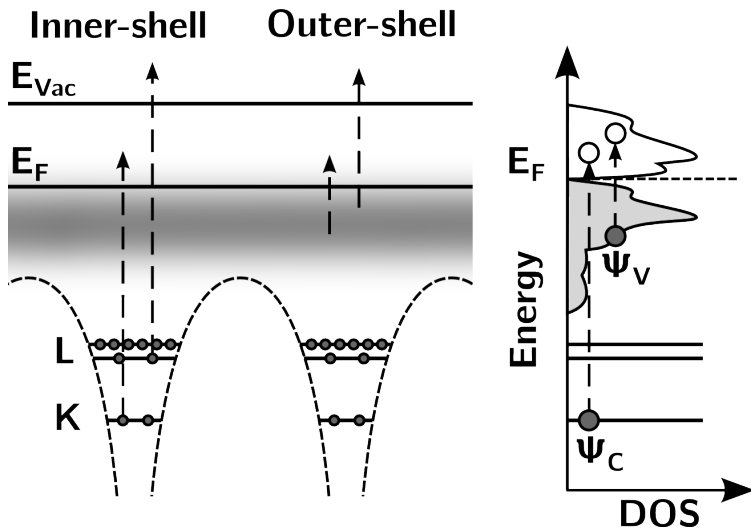


**Fig. 1.9** Representation of transitions in the solid state combining two equivalent views: energy level (right side) and DOS (left side). Inner-shell (core-loss) and outer-shell (low-loss) transitions are presented. The starting core state,  $\Psi_C$ , typically lies in an inner shell, similar to the single-atom ones. Meanwhile, the starting valence state,  $\Psi_V$ , lies closer to the Fermi energy, in a broad energy band. Finally, both are promoted to an unoccupied state, just above the Fermi energy  $E_F$ , or to vacuum, above  $E_{Vac}$ .

In turn, outer shells contain weakly bound electrons that participate actively in the chemical bond of material media. In solid-state physics, these levels are identified with the valence (or conduction) band. The application of Bethe theory is made more difficult by the fact that the wave functions of the valence electrons are radically modified by the chemical and structural environment. In addition, these electronic states can be very delocalized, as in the extreme case of the metallic materials. In this case, the conduction band electrons are nearly free and their behavior is only determined by collective effects, involving several atoms. The analysis of the low-loss EELS region is related with these effects, and although the Bethe picture is still valid, an alternative approach is preferred: the dielectric formulation.

The work presented in this thesis is devoted to the analysis of spectra in the low-loss region. This region is chosen because of the special importance that the band structure information has for the study of semiconductor materials. Understanding of the dielectric formulation is needed to extract information from the low-loss EELS. Nevertheless, some conclusions of Bethe theory are also useful for this analysis. These topics are thoroughly described in the following sections.

In what is left of the present section, additional general definitions concerning the EELS experiments are given.

### 1.2.4 Single, plural and multiple scattering

In this section, the description of scattering is extended from an heuristic point of view. The aim is to give an insight into the EELS experiment by describing the Poisson statistical model. This model is useful to present the situation in which scattering events occur repeatedly. Such a situation is common, as the typical thickness of an electron-transparent TEM sample is, in its thinner regions, around a few times the electron mean free path, in the order of 100 nm.

#### Poisson statistics

Suppose now that inelastic scattering events, or collisions, are stochastically independent<sup>i</sup>. This proposition states that the occurrence of one collision does not affect the probability of the other ones. As a direct consequence, the occurrence of these collisions obeys Poisson statistics. In this framework, the probability for one electron to suffer a number  $n$  of collisions,  $P_n$ , is completely defined by the mean number of collisions.

The mean value of collisions is the relative thickness,  $t/\lambda$ , given by the combined properties of the electron beam and the irradiated volume of the specimen. This relative thickness is equal to the ratio between thickness and mean free path. Thickness,  $t$ , is the physical distance in the sample through which an electron of the beam is transmitted. The mean free path,  $\lambda$ , is a material property dependent on the beam voltage. It corresponds to the mean distance a fast electron travels before an inelastic scattering event occurs.

Using the expression for  $P_n$  given by Poisson statistics,

$$P_n = \frac{I_n}{I_t} = \frac{(t/\lambda)^n}{n!} e^{-t/\lambda} \quad (1.18)$$

Where  $I_n$  is the scattering intensity associated with electrons that have suffered exactly  $n$  number of collisions, and  $I_t$  the total scattering intensity. These values can be obtained by integration of the EELS spectrum over the corresponding spectral regions. For instance consider  $I_0$ , the spectral intensity associated with electrons that have not suffered any collision at all. In terms of the real electron scattering recorded in EELS, the events in  $I_0$  are only identified with the direct beam, disregarding elastic scattering. Then it also becomes clear that the relative thickness can be expressed as,

---

<sup>i</sup>It can be proved than this assumption generally holds within the relaxation time approximation. See Ref. 15

$$t/\lambda = \log(I_t/I_0) \quad (1.19)$$

In a real case scenario, the EELS spectrometer is recording all of the transmitted electrons from all possible interactions; inelastic and elastic. However, so far elastic scattering events have been overlooked. Poisson statistics, as presented here, still needs to be re-formulated in order to account for them.

Typically, only a portion of the elastic scattering events are selected for the EELS spectrometer. As explained in last section, this portion can be estimated by looking at the characteristic angles,  $\theta_0$  for atomic scattering and  $\theta_B$  for Bragg scattering. Additionally, by imposing an angle limiting aperture, we may also modify the amount of recorded inelastic scattering. Again, for a thin specimen, the majority of the scattering intensity is concentrated at a narrow angular width and low energy-losses. This is the characteristic scattering angle,  $\theta_E$  (more about this assumption in the next section). Then, as long as a collection aperture is used such that,  $\beta \gg \theta_E$ , and the irradiated sample thickness is uniform and below the range  $t/\lambda > 5$ , these intensity variations will not affect the validity of Poisson statistics for thin samples. As it turns out, the result of a re-formulated theory is equivalent to the one already presented here, given that these assumptions are fulfilled<sup>7</sup>.

In other words, the stochastically independent collision supposition from above generally holds for the STEM-EELS set-ups. In these, the recorded scattering angles are typically small but well above  $\theta_E$ , e.g.  $\alpha \sim \beta \sim 10$  mrad. Moreover, each spectrum has been acquired by irradiating small sample volumes of uniform thickness. Conveniently enough, these conditions do not represent some rather impossible to obtain *sweet-spot*, but the normal operating conditions for STEM-EELS experiments.

Finally, with these guidelines we shall be able to obtain  $t/\lambda$  provided our spectra contain the ZLP and energy-loss intensity up to some tens of eV. Under this assumption,  $I_0$  and  $I_t$  would be the integral of the intensities below the ZLP and the whole spectral range, respectively. On one hand hand, Eq. (1.19) means that we can obtain an approximate measurement of the thickness of a specimen if its composition is known and uniform. On the other, if we have a composite specimen but we are able to prepare a uniform thickness sample, we shall be able to obtain compositional information from the mean free path values.

### 1.2.5 Resolution limits

The preceding sections have introduced the idea that STEM-EELS experiments can be used to obtain energy-resolved spectra with great spatial resolution. However, the actual resolution of the technique has not been completely discussed yet. For instance, a mention was made in Sec. 1.2.1 of the possibility of tuning down

the electron beam wavelength to sub-atomic dimensions. This explains the ability of the electron microscope to obtain atomic-resolution images. Nevertheless, picometer-scale spatial resolution is never achieved in the electron microscope, as one could naïvely expect from Fig. 1.5. In fact, the Rayleigh criterion as introduced in that section was incomplete, giving an unrealistic estimate of the resolution in an EELS set-up.

In this section, the limits of the EELS experiment are examined in more detail. In this sense, spatial and energy resolution are the figures of interest. Spatial resolution is limited by delocalization effects, through mainly three factors<sup>16</sup>: Coulomb delocalization, long-range nature of the excitations and instrumental broadening. The first two issues are addressed in the first section below. On the other hand, both instrumental delocalization and energy resolution depend on the instrument, and they are addressed in the following section.

### Delocalization length

Coulomb delocalization is related to the spatial range of the electromagnetic (EM) field set by an electron that moves swiftly, with velocity  $v$ . This field is responsible for the inelastic interaction with the atomic electrons, as will be explained in more detail in Sec. 1.3. In this interaction, the energy-loss is given by the field frequency,  $E = \hbar\omega$ . This problem was first examined by Bohr using a classic-oscillator analysis<sup>17</sup>. He found that the electromagnetic field extends to a distance known as the Bohr cut-off impact parameter,  $b_{max}$ . This formulation was generalized to relativistic fields by Jackson<sup>18</sup>, finding a value for the Bohr cut-off<sup>7,16,19</sup>,

$$b_{max} = \frac{\gamma v \hbar}{E} \quad (1.20)$$

This formula gives insight into some interesting properties of Coulomb delocalization. First, notice that the range of the field is inversely proportional to the energy-loss. In other words, Coulomb delocalization increases as smaller energy-loss are measured. Hence, this behavior is most relevant for low-loss EELS, as the increase in the range of the mediating EM field will increase the interaction volume. Additionally,  $b_{max}$  increases with the velocity, set in EELS by the beam acceleration voltage,  $E_0$ . This property can result in a (counterintuitive) decrease of spatial resolution with increasing  $E_0$ <sup>19</sup>. However, since the EM field diverges at its source, large interaction contrast is expected across small distances<sup>16</sup>, resulting in that  $b_{max}$  is a too crude an estimator of the effects of spatial delocalization.

The extended nature of the excitations that are probed has to be also taken into account in order to measure spatial delocalization. One way of doing this is by introducing the wave nature of the electron into the scattering event to

calculate a point-spread function (PSF)<sup>7</sup>. Such calculations can be used in simulations<sup>25</sup>, and some works have taken the time to exhaustively compare these results with experimental data (see Fig. 1.10).

It is perhaps more useful to consider a pragmatic approach to delocalization based on the correct application of the Rayleigh diffraction limit<sup>7</sup>,  $0.6\lambda/\beta$ . In the absence of a collection aperture, one half of the total inelastic scattering intensity is contained within a median scattering angle  $\langle\theta\rangle$ . Calculation of this angle using the Bethe-ridge angle  $\sqrt{2\theta_E}$  allows to estimate the object width containing 50 % of the scattered electrons,

$$L_{50} \approx 0.6\lambda/\langle\theta\rangle \approx 0.5\lambda/\theta_E^{3/4} \quad (1.21)$$

This formula relates the delocalization length to microscope parameters, and is a good estimator for low-loss EELS applications. In the case of high energy-loss applications, the effect of the collection aperture becomes apparent. It is then useful to examine the general trend (but getting just a rough estimate) combining in quadrature the effect of  $L_{50}$  with that of  $\beta$ ,

$$d_{50}^2 \approx (0.5\lambda/\theta_E^{3/4})^2 + (0.6\lambda/\beta)^2 \quad (1.22)$$

In fact,  $d_{50}$  is only relevant for large values of  $E$ , as shown in Fig. 1.11. This figure depicts the trend of  $d_{50}$  for three values of  $E_0$  and is included in order to give a visual guide to spatial delocalization, that can be used as a reference. The inset of the figure (portraying the behavior of  $d_{50}$  for low energy-losses) clearly shows that the spatial delocalization of EELS signal for  $E$  below 10 eV is above 1 nm. Indeed, when measuring EELS features lying in the lower- $E$  parts

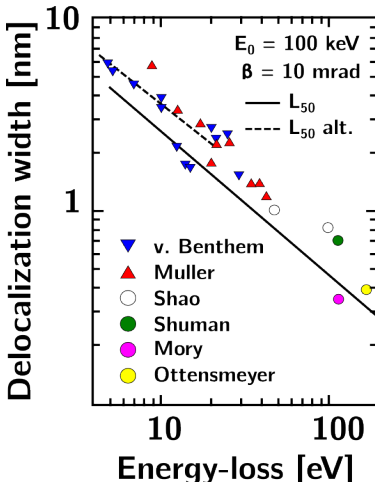


**Fig. 1.10** Comparison of theoretical calculations and experimental measurements of the delocalization width (symbols). The calculations are based on  $L_{50}$  (see Eq. (1.21)), using the Bethe ridge and the plasmon cut-off angles, depicted with solid and dashed lines, respectively. The experimental measurements represent EELS experiments from various sources<sup>20–24</sup>, with different microscope configurations. More information is available elsewhere as the figure is adapted from Ref. 7, p. 338.

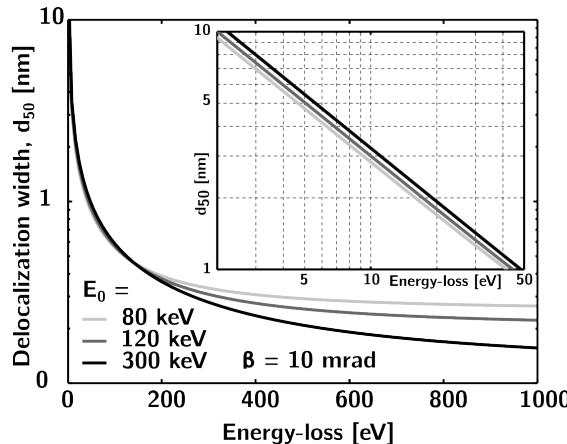


**Fig. 1.11** Calculation of the delocalization width using  $d_{50}$ , for  $E_0 = 80, 120, 300$  eV and  $\beta = 10$  mrad. Notice that, at high energy-losses, represented in the main panel using a semi-log scale,  $d_{50}$  is of sub-atomic size and improves with  $E_0$  (effect of  $\lambda$ ). Conversely, for low-energy losses, inset, represented using a log-log scale,  $d_{50}$  is above the nm range irrespective of  $E_0$  as  $d_{50} \sim L_{50}$ .

of the spectrum, the delocalization length is the main limiting factor for spatially resolved measurements, such as band gap determination<sup>26</sup>.

### Instrumental factors

Other factors that limit the resolution of EELS experiments are purely instrumental, determined by the electron microscope and the spectrometer optics. These factors have historically hindered electron microscopy as a whole, limiting both spatial and energy resolution. However, recent years have seen tremendous improvements in this field, and spatial and energy resolution below the eV and nm, respectively, are commonplace in modern instruments.

Historically, the main limiting factor to the spatial resolution of electron microscopy experiments was spherical and higher-order aberrations introduced by the imaging system. In fact, all electron-optical systems based upon rotationally symmetrical electron lenses are unavoidably affected by spherical aberration<sup>27</sup>, even if assuming that astigmatism is corrected and all the apertures in the illumination system are perfectly aligned.

Nowadays, aberration correction through the implementation of non-symmetrical electro-optic elements, known as multipole lenses, can solve this problem. The theory of aberration-correction was well known since 1947<sup>28</sup>; however, the multipole lenses were so difficult to engineer and control that the introduction of aberration correction to TEM was delayed till the improvement of computers in recent years made it possible. Modern aberration corrected TEMs feature complex multipole lenses; sextupole pair lenses, better suited for conventional TEM<sup>29–32</sup>, or quadrupole-octupole lenses, better suited for STEM applications<sup>33</sup>. Thanks to these advances, sub-Ångström resolution is achieved in

modern TEMs<sup>34</sup>, and the technology advances keep pointing towards the correction of higher order aberrations<sup>35</sup>.

Other limiting factors stem from the characteristics of the illumination source, the electron gun<sup>7,10</sup>. In ideal conditions (perfect coherence), the electron intensity distribution is a function of current and brightness, as well as the effective aperture. The brightness is the number of electrons emitted from the source per unit area per unit time. It is particularly important for EELS; by increasing it, both higher spatial resolution and analytical sensitivity are achieved. This is one of the reasons why microscopes designed mostly for analytical TEM applications, such as STEM-EELS, are equipped with some kind of field emission gun (FEG), commonly composed of a fine W needle and a mechanism to induce a strong electric field at the tip. The other major option for the electron gun, the LaB<sub>6</sub> thermionic source, only works better for low-magnification TEM.

The other main reason for the use of FEG sources is the spatial and temporal coherence of the electron beam, related to source size and energy spread, respectively. In sources with a high spatial coherence, more intensity of the beam can be concentrated into a smaller probe. More interesting to EELS applications is energy spread. Energy spread measures the energy distribution of the electrons in the beam. In a well-known example from visible light optics, a monochromatic laser source has a higher temporal coherency than a white light source. Similarly, an electron beam with a small energy spread is composed of electrons with similar energies.

In fact, a small energy spread is needed for EELS because energy spread limits the energy resolution. In a system with a large energy spread some features of the EELS spectrum can be impossible to measure. This is so because the energy spread leads to a broadening of the features in EELS spectra, so that weak features in the vicinity of stronger peaks can effectively disappear under their tails. Because of this, EELS is best performed when the contributions from this initial energy spread are minimized (as well as those introduced by the measuring set-up).

Typical values for the energy spread of cold-FEG sources can be as low as 0.3 eV, in optimal operation conditions. This value is quite good for most EELS applications. Nevertheless, these sources are expensive and their emission can be quite unstable. Because of this, modern microscopes can be equipped with an in-column energy filter<sup>36</sup>, appropriately called a monochromator, which can reduce the energy spread to around 0.1 eV<sup>37,38</sup>. This device uses an electromagnetic field that acts as the prism spectrometers used for EELS measurements, separating the electrons by their kinetic energy distribution. Then, an energy-selecting slit is used to discard the fraction of the electron beam with energies above or below certain thresholds (effectively acting as a band-pass filter). Notice that this operation does not only reduce the energy spread of the beam, but, critically, it

also reduces its intensity. Indeed, for all other TEM applications besides EELS, using the monochromator can effectively hinder the microscope performance.

Following this discussion, features in energy-loss spectra at  $E \simeq 20$  eV, such as plasmon excitation peaks in semiconductor materials<sup>7</sup>, can be estimated with a resolution limit of  $\Delta x \simeq 0.5 - 1.0$  nm (close, but above atomic column level). The limited dynamic range of the spectrometer when collecting the extremely intense ZLP simultaneously with the low-loss scattering region gives rise to a low signal-to-noise ratio (SNR) in individual spectra, hindering our ability to identify spectral features.

## 1.3 Physical elements for low-loss EELS

The following sections introduce physical concepts that are useful for the understanding of low-loss spectra. First, a dielectric response model is used to relate low-loss spectra to the macro- and microscopic aspects of the the response of material media to electromagnetic (EM) radiation. Additionally, this framework allows to construct simple models to analyze the spectral features. Finally, a dielectric formulation of low-loss EELS is presented that allows to calculate and predict the spectral features.

### 1.3.1 Dielectric model for material media

The linear dielectric formulation from classic electrodynamics serves as an heuristic presentation of the present subject. This theory dates from the time of J. C. Maxwell (XIXth century), but, within its application range, is perfectly valid from a macroscopic average point of view. It describes the behavior of electromagnetic fields in dielectric media, in terms of free and bound charges.

Consider, for instance, that a free charge distribution is introduced in a steady-state dielectric solid. Any free charges in this medium are the source of the displacement field,  $\mathbf{D}$ , following Gauss law,  $\nabla \cdot \mathbf{D} = \rho^f$ . The displacement field is defined through the medium constituent equation,

$$\mathbf{D} = \epsilon_0 \mathbf{E} + \mathbf{P} \quad (1.23)$$

where  $\epsilon_0$  is the vacuum permittivity,  $\mathbf{E}$  is the electric field and  $\mathbf{P}$  is the polarization field. The electric field in the medium induces a bound charge distribution  $\rho^b$ , which in turn is the source of the polarization field,  $\nabla \cdot \mathbf{P} = -\rho^b$ . The polarization is shaped by the permanent field of the bound distribution and an induced response to the appearance of the free charge distribution. In the case that the free charge distribution is small in comparison with the dimensions of the solid, one may treat the electric field as a small perturbation. Moreover, the

induced polarization has an approximately linear dependence with the weak electric field<sup>15</sup>. In homogeneous isotropic media, this linear response is represented by means of a complex tensor termed electric susceptibility,  $\chi_{ij}$ , such that,

$$\mathcal{P}_i(\mathbf{r}', t') = \varepsilon_0 \int \chi_{ij}(|\mathbf{r} - \mathbf{r}'|, |t - t'|) \mathcal{E}_j(\mathbf{r}, t) d\mathbf{r} dt \quad (1.24)$$

where Einstein notation is used to imply summation over the repeated indices of the components of the electric and polarization fields,  $\mathcal{E}_j$  and  $\mathcal{P}_i$ , respectively. Notice that two different space-time coordinates,  $(\mathbf{r}, t)$  and  $(\mathbf{r}', t')$ , are used to explicitly show the causality relationship between the fields. Without any loss of generality, the time-dependent electric field can be represented in terms of plane waves with wave-vector  $\mathbf{q}$  and frequency  $\omega$ . Then, the above integral may be analyzed in terms of the Fourier convolution theorem, obtaining,

$$\mathcal{P}_i(\mathbf{q}, \omega) = \varepsilon_0 \chi_{ij}(\mathbf{q}, \omega) \mathcal{E}_j(\mathbf{q}, \omega) \quad (1.25)$$

This equation defines the linear dielectric theory, where the induced response of an homogeneous medium to the electric field is contained in the electric susceptibility. The polarization field can now be omitted in an equation relating the displacement field with the electric field. This is possible by means of the constitutive equation above, Eq. (1.23). In this sense, it is helpful to define another complex tensor,  $\varepsilon_{ij}$ , such as,

$$\mathcal{D}_i(\mathbf{q}, \omega) = \varepsilon_0 \varepsilon_{ij}(\mathbf{q}, \omega) \mathcal{E}_j(\mathbf{q}, \omega) \Rightarrow \varepsilon_{ij}(\mathbf{q}, \omega) = 1 + \chi_{ij}(\mathbf{q}, \omega) \quad (1.26)$$

where  $\mathcal{D}_i$  are the components of the displacement field, and  $\varepsilon_{ij}$  is called the dielectric tensor. An interesting limiting case happens when the magnitude of  $\mathbf{q}$  is small in comparison with the bounding field spatial dependence. Then, the dielectric tensor  $\mathbf{q}$ -dependence can be dropped, obtaining the optical dielectric tensor,  $\varepsilon_{ij}(\omega)$ . The term optical comes from the fact that visible light wavelength is large in comparison with the typical interatomic spacings in a solid. Finally, in some cases the tensor nature of  $\varepsilon_{ij}$  may not be relevant, *e.g.* in isotropic and cubic systems. In these cases the tensor may be replaced in the equations by a scalar complex dielectric function (CDF),  $\varepsilon$ .

The elements of the dielectric tensor are bound by some general properties of linear and kinetic response coefficients. Because its elements are kinetic coefficients, the tensor has a symmetric nature, described by the Onsager relations,  $\varepsilon(-\mathbf{q}, -\omega) = \varepsilon^*(\mathbf{q}, \omega)$  and  $\varepsilon_{ij}(\mathbf{q}, \omega) = \varepsilon_{ji}(-\mathbf{q}, \omega)$ . Additionally, as defined above, the response of the medium in linear theory has to be causal, in that it should not precede its causes. This requirement ties the real and imaginary parts of the response coefficients by the Kramers-Kronig relations. All elements of the

tensor are complex functions such that  $\varepsilon = \varepsilon_1 + i\varepsilon_2$ . Then, the Kramers-Kronig relations state that are,

$$\varepsilon_1(\omega) - 1 = \frac{2}{\pi} \mathcal{P} \int_0^\infty \frac{\omega' \varepsilon_2(\omega') d\omega'}{\omega'^2 - \omega^2}, \quad \varepsilon_2(\omega) = -\frac{2\omega}{\pi} \mathcal{P} \int_0^\infty \frac{\varepsilon_1(\omega') d\omega'}{\omega'^2 - \omega^2} \quad (1.27)$$

So far, in the given description, a small moving free charge distribution is explicitly used as a source for the perturbation field. Nevertheless, the description is equally valid if only a pure EM radiation field perturbation is considered (no variation of the charge density involved), such as visible light. This choice is made for reasons that will become apparent in the next section.

### Microscopic dielectric formulation

A microscopical understanding of the physical properties reflected in dielectric coefficients can only be obtained from quantum examination, since it involves purely quantum objects (see Fig. 1.12). Indeed, pioneering works in the field showed that it was possible to build a quantum model of  $\varepsilon$ , actually using  $\chi^{39}$ . The translation of Eq. (1.25) to the microscopic world is made through the charge and current densities in Maxwell equations for the scalar and vector potentials. In this description, different strategies for solving the fields can be made, and increasingly complex effects can be included. In this section, a simplified semi-classical model for independent elemental excitations is presented, in order to generally introduce the solid state properties that will be relevant further ahead in this text. This approach is equal to the random phase approximation (RPA)

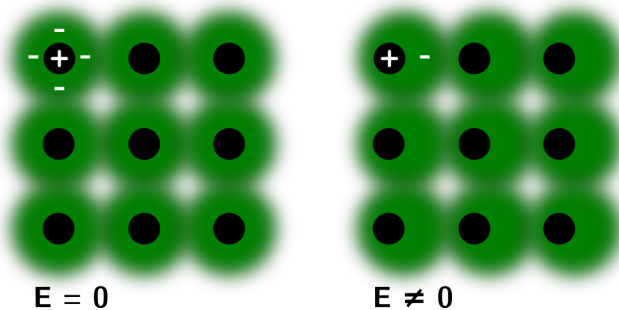


**Fig. 1.12** Polarization originated by the displacement of the electron clouds (green) relative to the ion cores (black). Notice that this is slightly different from the case in which a free charge is present, as the charge density would be changed and the displacement would only be induced locally.

calculation of Lindhard<sup>40</sup>, with the particularity that a Bloch-wave description for an isotropic medium is included<sup>41</sup>.

Our approach begins by constructing an effective independent particle Hamiltonian for the valence electron system, as the sum of two terms. The first term,  $\mathcal{H}_0$  is the Hamiltonian for the unperturbed system. In this term, a mean-field potential,  $V(\mathbf{r})$ , accounts for the crystal bonding. Consequently, no many-body effects, such as spin exchange or Coulomb correlation, are included in our description. More general formulations exist that include these effects<sup>42,43</sup>. The second term is introduced in order to work within the boundaries of linear perturbation theory:  $\mathcal{H}_{eR}$ , called the electron-radiation interaction Hamiltonian. The form of  $\mathcal{H}_{eR}$  depends on the chosen gauge. In the Coulomb gauge ( $\nabla \cdot \mathbf{A} = 0$ ), it involves the scalar and vector potentials,  $\phi$  and  $\mathbf{A}$ , and the momentum operator,  $\mathbf{p}$ . Adding these two terms, the total Hamiltonian is obtained,

$$\mathcal{H} = \mathcal{H}_0 + \mathcal{H}_{eR} = \frac{p^2}{2m} + V(\mathbf{r}) + e\phi - (e/m)\mathbf{A} \cdot \mathbf{p} \quad (1.28)$$

where second-order terms in  $\mathbf{A}$  have been neglected. Transversal and longitudinal EM interaction is quantized through this formulation. For instance, optical interaction is typically studied as a purely transverse interaction, with EM fields perpendicular to the propagation of the light-wave. Additionally, the free charge density is null, so in the medium  $\phi = 0$ , and the electric field only displaces the charge density. In the case of electronic interaction, pertinent to EELS, there is a variation in the charge density and the interaction takes place through Coulomb force, which is purely longitudinal. This means that the electric field takes a direction perpendicular to the wave-vector of the field. It is sufficient then to set  $\mathbf{A} = 0$ , and examine the variation induced in the bound charge density,  $\rho^{ind}$ ,

$$\chi(\mathbf{q}, \omega) = \frac{\rho^{ind}(\mathbf{q}, \omega)}{\varepsilon_0 q^2 \phi(\mathbf{q}, \omega)} \quad (1.29)$$

notice that since  $\phi$  is the potential corresponding to the  $\mathbf{E}$  field, this is just Eq. (1.25) rewritten. If interested in obtaining the transverse field from the time variation of the charge density, then the current density equation must also be used. This step will not be performed here; instead, the small- $\mathbf{q}$  limit that corresponds to optical excitations will be examined (also called electric dipole approximation). As it turns out for isotropic media within this limit and the RPA, tangential and longitudinal dielectric coefficients are equal<sup>16,40</sup>.

In our independent particle description, the bound charge density is represented by electrons described by their wave-functions. Notice that if generic wave-functions,  $\psi_i$ , are used to represent  $i$  states, then the charge density is obtained from the amplitude as,

$$\rho = e \sum_i f_i |\psi_i|^2 \quad (1.30)$$

where  $f_i$  is an occupation number for the  $i$ -th state. Additionally, the energy of each state,  $E_i$ , can be obtained using the unperturbed Hamiltonian,  $\mathcal{H}_0$ . In solid-state physics, the crystal lattice is represented by a periodic potential and Bloch functions are the natural choice for the bound electron wave-functions. The general shape of these wave-functions is  $|\psi_i\rangle = |\mathbf{K}, n\rangle e^{i\mathbf{K}\cdot\mathbf{x}}$ , with a wave-vector  $\mathbf{K}$  and band index  $n$ . In this text, this solid-state picture is used to analyze the transitions, for instance using expressions that refer to the reduced-scheme band-structure picture, as depicted in Fig. 1.13. It is also natural to represent the electric potential in its Fourier-analyzed form, following the same sign convention as for the macroscopic fields,

$$\phi(\mathbf{x}, t) = \sum_i \phi(\mathbf{q}, \omega) e^{i(\mathbf{q}\cdot\mathbf{x} - \omega t - i\gamma t)} \quad (1.31)$$

where a complex frequency term,  $\gamma$ , has been added to represent the life-time of the optical excitations. The induced charge density is proportional to the probability of transition per unit time, or transition rate. In the framework of

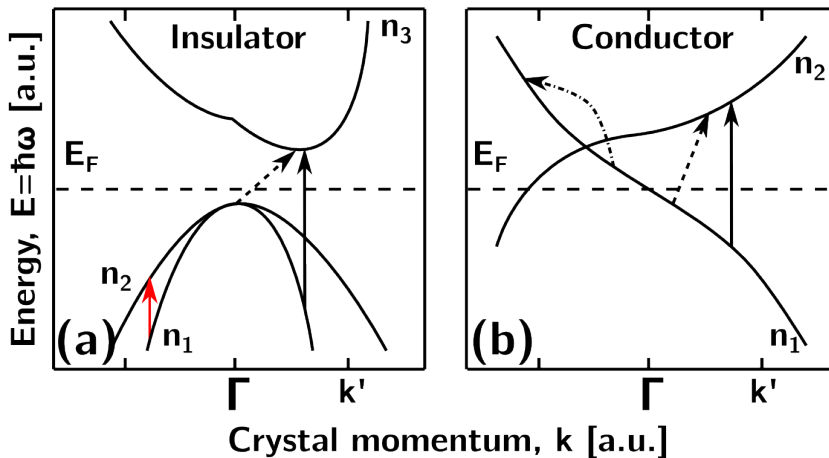


**Fig. 1.13** Idealized energy-momentum diagrams in the band reduced scheme, portraying intra- and inter-band transitions. In panel (a), an insulator material with direct or indirect inter-band transitions portrayed with solid or dashed arrows, respectively. In panel (b), a conductor material that, additionally, features intra-band transitions depicted with a dash-dot line (adapted from Ref. 44).

time dependent perturbation theory, this rate is obtained from the Fermi golden rule. In this rule the transition rate is proportional to the product of the density of final states and the transition matrix element. To obtain them, we take into account excitations that correspond to absorption or emission of photons by the electrons of the medium. Thus, the longitudinal dielectric coefficient takes the general form<sup>44</sup>,

$$\varepsilon(\mathbf{q}, \omega) = 1 - \frac{e^2}{\varepsilon_0 q^2 V} \sum_{\mathbf{K}, n, n'} \frac{\langle \mathbf{K} + \mathbf{q}, n' | \mathbf{K}, n \rangle \langle \mathbf{K}, n | \mathbf{K} + \mathbf{q}, n' \rangle}{E_{\mathbf{K}+\mathbf{q},n'} - E_{\mathbf{K},n} - \hbar\omega - i\gamma\hbar} (f_{\mathbf{K}+\mathbf{q},n'} - f_{\mathbf{K},n}) \quad (1.32)$$

where  $V$  is the volume of the lattice unit cell. In this formulation, electrons transition from occupied to empty states, with labels  $\mathbf{K}, n$  and  $\mathbf{K} + \mathbf{q}, n'$ , respectively, as denoted in the momentum matrix elements. Furthermore, the only permitted transitions are to empty states ( $f_{\mathbf{K}+\mathbf{q},n'} - f_{\mathbf{K},n} \neq 0$ ) and allowed by the crystal symmetry ( $\langle \mathbf{K}, n | \mathbf{K} + \mathbf{q}, n' \rangle \neq 0$ ).

This dielectric function contains both single and collective electron excitation modes. In the small damping case, the collective excitation mode appears for frequencies  $\omega_L$  such that  $\varepsilon_1(\omega_L) = 0$  and monotonically increasing<sup>45</sup>. These conditions imply a peak in the imaginary part called the bulk plasmon, because of the analogy with a quasi-free electron plasma oscillation (examined below).

Three kinds of single electron excitations (optical transitions) are allowed, when  $\hbar\omega = E_{\mathbf{K}+\mathbf{q},n'} - E_{\mathbf{K},n}$ . First, intra-band transitions, such that  $n = n'$  which means the transition is between states in the same band. These are only allowed in metals, where the conduction band is above the Fermi level. Second, direct inter-band transitions, such that  $n \neq n'$  but  $\mathbf{q} = 0$  meaning the transition is between states in different bands vertically aligned in the band reduced scheme. Finally, indirect inter-band transitions, such that  $n \neq n'$  and  $\mathbf{q} \neq 0$ , which locates the final state in a different band diagonally separated from the initial state.

Notably, RPA formulations similar to this one can be used for the theoretical prediction of the dielectric response of a material<sup>46</sup>. In fact, given the knowledge of the band structure, all the necessary ingredients for the calculation of Eq. (1.32) are accessible. However, a further generalization has to be implemented in order to include all possible transitions at frequency  $\omega$ . This way, the  $\varepsilon(\omega)$  is related to the joint density of states (JDOS) between occupied and unoccupied states. This is depicted in Fig. 1.14, that shows that some transitions are more probable than others (red arrows,  $\omega_1$  and  $\omega_2$ ), because they involve a greater JDOS. Notice also that  $\varepsilon_2$  is related with the products of the momentum matrix elements times the JDOS, averaged over the energy-loss spectrum.

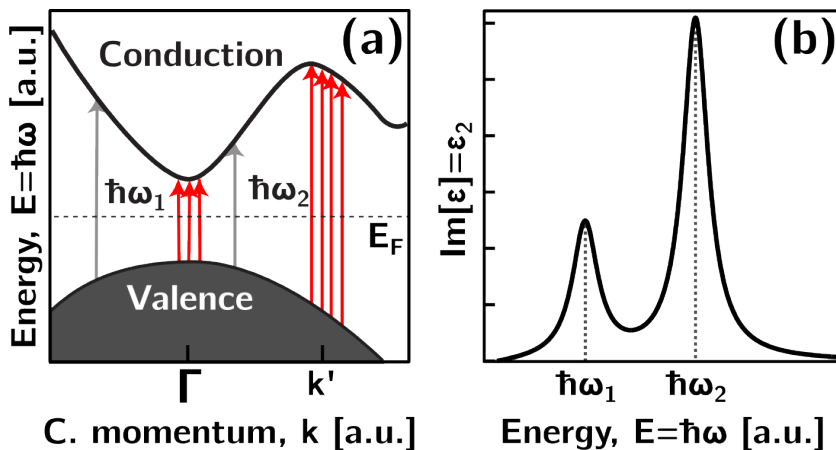


**Fig. 1.14** In panel (a), the continuum of transitions (arrows) near the band gap of an ideal insulator material. In panel (b), the imaginary part of the CDF,  $\varepsilon_2$ , showing that these populous inter-band transitions are translated into peaks of the optical absorption spectrum.

### Simple models for $\varepsilon(\omega)$

The dielectric function in Eq. (1.32) can be simplified after the  $\mathbf{K} \cdot \mathbf{p}$  expansion in the small- $\mathbf{q}$  limit (all transitions are direct). Such an approximation is too rough, and thus not useful to make predictions, but rather to give a phenomenological insight into the behavior of  $\varepsilon(\omega)$  in terms of optical transitions. In this sense, notice also that we are disregarding the  $\mathbf{q}$ -dependence, that is relevant but of lesser interest in this work. The formulation obtained is sometimes called generalized Lorentz model<sup>41</sup>,

$$\varepsilon(\omega) = 1 - \sum_{\mathbf{K}, n} \frac{\omega_P^2}{\omega^2 + i\gamma\omega} f_{\mathbf{K}, n, n} + \sum_{\mathbf{K}, n \neq n'} \frac{\omega_P^2}{\omega_{\mathbf{K}, n, n'}^2 - \omega^2 - i\gamma\omega} f_{\mathbf{K}, n, n'} \quad (1.33)$$

where  $\omega_P$  is the free-electron plasma frequency and  $\omega_{\mathbf{K}, n, n'}$  are inter-band transition binding frequencies, respectively. Moreover,  $f_{\mathbf{K}, n, n}$  and  $f_{\mathbf{K}, n, n'}$  are known as the intra- and inter-band dipole oscillator strengths, respectively. Their value is derived from the leading terms of the  $\mathbf{K} \cdot \mathbf{p}$  expansion as a function of the momentum matrix elements between valence and conduction band states,

$$f_{\mathbf{K},n,n} = \delta(E_F - E_{\mathbf{K},n}) \frac{|\langle \mathbf{K}, n | \hat{\mathbf{q}} \cdot \hat{\mathbf{p}} | \mathbf{K}, n \rangle|^2}{mn_v} \quad (1.34)$$

$$f_{\mathbf{K},n,n'} = 2f_{\mathbf{K},n} \frac{|\langle \mathbf{K}, n' | \hat{\mathbf{q}} \cdot \hat{\mathbf{p}} | \mathbf{K}, n \rangle|^2}{mn_v \hbar \omega_{\mathbf{K},n,n'}} \quad (1.35)$$

where  $n_v$  is the number of valence electrons per unit-cell. Notice that these elements are analogous to Eq. (1.30), if one considers that they represent the occupation number of each excited state. Indeed, if we index every possible optical excitation using  $i$ , our model must satisfy the constrain  $\sum_i f_i^2 = 1$ . It can be shown that this normalization is a consequence of total charge density conservation (see for instance Ref. 44), it is known as the oscillator sum rule, or alternatively as the Bethe  $f$ -sum rule<sup>13</sup>. This sum-rule allows to examine the meaning of the plasma and binding frequencies as well. Their names denote their relationship with the collective and single electron excitation modes, respectively. Indeed, because of the oscillator sum-rule, the value of  $\omega_P$  in our model is fixed to,

$$\omega_P = \sqrt{\frac{e^2 n_v}{\varepsilon_0 m}} \quad (1.36)$$

Notice that intra- and inter-band contributions appear separately in Eq. (1.33), in the first and second sum, respectively. In the case where the inter-band term is null, the value of  $\omega_P$  corresponds to  $\varepsilon_1(\omega_P) = 0$ . As discussed above, this case corresponds to the excitation of a bulk plasmon in a quasi-free electron approximation. This excitation has a classic analogue in the Drude model for the bulk plasmon in a conductor material<sup>15</sup>. Furthermore, the dielectric response is characterized by a plasmon excitation at  $\omega_P$  with a damping given by the phenomenological life-time term,  $\gamma$ ,

$$\varepsilon(\omega) = 1 - \frac{\omega_P^2}{\omega^2 + i\gamma\omega} \quad (1.37)$$

In general, the inter-band contribution to the dielectric response does not need to be null. Notice that the inter-band contribution introduces poles into the  $\varepsilon(\omega)$  model in Eq. (1.33). These poles appear at binding frequencies imposed by the energy difference between each transition initial and final states,

$$\omega_{\mathbf{K},n,n'} = \hbar^{-1}(E_{\mathbf{K},n'} - E_{\mathbf{K},n}) \quad (1.38)$$

In these cases the dielectric response can be critically modified, as depicted in Fig. 1.15. For instance when intra-band transitions are not allowed ( $f_{\mathbf{K},n,n}$

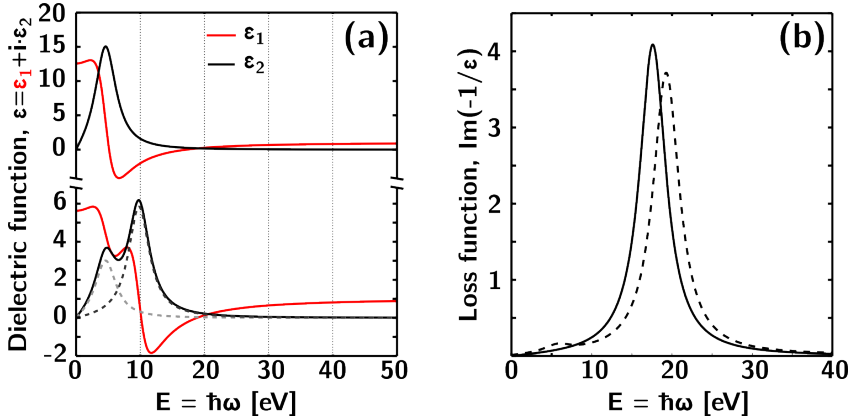


**Fig. 1.15** Panel (a) shows two CDF models, computed using a modified Drude model, such as Eq. (1.39), with  $E_P = \hbar\omega_P = 17$  eV and  $\Gamma = \hbar\gamma = 4$  eV in both cases. Top CDF has one transition, at an energy  $E_{eff} = \hbar\omega_{eff} = 5$  eV; bottom CDF has an additional one at 10 eV (strength  $f = 0.8$ ). In panel (b), the loss function  $\text{Im}(-1/\varepsilon)$  for both CDF models, in solid and dashed lines for the first and second models, respectively. The bulk plasmon is evidenced in this function by a strong peak that does not appear in  $\varepsilon_2$ .

$= 0$ ), or when the presence of inter-band transitions is important ( $f_{\mathbf{K},n,n} \sim f_{\mathbf{K},n,n'}$ ), the collective excitation mode  $\varepsilon_1(\omega_L) = 0$  occurs at frequencies  $\omega_L \neq \omega_P$ . Nevertheless, the Drude model is a useful approximation of  $\varepsilon(\omega)$  close to the plasmon excitation threshold and in the absence of inter-band transitions in the near spectral region. For instance, an effective inter-band binding frequency  $\omega_{eff}$  may be considered, resulting from the addition of all single electron excitations. In this approximation, a modified Drude model might be obtained from Eq. (1.33)<sup>45</sup>,

$$\varepsilon(\omega) = 1 + \sum_i \frac{\omega_P^2 f_i}{\omega_i - \omega^2 - i\gamma\omega} = 1 + \frac{\omega_P^2}{\omega_{eff}^2 - \omega^2 - i\gamma\omega} \quad (1.39)$$

in this model, the collective mode excitation energy threshold is shifted to  $\omega_L^2 = \omega_P^2 + \omega_{eff}^2$ . For some conductor and semiconductor materials, Drude functions can approximately model the plasmon response. Notice that the modified Drude function is useful given that  $\omega_{\mathbf{K},n,n'}$  are small compared to  $\omega_P$ . Some examples of these materials include alkali metals such as aluminum and semiconductors such as silicon, see Fig. 1.16a. For other materials, strong inter-band transitions can overlap or smear the collective excitation, in terms of Eq. (1.33), and the approximation leading to  $\omega_0$  does not hold. For instance, the presence of ion-core d states near the valence band of transition metals, such as the 3d band in gallium and semiconductor GaN, modifies critically the dielectric response;

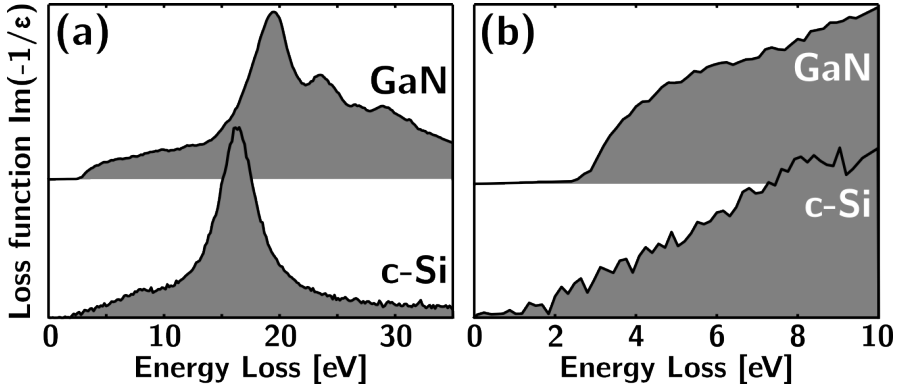


**Fig. 1.16** The  $\text{Im}(-1/\epsilon)$  (or energy-loss function) of GaN and c-Si evidences the different dielectric response of these two semiconducting materials. In panel (a), a general view, featuring a prominent collective excitation mode peaks and some inter-band transitions in both. In panel (b), a detail from the lower energy region, showing the first allowed inter-band transition, the band gap. These functions were obtained from EELS measurements, using the procedures explained ahead in the text.

again, this is portrayed in Fig. 1.16a.

Materials may present direct or indirect transitions, depending on their band structure. For instance, some semiconductor materials feature a direct band gap transition, such as GaN and others present an indirect band gap, as for Si. The dielectric response is changed accordingly, as depicted in Fig. 1.16b. Evidently, this fact is not taken into account in the simple dielectric model of Eq. (1.33).

The origin of these differences lies in the band structure of the materials and is expressed using the JDOS. Both the band structure and the JDOS can be calculated if the band structure of a material is known. For instance, in an insulating material (see Fig. 1.14), we may generalize the classical inter-band oscillator strengths to an integral carried out over the  $\mathbf{k}$ -space surface  $S$  defined by a constant energy difference between the bands,  $\hbar\omega_{vc} = \hbar(\omega_c - \omega_v)$ , to obtain the following expression<sup>45</sup>,

$$f_{vc}(\omega) = \frac{2\epsilon_0}{\pi^2 m n_v \hbar \omega} \int_S |M_{vc}|^2 \frac{dS}{|\nabla_{\mathbf{k}} \omega_{vc}|} \quad (1.40)$$

where the integrand is composed of  $M_{vc}$ , the momentum matrix elements between valence and conduction bands, and the JDOS function differential element. Indeed, this formulation will be useful to understand some methods applied to the analysis of EELS data. These methods will be addressed later on.

### 1.3.2 Dielectric formulation of low-loss EELS

Inelastic scattering in low-loss EELS is typically restricted by the characteristic energy and momentum exchanges that are studied. This restriction allows making an analogy with the framework of dielectric theory.

In a low-loss EELS experiment, electrons with a high initial kinetic energy interact with a material medium. The initial kinetic energy is so high that the velocity,  $v$ , of the fast electron is well above the mean velocity of the atomic electrons. This condition is sufficient for the first-order Born approximation to hold, and allows to apply a formalism analogous to the dielectric theory that was reviewed above. Moreover, the application of linear dielectric theory implies that the medium is treated as being continuous. Because of this, the scattering is restricted to small momentum transfers, compared to the inter-electronic spacing in the material. In this sense, the typical experimental conditions of EELS are consistent with the small- $\mathbf{q}$  limit dielectric theory.

The physical image corresponding to the fast electron is that of a small charged particle that follows a straight-line trajectory,  $\mathbf{r}(t)$ , crossing the origin at time  $t = 0$ . This image is expressed by the following charge distribution,

$$\rho = -e\delta(\mathbf{r} - \mathbf{vt}) \quad (1.41)$$

were the Dirac  $\delta$ -function is used. In the framework of classic dielectric theory this  $\rho$  is a small perturbing free-charge. The induced electromagnetic field distribution in the medium is considered. The inelastic scattering event is embodied in the force exerted back on the particle by the induced electric field. Consequently, the electron energy-loss,  $E = \hbar\omega$ , and the momentum transfer,  $\hbar\mathbf{q}$ , are equivalent to the frequency and wave-vector of the electric field,  $\mathcal{E}$ , acting back on the particle<sup>39</sup>. This is the so-called stopping force, and allows to calculate the energy absorption of the medium as,

$$dW = e\mathcal{E}(\mathbf{vt}, t)\hat{\mathbf{v}}d\mathbf{r} \quad (1.42)$$

This quantity, if examined in  $\mathbf{q}$ -space, is such that  $W(\mathbf{q}, \omega)$  is equal to the energy absorbed by the medium in units of  $\hbar\omega$ . Following this approach, it is evident that in order to calculate  $dW$  it is sufficient to obtain the  $\mathcal{E}$  induced by  $\rho$ . In the following section, the solution to this problem and its consequences are presented in the non-retarded limit. This is so because we are interested in obtaining separately the non-radiative bulk scattering distribution, for reasons that will become clear later. Notice that, while the EM field mediating the interaction is considered non-retarded, relativistic expressions are used to derive kinetic parameters. Afterwards, we will also consider the full-relativistic case, since for  $v > c\sqrt{\epsilon_1}$ , radiative energy-loss processes cannot be disregarded.

### Bulk and surface energy-loss

In the absence of a magnetic response, the induced electric field is obtained from the potential,  $\phi$ , following Maxwell equation  $\mathbf{E} = -\nabla\phi$ . In the non-retarded case, the potential may be obtained from Poisson equation in  $\mathbf{q}$ -space<sup>47</sup>,

$$\phi(\mathbf{q}, \omega) = \frac{\rho(\mathbf{q}, \omega)}{q^2 \varepsilon_0 \varepsilon(\mathbf{q}, \omega)} = \frac{e \delta(\mathbf{q}\mathbf{v} + \omega)}{q^2 \varepsilon_0 \varepsilon(\mathbf{q}, \omega)} \quad (1.43)$$

In this sense,  $\varepsilon$  can be interpreted as a measure of the screening strength in the interaction between free charge and bound charge distributions. If the electron movement is restricted to an arbitrary axis,  $x$ , an expression for the stopping power of an infinite homogeneous isotropic medium can be obtained,

$$\frac{dE}{dx} = \frac{\hbar^2}{\pi a_0 m_0 v^2} \int \int \frac{q_{\perp} \omega \operatorname{Im}[-1/\varepsilon(q, \omega)]}{q_{\perp}^2 + (\omega/v)^2} dq_{\perp} d\omega \quad (1.44)$$

where  $\mathbf{q}_{\perp}$  is the component of the momentum transfer perpendicular to  $\mathbf{v}$ , and  $E = -W$  is the electron energy-loss. Furthermore, the description of the dielectric response of the medium is introduced through the energy-loss function (ELF),  $\operatorname{Im}(-1/\varepsilon)$ . The calculation of the double-differential cross section can be recalled from the Bethe formalism presented in Sec. 1.2.3, particularly Eq. (1.17). Additionally, the stopping power is shown to have a definite dependence on the scattering angle, if the calculations are restricted to the dipole region of scattering (or small- $\mathbf{q}$ ). Within this small angle approximation, the definitions presented in Sec. 1.2.2 hold, and  $q_{\perp} \rightarrow \frac{mv}{\hbar}\theta$ ,  $dq_{\perp} \rightarrow k_0\theta$ ,  $d\Omega \rightarrow 2\pi\theta d\theta$  and  $\omega \rightarrow \frac{m_0}{\hbar}\theta_E$ . Finally, these approximations are wrapped into the scattering distribution for the bulk electron energy-loss in an infinite medium, first found by R.H. Ritchie<sup>48</sup>,

$$\frac{d^2\sigma}{d\Omega dE} \approx \frac{\operatorname{Im}[-1/\varepsilon(q, E)]}{\pi^2 a_0 m_0 v^2 n_a} \left( \frac{1}{\theta^2 + \theta_E^2} \right) \quad (1.45)$$

where  $n_a$  is the number of atoms per unit volume of the medium. Only the bulk effects are described by this equation, that is not directly applicable to a real sample, of finite geometry. In real samples, the scattering distribution is also affected by the boundary surfaces of the material media. In general, as the potential can be separated in bulk and boundary reflection terms, the inelastic scattering distribution can be separated in bulk and surface terms<sup>16</sup>.

The typical TEM specimen is a thin material slab. In the best case scenario it is considered to have perfectly parallel and clean boundary surfaces with vacuum. Hence, the material thickness,  $t$ , in the direction perpendicular to the surfaces is constant. Moreover, the extension of the foil is assumed to be infinite in the other two directions. For the slab case, the bulk term is simply equal to Eq. (1.45) times the electron path-length,  $t$ . Meanwhile, the surface term is

more complicated, as it may contain contributions from the dielectric response of additional media at the boundaries and the incidence angle of the beam. For the sake of simplicity, the full general solution will not be presented here (it can be found elsewhere<sup>7</sup>). A first solution to this problem was found using an hydrodynamic model for the surface charge distribution<sup>48</sup>. This procedure shows that bound charge oscillations can propagate through the boundaries between media, analogous to the propagation of bulk plasmons. The excitation of this collective mode is called a surface plasmon. The double differential scattering distribution for the case of normal beam incidence and clean unoxidized surfaces reduces to,

$$\frac{d^2\sigma_s}{d\Omega dE} \approx \frac{\text{Im}\left[\frac{-4}{1+\varepsilon(q,E)}\right] - \text{Im}\left[\frac{-1}{\varepsilon(q,E)}\right]}{\pi^2 a_0 m_0 v^2} \left(\frac{k_0 \theta}{\theta^2 + \theta_E^2}\right) \quad (1.46)$$

Because of the above conditions, this equation represents the surface-loss of one surface boundary to vacuum. The inelastic scattering distribution that we have presented relates the EELS experiment to the dielectric response of the material media. The correspondence to an energy-loss spectrum is obtained after angular integration, using the collection angle,  $\beta$ , as an integration limit. If this is done using Eq. (1.45) and Eq. (1.46), the corresponding single scattering distributions of bulk and surface losses are obtained,

$$S_b(E) = \frac{2I_0 t}{\pi^2 a_0 m_0 v^2} \text{Im}[-1/\varepsilon(E)] \log[1 + (\beta/\theta_E)^2] \quad (1.47)$$

$$S_s(E) = \frac{2I_0 k_0^{-1} \left[ \text{Im}\left(\frac{-4}{1+\varepsilon}\right) - \text{Im}\left(\frac{-1}{\varepsilon}\right) \right]}{\pi^2 a_0 m_0 v^2} \left[ \frac{\tan^{-1}(\beta/\theta_E)}{\theta_E} - \frac{\beta}{\beta^2 - \theta_E^2} \right] \quad (1.48)$$

were  $I_0$  is the ZLP intensity. Notice that the total single scattering distribution (SSD) intensity is  $S = S_b + S_s$ . The bulk term,  $S_b$ , is more important for thick samples, typically being the dominant contribution to an energy-loss spectrum. From Eq. (1.45) it becomes clear that the angular distribution of bulk scattering is peaked at zero scattering angle and decays from there. Conversely, from Eq. (1.45), the surface term,  $S_s$ , is independent of thickness, and its contribution to an energy-loss spectrum can be important for extremely thin samples ( $\lesssim 50$  nm). Additionally, its intensity cancels at very low scattering angles, and is symmetrically distributed at a mean angle. Notice that for a non-normal incidence case this symmetry is broken<sup>7</sup>. Because the expressions for  $S_b$  and  $S_s$  are relatively simple they can be used to extract the dielectric response information enclosed in the low-loss EELS spectra.

In this first approximation, we have not considered a purely geometric effect. Whenever the boundary surfaces are sufficiently close together, geometric

coupling of the EM-fields in the medium is possible. Because of this effect, the surface-plasmon contribution may depart from the formula given above even in a non-relativistic formulation. The following section addressed this issue and further corrections that are necessary for the relativistic case.

### Full-relativistic description

In order to give a full description of the inelastic scattering distribution, it is necessary to also take into account the retardation of the EM field mediating the energy-loss interaction. In this full-relativistic description, both bulk and surface loss scattering distributions depart from the expressions given above. In order to include both effects, the retarded version of the electric field has to be solved including the appropriate boundary conditions.

Radiative-loss excitation is possible when electrons move faster than photons propagating in the medium, emitting Čerenkov radiation. Whenever the dielectric response framework applies, the group velocity for electromagnetic waves is determined by  $c/\sqrt{\varepsilon_1}$ , and the Čerenkov condition can be expressed as  $\varepsilon_1(E) > c^2/v^2$ . This condition is easily fulfilled in the typical EELS experiment, given that electrons in the TEM beam travel at very high speeds (see Sec. 1.2.1). Indeed, because for insulating materials  $\varepsilon_1(E) > 0$  at low energy-losses, the radiative-loss mode can be an important contribution to the scattering distribution. For a graphical example, depicting the Čerenkov threshold using a dielectric response model, see Fig. 1.17. In this figure, the impact of beam energy,  $E_0$ , on the relativistic loss is explored using a model CDF.

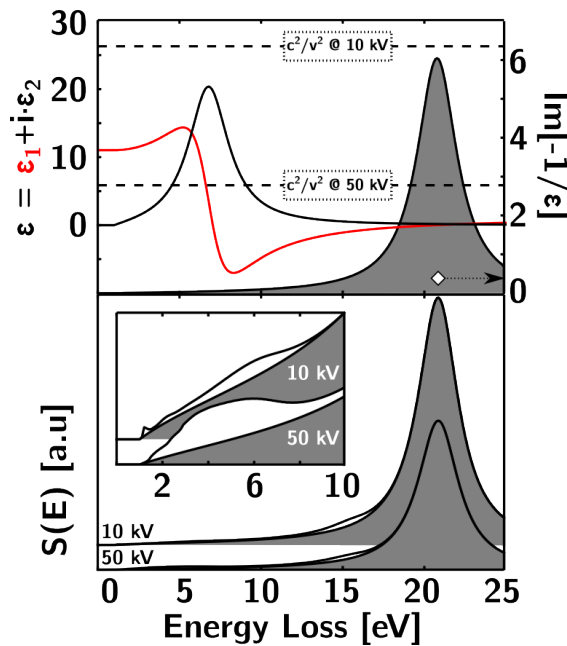
In a first approximation, the amount of Čerenkov radiation should depend on the path-length of the electron through the specimen. Hence, the radiative-loss contributes to the bulk-loss and is more important in thick samples. Additionally, a realistic surface scattering distribution also departs from the one presented above and is affected by the introduction of retardation effects. Furthermore, the presence of boundaries alters the radiative-loss contribution as well, which is a purely relativistic effect. Depending on the geometry, this effects account for the excitation of several modes within the sample.

A full-relativistic double differential cross section for normal incidence on a material slab of parallel infinite boundaries separated by a thickness,  $t$ , was found by E. Kröger<sup>49</sup>. To find this solution, it was necessary to solve the EM-wave equations with appropriate boundary conditions. The scattering distribution is,

$$\frac{d^2P}{d\Omega dE} = \frac{1}{\pi^2 a_0 m_0 v^2} \text{Im} \left[ \frac{t\mu^2}{\varepsilon^* \varphi^2} - \frac{2\theta^2(\varepsilon^* - \eta^*)^2}{k_0 \varphi_0^2 \varphi^2} (A + B + C) \right] \quad (1.49)$$

were  $\varepsilon^* = \varepsilon_1 - i\varepsilon_2$  is the complex conjugate of the dielectric function for the specimen, and  $\eta^*$ , idem for the surroundings ( $\eta^* = 1$  for vacuum). Moreover,

**Fig. 1.17** In the top panel, solid lines,  $\varepsilon(E)$  model obtained using Eq. (1.39) with  $E_P = 19$  eV,  $E_{eff} = 6$  eV,  $\Gamma = 3$  eV (see also Fig. 1.15). In order to simulate the band gap signal onset,  $\varepsilon(E)$  is shifted 1 eV and padded using a constant ramp. Also included, dashed lines,  $c^2/v^2$  values at  $E_0 = 10$  and 50 keV. They indicate the threshold of radiative loss, as explained in the text. Also included, gray color filled area,  $\text{Im}(-1/\varepsilon)$ . In the panel below, solid lines and gray color filled area, non-retarded (bulk only) and full-relativistic (surface included) calculations of the scattering distribution,  $S(E)$ . Other parameters,  $t = 150$  nm and  $\beta = 2.5$  mrad.



the equation is given as a function of the following adimensional terms:  $\mu^2 = 1 - \varepsilon^*(v/c)^2$ ,  $\varphi^2 = \lambda^2 + \theta_E^2$  and  $\varphi_0^2 = \lambda_0^2 + \theta_E^2$ , where  $\lambda^2 = \theta^2 - \varepsilon^*\theta_E^2(v/c)^2$  and  $\lambda_0^2 = \theta^2 - \eta^*\theta_E^2(v/c)^2$ . The A, B, and C terms represent the relativistic surface loss in the slab by surface-plasmon and guided-light modes. For the sake of simplicity, the relatively complex dependence of these terms on  $\theta$ ,  $E$  and  $t$  is not given here, their definitions can be found elsewhere<sup>7</sup>.

The full-relativistic  $S(E)$  is obtained after angular integration of Eq. (1.49), in which bulk and surface contributions again appear separately. In the case of the bulk term, the dependence on  $\varepsilon$  is rather complex when compared to the non-relativistic case. Hence, it is difficult to use a full-relativistic  $S(E)$  expression to obtain the dielectric response from EELS measurements. However, numerical integration can be performed if dielectric data are available. In this sense, Eq. (1.49) is a valuable source of information to assess EELS measurements using a theoretical prediction of  $S(E)$ .

A deeper understanding of the behavior of these theoretical scattering distributions can be gained by performing some calculations, as the ones depicted in Fig. 1.18. In this figure, Eq. (1.47) and Eq. (1.49) are used, together with the same  $\varepsilon(E)$  model as in Fig. 1.17, to simulate the dielectric response of semiconductor slabs for different thickness values. Let us examine first the non-retarded

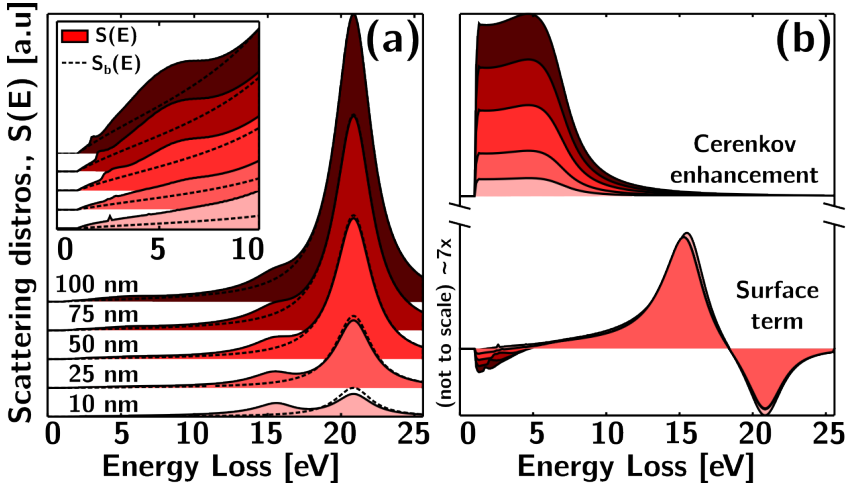


**Fig. 1.18** In panel (a), dashed lines and color filled areas, non-retarded (bulk only) and full-relativistic (surface included) calculations of the scattering distribution,  $S_b(E)$  and  $S(E)$ , respectively, for different thickness values in the  $10 - 100$  nm range ( $E_0 = 50$  keV and  $\beta = 2.5$  mrad). In panel (b), from the same simulation and using the same line and color conventions as in (a), the separate integrals of the Čerenkov enhancement and the surface term from Eq. (1.49) are given. The surface term is directly obtained from the calculation of  $S(E)$ . The Čerenkov enhancement is calculated as the difference between the relativistic and the non-retarded bulk scattering terms.

bulk scattering distributions,  $S_b(E)$  (panel (a), dashed lines). Because these distributions follow Eq. (1.47), their shape is independent of the thickness, that is only a multiplicative factor. Conversely, the shape of the full-relativistic total distributions,  $S(E)$  (panel (a), color filled areas), is drastically altered depending on the thickness. The most relevant modifications are in the lower energy-loss region (inset), and in the region preceding the bulk plasmon at  $\sim 15$  eV.

Since these regions correspond to the band gap onset energy and the surface plasmon, respectively, their alteration is related with the interplay of surface-loss and radiative-loss effects. Panel (b) in Fig. 1.18 compares these effects by extracting the bulk radiative-loss and the surface-loss term from  $S(E)$ . First notice that the bulk radiative loss (Čerenkov enhancement, at the top of the panel), increases its impact with thickness, as expected. This contribution peaks near the spectral onset (where  $\varepsilon_2 \neq 0$ ), and near the inter-band transition at  $E_{eff} = 6$  eV. The whole spectral region near the band gap onset is modified, as shown in the inset in panel (a). Because of guided-light modes in the specimen, the surface-loss term (at the bottom of the panel) shows a purely radiative contribu-

tion in this region also. Notice that this contribution is negative and of the order of the bulk-radiative loss (the figure is not at scale). In the lower energy region, both purely radiative bulk- and surface-loss contributions tend to compensate one another, with an interplay that depends on the thickness.

For the  $\varepsilon(E)$  used in this calculation, the Čerenkov condition is broken above  $\sim 7$  eV for  $E_0 = 50$  keV electrons (see Fig. 1.17). Hence, the region of the intense surface term at around  $\sim 15$  eV is free of radiative contributions. Here, only the non-retarded surface-plasmon contribution is relevant, and the scattering distribution for this voltage is mostly independent of thickness. Indeed, only a slight change is predicted for the smallest of the thickness values, corresponding to the geometric coupling of the surface-plasmon because of the proximity of the boundary surfaces. For most thickness values, the non-retarded Eq. (1.47) and Eq. (1.48) are sufficient for the prediction of the scattering distribution above  $\sim 5$  eV. Below this energy-loss range, the presence of radiative-loss contributions can modify the shape of the spectral intensity. Alternatively, in very thin samples, the surface-plasmon peak becomes more important (as the bulk intensity decreases), and its geometric coupling can modify the spectral shape.

The presented examples are given to demonstrate the different contributions to low-loss EELS data and their relative importance. This model-based approach is a relatively simple way to gain insight into the relatively complex Kröger equation, as the exploration of all its possible implications is beyond our interest. In the following chapter, the methods used for the analysis of the features in low-loss EELS will be presented.

## Bibliography

- [1] H. Busch. Über die Wirkungsweise der Konzentrierungsspule bei der Braunschen Röhre. *Archiv für Elektrotechnik*, 18:583–594, 1927.
- [2] M Knoll and E Ruska. Das Elektronenmikroskop. *Zeitschrift für Physik*, 78: 318–339, 1932.
- [3] A. Tonomura, J. Endo, T. Matsuda, T. Kawasaki, and H. Ezawa. Demonstration of single-electron buildup of an interference pattern. *American Journal of Physics*, 57:117–120, 1989.
- [4] R. P. Feynman, R. B. Leighton, and M. Sands. *The Feynman Lectures in Physics*. Addison Wesley, 3rd edition, 2005.
- [5] M. Inokuti. Inelastic collisions of fast charged particles with atoms and molecules — the Bethe theory revisited. *Reviews of Modern Physics*, 43: 297–347, 1971.

- [6] J. Hillier and R. F. Baker. Microanalysis by means of electrons. *Journal of Applied Physics*, 15:663, 1944.
- [7] R. F. Egerton. *Electron Energy-Loss Spectroscopy in the Electron Microscope*. Springer US, 3rd edition, 2011.
- [8] R. F. Egerton, Y. Y. Yang, and S. Y. Cheng. Characterization and use of the Gatan 666 parallel-recording electron energy loss spectrometer. *Ultra-microscopy*, 48:239–250, 1993.
- [9] R. Castaign and L. Henry. Filtrage magnétique des vitesses en microscopie électronique. *Comptes Rendus*, B255:76–78, 1962.
- [10] D. C. Williams and C. B. Carter. *Transmission Electron Microscopy*. Springer US, 2nd edition, 2009.
- [11] E. Rutherford. The scattering of  $\alpha$  and  $\beta$  rays by matter and the structure of the atom. *Philosophical Magazine*, 6:21, 1911.
- [12] W. L. Bragg. The diffraction of short electromagnetic waves by a crystal. *Proceedings of the Cambridge Philosophical Society*, 17:43–57, 1913.
- [13] H. Bethe. Zur Theorie des Durchgangs schnellen Korpuskularstrahlen durch Materie. *Annalen der Physik*, 5:325–400, 1930.
- [14] D. Bote and F. Salvat. Calculations of inner-shell ionization by electron impact with the distorted-wave and plane-wave Born approximations. *Physical Review A*, 77:042701, 2008.
- [15] N. W. Ashcroft and N. D. Mermin. *Solid State Physics*. Brooks/Cole, 1st edition, 1976.
- [16] F. J. García de Abajo. Optical excitations in electron microscopy. *Reviews on Modern Physics*, 82:209–275, Feb 2010. doi: 10.1103/RevModPhys.82.209. URL <http://link.aps.org/doi/10.1103/RevModPhys.82.209>.
- [17] N. Bohr. II. on the theory of the decrease of velocity of moving electrified particles on passing through matter. *The London, Edinburgh, and Dublin Philosophical Magazine and Journal of Science*, 25(145):10–31, 1913.
- [18] J. D. Jackson. *Classical electrodynamics*. John Wiley & Sons, Inc., New York, NY, 1999.
- [19] M. Stöger-Pollach. Low voltage TEM: Influences on electron energy loss spectrometry experiments. *Micron*, 41(6):577–584, 2010.

- [20] K. van Benthem, R. H. French, W. Sigle, C. Elsässer, and M. Rühle. Valence electron energy loss study of Fe-doped SrTiO<sub>3</sub> and a Σ13 boundary: electronic structure and dispersion forces. *Ultramicroscopy*, 86(3):303–318, 2001.
- [21] D. A. Muller and J. Silcox. Delocalization in inelastic scattering. *Ultramicroscopy*, 59(1):195–213, 1995.
- [22] H. Shuman, C.-F. Chang, and A. P. Somlyo. Elemental imaging and resolution in energy-filtered conventional electron microscopy. *Ultramicroscopy*, 19(2):121–133, 1986.
- [23] C. Mory, H. Kohl, M. Tence, and C. Colliex. Experimental investigation of the ultimate EELS spatial resolution. *Ultramicroscopy*, 37(1):191–201, 1991.
- [24] K. M. Adamson-Sharpe and F. P. Ottensmeyer. Spatial resolution and detection sensitivity in microanalysis by electron energy loss selected imaging. *Journal of Microscopy*, 122(3):309–314, 1981.
- [25] H. Kohl and H. Rose. Theory of image formation by inelastically scattered electrons in the electron microscope. *Advances in Electronics and Electron Physics*, 65:173–227, 1985.
- [26] M. Bosman, L. J. Tang, J. D. Ye, S. T. Tan, Y. Zhang, and V. J. Keast. Nanoscale band gap spectroscopy on ZnO and GaN-based compounds with a monochromated electron microscope. *Applied Physics Letters*, 95(10):101110, 2009.
- [27] O. Scherzer. Über einige Fehler von Elektronenlinsen. *Zeitschrift für Physik*, 101(9-10):593–603, 1936.
- [28] O. Scherzer. Zur Korrigierbarkeit von Elektronenlinsen. *Optik*, 2:114–132, 1947.
- [29] M. Haider, G. Braunshausen, and E. Schwan. Correction of the spherical aberration of a 200 kV TEM by means of a hexapole-corrector. *Optik*, 99(4):167–179, 1995.
- [30] M. Haider, S. Uhlemann, E. Schwan, H. Rose, B. Kabius, and K. Urban. Electron microscopy image enhanced. *Nature*, 392:768–769, 1998.
- [31] M. Haider, H. Rose, S. Uhlemann, B. Kabius, and K. Urban. Towards 0.1 nm resolution with the first spherically corrected transmission electron microscope. *Journal of Electron Microscopy*, 47(5):395–405, 1998.

- [32] M. Haider, H. Rose, S. Uhlemann, E. Schwan, B. Kabius, and K. Urban. A spherical-aberration-corrected 200 kV transmission electron microscope. *Ultramicroscopy*, 75(1):53–60, 1998.
- [33] O. L. Krivanek, N. Dellby, A. J. Spence, R. A. Camps, and L. M. Brown. Aberration correction in the STEM. In *Institute of Physics Conference Series*, volume 153, pages 35–40. Bristol (England); Boston: Adam Hilger, Ltd., c1985-, 1997.
- [34] P. E. Batson, N. Dellby, and O. L. Krivanek. Sub-ångstrom resolution using aberration corrected electron optics. *Nature*, 418(6898):617–620, 2002.
- [35] P. W. Hawkes. Aberration correction past and present. *Philosophical Transactions of the Royal Society A*, 367(1903):3637–3664, 2009.
- [36] D. S. Su, H. W. Zandbergen, P. C. Tiemeijer, G. Kothleitner, M. Hävecker, C. Hébert, A. Knop-Gericke, B. H. Freitag, F. Hofer, and R. Schlögl. High resolution EELS using monochromator and high performance spectrometer: comparison of v 2 o 5 ELNES with NEXAFS and band structure calculations. *Micron*, 34(3):235–238, 2003.
- [37] M. Terauchi, M. Tanaka, K. Tsuno, and M. Ishida. Development of a high energy resolution electron energy-loss spectroscopy microscope. *Journal of Microscopy*, 194(1):203–209, 1999.
- [38] S. Lazar, G. A. Botton, and H. W. Zandbergen. Enhancement of resolution in core-loss and low-loss spectroscopy in a monochromated microscope. *Ultramicroscopy*, 106(11):1091–1103, 2006.
- [39] E. Fermi. The ionization loss of energy in gases and in condensed materials. *Physical Review*, 57(6):485, 1940.
- [40] J. Lindhard. *On the properties of a gas of charged particles*. PhD thesis, Kgl. Danske Videnskab. Selskab Mat.-Fys. Medd., 1954.
- [41] P. Yu and M. Cardona. *Fundamentals of Semiconductors: Physics and Materials Properties*. Graduate Texts in Physics. Springer, 2010. ISBN 9783642007101. URL [http://books.google.es/books?id=5aBuKYBT\\_hsC](http://books.google.es/books?id=5aBuKYBT_hsC).
- [42] P. Nozieres and D. Pines. Electron interaction in solids. Characteristic energy loss spectrum. *Physical Review*, 113(5):1254, 1959.
- [43] H. Ehrenreich and M. H. Cohen. Self-consistent field approach to the many-electron problem. *Physical Review*, 115(4):786, 1959.

- [44] A. Benassi. *Role of the vacuum fluctuation forces in microscopic systems.* PhD thesis, Università degli studi di Modena e Reggio Emilia, 2008.
- [45] M. G. Bell and W. Y. Liang. Electron energy loss studies in solids; the transition metal dichalcogenides. *Advances in Physics*, 25(1):53–86, 1976.
- [46] R. Abt, C. Ambrosch-Draxl, and P. Knoll. Optical response of high temperature superconductors by full potential LAPW band structure calculations. *Physica B: Condensed Matter*, 2(0):1451–1452, 1994. ISSN 0921-4526. doi: [http://dx.doi.org/10.1016/0921-4526\(94\)91225-4](http://dx.doi.org/10.1016/0921-4526(94)91225-4). URL <http://www.sciencedirect.com/science/article/pii/0921452694912254>.
- [47] D. Pines. *Elementary excitations in solids: lectures on phonons, electrons, and plasmons*, volume 5. W. A. Benjamin New York and Amsterdam, 1964.
- [48] R. H. Ritchie. Plasma losses by fast electrons in thin films. *Physical Review*, 106(5):874, 1957.
- [49] E. Kröger. Berechnung der Energieverluste schneller Elektronen in dünnen Schichten mit Retardierung. *Zeitschrift für Physik*, 216(2):115–135, 1968.





# Chapter 2

# Methods

“Every square is just as likely to get hit again. The hits aren’t clustering. Mean density is constant.” Nothing on the map to the contrary. Only a classical Poisson distribution, quietly neatly sifting among the squares exactly as it should... growing to its predicted shape...

---

Thomas Pynchon, *Gravity’s Rainbow*

In this chapter, computational procedures for the analysis of materials properties in low-loss EELS are presented. The discussion is necessarily restricted to only some of these methods; of course, these are the tools that are used in the following chapters of this thesis. Hence, the stress is put into the signal processing, calculation and simulation tools designed for STEM-EELS experiments in semiconductor materials. First, the common analytical tools for the analysis of the low-loss EELS spectra are explained. Following that, statistical tools conceived for the analysis of multidimensional datasets are separately presented. Those are useful for the purposes of this thesis, but are perhaps less known to the typical EELS analyst. Finally, the band structure simulation tools that were used in this thesis are also presented.

## 2.1 Analytical tools for low-loss EELS

Most of the analytical tools that are explained in this section are commonplace tools, in the sense that are either extensively explained in the literature<sup>1</sup>, or that most scientists working in the field are acquainted with them. Hence, this section is intended as a broad introduction to the following chapters, disclosing the general methodology that is used there.

In order to present the methods in a consistent manner and using graphical examples, two experimental spectra are analyzed throughout this section. Both are low-loss EEL spectra from known semiconductor materials, one from n-doped silicon, and the other one from gallium nitride. Since all the materials that are analyzed in this thesis are either based on silicon or in III-V nitride compounds, these two semiconductor materials are ubiquitous. The spectra were acquired from the substrate part of thin samples, in defect-free crystalline regions. The experiments were performed using a probe-corrected 60-300 FEI Titan microscope, which is also used in the experiments throughout this thesis. This instrument is equipped with a Wien filter monochromator, which improves energy resolution in EELS down to the sub-eV range (see Sec. 1.2.1).

The most relevant parameters concerning the acquisition conditions and calibration of these spectra are included in Table 2.1. Notice that these two experiments were performed with different acquisition conditions, yielding different signal to noise ratios (SNR). In this sense, the Si low-loss spectrum was acquired using low  $E_0$  electrons in order to avoid radiative-loss processes, more important given the dielectric response of Si (which is demonstrated below). Notice that because of the smaller collection angle,  $\beta$ , that is used in the acquisition of the Si spectrum, a poorer SNR is expected. Conversely, this small collection angle ensures that the inelastic scattering comes from dipole-like interactions only (small- $\mathbf{q}$  limit).

For Si, only a single spectrum was collected, whilst the GaN experiment was an EELS spectrum line (SL) acquisition (see Sec. 1.2.1). For the analyses in this section, only a single spectrum from the GaN EELS-SL is shown or processed at once, unless otherwise stated.

Below, a series of computational procedures are explained. They are used for the dielectric characterization of the sampled materials using low-loss EELS. The experimental conditions are also discussed, as they can determine whether features in the spectra can be correlated with material properties. Of course, this is done by inscribing these features in the inelastic scattering distribution theoretical framework of Sec. 1.3. With this objective in mind, relevant information has to be separated from other spurious contributions to the spectral intensity using various spectral processing techniques. In order to do so, subtraction and de-

**Table 2.1** Relevant parameters for the example spectra; beam energy,  $E_0$ , collection angle,  $\beta$ , channel size,  $\Delta E$ , ZLP full width at half maximum, FWHM, zero-loss intensity,  $I_0$ , and relative thickness,  $t/\lambda$ .

	$E_0/ \text{keV}$	$\beta/ \text{mrad}$	$\Delta E/ \text{eV}$	FWHM / eV	$I_0/ \text{counts}$	$t/\lambda$
Si	80	2.5	0.02	0.24	$4.3 \cdot 10^7$	0.33
GaN	300	17.0	0.02	0.25	$10.4 \cdot 10^7$	0.35

convolution methods are presented. Finally, the dielectric properties in the form of  $\varepsilon(\omega)$  are revealed using Kramers-Kronig analysis (KKA). The presentation of this algorithm is culminated with the calculation of relevant dielectric properties, based on the Bethe f-sum rules.

### 2.1.1 Calibration and deconvolution

Figure 2.1 shows low-loss spectra obtained from Si and GaN semiconductor materials with the experimental conditions described above. Notice first that the most intense contribution to these spectra is the zero-loss peak (ZLP), located at the left-hand side of the image but not totally included. Indeed, for any thin sample, the ZLP dominates the low-loss EELS if acquired, being typically thousands of

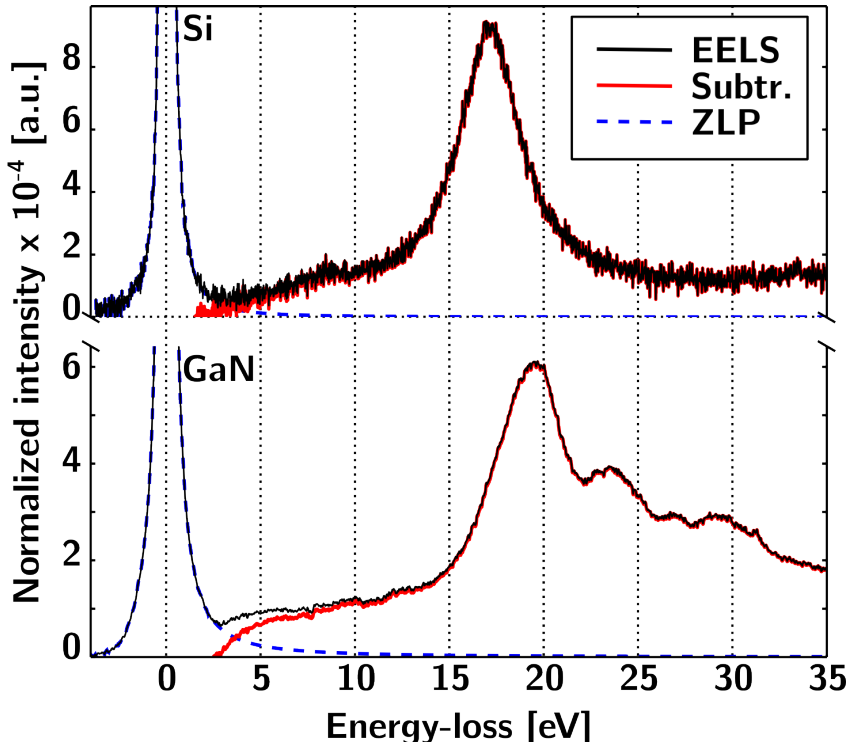


**Fig. 2.1** Two experimental low-loss spectra, from silicon (Si) and gallium nitride (GaN) semiconductor materials, black lines. In both cases, a power-law fit is used to model the ZLP tail, blue dashed lines. These ZLP models are subtracted from the EELS intensity, and the remaining intensity is depicted in dashed lines.

times more intense than the other features. As introduced in Sec. 1.2.2, this peak is related to electrons that have undergone elastic scattering, or no scattering at all. One might think that since no energy-loss has been detected for the spectral intensity in the ZLP, no information is enclosed in it, and its acquisition is uninteresting. However, this is far from the truth, and it is important to analyze this peak as it allows the calibration of the energy-loss axis, and provides with an estimate of the specimen thickness and the instrumental broadening.

The first **use of the ZLP** is in the **calibration of the energy-loss axis**. For this reason, it is reasonable to acquire the ZLP whenever considering low-loss EELS. Indeed, the energy axes of both spectra in Fig. 2.1 are calibrated using the maxima of each ZLP, which is better examined in Fig. 2.2. In the best case scenario, this procedure allows to obtain a calibration precision equal to the spectral channel bin size. This bin size is set in the acquisition, and in our cases is of  $\Delta E = 0.02$  eV (see Tab. 2.1). This precision can be improved if necessary, *e.g.* by modeling the ZLP shape with Gaussian or/and Lorentzian functions, in order to obtain sub-pixel precision. Another fast and reliable method to obtain sub-pixel precision is to measure the cross-correlation between ZLP features in a series of spectra and shift their energy-loss axis accordingly. Notice that this is useful when more than one spectrum is acquired at the same time, such as in the GaN EELS-SL. This is a typical working situation.

As described in Sec. 1.2.4, inelastic processes are governed by Poisson statistics and the **relative thickness of the sample** can be obtained from a simple formula, Eq. (1.19), related to the total and ZLP spectral intensities. If low-loss EELS is acquired up to moderately high energy-loss, well above the plasmon peak, the estimation of the relative thickness with the above mentioned formula

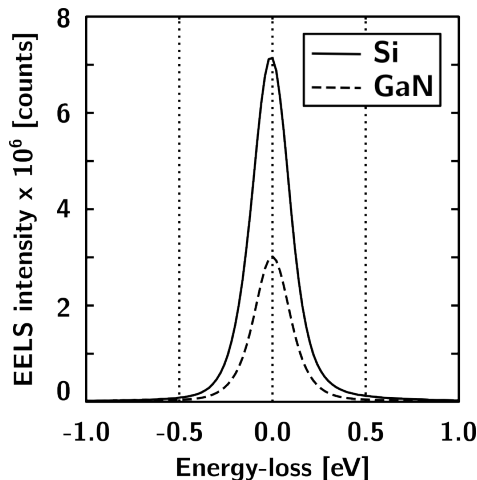


**Fig. 2.2** The complete, non-normalized, ZLP from the Si and GaN spectra, depicted with solid and dashed lines, respectively. The ZLP FWHM is of  $\sim 0.2$  eV in both cases, and the intensities are  $10.4 \cdot 10^7$  for the Si spectrum and  $4.3 \cdot 10^7$  for the GaN spectrum.

is accurate. This is because, for most thin film specimens of low-Z materials, low-loss EELS represents the majority of the total inelastic scattering intensity. Indeed, in these typical cases, the plasmon peak concentrates most of the intensity in the energy-loss spectrum. In the inelastic scattering theoretical framework, the values of the relative thickness,  $t/\lambda$ , are related to the fast electron path in the sample. Notice that from Eq. (1.42) and the definitions therein, it becomes clear that the electron mean-free-path,  $\lambda$ , is related to the stopping power. As a consequence, it has a dependence on the electron velocity, set up by the beam voltage,  $E_0$ , and on the collection angle,  $\beta$ .

In some cases, an estimation of the value of  $\lambda(E_0)$  can be obtained from tables in the literature<sup>1</sup>. Using this knowledge, the  $t/\lambda$  can provide with an approximation to the specimen thickness,  $t$ . For instance, the tabulated value for c-Si is  $\lambda = 145$  nm for  $E_0 = 200$  keV ( $\beta = 12$  mrad), which is reduced to about 130 nm for 80 keV electrons. The  $t/\lambda$  values obtained for the Si and GaN spectra were 0.33 and 0.35, respectively. These values indicate that these spectra were acquired in thin regions of the sample, with thicknesses around 50 nm. Notice that further corrections to this calculation would imply considering the  $\lambda(\beta)$  dependence.

Apart from its intensity, the **full width at half maximum (FWHM) of the ZLP** is also a relevant parameter to be assessed, because, as explained in Sec. 1.2.5, the width of this peak is related to the **instrumental broadening**. Indeed, if the beam and spectrometer were perfect, the zero-loss distribution would only occupy a single channel, and it would be possible to measure infinitely small energy-losses. In practice this is impossible because of the energy spread of the beam and the additional broadening introduced by the spectrometer. In this sense, two different effects are taken into account when assessing the ZLP width. First, notice that instrumental broadening affects all of the acquired EELS intensity, not only the ZLP. Thus, the determination of the ZLP FWHM gives an estimate of the energy resolution of the experimental set-up. This important information cannot be obtained from other intense EELS features, like the plasmon peak, because their width is strongly influenced by their respective excitation life-times.

A second reason to assess the ZLP FWHM is that the tails of the zero-loss distribution extend into the energy-loss spectrum, with an impact that can dominate the spectral intensity in the first few eV. This is most relevant for the low-loss EELS of semiconductor materials, because this region typically contains the first interband transition features, such as the band gap signal. Indeed, if one wants to measure these low-energy features, the use of TEM instruments equipped with a monochromator is more than advisable. Using a monochromator, energy spread of the beam is drastically improved, and the ZLP FWHM can be reduced to the sub-eV range.

When the ZLP is sufficiently narrow, its tail can be modeled and subtracted to reveal the low energy-loss features. There is a vast number of possible strategies for subtracting the ZLP, considering that the shape of this peak and the nature of the features to be measured are variables that depend on the instrument and the material, respectively. Because of this, let us review in detail the strategy that is used in this work, which is power-law subtraction. In this strategy, the ZLP tail above a selected energy threshold is modeled by a power-law function. This procedure is typically performed using a least-square fit to the spectral data in a fitting-window immediately preceding the threshold, with a width between 0.5 – 1.0 eV. For example, in order to obtain the ZLP models in Fig. 2.1, power-law extensions were applied using the following regions; 0.5 – 1.5 eV for Si and 1.5 – 2.5 eV for GaN. For this last material, the onset of its direct band gap, at  $\sim 3.4$  eV, is intense. Meanwhile, for Si, the indirect band gap onset, at  $\sim 1.5$  eV, is more faint. Nevertheless, both signals are visible in the acquired low-loss EELS data, owing to the fact that the ZLP FWHM in these experiments was  $\sim 0.25$  eV.

### Fourier-log deconvolution

It is indeed advisable, before other analytic procedures are performed to low-loss EELS data, to first consider spectral processing tools that can take advantage of the information within the ZLP. This section explains the deconvolution algorithms used for this processing, that deal with the spurious effects of plural scattering and instrumental broadening. Notice that the impact of these effects can also be attenuated to some extent by using adequate experimental conditions, *i.e.* regarding sample preparation and/or instrumentation. Whenever further improvement is not possible by experimental means, the deconvolution techniques come in handy. The most widespread algorithm is the Fourier-log deconvolution (FLD)<sup>2</sup>. This algorithm is useful for deconvolution of plural scattering, coupled with the subtraction of a ZLP model. A second algorithm, Richardson-Lucy deconvolution (RLD), capable of achieving deconvolution of broadening effects, also using a ZLP model, is described in the following sub-section.

As explained in Sec. 1.2.4, the transmitted electron can suffer inelastic scattering more than once before it emerges from the sample. This effect is known as plural or multiple scattering, giving rise to an additional spectral distribution that is governed by Poisson statistics. It is easy to see that the value of the  $t/\lambda$  parameter is related to the amount of plural scattering in a given spectrum. Indeed, we can estimate that for  $t/\lambda > 1$  these effects are important, and even below that, their impact is still sizable. Nevertheless, plural scattering is neglected in the usual theoretical models for EELS, *e.g.* the dielectric formulation of low-loss presented in Sec. 1.3.2, in which only a single scattering distribution (SSD) is taken into account. As including plural scattering in all these models

would constitute an unpractical solution, the sound approach is to eliminate it from our experimental measurements.

The FLD algorithm makes it possible to perform deconvolution of plural scattering using the information in the ZLP. This algorithm uses the relationship between the zero-loss, single and measured scattering distributions established by Poisson statistics. Using their Fourier representations, and naming these distributions  $z$ ,  $s$  and  $j$ , respectively, their relationship is given by,

$$s = I_0 \log(j/z) \quad (2.1)$$

were  $I_0$  represents the ZLP intensity as usual. To perform this calculation an algorithm based on the fast Fourier transform (FFT) was provided in Ref. 1. In the version that is used in the present work, found in Hyperspy<sup>3</sup>, the ZLP model is used in order to perform subtraction of this peak as well. This version is additionally modified to avoid noise problems and fills the spectral range with zeros in order to use a longer FFT vector (zero-padding). Whenever necessary, the high energy-loss end of the plasmon is extended to the next power-of-two, using a power-law tail. This is a standard pretreatment when performing Fourier analysis, to avoid introducing step-like artifacts at the spectrum extrema.

Figure 2.3 shows the result of processing the low-loss EELS of Si and GaN using this FLD algorithm. After FLD, the SSD are retrieved, in the figure in red lines. Notice that these SSD have been stripped of the ZLP and plural scattering,

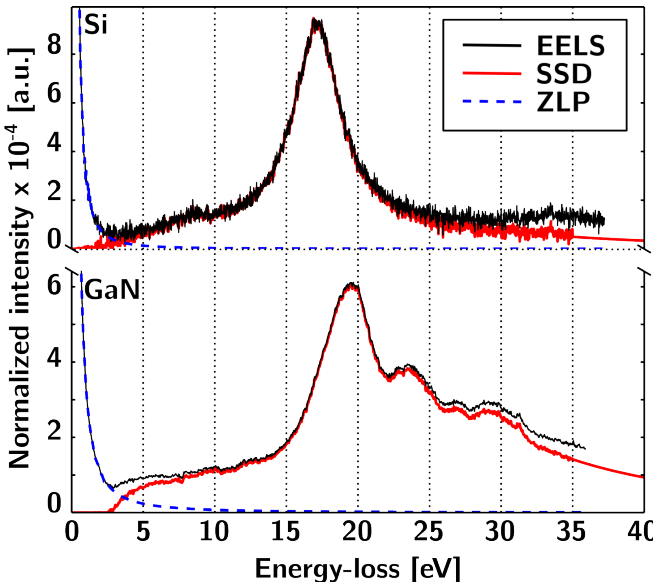


**Fig. 2.3** Same spectra and ZLP models as Fig. 2.1, but instead of just subtracting the ZLP models, Fourier-log algorithm is used to perform plural scattering deconvolution to reveal the SSD, depicted with dashed lines. A pretreatment for Kramers-Kronig analysis has also been performed, which does not affect the shape of the signal.

diverging from the experimental EELS data at the lower and higher energy-loss regions. The reduction at high energies corresponds to plural scattering deconvolution. It is perhaps better appreciated in the Si spectrum, in which the curvature after the plasmon is drastically affected. Finally, it can be appreciated that the ZLP subtraction in Fig. 2.1 produces a similar result at low energy-loss, without affecting higher energy-loss regions, of course.

Theoretically, FLD should eliminate both plural scattering and broadening effects from the scattering distribution. In practice, this is not possible, first, because of the noise content of the spectrum, and, ultimately, because of the energy resolution limitations<sup>1</sup>. This restricts the power of FLD to deconvolution of plural scattering, and the recovered SSD is affected by instrumental broadening just as the measured one is. In order to attenuate broadening effects as well, Bayesian algorithms can be of some help.

### **Richardson-Lucy deconvolution**

It is possible to attenuate the effect of instrumental broadening in a measured spectrum using Bayesian deconvolution methods. In these, a sharpening of the spectrum is obtained by including an estimate of the point spread function (PSF) of the system. The objective of these methods is then to invert the effect of the PSF, improving the energy resolution. This is typically done by iterative minimization of some functional. Further information is incorporated to these functionals, *e.g.* in order to restrict the possible solutions only to positive spectral intensities. The method used in this work is Richardson-Lucy deconvolution (RLD) adapted to EELS data<sup>1,4</sup>.

This iterative method was originally devised for image restoration for astronomical data from large telescopes in which the lens aberration produces a point spread<sup>5,6</sup>. It uses the maximum-likelihood Bayesian deconvolution, assuming a Poisson noise distribution, thus being adequate for EELS. The RLD algorithm needs an estimate of the PSF, used as a kernel in the iterative maximization process. The algorithm is known to be robust to small errors in the PSF, and the use of a ZLP acquired in vacuum using the same conditions as the spectrum to process is advisable. Other possible kernels include ZLP models from experimental data or using Gaussian and Lorentzian combined forms, as for the zero-loss distribution models used in FLD.

In practice, deviations from the assumptions of the Bayesian deconvolution cause the iterative loop to diverge, as artifacts are introduced in the result. For instance, unlike most noise sources in EELS that are of Poisson nature, as assumed by RLD, CCD readout noise is of Gaussian nature. This noise source is typically less important, and can be neglected in the majority of spectra, except for the noisier cases. Additional problems appear when the iterative method is carried out beyond the energy resolution limits, in particular affecting regions in

which large dynamic range variations are present. In these cases, characteristic ripple-like artifacts appear in the spectrum, localized in those regions, which are easy to detect and help determine the appropriate number of iterations. The ZLP tails are one example of such regions with a large dynamic range variation.

Let us demonstrate the application of the RLD algorithm by using the Si and GaN low-loss EELS data as examples, a process that is depicted in Fig. 2.4. In these two experiments the vacuum ZLP was not acquired, so it is necessary to build a ZLP model to use as a RLD kernel. The ZLP model that was built for FLD is the obvious choice. As RLD performs better with moderate noise levels, the spectral axes are rebinned by averaging in a 4-channel wide window (new channel width  $\sim 0.8$  eV). This process amounts to a reduction in the dimensions of the energy axis in both spectra from 2048 to 512 pixels. For the GaN EELS-SL the ZLP model can be further improved using median filtering to average adjacent pixels. This process removes noise from the models that impacts the spectral region of the ZLP tails.

The results from the application of the RLD algorithm with 5, 7, 15 and 25 iterations are portrayed with increasingly bold shades of red in Fig. 2.4. The performance of the RLD can be assessed by examining the ZLP FWHM, that in both cases is reduced below 0.15 eV from the original  $\sim 0.25$  eV. Additionally, the definition of the peaks is slightly improved, as clearly seen in the GaN spectrum. Characteristic ripple artifacts of RLD are visible at the high energy-loss ends of

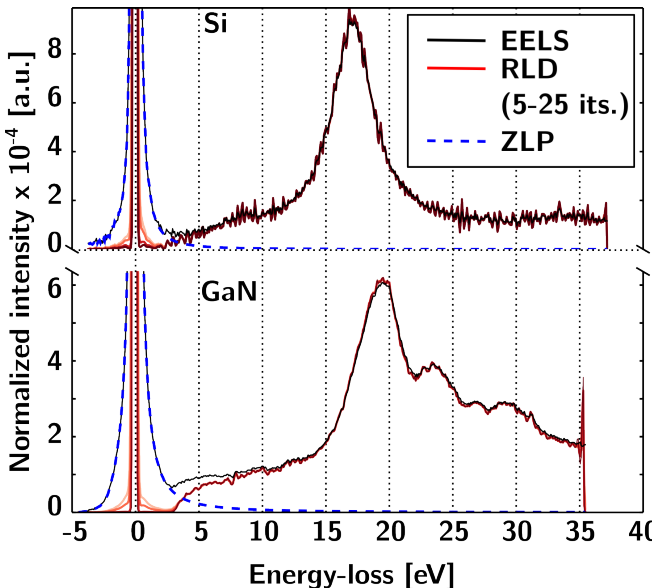


**Fig. 2.4** Various iterations (3-25) of the RLD algorithm applied to the Si and GaN spectra, using a ZLP model as a kernel; both depicted as in the preceding figures. The resulting sharpened spectra are depicted in shades of red, bolder for greater iteration numbers. The ZLP model for Si is obtained as in Fig. 2.1, the GaN one is obtained after a filtering process, as explained in the text.

the spectra, and at the tail of the ZLP. These artifacts are originated in large dynamic range variation regions, and since they are confined to these localized spectral regions, which can be discarded, they are of little importance. Further rippling affects noisy regions of the spectra, an effect that is more important in the noisier Si spectrum. In this case, the RLD algorithm fails to distinguish the elevated noise levels from the relatively faint signals. Since this is an intrinsic problem of the noise level of the Si spectrum, in this case, the application of the RLD algorithm is not recommended. In both cases, RLD reveals the band gap onset in the spectra, as the subtraction of the ZLP model by FLD did. Since the improvement in sharpness seems not worth the risk of introducing ripple artifacts in our spectra by over-smoothing, especially for the Si spectrum, this deconvolution method will not be used in the following calculations in this section.

### 2.1.2 Kramers-Kronig analysis

In most occasions, low-loss EELS data is acquired with the intention of revealing the dielectric properties of the sample enclosed in  $\varepsilon(E)$ , the CDF. For this purpose, the relatively simple expressions of the dielectric formulation of inelastic scattering in the non-retarded limit are useful. These expressions were introduced in Sec. 1.3.2, where it was shown that inelastic scattering from a thin film in this limit is only related to  $\text{Im}[-1/\varepsilon(E)]$ , the ELF, see Eq. (1.47). The following sections describe the Kramers-Kronig analysis (KKA) method, devised in order to reveal this information enclosed in low-loss EELS. The discussion here is based on Ref. 1, that explains the fast Fourier transform (FFT) method used in this work. The Kramers-Kronig transformation is explained first, as this property of the CDF enables KKA. The following sections describe the stages of the KKA iterative algorithm. First, the pretreatment of the SSD and the  $\text{Im}(-1/\varepsilon)$  normalization, that are performed before the transformation. Then, the iterative surface-loss removal procedure, that includes the transformation.

#### Kramers-Kronig transformation

One could think that  $\text{Im}(-1/\varepsilon)$  alone does not contain the full dielectric response information enclosed in  $\varepsilon$ . Nonetheless, the missing piece of this puzzle is found in the inherent properties of these functions, as dielectric response coefficients are bound by causality requirements (see Sec. 1.3.1). This mean that the Kramers-Kronig relations hold. The formulation presented in Eq. (1.27) can be then adapted for the CDF, to the inverse of the dielectric function as<sup>1</sup>,

$$\text{Re} \left[ \frac{1}{\varepsilon(E)} \right] = 1 - \frac{2}{\pi} \mathcal{P} \int_0^\infty \text{Im} \left[ \frac{-1}{\varepsilon(E)} \right] \frac{E' dE'}{E'^2 - E^2} \quad (2.2)$$

This relationship allows calculating  $\text{Re}(1/\varepsilon)$  from  $\text{Im}(-1/\varepsilon)$ , obtaining all the information necessary to compute  $\varepsilon$  by straightforward complex algebra. It is necessary to consider the way in which the Kramers-Kronig transformation is going to be integrated. Notice that the direct approach requires the whole range of  $\text{Im}[-1/\varepsilon(E')]$  to be integrated at each  $E$ , which, from the computational point of view, constitutes a time consuming algorithm.

Another fast and reliable method, used in this work, is based on the evaluation of the integrals in the time-domain, using fast Fourier transform (FFT) methods<sup>7</sup>. Considering the time-dependent dielectric function,  $1/\varepsilon(t) - \delta(t)$ , the cosine and sine transforms of its even and odd parts,  $p(t)$  and  $q(t)$ , are related to  $\text{Re}[1/\varepsilon(E)] - 1$  and  $\text{Im}[-1/\varepsilon(E)]$ , respectively. The causality assumption then reads  $1/\varepsilon(t') - \delta(t') = 0$  for  $t' < 0$ , and therefore,  $p(t) = \text{sgn}[q(t)]$ . In other words,  $q(t)$  can be computed as the FFT of  $\text{Im}(-1/\varepsilon)$ , and following a sign inversion this gives  $p(t)$ . Then,  $\text{Re}[1/\varepsilon]$  is obtained as the real part of the FFT of  $p(t)$ .

### KKA algorithm I: pretreatment

Irrespective of the selected algorithm, FFT or direct integration, it is advisable to let the EELS intensity smoothly decay to zero in order to perform the Kramers-Kronig transformation. Of course, the best way to do so is to acquire the low-loss data up to high enough energy-losses. However, this is not always possible, as we are interested in high energy resolution, decreasing the energy channel step size which, in turn, reduces the acquired energy range. In these cases, the EELS intensity is extended using a Power-law with a negative exponent that decays smoothly to zero. This procedure is applied before computing the transformation, extending the spectrum size up to at least the double of the closest power-of-two, in order to avoid the wrap-around problem of the FFT. Notice that a similar tail extension procedure is also customary in most cases when computing directly the integral in Eq. (2.2)<sup>1</sup>.

As any spurious low energy-loss intensity introduces an instability in the result, this part is also typically processed. One solution is to use a Hanning window between 0 eV and a threshold positive energy-loss, to taper this intensities without changing the SSD integral.

These pretreatments can be examined by comparing Fig. 2.1 and Fig. 2.3. In the first figure no pretreatment was applied; in the second one, Hanning taper and Power-law extension are depicted. In that figure, the Hanning taper was applied in different filtering windows for Si and GaN, starting from 0 eV in both, up to an energy-loss threshold of, 1.5 eV for Si and 2.5 eV for GaN. The Power-law extension was applied using a fit window of 4 eV, starting from the end of the spectrum. The final spectra have a length of  $2^{12} = 4096$  channels and decay smoothly to zero intensity.

### KKA algorithm II: normalization

Ignoring the contributions from different surface-loss terms, radiative-loss modes and instrumental broadening, Eq. (1.47), predicts the SSD in a thin film from  $\varepsilon(E)$ . The same equation can be used to compute  $\text{Im}(-1/\varepsilon)$  from the SSD obtained in a low-loss EELS experiment, *e.g.* after Fourier-log deconvolution as described in Sec. 2.1.1. This proportionality is obtained solving Eq. (1.47), which is revisited here for the sake of clarity in a slightly different form,

$$\text{Im} \left[ \frac{-1}{\varepsilon(E)} \right] = \left( \frac{I_0 t}{\pi^2 a_0 m_0 v^2} \right)^{-1} \frac{\text{SSD}}{\log [1 + (\beta/\theta_E)^2]} \quad (2.3)$$

With the definitions so far, it is possible to estimate values for all of the involved quantities in this equation except for one, the absolute specimen thickness  $t$ . In the cases where the value of  $t$  is not accurately known, the Kramers-Kronig sum rule can be used to obtain the remaining proportionality term (in parentheses). This sum rule is obtained from the  $E \rightarrow 0$  limit of Eq. (2.2),

$$1 - \text{Re} \left[ \frac{1}{\varepsilon(0)} \right] = \frac{2}{\pi} \int_0^\infty \text{Im} \left[ \frac{-1}{\varepsilon(E)} \right] \frac{dE}{E} \quad (2.4)$$

Considering the typical behavior of  $\varepsilon(E)$ , the left-hand side can be taken as 1 for a metal, and as  $1 - 1/\varepsilon_1(0)$  for an insulator, where  $\varepsilon_1(0) = n^2$ , the square of the refractive index for visible light. This normalization has the additional advantages that the values of  $v$  and  $\beta$  are not used, and that an estimate of  $t$  is obtained (given that  $E_0$  and  $I_0$  are known). Indeed, the absolute thickness determination is an additional result of KKA when  $n$  is used for normalization. In the cases where the value of  $n$  is not accurately known, an estimate of  $t$  can be used instead. Nevertheless, the normalization of  $\text{Im}(-1/\varepsilon)$  is very sensitive to small variations, giving large errors for small  $E$  when the FFT are computed.

### KKA algorithm III: surface-loss removal

In order to subtract the non-retarded surface-loss contribution from the SSD (ignoring surface coupling), Eq. (1.48) is implemented into KKA. In the formulation used in this work, a thin film specimen in vaccum is assumed. This equation gives an estimate of the surface-loss contribution from the  $\varepsilon$  obtained after normalization of  $\text{Im}(-1/\varepsilon)$  and Kramers-Kronig transformation.

Surface-loss removal is an important part of KKA, especially in very thin samples with  $t < 50$  nm. When implemented, KKA results in an iterative process in which the normalization, transformation and surface-loss removal steps are repeated until convergence is reached. Convergence largely depends on the shape of the low-loss EELS intensity at small  $E$ . Indeed, the iterative process may be

monitored through the variations of  $\varepsilon(E)$  in this region, that should approach the optical refractive index. Conversely, the absolute thickness estimation may be also used to monitor the iterative process.

The KKA iterative algorithm was applied to the SSD of Si and GaN (see Fig. 2.3), after the pre-processing explained in the last sections. For this purpose, the KKA algorithm in Hyperspy was used<sup>3</sup>. The CDF of both materials were obtained, which are given in Fig. 2.5. The refractive indices for both materials were used,  $n_{Si} = 3.8$  and  $n_{GaN} = 2.42$ . In both cases, the iterative process converged quite quickly, in 5 or less iterations. The absolute thickness estimates are  $\sim 51.5$  nm for Si and  $\sim 41.5$  nm for GaN. Considering the instrumental broadening ( $\sim 0.25$  eV), the shape of both  $\varepsilon(E)$  shows a moderately good agreement with the dielectric response functions determined by other methods for these materials.

Besides instrumental broadening, and the considered bulk and surface terms, other contributions affect the single scattering distribution. As introduced in Sec. 1.3.2, they include the surface coupling effect, and, in most cases, radiative contributions. Obviously, the formulation leading to KKA is only justified when the dominant contribution to inelastic scattering is the bulk non-retarded term, and surface coupling, in thin samples, and radiative contributions, in thick samples at high voltages, are negligible.

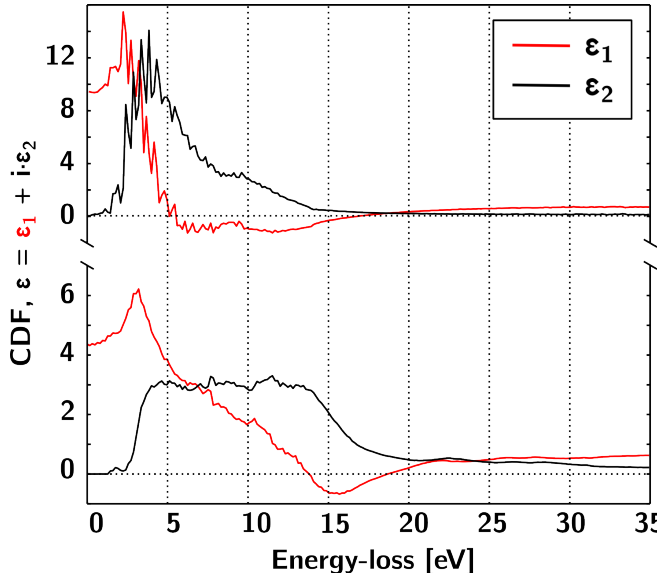


**Fig. 2.5** Complex dielectric function (CDF) of Si and GaN, depicted with black and red lines for the imaginary and real parts, respectively. The CDF is obtained after KKA, using the SSD obtained from FLD (see Fig. 2.3), and after applying the pre-treatments explained in the text.

### 2.1.3 Bethe f-sum

The study of the dielectric properties in low-loss EELS is complemented with the oscillator strength sum rules, introduced in Sec. 1.3.1. In this sense, the dielectric response of material media is defined by the properties of the JDOS, the convolution of valence and conduction bands. EELS experiments, as well as optical absorption, indirectly probe this JDOS. This is a valuable feature of these techniques, which reveals further information about the band character of the sampled material. In this section, a classical calculation based on these sum rules is presented: the calculation of the effective electron number.

The relevant dielectric coefficients for optical absorption and energy-loss experiments are  $\text{Im}(\varepsilon) = \varepsilon_2$  and  $\text{Im}(-1/\varepsilon)$ , respectively. Through their relationship with the JDOS and oscillator strength, Bethe f-sum rule is applied to both coefficients. For  $\varepsilon_2$ , this is done almost directly by analogy of the RPA CDF with the definition of the JDOS in Eq. (1.40). For  $\text{Im}(-1/\varepsilon)$ , Bethe theory, see Sec. 1.2.3, is implemented into the DDCS definition, in Eq. (1.45). In both cases  $n_v$ , the absolute number of valence electrons per unit volume is obtained,

$$n_v = \frac{2\varepsilon_0 m_0}{\pi n_a \hbar^2 e^2} \int_0^\infty E \varepsilon_2(E) dE = \frac{2\varepsilon_0 m_0}{\pi n_a \hbar^2 e^2} \int_0^\infty E \text{Im} \left[ \frac{-1}{\varepsilon(E)} \right] dE \quad (2.5)$$

These JDOS-functions are not equal, and they portray the differences between  $\varepsilon_2$  and  $\text{Im}(-1/\varepsilon)$ . The first one reflects only transverse optical absorption, with  $q \approx 0$ . The second one reflects longitudinal modes also (plasmon excitation). Notice that these integrals extend up to infinity, which is actually impossible to do experimentally, as the core-excitation energies overlap the spectrum. In order to gain insight into the JDOS of a material, one option is to examine the integrands in these equations as a function of  $E$ .

It is also possible to compute the effective number of electrons per unit atom (or unit cell),  $n_{eff}$ . This is an energy-loss dependent quantity, as it is obtained by computing the integrals in Eq. (2.5) up to a given  $E$ , instead of infinity. This operation can be performed for both the ELF and the CDF, giving rise to two different formulas for  $n_{eff}$ ,

$$n_{eff}(\varepsilon_2) = \frac{2\varepsilon_0 m_0}{\pi n_a \hbar^2 e^2} \int_0^E E' \varepsilon_2(E') dE' \quad (2.6)$$

$$n_{eff}[\text{Im}(-1/\varepsilon)] = \frac{2\varepsilon_0 m_0}{\pi n_a \hbar^2 e^2} \int_0^E E' \text{Im} \left[ \frac{-1}{\varepsilon(E')} \right] dE' \quad (2.7)$$

Because there is an  $1/E$  weighting factor between the ELF and CDF, favoring Eq. (2.6),  $n_{eff}$  calculated with Eq. (2.7) remains smaller up to large values of  $E$ .

For sufficiently large values of  $E$ , both  $n_{eff}(E)$  converge to a plateau value. In simple cases, this value corresponds to  $n_v$ , a known number of electrons in the valence band. Thus,  $n_{eff}$  can provide a comparison between theoretical models and the data derived from the dielectric formulation of low-loss EELS.

These integrals can be computed using the CDF that were derived from the experimental low-loss EELS of Si and GaN in the last section. The result of these calculations is given in Fig. 2.6 (The following number of atoms per  $m^3$  have been used:  $8.9 \cdot 10^{28}$  for GaN, and  $5.0 \cdot 10^{28}$  for Si). First, let us examine the JDOS functions, depicted with solid and dashed black lines. Notice that the plasmon peak only appears in the function that uses  $\text{Im}(-1/\varepsilon)$ . Meanwhile, the JDOS function that uses  $\varepsilon_2$  is related to the single electron transitions.

In solid and dashed red lines, the  $n_{eff}(E)$  curves show the expected behavior. For both Si and GaN, the result of computing  $n_{eff}$  using Eq. (2.6) remains larger than using Eq. (2.7), for the whole energy-loss range. Both curves seem to converge to a plateau value at large energy-losses, above plasmon excitation. Using the atomic densities given in the figure, the plateau values are found to be:  $4 e^-/\text{atom}$  for Si and  $3 e^-/\text{atom}$  for GaN.

These results can be related to the electronic structure of both materials. Silicon is the simpler case, as it is a single element crystal. Its ground state electronic shell configuration is  $[\text{Ne}]3s^23p^2$ , meaning that its valence band contains 4 electrons. In this case, the correspondence between the calculated  $n_{eff}$  values and the theoretical  $n_v$  is excellent.

In the case of GaN, this correspondence is harder to trace as inner-shell ex-

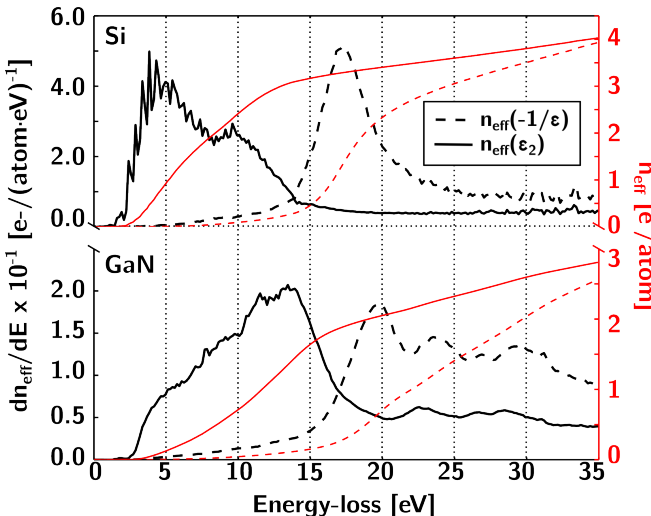


**Fig. 2.6** Effective electron number,  $n_{eff}$ , computed for Si and GaN. First, JDOS functions are derived using the CDF and ELF, portrayed with solid and dashed black lines, respectively. The cumulative integrals of these functions (see Eq. (2.6) and Eq. (2.7)) give  $n_{eff}$ , depicted with solid and dashed red lines, as above.

citations can occur before all valence JDOS has been exhausted. In this sense, notice that, although gallium has 3 electrons in the valence band, its semi-core 3d-band is also to be taken into account, as it is the origin of the fine structure observed for large  $E$ , above the GaN plasmon peak. It thus seems that the observed  $n_{eff} = 3 e^-/\text{atom}$  corresponds to the  $n_v = 3e^-$  in the valence band of gallium. Nevertheless, one cannot be completely sure of this fact: an EELS experiment in which the inelastic scattering is acquired up to a sufficiently large  $E$  might show a substantially larger plateau value before excitation of additional core-levels.

This calculation of  $n_{eff}$  is a general example of the broad many applications that low-loss EELS has in unraveling electronic properties of the probed materials<sup>1</sup>. In this sense, additional analytical methods will be presented along this thesis.

## Closing remarks

Semiconductors, such as Si and GaN, have large dielectric constants at low energy-losses. This increases the relative importance of the radiative-loss contribution. In some thick samples, the bulk Čerenkov contribution can dominate the energy-loss spectrum. It is necessary then to assess the impact of radiative losses, *e.g.* by performing calculations with the full-relativistic formulation of Eq. (1.49). For instance, such calculations have been performed for Si and GaN using reference optical data<sup>8</sup>. The calculations show that the radiative contribution strongly affects Si spectra for  $E_0 = 300 - 200$  eV, being guided-light modes the dominant term for thin specimens ( $t < 250$  nm). Similar calculations show that the impact of retardation effects in GaN spectra is negligible for thin films with thickness values below  $\sim 100$  nm. In the previous analyses, it was estimated that the Si and GaN low-loss EELS were acquired in thin regions with  $t \approx 50$  nm. In these cases, bulk radiative losses and surface coupling are negligible. However, from the above considerations, radiative surface-losses from guided-light modes can still modify the Si spectrum.

Finally, notice that the experimental conditions for the Si experiment were designed with these issues in mind. The microscope voltage was lowered to  $E_0 = 80$  keV, restricting the radiative contributions to a smaller energy-loss region and making it easier to retrieve the dielectric response information from EELS. Additionally for this experiment, sample sensibility demanding the use of low voltages was also a concern. Nevertheless, the discussion of this issue corresponds to the results sections, where it is appropriately addressed.

## 2.2 Hyperspectral analysis

STEM-EELS, the experimental technique that is used in this thesis, features an extremely localized probe, with typical sizes in the order of the Å. This is one of the most valuable characteristics of the technique, as it allows measurements of properties from very small material volumes. For instance, one can characterize the different nanometer-size structural components of a modern electronic device by positioning the STEM probe directly on them. Also, STEM-EELS produces spectra that contain a high amount of information. The interesting spectral features are typically convolved with one another and with various spurious sources (*e.g.* instrumental broadening, noise). In this sense, the information content is of mixed nature, and sometimes the analysis of the spectra is an issue that is difficult to tackle.

Nevertheless, with the development of the appropriate instrumentation, hyperspectral acquisition modes are nowadays a common analysis tool for most material scientists working in the EELS field, as well as many other spectroscopic techniques. These hyperspectral modes consist in the acquisition of spectral series that portrait spatial features or the time evolution of the studied sample. In the present work, spatially localized spectral series along lines and areas are analyzed, *i.e.* spectrum lines and images (SL and SI), respectively. These acquisitions represent a high throughput data source, as often thousands of spectra have to be analyzed at once. Obviously, following the discussions in the preceding sections, their analysis is only possible by using fast and reliable computational tools.

Some of these computational tools have been already reviewed in the previous sections, as deconvolution and dielectric analyses that can be carefully applied to several spectra at once. Modeling techniques, most importantly for the present thesis model-based fitting based on non-linear least squares, are also applied extensively. However, these are well known mathematical techniques that we are not going to review here. Less known are the analysis tools based on machine learning, which are increasingly popular in various applied science fields. They are useful to sort through vast amounts of data, deal effectively with noise, and to extract the information of interest. They are perhaps better known in the EELS field for their applications in the analysis of core-loss EELS<sup>9,10</sup>. It is interesting to take some time to introduce them, as they will be useful at some point in this thesis.

### 2.2.1 Multivariate analysis

Broadly speaking, multivariate analysis (MVA) comprises a group of mathematical algorithms, within the field of machine learning, that sort large and noisy data arrays. The datasets generated in hyperspectral EELS acquisition fit into

this category and recent years have seen an increase in the use of MVA methods<sup>1</sup>. In this context, the EELS dataset is regarded as a  $N \times M$  matrix, where  $M$  is the total number of pixels and  $N$  is the spectral size. For instance, a spectrum image dataset is  $\mathbf{D}(x, y, E)$ , with  $N$  equal to the pixel-area covered by  $x$  and  $y$ . One way to sort this data array is to solve the matrix factorization problem in the linear mixing model, by proposing a new representation of  $\mathbf{D}$  as a combination of components,

$$\mathbf{D}(x, y, E) = \mathbf{S}_n(x, y)\mathbf{L}_n^T(E) \quad (2.8)$$

where  $n$  is the component index, that runs up to the minimum between  $N$  and  $M$ . Moreover, each  $\mathbf{S}$  is a score matrix and  $\mathbf{L}^T$  is the transpose of the loading matrix. Notice that score and loading matrices keep the spatial and spectral dimensions, respectively.

### Decomposition using PCA

One method that finds a general solution to this problem is principal component analysis (PCA). This method is mathematically equivalent to solving Eq. (2.8) as an eigenvalue problem, because it is based on imposing an orthogonality requirement on the loadings. Fast and reliable algorithms exist to solve such problems, like singular value decomposition (SVD), and PCA decomposition is a relatively cheap algorithm, computationally speaking. Typically in the PCA algorithms, the amount of information enclosed in each component is identified with its explained variance. This variance can be measured in various ways, for instance by the magnitude of the loading matrix. In this framework, once that the data array is decomposed the components are sorted depending on their variance, and a threshold component index may be found above which the information content is negligible (noise).

In favorable cases when this limit can be found, only the leading high-variance components below that index are used to approximately model the data array using Eq. (2.8), effectively eliminating the majority of noise contributions. This threshold is typically small and it is found, in practice, using the so-called scree plot method. When working with real EELS data, some additional methods are used to improve the results of PCA. Among these methods, Poisson-weighted normalization of the data is a typical preprocessing, critical in reducing the number of components<sup>11</sup>. Other methods include; removing plural scattering for thicker samples; removing so-called spikes, or high intensity artifacts; and, aligning the spectral axis in order to prevent shifting artifacts in the PCA components. The results from one PCA analysis are depicted in Fig. 2.7.

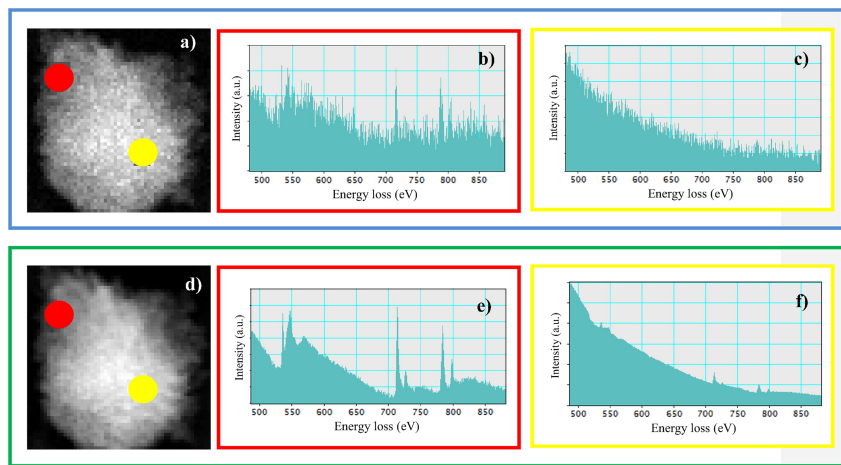


**Fig. 2.7** EELS-SI from a  $\text{Fe}_x\text{Co}_{3-x}\text{O}_4@\text{Co}_3\text{O}_4$  mesoporous nano particle, before and after PCA noise reduction, framed in blue and green, respectively. The side panels depict individual spectra from a thin part, (b) and (e), in red, and from a thicker part, (c) and (f), in yellow (Adapted from Ref. 9, courtesy of Dr. Yedra).

### Blind source separation

The objective of the approximate factorization by PCA decomposition described above is the separation of a set of source signals from a set of mixed signals and noise, with little consideration about these signals or the mixing process. This mathematical problem is also known as blind source separation (BSS). In general BSS constitutes an ill-posed problem<sup>12</sup>, to which it is difficult to find an exact solution. Nevertheless, useful approximations can be derived by imposing appropriate conditions.

One method of performing BSS is to impose mutual independence to the source components, known as independent component analysis (ICA)<sup>13</sup>. In order to be able to use this method, the dimensionality of the dataset has to be reduced. This is done by previously performing PCA, and selecting a principal component threshold. In favorable cases, ICA is able to transform the principal components from PCA into independent components with improved physical meaning. Because of the necessary PCA step, the preprocessing for ICA is as for PCA and datasets which are poorly sorted by PCA will be hard to analyze using ICA.

One of the drawbacks of PCA and ICA methods is the frequent occurrence of results that are hard to interpret or unphysical, as the linear mixing involves counterintuitive cancellations between positive and negative components. Thus,

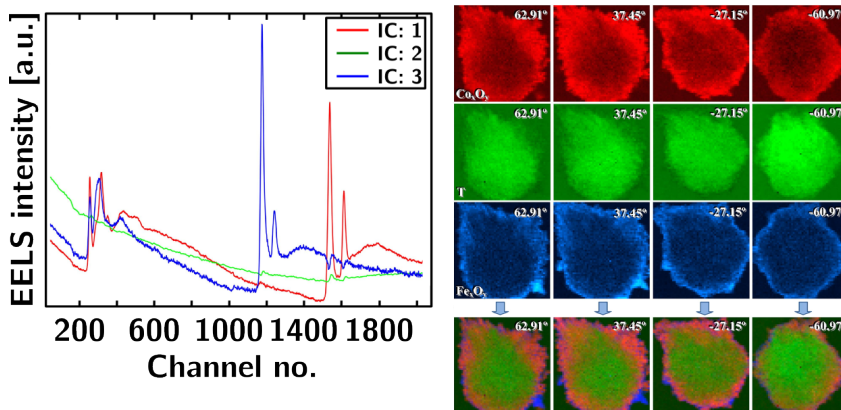


**Fig. 2.8** The left panel shows the loadings from ICA which are proportional to cobalt oxide (red), iron oxide (blue) and thickness of the sample (green). The top right panels show the corresponding score maps, for four different projections in a tilt series: cobalt oxide ( $\text{Co}_x\text{O}_y$ ) in red, thickness (T) in green, and iron oxide ( $\text{Fe}_x\text{O}_y$ ) in blue. Below that, RGB composites are given for the four tilt angles in order to compare the spatial distribution and magnitude of each component (Adapted from Ref. 9, courtesy of Dr. Yedra)

it is useful to review methods capable of performing BSS without a previous PCA step, such as non-negative matrix factorization (NMF)<sup>14</sup>. This method finds an approximate solution to Eq. (2.8), for a limited number of components and imposing a non-negativity constrain to all the possible loadings. This limitation is based on a physically meaningful constraint, as only additive combinations are allowed and no subtractions can occur. In this notion, NMF gives an approximate parts-based representation, and is sometimes capable of finding a more intuitive solution to the BSS problem in cases where ICA fails to perform<sup>15</sup>.

Both ICA and NMF methods have been tested for core-loss EELS applications<sup>16,17</sup>, and they are available along with PCA in the Hyperspy toolbox<sup>3</sup>. One example of the successful application of PCA and ICA is in the work of Yedra et al.<sup>9</sup> that proposes using MVA to enhance the electron tomographic series reconstruction from a  $\text{Fe}_x\text{Co}_{3-x}\text{O}_4@\text{Co}_3\text{O}_4$  mesoporous nano particle. In this data acquisition, the noise level in the spectra was in principle excessively high for any further quantification at any position. Following PCA analysis, portrayed in Fig. 2.7, it was possible to eliminate the noise components of the signal. The PCA reconstruction of the signal resulted in sharp edges, suitable for quantification procedures. Performing BSS by ICA, as depicted in Fig. 2.8, three independent components were identified. One of them was a thickness component, that

prevails in the centre of the particle. Meanwhile, the other two components are identified with cobalt and iron oxides, that dominate at the border. The MVA analysis reveals that the two oxides are not found together all over the particle, as iron oxide is clearly seen on its own at some points, unlike cobalt oxide, which is always associated to iron oxide.

## 2.3 Ab-initio simulation tools

From the quantum mechanical point of view described in Sec. 1.3, energy-loss spectra can be related to a joint density of states (JDOS) and the momentum matrix elements for the involved transitions. This view is helpful in order to build phenomenological models, that can be used to analyze spectra and relate their features to materials properties, but with little predicting power. In order to use the full predicting power of this formulation, ab-initio simulation methods are necessary. These methods are capable of obtaining fundamental material properties from first principles. In other words, ab-initio methods usually start from a very reduced set of material parameters, for instance chemical composition and crystalline structure. Then, a set of physical rules is implemented so that, within certain limits, they enable to calculate the considered properties.

There are two families of ab-initio methods that have been applied to the calculation of excited properties and, thus, are relevant to EELS<sup>18</sup>. One of them are the multiple scattering and time-dependent density functional theory (TDDFT) algorithms, that perform real-space calculations and direct calculations of the spectra. These methods go beyond some of the simple independent particle transitions in Sec. 1.3, and, because of this, they are theoretically best suited for the calculation of excited-state properties. Fig. 2.9 depicts schematically these departures from simple independent particle transitions between ground states, to account for the relaxation of the valence and conduction states, including the electron and hole interactions. Additionally, the calculation of spatially resolved properties is also possible. However, a separate simulation has to be set for each property, resulting in a computational high cost and difficulties of implementation. Some examples of software implementing these methods are FEFF<sup>19</sup> and Yambo<sup>20</sup>, that are based on multiple scattering and TDDFT, respectively.

The other relevant ab-initio methods are band structure algorithms, that perform reciprocal-space calculations. They calculate ground-state properties of periodic structures, and they have been shown to obtain a reasonably good approximation of excited-state properties<sup>18</sup>. Typically, band structure methods are computationally cheaper and easier to implement. Probably, the most popular band structure simulation method is density functional theory (DFT), that is the one used in this thesis. This method is implemented in many software packages, such as CASTEP<sup>22</sup> and Wien2k<sup>23</sup>. The latter is our package of choice for the

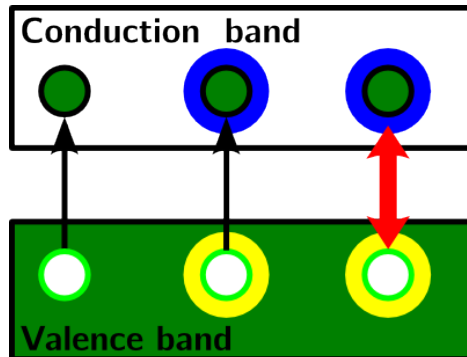


**Fig. 2.9** From left to right, in order of increasing complexity, independent transitions, quasi-particle transitions and two-body excitonic interaction. Adapted from Ref. 21.

calculations in this thesis. The main reasons for this are its extensive use for EELS simulations<sup>18</sup>, a large and well documented collection of routines and a thriving community of users<sup>21</sup>.

### 2.3.1 DFT simulations with Wien2k

DFT is used to study material media as systems formed by the atomic electrons and fixed nuclei. Such systems pose a complex problem involving the many-body Schrödinger equation. However DFT reduces the formulation to a set of single particle equations thanks to the Hohenberg-Kohn theorem<sup>24</sup>. The key quantity in this theorem is the electronic density,  $\rho(r)$ , as it states that the expectation value of any observable can be obtained from a unique functional of  $\rho$  that minimizes the energy functional  $E[\rho]$ <sup>i</sup>. This way, a set of equations is found that give a density of states equal to the real ground state density of the many body system, the Kohn-Sham (KS) equations<sup>25</sup>,

$$(T + V_H + V_{ext} + V_{xc})\varphi_i(r) = \epsilon_i\varphi_i \quad (2.9)$$

In these equations,  $T$  is the kinetic energy operator, and  $V_H$ , the Hartree potential, which are known. The last term,  $V_{xc}$ , is obtained from a functional of the exchange and correlation energy, of the form  $\delta E_{xc}[\rho]/\delta\rho$ . The explicit expression for this  $E_{xc}$  is unknown since it includes all kinds of correlations between the particles in the system. Because of this, an approximation of  $V_{xc}$  is needed in order to solve the KS equations. These approximations depend largely on the DFT implementation and the properties of interest, so they can vary from one calculation to another (more below). Once this is set up, the KS equations are solved, typically in an iterative process called the self-consistent field (SCF) cy-

<sup>i</sup>If the spin,  $\sigma$ , is also taken into account, a spin density,  $\rho_\sigma(r)$ , is formulated instead.

cle, that is carried out until convergence of a given parameter (*e.g.* total energy, charge density...).

The Wien2k DFT software package is used to perform simulations of periodic systems (crystals)<sup>23</sup>. This implementation of DFT uses the *full-potential* linearized augmented plane wave (LAPW) method for solving the KS equations<sup>26</sup>. In this framework, a wave-function basis set is devised in order to obtain the ground state density, total energy and KS eigenvalues (energy bands) of a many-electron system. All calculations are performed in  $\mathbf{K}$ -space; however, this basis set consists in different mathematical functions depending on the location in the unit cell. Two regions are defined, using a different basis set in each, the non overlapping atomic spheres and an the interstitial region (see Fig. 2.10). In the first region, a linear combination of radial functions times spherical harmonics is used. In the interstitial region, a plane wave expansion based on the reciprocal lattice vectors,  $\mathbf{K}$ , is used. This expansion can be represented by the following schematic *full-potential*,

$$V(\mathbf{r}) = \begin{cases} \sum_{l,m} V_{l,m}(r) Y_{l,m}(\hat{\mathbf{r}}) & \text{inside a sphere} \\ \sum_{\mathbf{K}} V_{\mathbf{K}} e^{i\mathbf{K}\cdot\mathbf{r}} & \text{outside a sphere} \end{cases} \quad (2.10)$$

Where the charge densities have an analogous shape. The convergence of such basis set is controled by a cut-off parameter  $R_{MT}K_{max} = 6 - 9$ , where  $R_{MT}$ , literally muffin-tin radius, is the radius of the smallest atomic sphere and  $K_{max}$  is the magnitude of the largest  $\mathbf{K}$ -vectors used in the expansion. In order to improve the performance and to treat semicore and valence states in a consistent way, additional basis functions are sometimes added, called local orbitals (LO).

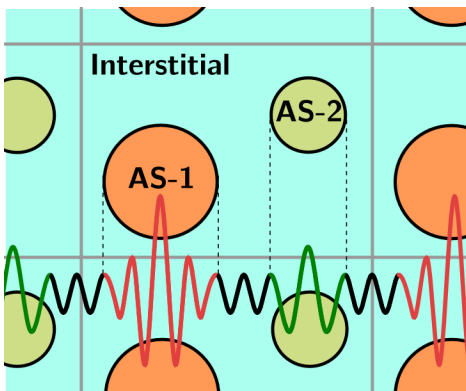


**Fig. 2.10** Model of a unit cell for DFT calculations showing the interstitial region and atomic spheres (AS). The schematic basis set of Eq. (2.10) follows this model. In this sense, plane waves and spherical harmonics are represented in the image using black and color (red or green) curves, respectively.

## Choice of XC-potential

An exchange-correlation (XC) potential is necessary to complement the KS formulation of DFT<sup>24,25</sup>. A simple, yet in most cases accurate, approach is to suppose that the energy contribution of the XC-potential only depends on the electron density at each point of space, which is known as linear (spin) density approximation (LSDA). For some solid-state systems, LSDA yields accurate results, but, however, it fails when density changes rapidly. An improvement is obtained by considering the gradient of the electron density, this is the so-called generalized gradient approximation (GGA)<sup>27</sup>.

As already explained, DFT is a ground state theory and its description of excited state properties is limited. For instance, the band gap of insulator or semiconductor materials is usually underestimated when one uses the KS equation with LSDA and GGA to determine the electronic density<sup>21</sup>. Because of this, there are alternative ways to estimate the experimental band gap. These methods may lie outside the framework of the KS equation, for instance, by introducing a non-multiplicative potential.

In many works where low-loss spectra are theoretically studied using DFT, the exchange correlation effects are treated using GGA<sup>21,28,29</sup>. Nevertheless, if one wants to stay in the KS framework and still use a computationally cheap semilocal method that leads to theoretical band gap energy predictions which are close to the experimental values<sup>30</sup>, the modified Becke-Johnson (mBJ) potential can be a good starting point. The mBJ potential reads as follows:

$$v_{x,\sigma}^{mBJ}(r) = cv_{x,\sigma}^{BR}(r) + (3c - 2)\frac{1}{\pi}\left(\frac{5}{6}\frac{t_\sigma(r)}{\rho_\sigma(r)}\right)^{1/2} \quad (2.11)$$

Where  $\rho_\sigma(r)$  is the density of states,  $t_\sigma(r)$  is the kinetic energy density,  $v_{x,\sigma}^{BR}$  is the Becke-Roussel potential and  $c$  a parameter that changes the relative weights of the two terms in mBJ potential:

$$v_{x,\sigma}^{BR}(r) = \frac{-1}{b_\sigma(r)} \left(1 - e^{-x_\sigma(r)} - \frac{1}{2}x_\sigma(r)e^{-x_\sigma(r)}\right) \quad (2.12)$$

$$c = \alpha + \beta \left(\frac{1}{V_{cell}} \int_{cell} \frac{|\nabla \rho(r')|}{\rho(r')} d^3 r'\right)^{1/2} \quad (2.13)$$

Where  $b_\sigma = (x_\sigma^3 e^{-x_\sigma} / (8\pi\rho_\sigma))^{1/3}$ ,  $\alpha$  and  $\beta$  are parameters and  $x_\sigma(r)$  is determined from a non-linear equation involving  $\rho_\sigma$ ,  $\nabla\rho_\sigma$ ,  $\nabla^2\rho_\sigma$ .

In the present work we implement the mBJ XC-potential, as a way to improve the calculation of the excited state quantities, such as the band gap energy or the behavior of the plasmon peak. Additionally, we have also implemented the

GGA XC-potential developed by Perdew, Burke and Ernzerhof<sup>31</sup>, also called PBE-GGA.

### Calculation of properties

In general, the result of a DFT calculation after having solved the KS equations is the ground-state band structure, *i.e.* for each band  $n$  at each point  $\mathbf{K}$  the KS electron wave-functions and energies. In the independent particle and random phase approximations, as exposed in Sec. 1.3 (see also Fig. 2.9), the theoretical dielectric function can be calculated from a Fermi golden-rule. Notice that this band structure is analogous to the real  $|\mathbf{K}, n\rangle$  and  $E_{\mathbf{K},n}$  only in the sense that they supposedly generate the correct electron density<sup>21</sup>.

A DFT calculation with Wien2k starts by setting up the crystal structure and other program inputs in order to generate an initial charge density. This is done in a semi-automated way using the `init_lapw` algorithm, that suggests values for most of the relevant quantities, *e.g.*  $R_{MT}K_{max}$  and size of the  $\mathbf{K}$ -mesh, and helps the user to detect possible errors. After this process, an algorithm for the SCF cycle is selected, *e.g.* `run_lapw`, that follows series of fixed steps in order to reach the targeted convergence criterion. For instance, if an energy criterion is selected, the SCF cycle stops when the total energy difference between iterations is smaller than a given threshold.

After the SCF cycle is successfully converged,  $\varepsilon(\mathbf{q}, E)$  can be obtained within the RPA from the LAPW basis set wave-functions. The implementation of this formalism was developed by R. Abt and C. Ambrosch-Draxl<sup>32,33</sup>, and it is implemented in the `optic` algorithm. The software calculates the momentum matrix elements, plasma frequency and JDOS, obtaining from them the imaginary part of the CDF,  $\varepsilon_2$ . The precise calculation of the momentum matrix elements is more demanding than the SCF cycle and is usually carried out using a larger  $\mathbf{K}$ -mesh for accuracy. After this, the real part of the CDF,  $\varepsilon_1$ , is obtained through Kramers-Kronig transformation. Other quantities that help to understand the dielectric response, such as the DOS, electron densities and band structure, are also calculated in Wien2k. This is done in a consistent way, using the results from the same SCF cycle<sup>21,23</sup>.

The following chapter, which is the first results chapter of this thesis, addresses the DFT calculation using Wien2k of the EELS spectra of some III-V semiconductor materials.

## Bibliography

- [1] R. F. Egerton. *Electron Energy-Loss Spectroscopy in the Electron Microscope*. Springer US, 3rd edition, 2011.

- [2] D. W. Johnson and J. H. Spence. Determination of the single-scattering probability distribution from plural-scattering data. *Journal of Physics D: Applied Physics*, 7(6):771, 1974.
- [3] F. de la Peña, P. Burdet, M. Sarahan, M. Nord, T. Ostasevicius, J. Taillon, A. Eljarrat, S. Mazzucco, V. T. Fauske, G. Donval, L. F. Zagonel, I. Iyengar, and M. Walls. Hyperspy 0.8, April 2015. URL <http://dx.doi.org/10.5281/zenodo.16850>.
- [4] A. Gloter, A. Douiri, M. Tencé, and C. Colliex. Improving energy resolution of EELS spectra: an alternative to the monochromator solution. *Ultramicroscopy*, 96(3–4):385 – 400, 2003. ISSN 0304-3991. doi: [http://dx.doi.org/10.1016/S0304-3991\(03\)00103-7](http://dx.doi.org/10.1016/S0304-3991(03)00103-7). URL <http://www.sciencedirect.com/science/article/pii/S0304399103001037>. Proceedings of the International Workshop on Strategies and Advances in Atomic Level Spectroscopy and Analysis.
- [5] W. H. Richardson. Bayesian-based iterative method of image restoration. *Journal of the Optical Society of America*, 62(1):55–59, 1972.
- [6] L. B. Lucy. An iterative technique for the rectification of observed distributions. *The astronomical journal*, 79:745, 1974.
- [7] D. W. Johnson. A fourier series method for numerical kramers-kronig analysis. *Journal of Physics A: Mathematical and General*, 8(4):490, 1975.
- [8] R. Erni and N. D. Browning. The impact of surface and retardation losses on valence electron energy-loss spectroscopy. *Ultramicroscopy*, 108(2):84–99, 2008.
- [9] L. Yedra, A. Eljarrat, R. Arenal, E. Pellicer, M. Cabo, A. Lopez-Ortega, M. Estrader, J. Sort, M. D. Baró, S. Estradé, and F. Peiró. EEL spectroscopic tomography: Towards a new dimension in nanomaterials analysis. *Ultramicroscopy*, 122:12–18, 2012.
- [10] L. Yedra, A. Eljarrat, J. M. Rebled, L. López-Conesa, N. Dix, F. Sánchez, S. Estradé, and F. Peiró. EELS tomography in multiferroic nanocomposites: from spectrum images to the spectrum volume. *Nanoscale*, 6(12):6646–6650, 2014.
- [11] M. R. Keenan and P. G. Kotula. Accounting for poisson noise in the multivariate analysis of ToF-SIMS spectrum images. *Surface and Interface Analysis*, 36(3):203–212, 2004.

- [12] J. M. Bioucas-Dias, A. Plaza, N. Dobigeon, M. Parente, Q. Du, P. Gader, and J. Chanussot. Hyperspectral unmixing overview: Geometrical, statistical, and sparse regression-based approaches. *Selected Topics in Applied Earth Observations and Remote Sensing, IEEE Journal of*, 5(2):354–379, 2012.
- [13] A. Hyvärinen and E. Oja. Independent component analysis: algorithms and applications. *Neural networks*, 13(4):411–430, 2000.
- [14] P. Paatero and U. Tapper. Positive matrix factorization: A non-negative factor model with optimal utilization of error estimates of data values. *Environmetrics*, 5(2):111–126, 1994.
- [15] D. D. Lee and H. S. Seung. Learning the parts of objects by non-negative matrix factorization. *Nature*, 401(6755):788–791, 1999.
- [16] F. de la Peña, M.-H. Berger, J.-F. Hochepied, F. Dynys, O. Stephan, and M. Walls. Mapping titanium and tin oxide phases using EELS: An application of independent component analysis. *Ultramicroscopy*, 111(2):169–176, 2011.
- [17] O. Nicoletti, F. de La Peña, R. K. Leary, D. J. Holland, C. Ducati, and P. A. Midgley. Three-dimensional imaging of localized surface plasmon resonances of metal nanoparticles. *Nature*, 502(7469):80–84, 2013.
- [18] C. Hébert. Practical aspects of running the WIEN2k code for electron spectroscopy. *Micron*, 38(1):12–28, 2007.
- [19] J. J. Rehr and R. C. Albers. Scattering-matrix formulation of curved-wave multiple-scattering theory: Application to x-ray-absorption fine structure. *Physical Review B*, 41(12):8139, 1990.
- [20] A. Marini, C. Hogan, M. Grüning, and D. Varsano. Yambo: an ab initio tool for excited state calculations. *Computer Physics Communications*, 180(8):1392–1403, 2009.
- [21] V. J. Keast. An introduction to the calculation of valence EELS: Quantum mechanical methods for bulk solids. *Micron*, 44:93–100, 2013.
- [22] V. Milman, K. Refson, S. J. Clark, C. J. Pickard, J. R. Yates, S.-P. Gao, P. J. Hasnip, M. I. J. Probert, A. Perlov, and M. D. Segall. Electron and vibrational spectroscopies using dft, plane waves and pseudopotentials: CASTEP implementation. *Journal of Molecular Structure: THEOCHEM*, 954(1):22–35, 2010.

- [23] P. Blaha, K. Schwarz, G. K. H. Madsen, D. Kvasnicka, and J. Luitz. *WIEN2K, An Augmented Plane Wave + Local Orbitals Program for Calculating Crystal Properties*. Karlheinz Schwarz, Techn. Universität Wien, Austria, 2001.
- [24] P. Hohenberg and W. Kohn. Inhomogeneous electron gas. *Physical Review*, 136:B864–B871, Nov 1964. doi: 10.1103/PhysRev.136.B864. URL <http://link.aps.org/doi/10.1103/PhysRev.136.B864>.
- [25] W. Kohn and L. J. Sham. Self-consistent equations including exchange and correlation effects. *Physical Review*, 140:A1133–A1138, Nov 1965. doi: 10.1103/PhysRev.140.A1133. URL <http://link.aps.org/doi/10.1103/PhysRev.140.A1133>.
- [26] K. Schwarz, P. Blaha, and G. K. H. Madsen. Electronic structure calculations of solids using the WIEN2k package for material sciences. *Computer Physics Communications*, 147(1):71–76, 2002.
- [27] Y. Wang and J. P. Perdew. Spin scaling of the electron-gas correlation energy in the high-density limit. *Physical Review B*, 43:8911–8916, Apr 1991. doi: 10.1103/PhysRevB.43.8911. URL <http://link.aps.org/doi/10.1103/PhysRevB.43.8911>.
- [28] V. J. Keast, M. J. Kappers, and C. J. Humphreys. Electron energy-loss near edge structure (ELNES) of InGaN quantum wells. *Journal of Microscopy*, 210(1):89–93, 2003. ISSN 1365-2818. doi: 10.1046/j.1365-2818.2003.01180.x. URL <http://dx.doi.org/10.1046/j.1365-2818.2003.01180.x>.
- [29] J. Palisaitis, C.-L. Hsiao, M. Junaid, J. Birch, L. Hultman, and P. O. Å. Persson. Effect of strain on low-loss electron energy loss spectra of group-III nitrides. *Physical Review B*, 84:245301, Dec 2011. doi: 10.1103/PhysRevB.84.245301. URL <http://link.aps.org/doi/10.1103/PhysRevB.84.245301>.
- [30] D. Koller, F. Tran, and P. Blaha. Merits and limits of the modified becke-johnson exchange potential. *Physical Review B*, 83:195134, May 2011. doi: 10.1103/PhysRevB.83.195134. URL <http://link.aps.org/doi/10.1103/PhysRevB.83.195134>.
- [31] J. P. Perdew, K. Burke, and M. Ernzerhof. Generalized gradient approximation made simple. *Physical Review Letters*, 77:3865–3868, Oct 1996. doi: 10.1103/PhysRevLett.77.3865. URL <http://link.aps.org/doi/10.1103/PhysRevLett.77.3865>.

- [32] R. Abt, C. Ambrosch-Draxl, and P. Knoll. Optical response of high temperature superconductors by full potential LAPW band structure calculations. *Physica B: Condensed Matter*, 2(0):1451–1452, 1994. ISSN 0921-4526. doi: [http://dx.doi.org/10.1016/0921-4526\(94\)91225-4](http://dx.doi.org/10.1016/0921-4526(94)91225-4). URL <http://www.sciencedirect.com/science/article/pii/0921452694912254>.
- [33] C. Ambrosch-Draxl and J. O. Sofo. Linear optical properties of solids within the full-potential linearized augmented planewave method. *Computer Physics Communications*, 175(1):1–14, 2006.



## Chapter 3

# DFT modeling of wurtzite III-nitride ternary alloys

(...) I do not attribute to nature either beauty or deformity, order or confusion. Only in relation to our imagination can things be called beautiful or ugly, well-ordered or confused.

---

Baruch Spinoza, *Letters*

This chapter describes DFT band structure calculations that were performed in order to simulate the dielectric response of III-nitride semiconductors. The aim of this study is to improve our understanding of the features in the low-loss electron energy-loss spectra of ternary alloys, but the results are also relevant to optical and UV spectroscopy results. For these DFT calculations, the standard tools found in Wien2k software were used. The novel modified Becke-Johnson (mBJ) exchange-correlation potential was also implemented, in order to improve the band structure description of these semiconductor compounds. The results from these calculations include band structure, density of states and complex dielectric function for the whole compositional range. When compared with standard generalized gradient approximation (GGA), the predicted band gap energies for the novel potential were found to be larger and closer to experimental values. Additionally, the dependence of the most interesting features with composition was described by applying a Vegard law to band gap and plasmon energies. For this purpose, three wurtzite ternary alloys, from the combination of binaries AlN, GaN and InN, were simulated through the whole compositional range (*i.e.*,  $\text{Al}_x\text{Ga}_{1-x}\text{N}$ ,  $\text{In}_x\text{Al}_{1-x}\text{N}$  and  $\text{In}_x\text{Ga}_{1-x}\text{N}$ , with  $x = [0, 1]$ ). Moreover, a detailed analysis of the collective excitation mode in the dielectric response co-

efficients (CDF and ELF) was performed by model based analysis. This reveals their compositional dependence, which sometimes departs from a linear behavior. Finally, an advantageous method for measuring the plasmon energy dependence from these calculations was also developed.

### 3.1 Introduction

Group-III nitride semiconductors have attracted the interest of the scientific community since the early 1990s due to their promising industrial applications. Their direct band gap combined with a high excitonic binding energy provides a high light emission efficiency. On top of the third column of the periodic table one finds aluminum, gallium and indium. In combination with nitrogen, they form the binary compounds AlN, GaN and InN. In actual devices, mostly for optoelectronic applications, they are often found as non-stoichiometric ternary compounds, *e.g.*  $\text{In}_x\text{Ga}_{1-x}\text{N}$  with  $0 < x < 1$ . The huge variation of their room-temperature band gap energies, from the infrared (InN,  $\sim 0.7$  eV) to the ultraviolet (AlN,  $\sim 6.2$  eV) range, offers a unique possibility to cover the entire visible range with only one group of materials. In particular, the development of InGaN active layers for III-nitride optoelectronic devices allowed the fabrication of blue/green/white light emitting diodes (LED) that revolutionized the LED market<sup>1,2</sup>. Indeed, recently (2014), the Nobel Prize in Physics was awarded jointly to I. Akasaki, H. Amano and S. Nakamura “for the invention of efficient blue light-emitting diodes which has enabled bright and energy-saving white light sources”<sup>3</sup>.

The electronic properties of these materials strongly depend on composition, structure and strain. As the size of semiconductor devices shrinks, the need for a characterization tool with an appropriate spatial resolution is evidenced. EELS analysis can be highly revealing, provided an accurate analysis of the energy-loss spectra can be performed. In this sense, a clear understanding of the dielectric response of the nitride compounds is needed<sup>4–6</sup>. Optoelectronic properties can be predicted from ab-initio band structure calculations. In this sense, a complete DFT modeling of III-nitride ternary alloys will be carried out.

One of the main advantages of DFT ab-initio simulations is that, once a band structure model is obtained, it may be used to compute many different observable quantities. For instance, we may, in principle, predict the shape of both core-loss and low-loss EELS spectra using the results of a DFT calculation. Nevertheless, theoretical studies for EELS have been typically centered on the core-loss region<sup>6–9</sup>, which is useful for the analysis of the chemical composition of the sample. Conversely, the calculations of the low-loss spectra, which yields further information about the electronic and optical properties and includes the plasmon peak, are relatively less common<sup>4,10</sup>. It is possible, one may argue, that the reason for this bias is that in DFT simulations it is inherently difficult to

obtain reliable predictions of some band structure quantities<sup>11</sup>. These quantities include such relevant parameters for the study of low-loss EELS as the band gap values. In fact, the existing theoretical studies for III-nitrides as a function of composition do not extend to valence band effects and their relationship with the low-loss EELS spectrum<sup>6</sup>.

### 3.1.1 Band structure based calculations

For the present work, several band structure calculations were devised in order to study the behavior of the plasmon peak position as a function of composition in ternary compounds  $\text{Al}_x\text{Ga}_{1-x}\text{N}$ ,  $\text{In}_x\text{Al}_{1-x}\text{N}$  and  $\text{In}_x\text{Ga}_{1-x}\text{N}$ , through the whole compositional range.

These calculations were performed using the Wien2k DFT program package, which was introduced in Sec. 2.3. Whenever low-loss spectra had been theoretically studied using DFT, the exchange correlation effects were treated using the GGA exchange-correlation potential<sup>4,9,10</sup>. In the present work, we went a step further and used the novel mBJ exchange-correlation potential, which had shown promising results in the prediction of band gap energies for other compounds<sup>12</sup>. This quantity is strongly related to the energy-loss spectra of semiconductors: mBJ is thus implemented in order to improve the calculation of the excited state quantities, such as the band gap energy or the behavior of the plasmon peak. Additionally, we also implemented the GGA XC-potential developed by Perdew, Burke and Ernzerhof<sup>13</sup>, also called PBE-GGA. All calculations were performed with both mBJ and GGA, for comparison, except for the initial structural relaxation, in which mBJ was included only at the end.

The aim of these simulations was to use the obtained band structures to compute the complex dielectric function (CDF),  $\varepsilon(\mathbf{q}, E) = \varepsilon_1 + i\varepsilon_2$ , and from them, extract the energy-loss function (ELF),  $\text{Im}[-1/\varepsilon(E)]$ . The simulations were performed for the binary compounds and ternary alloys, as explained in the following sections. Before we address them, let us briefly review some properties derived from dielectric response theory that were taken into account for the analysis of the results.

### 3.1.2 Modeling the dielectric response

If we rely on the dielectric formulation to describe inelastic scattering of electrons through small angles, the measured energy-loss spectra can be related to theoretical calculations of the dielectric response coefficients (see Sec. 1.3). Then, simple phenomenological models can be used in order to interpret energy-loss features that are connected to valence band features of the modeled materials.

Within the dielectric response framework, phenomenological models for the CDF of a semiconductor can be formulated taking into account single electron

transitions and collective mode excitations, as shown in Sec. 1.3.1. As it turns out, many metals and some semiconductors have none or a small number of weak interband transitions, and their collective modes (*i.e.* plasmon excitation) near the excitation threshold can be approximately described by these coarse free-electron models.

In the semi-classic approximation, bulk inelastic electron scattering from a material, as measured in EELS, is determined by the ELF, as shown in Sec. 1.3.2. A simple, yet powerful and widely used, model for the ELF is obtained in the free-electron approximation (Drude model, no interband transitions)<sup>14,15</sup>,

$$\text{Im}[-1/\varepsilon(E)] = \frac{EE_P^2\Gamma}{(E^2 - E_P^2)^2 + (E\Gamma)^2} \quad (3.1)$$

with  $E_P$ , the plasmon energy, and  $\Gamma$ , the plasmon width. This model is typically used to fit semiconductor EELS experimental data, in order to extract information from the plasmon energy and width. Notice that it is essentially the same as the models for the CDF in Eq. (1.37).

In summary, the model above predicts the shape of the plasmon peak using a “quasi-free” electron gas approximation. Such a model is useful for the determination of the plasmon energy and width as long as inter-band transitions do not strongly affect the spectral shape near the plasmon peak<sup>16</sup>. Indeed, the presence of single electron transitions will inevitably modify the shape of the CDF. In some semiconductor materials, these transitions do not seriously affect the shape of the plasmon region and mostly introduce a shift in the resonance peak (see  $\omega_{eff}$  in Eq. (1.39)). However, pathological cases in which transitions overlap the plasmon region will present a different peak shape than the one predicted by Eq. (3.1). In these cases, it is useful to remember that presence of a collective mode excitation is also indicated by the real part of the CDF crossing the zero-axis,  $\varepsilon_1(E_{cut}) = 0$ , from negative values, with  $E_{cut} \neq E_P$ .

## 3.2 Simulation of the binary compounds

In our approach, a structural relaxation of the binary compounds was initially performed, in order to determine their wurtzite crystal structure parameters for DFT simulation. The description of these simulations is completed with an analysis of the results that were obtained: band structure, DOS, CDF and ELF.

### 3.2.1 Initial set-up of the structures

The binary and ternary compounds can, in principle, exist in two different stable crystalline structures: wurtzite and zinc-blende<sup>17</sup>. In this study, we focused on the wurtzite structure. The wurtzite structure is an hexagonal lattice with

an atomic basis of 4 atoms (2 of nitrogen and 2 of a group-III element). The hexagonal lattice is defined by two lattice parameters,  $a$  and  $c$ , its primitive vectors being,

$$\begin{aligned}\mathbf{a}_1 &= 1/2(a\hat{x} - \sqrt{3}a\hat{y}) \\ \mathbf{a}_2 &= 1/2(a\hat{x} + \sqrt{3}a\hat{y}) \\ \mathbf{c} &= c\hat{z}\end{aligned}\quad (3.2)$$

Where  $\hat{x}$ ,  $\hat{y}$  and  $\hat{z}$  are unitary vectors defining the cartesian coordinates. The III-group atoms (Al, Ga and In) are found in the  $(0, 0, 0)$  and  $(2/3, 1/3, 1/2)$  positions, with the nitrogen atoms in the  $(0, 0, 3/8)$  and  $(2/3, 1/3, 7/8)$  positions. The generic crystal-cell is represented in Fig. 3.1 (actually using gallium atoms). Notice that because of the representation used in this image the uppermost Ga atom is repeated.

### Structural relaxation

It is generally accepted that the prediction of the equilibrium lattice parameters for a given structure by DFT is almost impossible. As a consequence, the equilibrium lattice parameters used in DFT calculations are different from the experimental ones. In this work, we performed a standard structural relaxation of the binaries. This is achieved by performing several simulations with different lattice parameters and measuring the energy variation. First, some initial parameters,  $a_i$ ,  $c_i$ , were introduced and the simulations performed with small

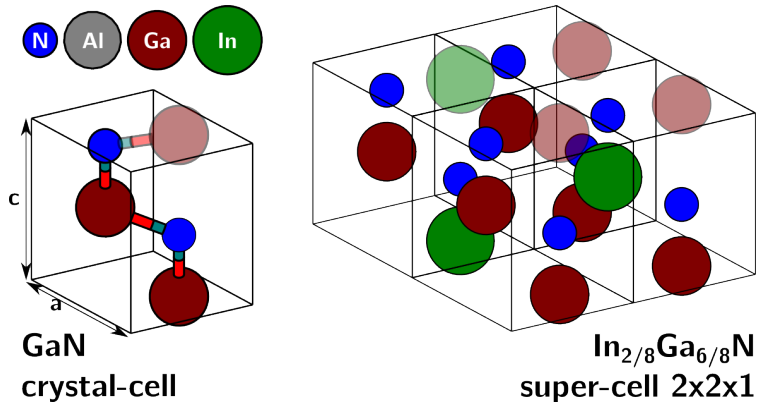


**Fig. 3.1** Scheme of the wurtzite GaN crystal-cell and an  $\text{In}_{2/8}\text{Ga}_{6/8}\text{N}$  super-cell, with the size difference between the III-group elements represented through their covalent radii, using XCrysDen software<sup>18</sup>.

variations around these values. We chose the initial values of the lattice parameters for AlN, GaN and InN from the literature<sup>19,20</sup>. These values are included in Table 3.1, together with the main features of the structural relaxation process, that are explained below.

The relaxed structure has the lowest energy and, hence, it can be found by fitting a model to the simulated data. This model depends on the type of optimization applied to the lattice parameters. We first performed a volume optimization by fixing the  $c/a$  ratio and the angles, this way we do not alter the wurtzite structure. For each binary material we performed 7 simulations by changing the volume between values in the range 94 – 106 % of the initial volume. Notice that the volume of the hexagonal unit cell is  $V = a^2 c \sin(\pi/3)$ . These calculations were carried out using a 10000  $k$ -point mesh, in an iterative self-consistent cycle (SCF) with an energy convergence criterion of 0.0001 Ry<sup>i</sup>. See Table 3.1, for the computational details dependent on the material, the muffin-tin radius reduction,  $R_{MT}$ , and the core/valence cut-off energy,  $E_{core}$ . Default values were used for the other simulation parameters. The optimal volume is obtained by a non-linear least squares fit to the energy expression given in Ref. 21,

$$E = k_1 + k_2 V^{-1/3} + k_3 V^{-2/3} + k_4 V^{-1} \quad (3.3)$$

Once the minimum point was determined, the final (relaxed) lattice parameters,  $a_f$ ,  $c_f$ , were retrieved from the following relationships;  $a_f = a_i (V_f/V_i)^{1/3}$  and  $c_f = c_i (V_f/V_i)^{1/3}$ . The final lattice parameters that were found after this process are also included in Table 3.1.

In the following step, we explored the  $c/a$  ratio optimization, using the lattice parameters obtained with the first simulation, with fixed volume and angles. As in the volume-optimization process, we performed 7 simulations by changing the  $c/a$  ratio between 97% and 103%. Again, calculations were carried out using a 10000  $k$ -point mesh and an energy convergence criterion of 0.0001 Ry. However, the results of this optimization process gave us values with differences below one thousandth of the volume-optimized ones. Consequently, the values we used for the following simulations correspond to the volume-optimized lattice parameters.

---

<sup>i</sup>1 Ry = 13.6056923(12) eV

**Table 3.1** Main features of the structural relaxation process (see text).

Material	$a_i$ , $c_i$ / Å	$R_{MT}$ / %	$E_{core}$ / Ry	$a_f$ , $c_f$ / Å
AlN	3.111, 4.981	3	-6.0	3.134, 5.017
GaN	3.188, 5.176	3	-8.0	3.226, 5.239
InN	3.532, 5.691	4	-6.0	3.587, 5.780

### 3.2.2 Band structure and density of states

The band structure diagrams of the three binary compounds from simulations performed using the final lattice parameters are shown in Fig. 3.2. Notice that the mBJ XC-potential was included in these calculations. The Kohn-Sham band structure diagram can be used to find the available energies for an electron in solid-state physics, with wave function  $|\mathbf{K}, n\rangle$ . The DOS plots, presented in Fig. 3.3, give further information, as they describe the number of states available to the solid-state electrons per interval of energy. In both, band structure diagrams and DOS, occupied states are found below the Fermi energy,  $E_F$ , and unoccupied states, above. By examining them, we can start to understand the dielectric response of the materials, learning about their electronic structure.

In the band structure diagrams, the energy difference between the maximum of valence band and minimum of conduction band represents the band gap value,  $E_{gap}$ . It becomes clear that a direct band gap ( $\mathbf{K} = \mathbf{K}'$ ) is predicted for all the studied materials, as expected. The obtained values can be found in Table 3.2. Compared with the ones obtained from calculations using GGA only, the implementation of mBJ yielded larger band gap values. This resulted in an improvement in the description of the band structure for the three binaries, primarily because the predicted band gaps for GGA calculations were well below the experimental measurements. Band gap adjustments thus improved in mBJ. Ad-

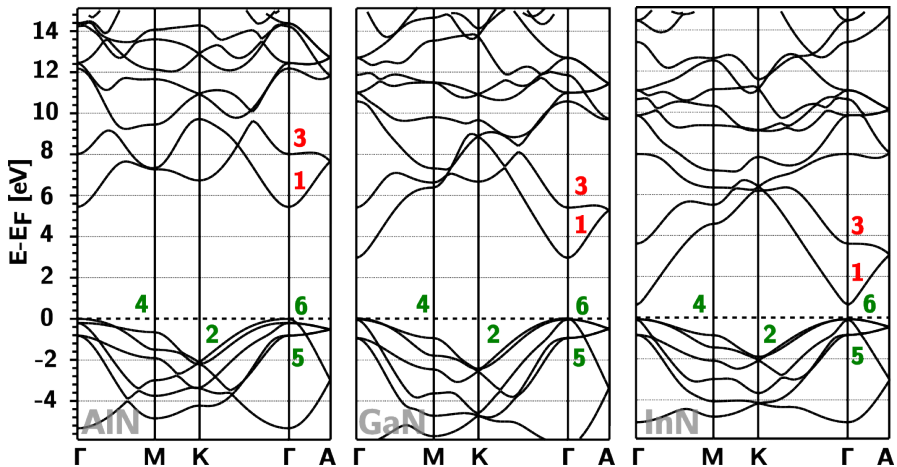


**Fig. 3.2** Band structure of the binary compounds, AlN, GaN and InN, obtained after the structural relaxation (mBJ included in the simulation). Green and red labels are used to indicate some of the critical points in the valence and conduction bands that are the start and end points of some interband transitions, respectively.

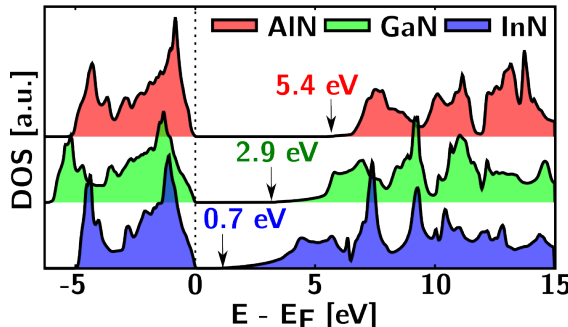


**Fig. 3.3** The obtained DOS for the three binary compounds AlN, GaN and InN. The band gap onset energy is indicated in the three cases. This would be the onset energy of the first signal in the energy-loss spectrum from these semiconducting materials.

**Table 3.2** Comparison of experimental and theoretical band gap values.

Material	$E_{gap}^{exp}$ / eV <sup>(a)</sup>	$E_{gap}^{GGA}$ / eV <sup>(b)</sup>	$E_{gap}^{mBJ}$ / eV <sup>(b)</sup>	$E_{gap}^{fit}$ / eV <sup>(c)</sup>
AlN	6.2	4.06	5.44	5.4
GaN	3.4	1.68	2.94	2.8
InN	0.7	0.00	0.69	0.7

<sup>(a)</sup> Experimental values, from Ref. 17. <sup>(b)</sup> Theoretical band gap predictions by GGA and mBJ, presented in this section. <sup>(c)</sup> Fitted coefficients for the ternary simulation series by mBJ, presented in the next section.

ditionally, the GGA calculation for InN did not show any band gap. This means that the simulation rendered the behavior of this material as metallic whereas we know it to be a semiconductor. This was corrected in the case of the mBJ calculation.

We focus now on the DOS of the binary materials, also obtained in our calculations. They can be found in Fig. 3.3, showing the DOS of AlN, GaN and InN, for calculations with implemented mBJ. In this figure, the band gap is also observed as the region where the DOS is zero above  $E_F$ . Additionally, the strength of each interband transition is also featured, as maximum values of the DOS are found in those energies where the critical points are located. The critical points, or van Hove singularities, are regions in the energy bands where the reciprocal space gradient becomes 0 at least in one direction. The position of some of these points was already hinted in the band structure diagrams in Fig. 3.2.

Following the discussion of the JDOS in Sec. 1.3.1, as critical points have a high DOS, the most probable interband transitions occur between two of them<sup>17</sup>. It is possible to detect how these transitions are reflected in the calculated CDF and ELF for the binary and ternary materials, that are presented in the following section. Notice also that, in GaN and InN, more important single electron transitions are expected, by the presence of 3d-band transitions.

### 3.2.3 Complex dielectric and energy-loss functions

The imaginary part of the CDF,  $\varepsilon_2$ , was obtained from our simulations, within the RPA<sup>22,23</sup>. Following this, the complete CDF,  $\varepsilon = \varepsilon_1 + i\varepsilon_2$ , was obtained from Kramers-Kronig transformation. Figure. 3.4 (a) shows three  $\varepsilon_1$ , obtained from the studied binaries. Notice that, from each simulation, a CDF with the form  $\varepsilon(E)$  was obtained in the 0 – 50 eV range, as typically attributed to the low-loss region. For the sake of simplicity, we restricted our study to the dielectric response to an electron propagating in the  $\mathbf{a}_1$  or  $\mathbf{a}_2$  primitive vectors direction, see Eq. 3.2, that corresponds to typical experimental cross-section observation. Nevertheless, calculations for the  $\mathbf{a}_3$  direction from other authors<sup>4</sup>, as well as our own, have only shown small differences between the responses for each direction.

Once the CDFs were obtained, the ELF can be directly computed from them as  $\text{Im}[-1/\varepsilon(E)]$ . The ELF for the binaries are depicted in Fig. 3.4 (b). In the ELF, the plasmon peak can usually be identified, as it is the most intense excitation. The ELF of AlN, on top of the panel, shows a very intense plasmon peak and few less intense transitions. For GaN, in the middle, the interband transitions are more intense and appear alongside the plasmon peak. Finally, in the ELF of InN, at the bottom, the interband transitions are the most visible features in the dielectric response. For comparison, notice that the experimental plasmon energies for AlN, GaN and InN are 21.1, 19.7 and 14.95 eV<sup>24–29</sup>, respectively.

It is necessary to apply a broadening factor to the theoretical calculations in order to compare them with data from the experimental spectrometer resolu-

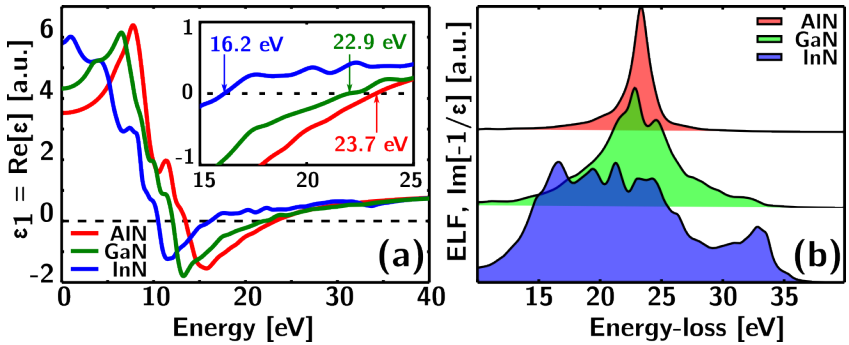


**Fig. 3.4** In panel (a), three  $\varepsilon_1(E)$  curves, obtained for the three binary compounds, AlN, GaN and InN, after simulations with implemented mBJ. In the inset, the 15 – 25 eV region is shown in detail. This is the region where the zero-crossing energies,  $E_{cut}$ , such that  $\varepsilon_1(E_{cut}) = 0$ , are found. In panel (b), the three energy-loss functions (ELFs) derived from these CDFs as  $\text{Im}(-1/\varepsilon)$ . Notice that these ELFs have been scaled to the same height.

tion typically obtained in EELS. Disregarding its physical origin, the resolution limiting factors are translated as an approximately Gaussian broadening of the spectra. In order to study different characteristics in the CDF and ELF, an 0.4 eV broadening was selected as an approach to the spectral resolution of the energy-loss spectra from for a typical instrument. This broadening was applied to the CDF and affects the ELF as well, because it was calculated directly from the CDF as  $\text{Im}[-1/\varepsilon(E)]$ .

In the dielectric formulation, the  $E_{cut}$  points where  $\varepsilon(E_{cut}) = 0$  and the function is increasing from negative values indicate the collective mode excitation, as described in 3.1.2. In the inset of Fig. 3.4 (a), these CDF zero-crossing energies,  $E_{cut}$ , are also indicated. In AlN and GaN, the  $E_{cut}$  values are similar to the  $E_P$  values that we obtain from model-based fits using Eq. (3.1). Conversely, in InN it is hard to determine the position of the plasmon peak, as it is smeared out by strong inter-band transitions. This nuisance becomes more relevant in the following section, in which we study the dependence of the band gap and plasmon features on composition.

### 3.3 Simulation of the ternary alloys

Once the lattice parameters for the three binary compounds were determined, we built simulation super-cells for the ternary structures. Using this super-cell approach, we were able to simulate a wide compositional range of ternary alloys. These calculations were then used to predict the composition dependence of band gap and plasmon energies, studied through the fitting of parabolic models.

#### 3.3.1 Super-cell approach

In order to build the simulation super-cells, different utilities of the program `structeditor`<sup>ii</sup>, bundled with Wien2k, were used to automate the process. In this process, a 2x2x1 super-cell is first generated from a starting binary compound, with a total of 8 group-III atoms. Then, a number of group-III atoms are replaced by other group-III atoms, in random positions. For instance, two gallium atoms from GaN can be replaced by two indium atoms in order to have  $\text{In}_{2/8}\text{Ga}_{6/8}\text{N}$  (represented graphically in Fig. 3.1). By doing so, we can explore the whole compositional range,  $0 < x < 1$ , with a step size of  $x = 0.125$ .

For each replaced atom,  $R_{MT}$  is modified, according to Table 3.1, in order to make the atomic behavior more realistic, and to reduce computational time. In the simulations presented in this section, a linear Vegard law was applied to obtain the lattice parameters of the ternary compounds in the set-up of the

---

<sup>ii</sup>This useful package was developed by Robert Laskowski. [rolask@theochem.tuwien.ac.at](mailto:rolask@theochem.tuwien.ac.at)

super-cells used in the calculations. In this formulation, Vegard law states that for an arbitrary ternary nitride alloy,  $A_xB_{1-x}N$ , where species A and B are found with concentrations  $x$  and  $(1 - x)$ , respectively, a given lattice parameter,  $a$ , can be obtained by the following equation,

$$a^{A_xB_{1-x}N} = xa^{AN} + (1 - x)a^{BN} \quad (3.4)$$

Additionally, Vegard law can be applied to features in the energy-loss spectra that depend on the lattice parameters, such as the band gap and plasmon peak energies. If we call  $E_i$  the characteristic energy for one of these properties, and adding a non-linear concentration dependence, weighted by the so-called bowing parameter,  $b$ .

$$E_i^{A_xB_{1-x}N} = xE_i^{AN} + (1 - x)E_i^{BN} + x(1 - x)b \quad (3.5)$$

The bowing parameter for III-V alloys is typically positive, with its physical origin in disorder effects created by the presence of different cations and anions<sup>30</sup>. In this work, parabolic Vegard laws were used to model the evolution of the predicted band gap and plasmon energies.

Once each super-cell for a given composition of a ternary compound was generated, we carried out the band structure simulation. As mentioned, both mBJ and GGA approaches were used to treat the XC-potentials. The SCF cycles were performed using a mesh size of 1000  $k$ -point and an energy convergence criterion of 0.0001 Ry. Optimal mesh size was determined by trial and error from 500 to 2000  $k$ -point. After each SCF had successfully finished, the Band structures, CDF and ELF were obtained.

### 3.3.2 Band gap

A series of band gap values is obtained from the simulation of each ternary alloy super-cell series. For instance, if  $Al_xGa_{1-x}N$  compounds are simulated, there are 8 values of the band gap corresponding to the serial simulation of 1,2,...8 Al atom substitutions in the original 2x2x1 GaN super-cell. As the GGA band gap prediction was poorer (see Sec. 3.2.2), only the mBJ XC-potential was used.

For each ternary compound series, a regression of the band gap as a function of composition was performed, following a non-linear Vegard Law formula, Eq. 3.5. The obtained equations for the three series are,

$$\begin{aligned} E_{gap}^{Al_xGa_{1-x}N} &= 5.4x + 3.0(1 - x) - 0.07x(1 - x) \\ E_{gap}^{In_xAl_{1-x}N} &= 0.7x + 5.4(1 - x) - 2.7x(1 - x) \\ E_{gap}^{In_xGa_{1-x}N} &= 0.7x + 2.9(1 - x) - 0.4x(1 - x) \end{aligned} \quad (3.6)$$

where the precision in the fitted coefficients is of around  $\pm 0.2$  for the linear ones, and of  $\pm 0.8$  for the non-linear ones; with a confidence of 95 %. Notice that, in this Vegard Law formulation, the linear coefficients correspond to the band gap energies for the pure binaries and the non-linear coefficients, to a bowing parameter.

Included in Table 3.2 are the band gap values of the binaries,  $E_{gap}^{fit}$ , calculated after the adjustment of the band gap values of the ternaries by a parabolic law. The band gap energies of the pure binaries from GGA and mBJ calculations are in good agreement with the linear coefficients from this fitting procedure. The results predict almost negligible bowing parameters for  $\text{Al}_x\text{Ga}_{1-x}\text{N}$  and  $\text{In}_x\text{Ga}_{1-x}\text{N}$ , indicating an approximately linear dependence with composition. The non-linear behavior is more clear in  $\text{In}_x\text{Al}_{1-x}\text{N}$ , as indicated by the higher bowing parameter. This was already expected, as ternary bowing increases with the Z difference between the binaries: among the three III-group atoms, aluminum is the smallest one and indium is the largest one.

### 3.3.3 Plasmon energy

The simulation of the super-cell series resulted also in three ELF-series, one for each of the corresponding ternary compounds. These series are depicted in the three panels of Fig. 3.5. Implicit in these results, the ELFs from the pure binary compounds appear at the bottom and top of the series.

For all the studied cases, the series showed the composition dependence of the plasmon peak. A visual examination of Fig. 3.5(a) evidences that, in  $\text{Al}_x\text{Ga}_{1-x}\text{N}$ , this dependence is still approximately linear, as for the band gap. However, it is harder to identify and follow the plasmon peak evolution in the compounds with high indium content.

As a first approach to study the plasmon composition dependence, we used a non-linear model based fit following Eq. 3.1. The fitting interval was chosen around the peak maximum energy position, with a width of 2 eV around this value. This was done in order to minimize the impact of other spectral features in our fitting interval, since the model does not account for those. Once this procedure was performed, a series of Drude plasmon energies,  $E_P$ , were obtained as a result. We proceeded to analyze them in terms of the Vegard law equation, as done above for the band gap values. The obtained equations for the three series are,

$$\begin{aligned} E_P^{\text{Al}_x\text{Ga}_{1-x}\text{N}} &= 23.4x + 22.8(1 - x) + 0.2x(1 - x) \\ E_P^{\text{In}_x\text{Al}_{1-x}\text{N}} &= 21.3x + 23.3(1 - x) + 0.5x(1 - x) \\ E_P^{\text{In}_x\text{Ga}_{1-x}\text{N}} &= 21.3x + 22.7(1 - x) + 0.7x(1 - x) \end{aligned} \quad (3.7)$$

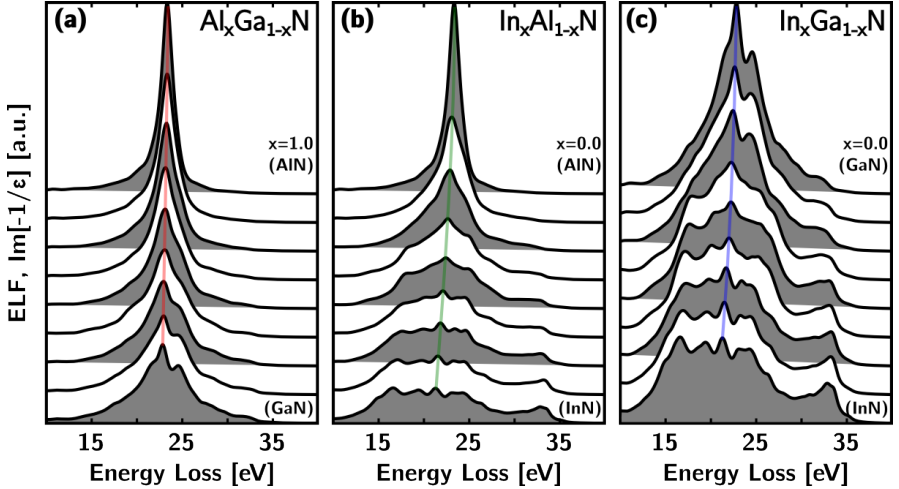


**Fig. 3.5** The obtained ELF-series after the simulation of the three ternary compounds,  $\text{Al}_x\text{Ga}_{1-x}\text{N}$ ,  $\text{In}_x\text{Al}_{1-x}\text{N}$  and  $\text{In}_x\text{Ga}_{1-x}\text{N}$ . The concentration varies linearly in steps of 0.125. In panel (a), the ELF-series for  $\text{Al}_x\text{Ga}_{1-x}\text{N}$ , from AlN to GaN (both included). For panels (c) and (d), the ELF-series for  $\text{In}_x\text{Al}_{1-x}\text{N}$  and  $\text{In}_x\text{Ga}_{1-x}\text{N}$ , from AlN and GaN, respectively, to InN. The ascending or descending ordering corresponds to the relative intensity variation only, as the spectra have not been normalized in any way whatsoever. Moreover, the panels are not at scale; for instance, the GaN ELF at the bottom of panel (a) is the same as displayed on top of panel (c). The positions of the plasmon maxima are indicated with colored lines, as an eye-guide.

where the precision in the fitted coefficients is of  $\pm 0.2$  for the linear ones, and of  $\pm 0.8$  for the non-linear ones, with a confidence of 95 %. As for the band gap fit above (Eq. 3.6), the linear fit coefficients were identified with the Drude plasmon energies for the pure binaries. Recalling the experimental plasmon energies, given in Sec. 3.2.3, it seems that the calculated ELF systematically overestimates this parameter. Meanwhile, the non-linear coefficients were identified with bowing parameters for the plasmon energy. Notice that the bowing parameters for the band gap and plasmon need not be equal, as experimentally there can usually be some small discrepancy.

However, this time the discrepancy is rather large, as the bowing parameters for all ternary compounds are rather small and all positive. This is found to be in contradiction with the calculated composition dependence of  $E_{gap}$  presented above (Eq. 3.6), in the case of  $\text{In}_x\text{Al}_{1-x}\text{N}$  and  $\text{In}_x\text{Ga}_{1-x}\text{N}$ . These series both show a negative bowing of the band gap values, with a sizable value in the case of  $\text{In}_x\text{Al}_{1-x}\text{N}$ . By examination of the relatively small bowing parameters

in Eq.3.7, it seems that the composition dependence of  $E_P$  should follow an approximately linear law. Nevertheless, we expected from experimental studies that the bowing parameters in the case of ternary compounds with indium showed be more important<sup>31</sup>.

We observe that including indium in the alloys produces theoretical ELF that are difficult to analyze by the model-based fit procedure. This should be directly related to the increased importance of the interband transitions in compounds with indium. We also have to keep in mind that electronic transitions truly are excited-state properties of material media. DFT is a ground-state theory, with inherent limitations in the prediction of excited-state properties. This deficiency can cause DFT to fail on assigning the correct intensities and life-times for the excitations. When calculating the CDF or the ELF, the main limitation is the impossibility to predict the width of the peaks from imprecise transition life-times.

In the In-rich ternary compounds, the intensity of the collective mode is reduced as interband transitions become more important. On a first approximation, we interpret that a smaller plasmon peak is smeared by other surrounding peaks. In this sense, our ability to predict the behavior of the  $E_P$  that is observed in experimental energy-loss spectra is compromised. This limitation can be circumvented by directly examining the CDF, as shown in the following section.

### 3.3.4 CDF zero-cut energy

There was one simulated CDF-series for each ternary compound, from which the ELF-series above were calculated. A series of  $E_{cut}$  values was extracted from each one of them, using linear interpolation around the 15 – 30 eV region. The linear interpolation was used to increase accuracy to sub-pixel precision. Once this procedure was performed, we were left with three  $E_{cut}$ -series, each one corresponding to a ternary compound.

We proceeded to analyze them using the Vegard law equation (Eq. 3.5), as for  $E_{gap}$  and  $E_P$  above. The obtained equations for the three series are,

$$\begin{aligned} E_{cut}^{\text{Al}_x\text{Ga}_{1-x}\text{N}} &= 23.2x + 22.0(1 - x) + 0.5x(1 - x) \\ E_{cut}^{\text{In}_x\text{Al}_{1-x}\text{N}} &= 15.9x + 23.7(1 - x) - 1.9x(1 - x) \\ E_{cut}^{\text{In}_x\text{Ga}_{1-x}\text{N}} &= 16.2x + 22.3(1 - x) - 5.3x(1 - x) \end{aligned} \quad (3.8)$$

where the precision in the fitted coefficients is of around  $\pm 0.2$  for the linear ones, and of  $\pm 0.8$  for the non-linear ones; with a confidence of 95 %. Notice that the linear coefficients corresponding to AlN and GaN for  $E_{cut}$ , in Eq. 3.8, are similar to the ones for  $E_P$ , in Eq. 3.7.

This correspondence is maybe better appreciated using a graphical representation of the data (see Fig. 3.6). This figure summarizes the results from the three energy-determination procedures in this work,  $E_{gap}$ ,  $E_P$  and  $E_{cut}$ . In these plots, we observe the negative or positive bowing in the curvature of the fit lines. It becomes clear that  $E_{gap}$  and  $E_{cut}$  both have negative bowing in  $\text{In}_x\text{Al}_{1-x}\text{N}$  and  $\text{In}_x\text{Ga}_{1-x}\text{N}$ ; more so in the case of  $E_{cut}$ . Nevertheless, bowing in the  $E_P$ -series for the In-containing compounds does not follow the same trend, and is positive. This is to say that we do not find similar behaviors in  $E_P$  and  $E_{cut}$  for the same ternaries, as we may had naïvely expected in the beginning.

Remember that within their respective frameworks, both  $E_{cut}$  and  $E_P$  represent a characteristic energy-loss for the excitation of collective modes. Whereas  $E_P$  relies on the free-electron approximation,  $E_{cut}$  is more general. However, the plasmon peak in most semiconductors is typically well described by a (quasi) free-electron approximation. Experimentally it is also easier to measure  $E_P$  from EELS, by a model-based fit, than obtaining  $E_{cut}$ . In order to obtain  $E_{cut}$  from EELS, Kramers-Kronig analysis is needed<sup>15</sup>, which is difficult and not always feasible<sup>32,33</sup>.

These disagreements between the collective mode excitation energies can be related to the introduction of indium in the III-nitride alloys. As the indium content is increased, the number of intense inter-band transitions increases. At the same time, the collective excitation mode is weaker (also broader in our ELF). These combined effects make it harder to trace the collective excitation mode as indium content increases. Thus, in this case, the model-based fit procedure is not appropriate and the assessment of the CDF zero-cut energy is more advantageous.

Notice that for In-containing alloys, especially for InAlN, some deviation from the parabolic dependence is found for  $E_{gap}$  and  $E_{cut}$ . Earlier theoretical calculations also predicted this deviation for the band gap in (In, Ga, Al)N alloys, more so in InAlN<sup>34</sup>. In this sense, a strong increase in InAlN bowing parameter with decreasing InN molar fraction is expected, as qualitatively confirmed by some experimental measurements<sup>30,35</sup>. This effect becomes relevant in the following chapter, where we observe it experimentally.

## 3.4 Conclusions

- We simulated the dielectric response for  $\text{Al}_x\text{Ga}_{1-x}\text{N}$ ,  $\text{In}_x\text{Al}_{1-x}\text{N}$  and  $\text{In}_x\text{Ga}_{1-x}\text{N}$ , three of the most relevant ternary III-nitride semiconductors, using advanced DFT methods in Wien2K. In an initial structural relaxation phase, the binary lattice parameters were optimized for DFT calculation, using GGA. Using the mBJ XC-potential, we observed an improvement in the calculation of band structure related parameters. In this sense, theoretical band structures for the three binary compounds were obtained, showing

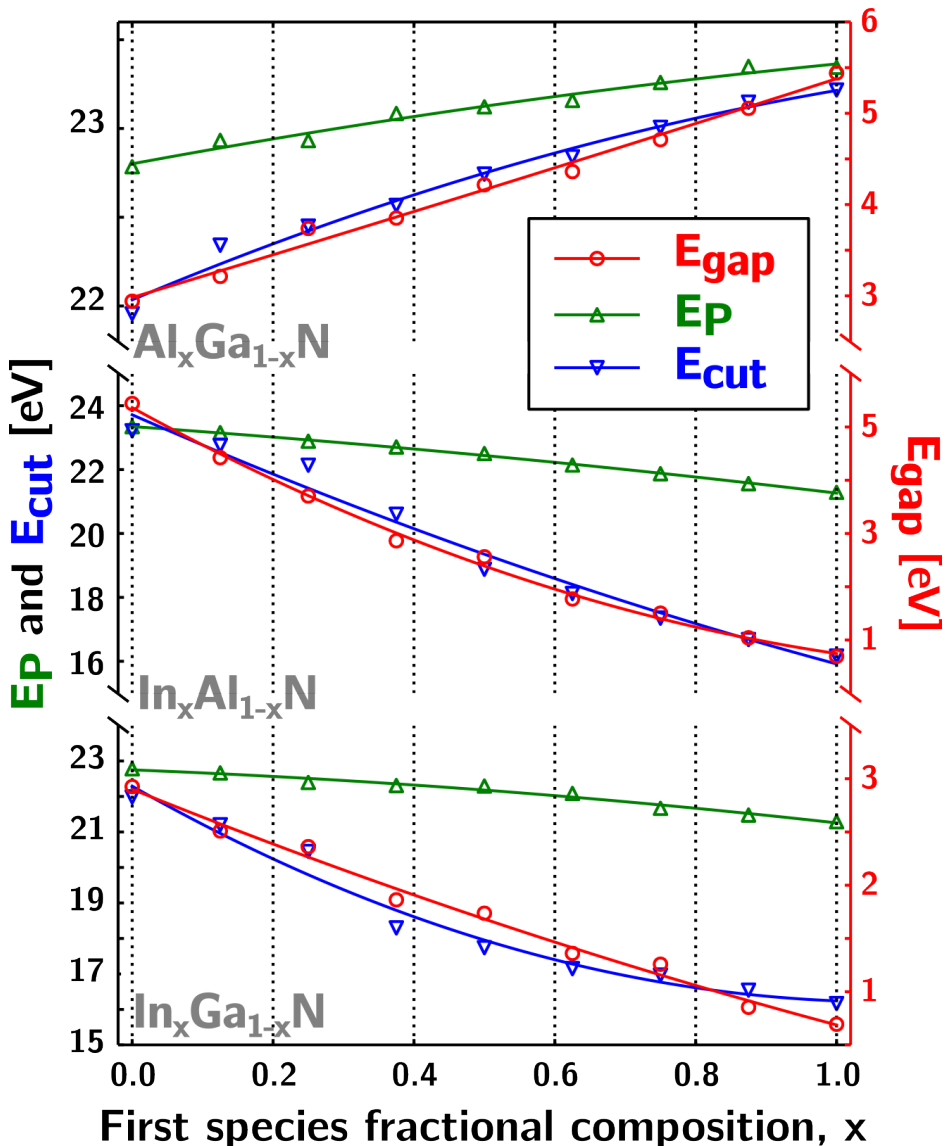


Fig. 3.6 Summary of the results from the ternary series simulation of  $\text{Al}_x\text{Ga}_{1-x}\text{N}$ ,  $\text{In}_x\text{Al}_{1-x}\text{N}$  and  $\text{In}_x\text{Ga}_{1-x}\text{N}$ , and Vegard Law fit for each series (solid lines). Included are: band gap energy,  $E_{gap}$  (red circles); Drude plasmon energy,  $E_P$  (green upward triangles); CDF-zero cut energy,  $E_{cut}$  (blue downward triangles).

a direct band gap in all cases.

- We also found that, for these wurtzite structures, the total energy strongly depends on the volume of the primitive cell (keeping the ratio between the lattice parameters). We observed a much weaker dependence on  $c/a$  ratio (constraining the volume to the optimized one). The optimization results are relevant, as these III-nitrides often grow epitaxially in the  $c$  direction on an hexagonal substrate with similar lattice parameters.
- The improvement upon implementing mBJ was critical, as we found that GGA calculation wrongly predicted a metallic behavior ( $E_{gap} = 0$ ) for InN. With mBJ, we found that theoretical band gap energies were also closer to the experimental measurements than the ones calculated using GGA. However, the calculated band gap was always underestimated for both XC-potentials.
- We then studied the composition dependence of band gap energy in the ternary compounds. A parabolic Vegard law was used in order to do so in a systematic manner. In the case of  $\text{Al}_x\text{Ga}_{1-x}\text{N}$ , we obtained an almost linear dependence for both band gap and plasmon energies, as expected from other studies<sup>29,36</sup>. In the case of ternary compounds with indium content,  $\text{In}_x\text{Al}_{1-x}\text{N}$  and  $\text{In}_x\text{Ga}_{1-x}\text{N}$ , an accurate prediction becomes more complicated as bowing and interband transitions become more relevant<sup>31,34</sup>. In these cases, we found that it is more advantageous to examine the real part of the CDF in order to predict the plasmon energy composition dependence using  $E_{cut}$ .
- As in other related works using DFT<sup>4</sup>, the calculated plasmon peaks showed higher energies than the experimental observed ones. In this sense, we discussed a method for the theoretical assessment of the collective excitation mode in the CDF, through  $E_{cut}$ . This method does not rely on the assumption of a free-electron like response, as the model-based fit one does. Using  $E_{cut}$ , the prediction of the composition dependence of the plasmon was improved. Additionally, this dependence was seen to be consistent with the one found for the band gap energy.

## Bibliography

- [1] S. Nakamura, S. Pearton, and G. Fasol. *The Blue Laser Diode. The Complete Story*. Springer New York, 1997.
- [2] M. Ikeda and S. Uchida. Blue-violet laser diodes suitable for blu-ray disk.

- Physica Status Solidi A: Applications and Materials Science*, 194(2):407–413, 2002.
- [3] The nobel prize in physics 2014. Nobelprize.org. Nobel Media AB 2014. Web, Jun 2015. URL [http://www.nobelprize.org/nobel\\_prizes/physics/laureates/2014/](http://www.nobelprize.org/nobel_prizes/physics/laureates/2014/).
  - [4] J. Palisaitis, C.-L. Hsiao, M. Junaid, J. Birch, L. Hultman, and P. O. Å. Persson. Effect of strain on low-loss electron energy loss spectra of group-III nitrides. *Physical Review B*, 84:245301, Dec 2011. doi: 10.1103/PhysRevB.84.245301. URL <http://link.aps.org/doi/10.1103/PhysRevB.84.245301>.
  - [5] J. Palisaitis, C.-L. Hsiao, M. Junaid, M. Xie, V. Darakchieva, J.-F. Carlin, N. Grandjean, J. Birch, L. Hultman, and P. O. Å. Persson. Standard-free composition measurements of  $\text{Al}_x\text{In}_{1-x}\text{N}$  by low-loss electron energy loss spectroscopy. *Physica status solidi rapid research letters*, 5(2):50–52, 2011. ISSN 1862-6270. doi: 10.1002/pssr.201004407. URL <http://dx.doi.org/10.1002/pssr.201004407>.
  - [6] M. M. Soumelidou, J. Kioseoglou, H. Kirmse, Th. Karakostas, and Ph. Kominou. Electron energy loss near edge structure of  $\text{In}_x\text{Al}_{1-x}\text{N}$  alloys. *Microelectronic Engineering*, 112(0):198 – 203, 2013. ISSN 0167-9317. doi: <http://dx.doi.org/10.1016/j.mee.2013.04.006>. URL <http://www.sciencedirect.com/science/article/pii/S0167931713004097>.
  - [7] D. Holec, P. M. F. J. Costa, P. D. Cherns, and C. J. Humphreys. A theoretical study of ELNES spectra of  $\text{Al}_x\text{Ga}_{1-x}\text{N}$  using Wien2k and telnes programs. *Computational Materials Science*, 44(1):91 – 96, 2008. ISSN 0927-0256. doi: <http://dx.doi.org/10.1016/j.commatsci.2008.01.029>. URL <http://www.sciencedirect.com/science/article/pii/S0927025608000694>. International Conference on Materials for Advanced Technologies 2007 (ICMAT 2007) Selected papers of Symposium O: Frontiers in Computational Materials Science.
  - [8] D. Holec, P. M. F. J. Costa, P. D. Cherns, and C. J. Humphreys. Electron energy loss near edge structure (ELNES) spectra of AlN and AlGaN: A theoretical study using the wien2k and telnes programs. *Micron*, 39(6):690 – 697, 2008. ISSN 0968-4328. doi: <http://dx.doi.org/10.1016/j.micron.2007.10.013>. URL <http://www.sciencedirect.com/science/article/pii/S096843280700162X>. Proceedings of the Annual Meeting of the Microscopical Society of Canada 2007.
  - [9] V. J. Keast, M. J. Kappers, and C. J. Humphreys. Electron energy-loss near edge structure (ELNES) of InGaN quantum wells. *Journal of Microscopy*,

- 210(1):89–93, 2003. ISSN 1365-2818. doi: 10.1046/j.1365-2818.2003.01180.x. URL <http://dx.doi.org/10.1046/j.1365-2818.2003.01180.x>.
- [10] V. J. Keast. An introduction to the calculation of valence EELS: Quantum mechanical methods for bulk solids. *Micron*, 44:93–100, 2013.
- [11] J. P. Perdew. Density functional theory and the band gap problem. *International Journal of Quantum Chemistry*, 28(S19):497–523, 1985. ISSN 1097-461X. doi: 10.1002/qua.560280846. URL <http://dx.doi.org/10.1002/qua.560280846>.
- [12] D. Koller, F. Tran, and P. Blaha. Merits and limits of the modified becke-johnson exchange potential. *Physical Review B*, 83:195134, May 2011. doi: 10.1103/PhysRevB.83.195134. URL <http://link.aps.org/doi/10.1103/PhysRevB.83.195134>.
- [13] J. P. Perdew, K. Burke, and M. Ernzerhof. Generalized gradient approximation made simple. *Physical Review Letters*, 77:3865–3868, Oct 1996. doi: 10.1103/PhysRevLett.77.3865. URL <http://link.aps.org/doi/10.1103/PhysRevLett.77.3865>.
- [14] M. K. Kundmann. Study of semiconductor valence plasmon line shapes via electron energy-loss spectroscopy in the transmission electron microscope. Technical report, Lawrence Berkeley Lab., CA (USA), 1988.
- [15] R. F. Egerton. *Electron Energy-Loss Spectroscopy in the Electron Microscope*. Springer US, 3rd edition, 2011.
- [16] A. M. Sánchez, R. Beanland, M. H. Gass, A. J. Papworth, P. J. Goodhew, and M. Hopkinson. Mapping quantum dot-in-well structures on the nanoscale using the plasmon peak in electron energy loss spectra. *Physical Review B*, 72:075339, Aug 2005. doi: 10.1103/PhysRevB.72.075339. URL <http://link.aps.org/doi/10.1103/PhysRevB.72.075339>.
- [17] P. Yu and M. Cardona. *Fundamentals of Semiconductors: Physics and Materials Properties*. Graduate Texts in Physics. Springer, 2010. ISBN 9783642007101. URL [http://books.google.es/books?id=5aBuKYBT\\_hsC](http://books.google.es/books?id=5aBuKYBT_hsC).
- [18] A. Kokalj. Computer graphics and graphical user interfaces as tools in simulations of matter at the atomic scale. *Computational Materials Science*, 2003. URL <http://www.xcrysden.org/>.
- [19] M. E. Levinshtein, S. L. Rumyantsev, and M. S. Shur. *Properties of Advanced Semiconductor Materials: GaN, AlN, InN, BN, SiC, SiGe*. A Wiley-Interscience publication. Wiley, 2001. ISBN 9780471358275. URL [http://books.google.es/books?id=u26CpULkD\\_wC](http://books.google.es/books?id=u26CpULkD_wC).

- [20] W. Gian, M. Skowronski, and G. S. Rohrer. Structural defects and their relationship to nucleation of gan thin films. In *Symposium E – III-Nitride, SiC, and Diamond Materials for Electronic*, volume 423 of *MRS Proceedings*, 1 1996. doi: 10.1557/PROC-423-475. URL [http://journals.cambridge.org/article\\_S1946427400197313](http://journals.cambridge.org/article_S1946427400197313).
- [21] D. M. Teter, G. V. Gibbs, M. B. Boisen, D. C. Allan, and M. P. Teter. First-principles study of several hypothetical silica framework structures. *Physical Review B*, 52:8064–8073, Sep 1995. doi: 10.1103/PhysRevB.52.8064. URL <http://link.aps.org/doi/10.1103/PhysRevB.52.8064>.
- [22] R. Abt, C. Ambrosch-Draxl, and P. Knoll. Optical response of high temperature superconductors by full potential LAPW band structure calculations. *Physica B: Condensed Matter*, 2(0):1451–1452, 1994. ISSN 0921-4526. doi: [http://dx.doi.org/10.1016/0921-4526\(94\)91225-4](http://dx.doi.org/10.1016/0921-4526(94)91225-4). URL <http://www.sciencedirect.com/science/article/pii/0921452694912254>.
- [23] C. Ambrosch-Draxl and J. O. Sofo. Linear optical properties of solids within the full-potential linearized augmented planewave method. *Computer Physics Communications*, 175(1):1–14, 2006.
- [24] A. D. Dorneich, R. H. French, H. Müllejans, S. Loughin, and M. Rühle. Quantitative analysis of valence electron energy-loss spectra of aluminium nitride. *Journal of Microscopy*, 191(3):286–296, 1998. ISSN 1365-2818. doi: 10.1046/j.1365-2818.1998.00370.x. URL <http://dx.doi.org/10.1046/j.1365-2818.1998.00370.x>.
- [25] G. Brockt and H. Lakner. Nanoscale EELS analysis of dielectric function and bandgap properties in GaN and related materials. *Micron*, 31(3):435–440, 2000.
- [26] S. Lazar, G. A. Bottom, C. M. Wu, F. D. Tichelaar, and H. W. Zandbergen. Materials science applications of HREELS in near edge structure analysis and low-energy loss spectroscopy. *Ultramicroscopy*, 96(3-4):535–546, 2003.
- [27] J. Arbiol, S. Estradé, J. D. Prades, A. Cirera, F. Furtmayr, C. Stark, A. Laufer, M. Stutzmann, M. Eickhoff, M. H. Gass, A. L. Bleloch, F. Peir'o, and Morante. Triple-twin domains in Mg doped GaN wurtzite nanowires: structural and electronic properties of this zinc-blende-like stacking. *Nanotechnology*, 20(14):145704–145713, 2009.
- [28] M. Benaissa, L. Gu, M. Korytov, T. Huault, P. A. van Aken, J. Brault, and P. Vennegues. Phase separation in GaN/AlGaN quantum dots. *Applied Physics Letters*, 95(14):141901,141904, 2009.

- [29] A. Eljarrat, L. López-Conesa, C. Magén, Ž. Gačević, S. Fernández-Garrido, E. Calleja, S. Estradé, and F. Peiró. Insight into the compositional and structural nano features of AlN/GaN DBRs by EELS-HAADF. *Microscopy and Microanalysis*, 19(03):698–705, 2013.
- [30] I. Vurgaftman, J. R. Meyer, and L. R. Ram-Mohan. Band parameters for III-V compound semiconductors and their alloys. *Journal of Applied Physics*, 89(11):5815–5875, 2001.
- [31] A. Eljarrat, S. Estradé, Ž. Gačević, S. Fernández-Garrido, E. Calleja, C. Magén, and F. Peiró. Optoelectronic properties of InAlN/GaN distributed Bragg reflector heterostructure examined by valence electron energy loss spectroscopy. *Microscopy and Microanalysis*, 18:1143–1154, 10 2012. ISSN 1435-8115. doi: 10.1017/S1431927612001328. URL [http://journals.cambridge.org/article\\_S1431927612001328](http://journals.cambridge.org/article_S1431927612001328).
- [32] M. Stöger-Pollach. Optical properties and bandgaps from low loss EELS: Pitfalls and solutions. *Micron*, 39(8):1092–1110, 2008.
- [33] P. L. Potapov, H.-J. Engelmann, E. Zschech, and M. Stöger-Pollach. Measuring the dielectric constant of materials from valence EELS. *Micron*, 40 (2):262–268, 2009.
- [34] Z. Dridi, B. Bouhafs, and P. Ruterana. First-principles investigation of lattice constants and bowing parameters in wurtzite  $\text{Al}_x\text{Ga}_{1-x}\text{N}$ ,  $\text{In}_x\text{Ga}_{1-x}\text{N}$ ,  $\text{In}_x\text{Al}_{1-x}\text{N}$ . *Semiconductor science and technology*, 18(9):850, 2003.
- [35] E. Iliopoulos, A. Adikimenakis, C. Giesen, M. Heuken, and A. Georgakilas. Energy bandgap bowing of InAlN alloys studied by spectroscopic ellipsometry. *Applied Physics Letters*, 92:191907–191910, 2007.
- [36] H. Amari, H. Y. Zhang, L. Geelhaar, C. Chèze, M. J. Kappers, and T. Walther. Nanoscale EELS analysis of elemental distribution and bandgap properties in AlGaN epitaxial layers. In *Journal of Physics: Conference Series*, volume 326, page 012039. IOP Publishing, 2011.



## Chapter 4

# AlN/GaN and InAlN/GaN DBRs

“We did not really believe that we had picked up signals from another civilization, but obviously the idea had crossed our minds and we had no proof that it was an entirely natural radio emission. It is an interesting problem - if one thinks one may have detected life elsewhere in the universe how does one announce the results responsibly? Who does one tell first?”

---

S. Jocelyn Bell Burnell, *Little Green Men, White Dwarfs or Pulsars?*

This chapter presents the high resolution monochromated STEM-EELS characterization of two distributed Bragg reflector (DBR) multilayer heterostructures, composed of a periodic stacking of III-nitride layers. These heterostructures were grown by the group of E. Calleja at the *Instituto de Sistemas Optoelectrónicos y Microtecnología* (ISOM), from *Universidad Politécnica de Madrid*. One of these DBR is composed of an alternate stacking of AlN and GaN layers, and the other one, of InAlN lattice matched to GaN. EELS at sub-nanometric spatial resolution and < 200 meV energy resolution was used to assess the electronic properties of the structures. The EELS signal was treated using ZLP subtraction and deconvolution methods, and non-linear fitting tools complemented with theoretical modeling of the electron scattering distribution. In this sense, the log-ratio formula was used to calculate the relative thickness, related to the electron inelastic mean free path. Moreover, fitting of the bulk plasmon peak was performed using Lorentzian and Drude free-electron models. As we have seen, in group-III nitride alloys, the energy position of this peak can be related to the chemical composition variation through Vegard law. Also, within the context of the Drude plasmon

model, information regarding the structural properties of the material can be obtained from the lifetime of the oscillation. This structural and chemical characterization of the layers was complemented with experimental and simulated high angle annular dark field (HAADF) images. Finally, information related to the dielectric response of the materials was extracted using Kramers-Kronig analysis. Our results significantly improve the understanding of previous macroscopic characterizations of the electro-optical properties of these structures.

## 4.1 Introduction

Group-III nitrides staged a major breakthrough in optoelectronic applications with the development of blue-violet light emission by solid state devices in the early 1990s<sup>1,2</sup>. Owing to their widely-tunable room-temperature band gap energy, these materials are of great promise for the design of optoelectronic devices that cover the entire visible range. Additionally, they are interesting materials for building distributed Bragg reflector (DBR) devices because of their relatively high refractive index contrast, plus design and growth simplicity<sup>3</sup>. However, the huge potential of this new group of materials has been significantly constrained by several inherent problems.

In-plane lattice mismatch between the binary components is an issue that affects their growth, and defects and chemical segregations are usual, finally decreasing the overall performance of the devices<sup>4</sup>. Consider, for instance, the high in-plane lattice mismatch between the three most common binaries (InN, GaN and AlN)<sup>5</sup>. An early theoretical calculation for the alloys (In, Ga, Al)N, based on a strictly regular solution model, predicted high mixing instability and proneness to spinodal decomposition<sup>6</sup>, especially strong in the case of indium containing alloys. This leads to the formation of layers with two separated zones, such as inter-diffusions of the metallic species forming metal-rich and -poor regions, and the appearance of metallic isles and other defect structures<sup>7–9</sup>. Obviously, these mechanisms lead to defect formation at the heterostructure interfaces, affecting the electrical and optical properties of the devices.

Despite these difficulties, experimental results reported during the last decade, for systems obtained mainly by metal-organic vapor phase epitaxy (MOVPE), have proven that lattice matched InAlN / GaN heterostructures of excellent quality can be grown; high reflectivity DBRs<sup>10</sup>, resonant-cavity LEDs<sup>11</sup>, planar micro cavities (MCs, see Feltin et al.<sup>12</sup>) and optically pumped vertical cavity surface emitting lasers (VCSELs, see Feltin et al.<sup>13</sup>) have already been demonstrated. Reports concerning molecular beam epitaxy (MBE) growth are very scarce and have been focused mainly on high electron mobility transistor structures (HEMT, in various publications<sup>14–16</sup>). The first systematic studies of the material growth have been reported recently<sup>17,18</sup>, as well as short LM InAlN /

GaN super-lattices and ten-period DBR devices<sup>19–21</sup>. The DBRs are optoelectronic devices composed of a periodic and alternate staking of layers with different refractive indices. Bearing in mind that the MBE technique allows the formation of flat and abrupt interfaces, it can be argued that, in the field of InAlN / GaN heterostructures, the potential of this growth technique has not been fully exploited yet. The main reason for this is the huge difference in optimal growth temperatures for the two binaries (400 and 800°C for InN and AlN, respectively).

In order to optimize the performance of these devices, it is of fundamental importance to determine the structural, optical and electrical properties of the layers, and to correlate them to one another. For this purpose, techniques such as atomic force microscopy (AFM)<sup>22</sup>, optical reflection spectroscopy (ORS) and transmission electron microscopy (TEM) have been widely considered<sup>20,21,23</sup>. Optical techniques traditionally used for band gap determination have excellent energy resolution (down to the meV range) but are limited to macroscopic measurements due to their micron-range spatial resolution. However, the growth issues of group-III nitride ternary compounds and their application to DBR structures require characterization techniques providing precise information with exceptionally high spatial resolution, like EELS does<sup>24,25</sup>.

In this chapter we undertake the detailed characterization of nitride heterostructures grown by MBE for the configuration of DBR devices (see Fig. 4.1). In our case, these layers are composed of group-III nitride binaries and N-based ternary alloys. More specifically, the two examined DBR systems are based on AlN / GaN and InAlN / GaN heterostructures, respectively, with layer size in the range of 50 nm and below.

Theoretical calculations for the (In, Ga, Al)N systems, such as our own simulations presented in Chapter 3, predict a band gap and a plasmon shift that can be used in the framework of Vegard law to study alloy composition. However, as shown by our own results, some deviation from the usual parabolic dependence

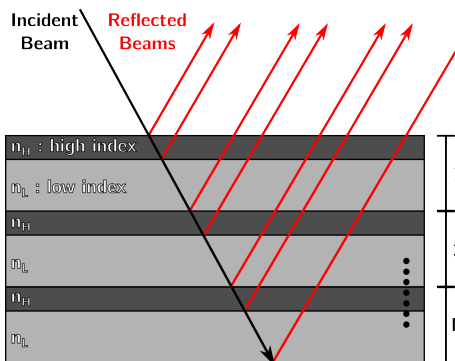


**Fig. 4.1** Schematic diagram of a distributed Bragg reflector structure, showing the periodic staking of alternate high and low refractive index materials. Notice that the structure is intended to reflect light beams, of a specific wavelength.

can be expected in the case of InAlN, which has been attributed to the large electronegativity difference between aluminum and indium atoms<sup>26</sup>. Experimental measurements have confirmed the strong increase in InAlN bowing parameter with decreasing InN molar fraction, in qualitative agreement with our simulations and other theoretical findings<sup>5,27</sup>. Also in good agreement with our results from Chapter 3, it has been recently reported that, for AlGaN alloys, both band gap and plasmon energies vary linearly with composition<sup>28</sup>.

## 4.2 System I: AlN / GaN DBR

### 4.2.1 Sample details and previous characterization

In this section we address the characterization of a 20-period (Al, Ga)N multilayer DBR, designed to present a peak reflectivity centered around  $\sim 400$  nm. Semi-periods thicknesses were set to be 49.3/41.0 nm (AlN / GaN) to obtain the targeted reflectivity. The growth was carried out in a RIBER Compact 21 MBE system equipped with a radio-frequency plasma nitrogen source and standard Knudsen cells for gallium and aluminum. Both GaN and AlN layers were grown below GaN decomposition threshold temperature, at 720°C. To improve AlN crystalline quality, Ga was used as a surfactant<sup>23</sup>.

Preliminary results from optical and X-ray techniques, obtained by the ISOM group, provided a macroscopic characterization of the sample. A noticeable deviation from the theoretically expected values was revealed in the reflectivity of the samples, 92 instead of 99 %, as measured by spectrophotometry. The high in-plane lattice mismatch present in this structure ( $\sim 2.5$  %) is known to lead to a strong tensile stress in the AlN layers and to the formation of cracks in the heterostructure<sup>29,30</sup>. In spite of this, no cracks were found by optical microscopy examination of the structure. X-ray diffraction-reciprocal space mapping (XRD-RSM) measurements hinted the presence of AlGaN inclusions<sup>23</sup>. In the following, we demonstrate the strong potential of the STEM-EELS technique to elucidate the ultimate reasons for the observed optical performance.

Electrotransparent thin foil samples were prepared for TEM observation by mechanical polishing and ion bombardment, as explained in Appendix A. Figure 4.2 (a) displays a HAADF-STEM image of the whole sample. The 20 AlN / GaN periods could be seen in this figure, maintaining the periodicity and layer flatness for the whole stack. However, at higher magnification, HAADF observations revealed that the (AlGaN) heterostructure is composed of a periodic four layer structure. According to dependence on Z of the HAADF intensity, the bright and dark bands are expected to correspond to GaN and AlN, respectively, with an intermediate composition in the gray regions (see Fig. 4.2 (b)). Yet, the chemical composition of these layers, using only Z-contrast images, could not be

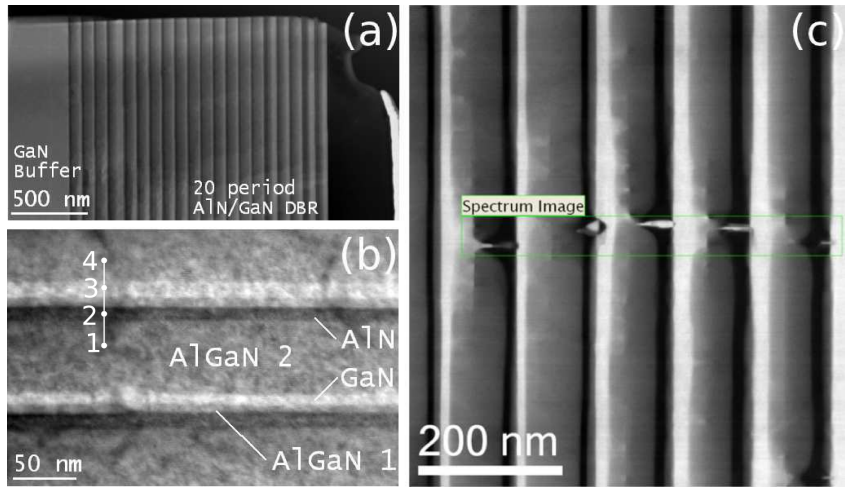


**Fig. 4.2** (a) HAADF-STEM image of the 20-period (AlGaN) full structure. The high periodicity of the structure is appreciated in this image. (b) shows a detail of two successive periods. Four layers of different contrast are clearly visible. Finally, (c) presents the detail of an area where anomalous segregations are detected, and its surroundings.

determined. Moreover, some anomalous segregations were detected in localized regions of the sample (see Fig. 4.2 (c)).

From this information we knew that the sample presented a highly stable four-layer periodic heterostructure and some localized growth irregularities. Given the small size and unknown composition of these features, an EELS-based analysis was the obvious choice for the examination of this structure. In this sense, several hyperspectral EELS data-sets were acquired to monitor the behavior of the plasmon peak, as explained in the following section.

#### 4.2.2 Characterization through plasmon peak position

The continuous line through a whole period of the stack in Fig. 4.2 (b), displays the profile along which a typical EELS spectrum line (SL) was measured. In Fig. 4.3 (a) four single spectra of this EELS-SL, corresponding to the highlighted points in Fig. 4.2 (b), are shown as an example. Spectra from points 2 and 3 were identified as energy-loss spectra of pure AlN and GaN because of their plasmon energy position, very close to the expected experimental plasmon energies for the pure binaries ( $E_{max}^{AlN} = 21.1$  eV and  $E_{max}^{GaN} = 19.7$  eV)<sup>31–35</sup>, in good agreement with our previous qualitative estimation from Z-contrast in HAADF images. Spectra

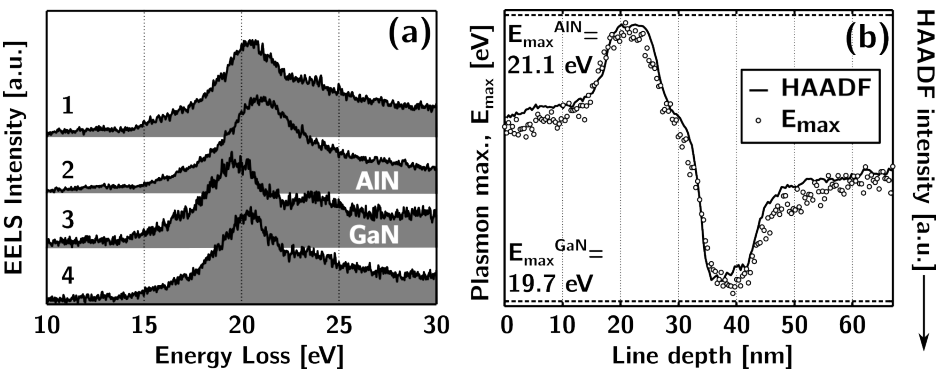


**Fig. 4.3** Panel (a) displays four energy-loss spectra, from the highlighted points in Fig. 4.2 (b); a line shows their determined plasmon maxima. Spectra taken from pure AlN and GaN regions are indicated. Panel (b) displays the determined plasmon maximum energy,  $E_{max}$  (circles), and the HAADF intensity (line) profiles through one period. These signals have been centered and normalized to allow for a comparison of the contrasts that they provide. Additionally, the HAADF intensity axis has been inverted.

from points 1 and 4 have intermediate plasmon energy values, and thus, the composition in these regions is expected to be that of an intermediate AlGaN alloy.

### Plasmon profiling

In order to extract more quantitative information from the analysis of the hyperspectral EELS datasets, we used the Drude plasmon model (DPM),

$$\text{Im}[-1/\varepsilon(E)] = \frac{EE_P^2\Gamma}{(E^2 - E_P^2)^2 + (E\Gamma)^2} \quad (3.1)$$

This model function, already introduced in Sec. 3.1.2, provides two fitting parameters that contain relevant information from the material<sup>36–38</sup>. One is related to the energy threshold of the collective excitation mode, also called the (modified) plasmon energy,  $E_P$ . This parameter includes the effects of band transitions and core electrons to the plasmon excitation. The other one is related to the broadening of the peak,  $\Gamma$ . We are also interested in obtaining the maximum of the plasmon peak,  $E_{max}$ , useful for the application of Vegard law,

$$E_{max}(E_P, \Gamma) = \left( \frac{2E_P - \Gamma^2 + \sqrt{(2E_P - \Gamma^2)^2 + 12E_P^4}}{6} \right)^{1/2} \quad (4.1)$$

Plasmon profiling can be performed using simple Gaussian or Lorentzian models that correctly obtain  $E_{max}$ , but give a worse estimation of  $\Gamma$ . Interestingly, it is possible to use the DPM for the calculation of parameters such as the lifetime of the plasmon excitation,  $\tau = \hbar/\Gamma$ , in addition to  $E_{max}$ <sup>37</sup>.

Figure 4.3 (b) presents  $E_{max}$ , as determined by DPM in comparison with the experimental HAADF intensity profile, for the whole EELS-SL depicted in Fig. 4.2 (b). Notice that the HAADF intensity axis is inverted, higher values at the bottom, as a help to the eye to compare it to the plasmon profile. In Z-contrast, a higher HAADF intensity (lower values in the image) corresponds to heavier compounds. In this case, gallium is heavier than aluminum, and the correspondence with the plasmon profile appears to be excellent.

### Composition determination from Vegard law

Our DFT simulations, presented in Chapter 3, indicate that both band gap and plasmon energies in the  $\text{Al}_x\text{Ga}_{1-x}\text{N}$  system can be related to binary nitride composition through a linear law (negligible bowing). These findings, in good agreement with other theoretical and experimental works<sup>39</sup>, suggest that the plasmon energy in an  $\text{Al}_x\text{Ga}_{1-x}\text{N}$  layer is given by the ratio of each component through a Vegard-like Law of the form,

$$E_P^{\text{AlGaN}} = xE_P^{\text{AlN}} + (1 - x)E_P^{\text{GaN}}, \quad (4.2)$$

Using the experimental bulk plasmon peak maximum energies of the binary compounds (presented above), the aluminum nitride composition can be determined. Notice that the available experimental data correspond to  $E_{max}$ , but we expect a linear behavior similar to that of  $E_P$ . Assuming the validity of Eq. (4.2) for the whole spectrum line, and once the plasmon position profiles are processed using Vegard Law, the composition of one of this periods is well described by the variation of the aluminum nitride composition, here called  $x$ , along the spectrum line. This result is given in Fig. 4.4 (a). In this profile, it is possible to distinguish each of the layers that compose the repeating four-layer heterostructure. We are, thus, able to resolve the GaN, AlN and intermediate AlGaN regions and to read from the profile the composition variation.

In Fig. 4.4 (a), corresponding to the scanned line in Fig. 4.2, we can distinguish the transition corresponding to the ending of the AlGaN2 layer, with  $x \simeq 0.6$ , at a line depth of  $\sim 15$  nm. Two nearly-pure binary layers are detected after this,  $x \simeq 0.1$  and  $x \simeq 0.9$ , with the narrow AlGaN1 layer between them,  $x \simeq 0.5$ . Finally, the beginning of the next AlGaN2 layer (this is a periodic structure) has a composition of  $x \simeq 0.4$ . In fact, the AlGaN2 layer appears to have a graded composition, with higher AlN content at the top. The average AlN content in the periods was calculated, finding  $\langle x \rangle \simeq 0.5$  for all examined periods, as expected.

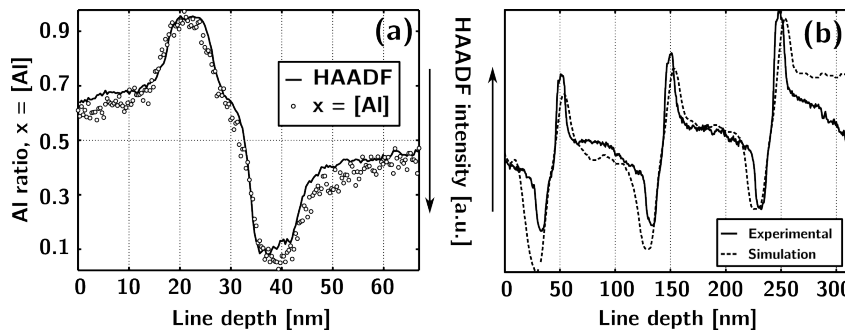


**Fig. 4.4** Left panel, (a), shows the aluminum ratio (circles) profiles calculated through Vegard Law analysis of the plasmon excitation energy position and the HAADF intensity profile (line) corresponding to the spectrum line from 1 to 4 in Fig. 4.2 (b). At the left side, (b), compares the HAADF integrated intensity profiles, experimentally acquired and simulated, along 3 periods.

The width of the different layers that compose the periodic heterostructure, as determined by EELS analysis is of  $\sim 10$ ,  $15$ ,  $50$  and  $15$  nm for AlGaN1 (AlN-on-GaN), GaN, AlGaN2 (GaN-on-AlN) and AlN layers, respectively.

### HAADF simulations

An experimental HAADF profile spanning three periods is shown in Fig. 4.4 (b). Notice the gradual intensity variation in this profile due to the thickness gradient of the sample.

In parallel to the EELS analysis above, the log-ratio method was applied to the spectra to calculate thickness to inelastic mean free path ratios,  $t/\lambda$ . The logarithm of the ratio between the total and the elastic intensities is equal to  $t/\lambda$ , as explained in Sec. 1.2.4. The obtained  $t/\lambda$  profiles point towards an increase of sample thickness along the direction of the line scan (as we approach the buffer layer), a quite appreciable  $\sim 40\%$  mean variation after 3 DBR periods, as expected from the sample preparation procedure. Composition through the three periods was determined by plasmon energy analysis, as explained above.

Following those calculations, HAADF contrast simulations were performed using the obtained composition and thin foil thickness profiles. This was done in order to compare them with the experimental HAADF intensity profiles and, hence, to validate the estimated composition derived from plasmon energy determination. An atomic model for three periods, with the expected thickness variation was created using the RHODIUS software<sup>40,41</sup>. Then the STEM probe propagation through the atomic potential was calculated by the multislice method

using the TEM-SIM software<sup>42</sup>. The simulated integrated intensity profiles are also shown in Fig. 4.4 (b) as a dotted line. As a linear variation in thickness was assumed in the simulations for the sake of simplicity; thus there is not a perfect agreement between simulated and experimental data. However, the simulation roughly shows the expected thickness dependence of the HAADF signal and a fairly good agreement with the intensity variation arising from compositional changes.

The present analysis produced a detailed compositional and structural characterization of the multilayer structure. This information allowed to implement a model for the optical properties of the DBR. The result is presented in Fig. 4.5, which shows experimental and simulated optical reflectivity profiles. For the simulations, a reduced refractive index contrast approximation (RRICA) was used<sup>23</sup>, a novel method which yields an excellent agreement.

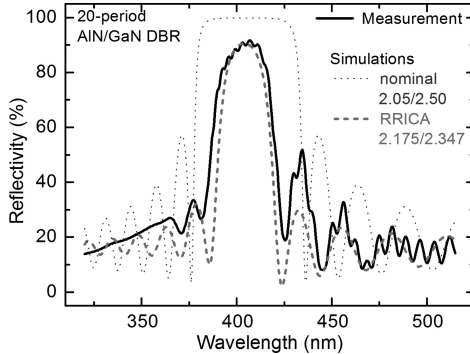


**Fig. 4.5** Comparison between the experimental and simulated reflectivity profiles. Two simulations are presented, a nominal DBR with 2.05/2.50 refractive indices and a DBR with reduced refractive index contrast 2.175/2.347, with optical properties equivalent to the formed four-layer period structure. Adapted from Ref. 23.

### 4.2.3 Anomalous segregation regions

We now focus our attention on the anomalous segregations noticed in some regions of the AlN / GaN heterostructure. HAADF images and energy-loss spectra in two dimensions (spectrum images, SI) were simultaneously acquired in three of such regions. In the first region, see Fig. 4.6, it appears as if a nanometer-size bulging was formed in the GaN layer, judging by the Z-contrast in the HAADF image. In the case of the other two probed regions (see Fig. 4.7 and Fig. 4.8 for the second one, and Fig. 4.9 for the third one), more severe segregations were found. We observe, in these HAADF images, that the local shape of the structure has been much altered, with segregations sometimes affecting several consecutive layers.

EELS-SI from these three different regions were analyzed using a non-linear fitting to the DPM. The relative thickness,  $t/\lambda$ , was also calculated. The DPM fit outputs two parameters,  $E_P$  and  $\Gamma$ . Using the associated formulas included

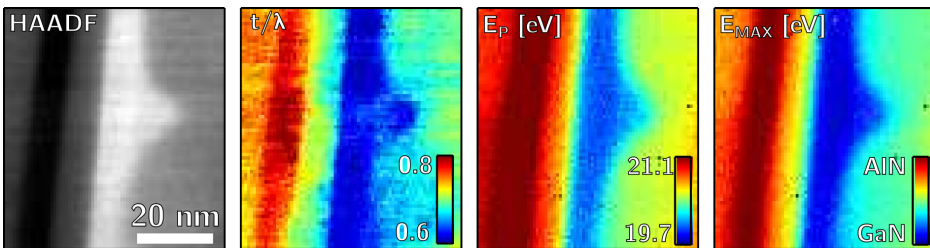


**Fig. 4.6** HAADF image and  $t/\lambda$ ,  $E_P$  and  $E_{max}$  maps calculated from the EELS-SI for the first examined anomalous segregation region.

in the model, we can recover the position of the peak maximum,  $E_{max}(E_P, \Gamma)$ , and the lifetime of the plasmon excitation,  $\tau(\Gamma)$ . A Lorentzian model fit was also applied to the EELS data to obtain  $E_{max}$ , for comparison purposes, showing an almost perfect agreement in all cases.

The HAADF image from the first segregation region is presented in Fig. 4.6, together with the calculated maps  $t/\lambda$ ,  $E_P$  and  $E_{max}$ . There is a striking resemblance between the images in all three panels in spite of the different calculation procedures involved and the particular nature of the information displayed in each of them. Notice that the contrast for the (modified) plasmon energy map,  $E_P$ , is not exactly the same as for the peak maximum,  $E_{max}$ . This is expected in the context of the DPM.

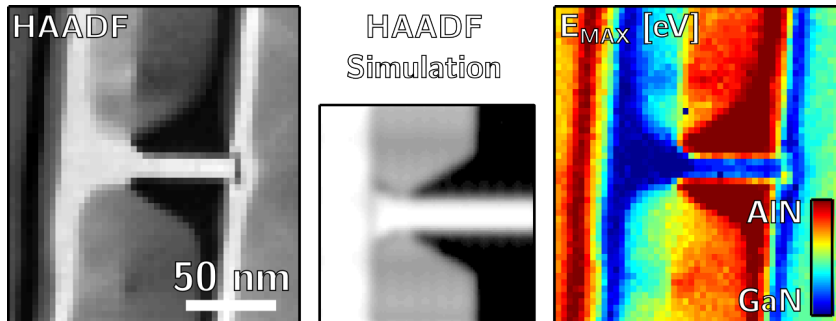


**Fig. 4.7** HAADF images, experimental and simulated, along with  $E_{max}$  map, for the second examined segregation region. The experimental HAADF and  $E_{max}$  show, again, a good agreement; the simulated HAADF image is in good accordance as well. This exit wave reconstruction simulation (size  $363 \times 356$  pixel) was performed using an atomistic model based on the chemical information from  $E_{max}$  and Vegard Law. The increased abruptness of the AlN / GaN interface in the clamped region can be assessed.

The results from the fits also produce a map of  $\Gamma$ , related to the damping of the plasmon. With this result we can calculate  $\tau(\Gamma)$  values, but, in this case, the broadening of the plasmon could not be correlated to any particular property of the examined region, as the maps were found to be homogeneous. A  $\Gamma$  of  $\sim 5$  eV ( $\tau \simeq 0.13$  fs) was found in the whole region.

Because of the small size of this region, we expect the sample thickness gradients to be small. Under this condition, the  $t/\lambda$  parameter is related to the different electron mean free paths,  $\lambda$ , present in the region. Notice that this parameter is computed by means of the log-ratio formula, Eq. (1.19), which uses the integrals of spliced parts of the EEL spectrum, which is remarkably different from the non-linear fit procedure. We can conclude that, for this region, the composition dependence of  $\lambda$  appears to be linear, as it is for the plasmon excitation energy or the HAADF intensity.

Figure 4.7 shows another region, with a more complex structure of reduced size. Observing the HAADF image of this second anomalous segregation region and the corresponding  $E_{max}$  map, we can see how the GaN material of one period has been clamped down into the AlN layer of the next period. An atomic model was built using the information in the plasmon position map and, through exit wave reconstruction, the contrast in the HAADF image was simulated, also shown in Fig. 4.7. This simulation confirmed the correspondence between the information in the two maps. Notice that, due to computational limitations, only a fraction of the structure that is seen in the images was simulated. The simulation recreates the HAADF contrast from a GaN layer being clamped into the next period AlN layer, with a good agreement with the experimental HAADF

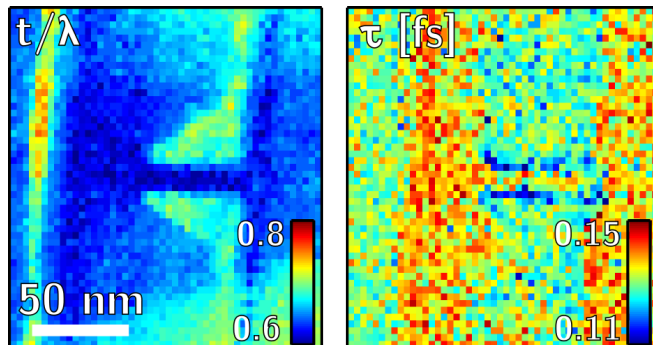


**Fig. 4.8** Two additional EELS-calculated property maps from the second examined segregation region. The left panel shows the relative thickness map, which is quite different from the chemically sensitive pictures in Fig. 4.7. The right panel shows the DPM lifetime  $\tau$ .

image.

Corresponding  $t/\lambda$  and  $\tau$  maps are presented in Fig. 4.8: on one hand, the  $t/\lambda$  of the material, through the inelastic electron mean free path,  $\lambda$ , shows two regions, higher/lower relative thickness or shorter/longer  $\lambda$  (red/blue in the image). On the other hand, it would seem that not much information can be inferred from the blurry  $\tau$  map, but on the central region there is a hint of a low plasmon-lifetime area (high damping, blue again). When compared with the other maps and the HAADF image, two parallel stripes are found, on the AlN / GaN interface.

In this region, the map for the  $t/\lambda$  parameter now shows a contrast which deviates from the linear behavior that was observed in the previous region. Notice that the  $t/\lambda$  parameter is in the same range as it was in the previous region (see Fig. 4.6), indicating that the absolute thickness is similar. But, this time, although the contrast for the AlN layers is preserved, the GaN and AlGaN regions appear blurred out in the map. The  $\tau$  maps for this region show a contrast which is related to the damping of the plasmon oscillation. In this case the abruptness of the AlN/GaN interface is greatly increased, with an effect on the measured  $\Gamma$  and  $\tau(\Gamma)$  parameters from the interface region. The maximum of  $\Gamma$  and minimum of plasmon lifetime,  $\tau$ , appear to lie close to the interface. This is just where the maximum strain gradient in the material should be, as the lattice mismatch between AlN and GaN is important.

Finally, Fig. 4.9 shows a HAADF image of a region with a segregation spanning five periods, dramatically reshaping the layers in a zone almost 500 nm long and 80 nm wide. The  $t/\lambda$  map shows the red/blue region that seems to indicate two repeating constant  $\lambda$  regions. Also, this property is affected by the thickness variation expected from the wedge shape of the sample, that offsets the contrast between the lateral ends. Moreover, the good correspondence between the HAADF features and the  $t/\lambda$  map also points towards a linear dependence on composition, except for the central parts of the segregation.

In the plasmon energy map in Fig. 4.9, two island-shaped regions draw our attention to the center of the image. The plasmon energy inside these two islands is  $\sim 15$  eV, well below the rest of the map, where it lies between the pure GaN and AlN plasmon peak energies. This map, once again, shows a good correspondence with the HAADF signal.

In the  $\tau$  map (bottom panel in Fig. 4.9) the island regions are still visible but show a different type of contrast. The origin of these features in the map is a consistent broadening of the plasmon around the island and a narrowing inside it. This is interpreted in the model as a decrease of  $\tau$  around the island and an increase inside it.

The measured value for the plasmon energy ( $\sim 15$  eV) corresponds to the expected value for pure Al. This fact, plus the narrowing of the peak suggest a

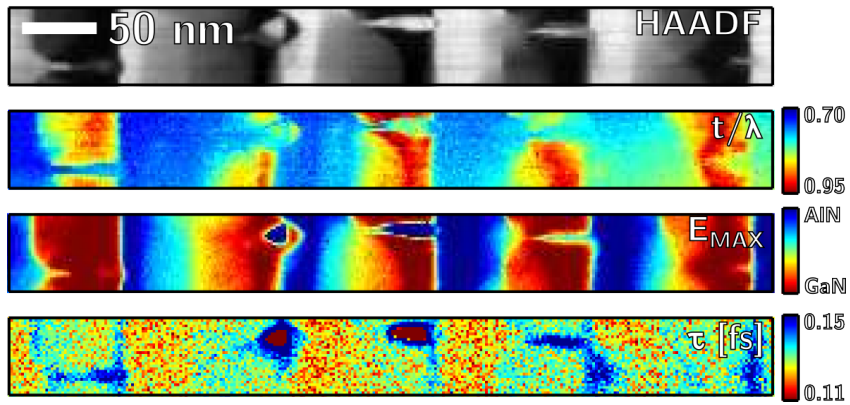


**Fig. 4.9** HAADF image and three EELS-calculated property maps from the third EELS-SI,  $t/\lambda$ ,  $E_{max}$  and  $\tau$ .

metallic aluminum composition for these islands. Indeed, the islands cannot be easily identified in the  $t/\lambda$  map, but are clearly characterized by the plasmon energy of pure Al,  $\sim 15$  eV. Interestingly, the  $\tau$  parameter is lower around the island and higher inside it, confirming the existence of an halo-like signal surrounding the island. The possibility that an halo-like area for the  $\Gamma$  parameter surrounds strained or amorphized areas has been mentioned by other authors<sup>36,37</sup>.

In brief, plasmon damping, measured through the  $\Gamma$  parameter of the plasmon fit, showed halo-like contrast only in situations where the structure had unusually abrupt interfaces, AlN-to-GaN or AlN-to-Al. While we can rely on the compositional sensitivity of the plasmon peak, our analysis indicates that the  $\tau$  parameter may have a great structural sensitivity. Moreover, for the latter two segregations, linear contrast correspondence is lost in some zones of the  $t/\lambda$  maps. The plasmon energy and HAADF contrast are strongly correlated with composition, while, as other authors have already pointed out<sup>43</sup>, an extensive study of the  $\lambda(Z)$  behavior is needed in order to predict the dependence of this parameter.

### 4.3 System II: InAlN / GaN DBR

The substitution of one binary material by a ternary compound is a potential solution for lattice mismatch related problems. In this sense, an option, based on the same AlN / GaN heterostructure, is the substitution of AlN for InAlN. With approximately 18 % of indium, this compound gets in-plane lattice-matched (LM) to GaN, allowing the growth of strain-free InAlN/GaN heterostructures. However, as already mentioned, the growth of the (In, Al)N system is not an

easy task<sup>6</sup>, as the material exhibits proneness to spinodal decomposition due to the large covalent bonds mismatch between the InN and AlN binaries.

#### 4.3.1 Sample details and previous characterization

A 10-period nearly lattice-matched InAlN / GaN DBR system, with peak reflectivity centered around  $\sim 400$  nm, was grown using a RIBER MBE instrument, equipped with a radio-frequency plasma nitrogen source and standard Knudsen cells for gallium, aluminum and indium. The InAlN semi-periods were grown under effective stoichiometry at  $535^{\circ}\text{C}$ . This growth temperature provides good InAlN crystalline quality and good control over the targeted 18 % In content<sup>17</sup>. Due to the high thermal sensitivity of In-N bonds, the InAlN semi-periods were buried by consecutive growth of GaN semi-periods, grown at the same temperature without growth interruptions. As  $535^{\circ}\text{C}$  growth temperature is too low for good GaN quality (its optimal growth temperature is  $\sim 700^{\circ}\text{C}$ ), excess indium was used as a surfactant, as a liquid indium layer on the growth surface enhances Ga adatoms surface mobility, thus improving the GaN crystalline quality. Indium atoms incorporate only residually into the growing GaN crystal (being the InN molar fraction typically below 1 %). Instead, they accumulate on the growth surface as metal droplets. At the end of each GaN semi-period, samples were thermally annealed at temperatures above  $600^{\circ}\text{C}$  to allow for desorption of excess indium droplets and to recover a clean and flat surface. To fabricate ten-period DBRs, the same procedure was repeated ten consecutive times.

Samples were prepared for TEM observation by mechanical methods, as explained in Appendix A. A preliminary HREM characterization of the DBR confirmed the expected epitaxial relationships<sup>21</sup>, both between GaN and sapphire:  $(0001) [01\bar{1}0] \text{Al}_2\text{O}_3 \parallel (0001) [11\bar{2}0] \text{GaN}$ , and between the GaN and InAlN bilayers:  $(0001) [11\bar{2}0] \text{InAlN} \parallel (0001) [11\bar{2}0] \text{GaN}$ . A typical net of threading dislocations was also revealed, with high uniformity of hexagonal wurtzite phase in the InAlN semi-periods, according to selected-area electron diffraction results. Surprisingly, GaN semi-periods showed a clear coexistence of hexagonal wurtzite and cubic zinc-blende phases<sup>21</sup>.

Fig. 4.10 (a) shows a general HAADF image of the ten-period DBR. Fig. 4.10 (b) displays an atomic resolution image corresponding to one of the GaN/InAlN interfaces observed along the  $(11\bar{2}0)$  zone axis. The multilayer grows epitaxially along the  $(0002)$  axis of wurtzite structure and presents good lattice matching between the layers. Notice that the GaN layer appears (bright) at the bottom of the image whereas InAlN appears (darker) at the top. Between GaN and InAlN, a third region appears with intermediate contrast, which is believed to be an In-rich zone of InAlN, according to Z-contrast in the HAADF images and taking into account the conditions used during the growth of GaN layers, with indium acting

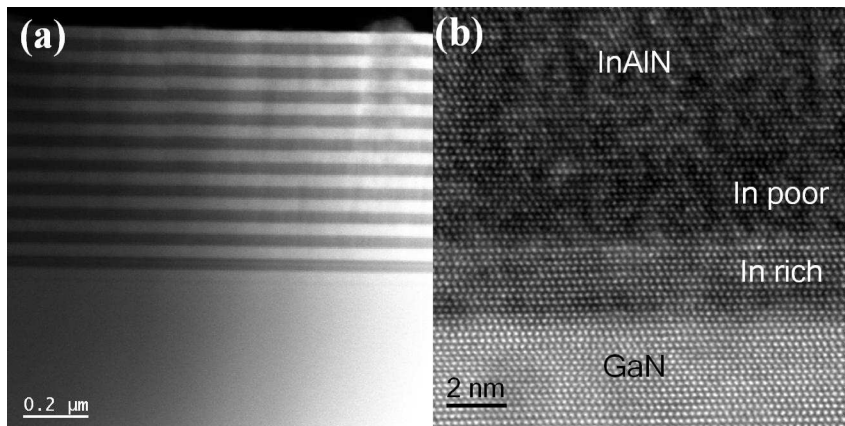


**Fig. 4.10** Panel (a) shows a HAADF general view of the structure observed along the  $(11\bar{2}0)$  zone axis. Panel (b) portrays a high-resolution HAADF image of the interface between an InAlN (topmost, dark regions) and a GaN (bottom, lighter layer), observed along the same direction.

as a surfactant. Additionally, these high resolution HAADF images confirm the preparation of a very thin sample ( $\sim 50$  nm) without amorphisation.

In summary, although epitaxial growth of this system was confirmed, the co-existence of wurtzite and zinc-blende phases in the GaN semi-periods and the existence of an In-rich InAlN interlayer at the GaN / InAlN interfaces, detrimental to the optical properties of the DBR, suggested the need for a detailed compositional and electronic characterization at high spatial resolution.

### 4.3.2 Low-loss EELS data treatment

In order to analyze the different regions, we acquired EELS-SLs through the layers, as depicted in Fig. 4.11. In the energy-loss spectra, see panel (b) for some examples, the plasmon energy shift is more subtle than for the AlN / GaN DBR. However, there are important changes in the shape of these spectra; see, for instance, the smoothing of the low-loss EELS in the InAlN layer as typical inter-band transitions from GaN disappear.

EELS analysis was centered in the detailed characterization of the low-loss features, including band gap signal. Notice that band gap characterization requires a careful removal of the zero-loss peak (ZLP) tails from the spectrum. As for the AlN / GaN system, we carried out a plasmon energy analysis to determine local composition. Further optoelectronic properties were also determined from low-loss EELS data.

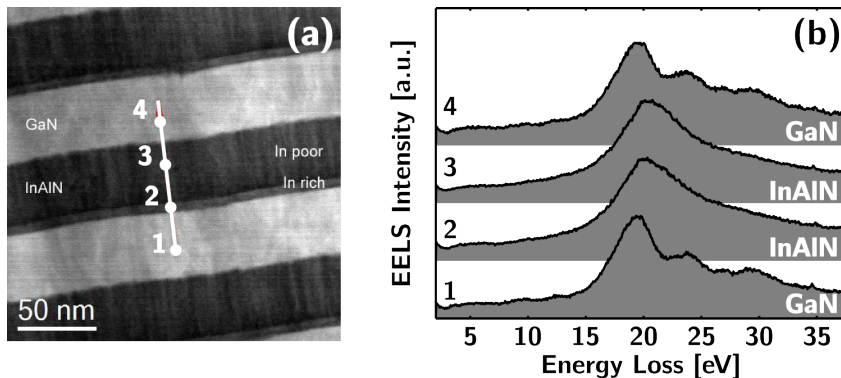


**Fig. 4.11** Panel (a) shows a HAADF image that depicts the examined region. A clear contrast can be appreciated in the InAlN region. The profile over which a typical EELS-SL was acquired is depicted. Panel (b) shows 4 selected spectra from the analyzed data-set. The spectra spatial location can be read from the numbered labels.

The most common ways to separate elastic and inelastic contributions to the signal are based on deconvolution or subtraction methods. For this work, we tested some of these methods, as they are crucial for the characterization that is performed afterwards. Subtraction methods have the advantage of being relatively easy to implement but their result depends on the user ability to find a good tail-fit. The shape and symmetry of the ZLP, as well as the negligible plural scattering contribution (thin sample), allow for the use of simple tail subtraction methods, such as power law (PL) fit subtraction or mirrored tail (MT) subtraction.

The first one fits a PL function to the right end of the ZLP (See Fig. 4.12). This fit has to be set before the onset of the band gap signal. A computer routine then searches for the inflection points in each spectrum, within a given energy window, indicating the onset of the inelastic scattering signal. The designed program included a SNR measuring scheme based on the two area method<sup>38</sup> in order to help improve the results. The MT method uses the mirrored left part of the ZLP (negative energies) to subtract the elastic contribution only. This method is considered to be suitable owing to the symmetric nature of the ZLP in monochromated instruments<sup>44,45</sup>. However, the PL subtraction was preferred as it reproduced the ZLP tail more precisely.

Among the ZLP deconvolution methods considered in this work, the chosen method was Fourier-log which, as explained in Sec. 2.1.1, suppresses plural scattering. It is important to examine the deconvolved signal and make sure all the original features are still present, especially in the case of very low energies, near

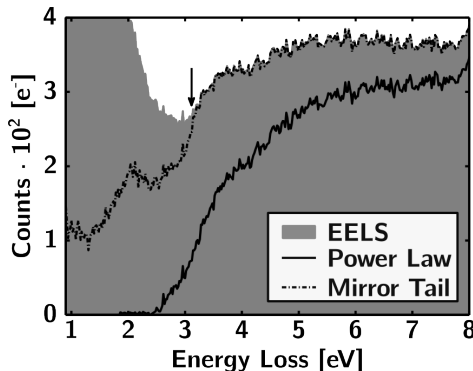


**Fig. 4.12** The plot shows the result of the two used tail-subtraction routines together with the original data (20 spectra spatial-averaging is performed to increase SNR) from the InAlN layer. The image shows the band gap region in detail. A 1 eV fit interval before the inflection point was chosen for the power law fit.

the ZLP, when the selection of a good cut-off energy point between ZLP and inelastic signal is crucial to avoid losing valuable information. Again, this cut-off energy was separately determined for each spectrum as an inflection after the ZLP. Fig. 4.13 (a) shows a raw spectrum from an InAlN region and the result of the deconvolution routine. In the panel below, Fig. 4.13 (b), the resulting average of deconvolved spectra from a GaN region is given. The labeled arrows in this panel point to inter-band transition features (A, B and C) found before the plasmon,

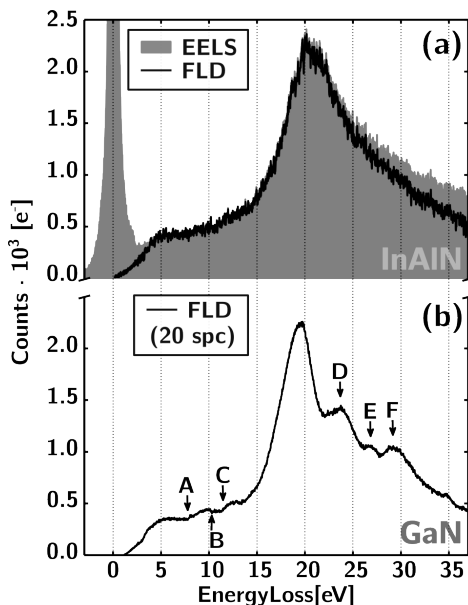


**Fig. 4.13** Panel (a) shows the deconvolution of a single spectrum (no averaging, low SNR) in the InAlN layer; the ZLP is subtracted and information down to the band gap transition signal can be used. Panel (b) shows the result of a 20 spectra average in the GaN layer.

and other single-electron transitions from the Ga 3d band (D, E and F). Below  $\sim 5$  eV errors are liable to appear as the signal can get smoothed. The occurrence of these errors is easy to detect by direct examination of the remaining intensity in this energy-loss region. In our case, inelastic SSDs with useful information below 3 eV were retrieved from the energy-loss spectra.

### 4.3.3 Composition and bowing parameter from Vegard law

Once the spectra were appropriately deconvolved, with an ad-hoc designed routine we could determine the energy position of the plasmon peaks along the given spectrum line (see Fig. 4.11). In this case we used a simple model-based fit. For this purpose, Gaussian and Lorentzian functions were tested; the latter showed better results and were finally chosen. The Lorentzian peak fit, as depicted in Fig. 4.14, determines  $E_{max}$  with great precision. The experimental resolution is given by the ZLP FWHM, which in this case is  $\lesssim 0.2$  eV.

The determined  $E_{max}$  values in the InAlN region, see Fig. 4.15, can be related to the ternary alloy content using a parabolic version of Vegard Law. This is in contrast with the (Al, Ga)N system, in which a linear law suffices. In the (In, Al)N system, the great mismatch between indium and aluminum species leads to a sizable deviation from a linear composition dependence both for the band gap energies<sup>5,26,27</sup>, and for the plasmon energies, as shown in our simulations in Chapter 3. This deviation is typically modeled by a parabolic version of Vegard law.

Notice that it is necessary to determine the bowing parameter for this particular case, which is, in principle, unknown. We did that by imposing the average indium content to  $\sim 18\%$ , as estimated by X-ray diffraction for the studied system<sup>21</sup>. Plasmon energy in  $In_xAl_{1-x}N$  can be related with  $x$ , the In ratio, through

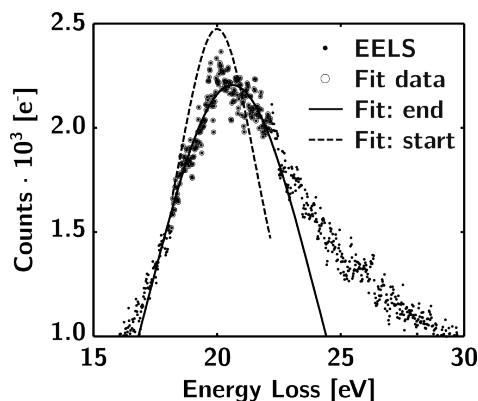


**Fig. 4.14** The Lorentzian peak is optimal for the determination of  $E_{max}$ . The single spectrum shown, from a InAlN layer, has not been treated by any other method than FLD. The fit uses data points within a symmetric interval  $\sim 4$  eV wide around the peak maximum.

a Vegard law with a bowing parameter,  $b$ ,

$$Ep^{InAlN} = xEp^{InN} + (1 - x)Ep^{AlN} + bx(1 - x). \quad (4.3)$$

For the adjustment of the bowing parameter, Vegard law was first applied to each spectrum across the InAlN layer, considering an initially null bowing parameter,  $b = 0$ . From this, the shape of the graded In concentration profile,  $x$ , was found. Then, the calculation of the integral of all the determined indium concentration values was performed, and the average In content could be calculated as a function of bowing parameter. A new value of the bowing parameter was finally chosen to recover the nominal average In content of 18 %, which yielded a bowing parameter  $b = 3.1\text{ eV}$ . The plasmon energies for the binary compounds were taken from the literature<sup>46,47</sup>,  $E_{max}^{GaN} = 19.4\text{ eV}$   $E_{max}^{InN} = 15.7\text{ eV}$  and  $E_{max}^{AlN} = 21.1\text{ eV}$ . The plasmon energy values obtained in the GaN layers were in good agreement with the expected plasmon energy for GaN and with measurements in other works<sup>32,33,48</sup>; however, we could not relate our measure of the bowing parameter to any other work. Our simulations in Chapter 3 suggest that higher order terms might affect the bowing of the  $In_xAl_{1-x}N$  system, for small values of  $x$ .

The resulting indium concentration profile is depicted in Fig. 4.15 (b). Notice that this profile is taken through the  $In_xAl_{1-x}N$  layers, along the growth direction, [0001]. Our aim was to elucidate, using EELS, whether Indium is homogeneously incorporated along the growth direction.

According to Fig. 4.15 (b), the In concentration decreases from 30 % (above the nominal value, 18 %) approximately linearly within the first 10 nm of the

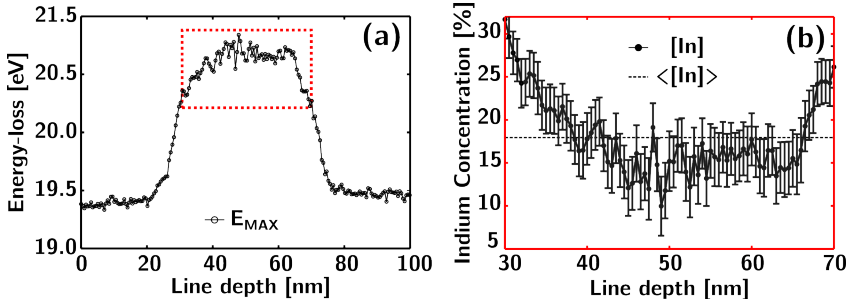


**Fig. 4.15** (a) presents the  $E_{max}$  determined through the whole EELS-SL indicated in Fig. 4.11. A red square highlights the InAlN layer. (b) shows the Indium ratio through the 40 nm wide InAlN layer, as calculated by applying Vegard Law with a bowing parameter fitted to impose the mean  $[In]$  value,  $\sim 0.18$ , which yields  $b \approx 3.1\text{ eV}$ . Error bars are included, they were calculated from the plasmon peak Lorentzian fits.

InAlN semi-period down to near nominal values. Then, it remains nearly constant at a value slightly below the nominal one until the last few nanometers, where a certain increase is found. The existence of two different regions in the InAlN layer, a decreasing-ratio [In] rich region and a poor, and approximately [In] constant region, previously noticed in HAADF, is confirmed through EELS. Energy loss precision given by the ZLP FWHM yields an average  $\pm 3\%$  standard deviation of the calculated [In] values.

Concerning the possibility of an in-plane composition modulation, the contrast in the HAADF images does not seem to suggest it (see, for instance, Fig. 4.10). In addition, further EELS data were analyzed to rule out this possibility. In this sense, high resolution EELS-SLs parallel to the interfaces were acquired and analyzed, showing no traces of in-plane composition modulation.

#### 4.3.4 Optoelectronic and structural properties

##### Kramers-Kronig Analysis

DKA was performed on the EELS-SL data as explained in the Methods section, Sec. 2.1.2. As discussed there, certain calculations in the mathematical routine involve the use of fast Fourier transformations (FFT). For FFT analysis purposes it is convenient that all signals start and end at zero (or almost zero) counts, without sharp peaks. At low energies, below the cut-off value for deconvolution, negative data points and at least the first channel of all SSD data arrays are set to zero. As the plasmon tail was not measured completely on these spectra because of the chosen energy-loss range, the function  $Ar^{-3}$  suggested by the Drude model was used to extrapolate data to zero. Finally the SSD arrays were padded with zeros up to twice their actual length, a procedure which is bound to reduce the noise coming from sampling in Fourier space.

At this point, refraction index (commonly denoted as  $n$ ) values were needed for the normalization loop. The values used for the calculations were taken from experimental data<sup>21</sup>, as were the refraction indices used for normalization of the SSD ( $n_{\text{GaN}} = 2.5$ ,  $n_{\text{In}_{0.18}\text{Al}_{0.82}\text{N}} = 2.3$ ). Different values were tested which did not substantially improve the results, with the exception of using a higher value of  $n$  in the In rich region.

Since the composition of the InAlN layer in the In rich region is not uniform, the local value of  $n$  may vary in this region. Indeed, in the case of the InAlN region, the refraction index values obtained from optical techniques do not seem appropriate for our sub-nm-resolved spectra. Possible solutions, in this particular case, are to check the outcome with results from a better known layer, such as GaN, or, if possible, to normalize the SSD using a different method, such as sample thickness. We finally chose to limit the use of  $n_{\text{In}_{0.18}\text{Al}_{0.82}\text{N}}$  to the InAlN layer regions where the Indium content (plasmon peak position) stays constant,

and all the results concerning InAlN discussed from now on will refer to these data.

Once KKA was correctly performed, the complex dielectric function (CDF,  $\varepsilon = \varepsilon_1 + i\varepsilon_2$ ) was obtained. CDFs were recovered point by point, each one corresponding to an individual spectrum. Fig. 4.16 shows CDFs, averaged from 20 adjacent pixels, derived from KKA of Fourier-log deconvolved spectra. This procedure was considered the best possible one in order to assess features in lower energy losses. The shapes of the functions are in good agreement with the ones expected for a semiconductor material<sup>49</sup>: Before the band gap onset, lowest energy-loss values are characterized by  $\varepsilon_2 = 0$  and  $\varepsilon_1 \approx n^2$ , which is shown in the inset of Fig. 4.16. At a higher energy-loss, the real part,  $\varepsilon_1$ , becomes positive, indicating the collective mode excitation, and the real and imaginary parts present a crossing point just after the plasmon peak energy.

### Band gap onset energy

The band gap signal could be directly observed in the original spectra, shown in Fig. 4.11 (b). The observed direct band gaps remained close to  $\sim 3$  eV through the examined GaN and InAlN layers, as shown in Fig. 4.12, and in the two panels of Fig. 4.13. More precise band gap energy values for selected areas of the examined layers were calculated from the energy-loss function (ELF),  $\text{Im}(-1/\varepsilon)$ .

After averaging in selected regions of the InAlN and GaN layers to improve the

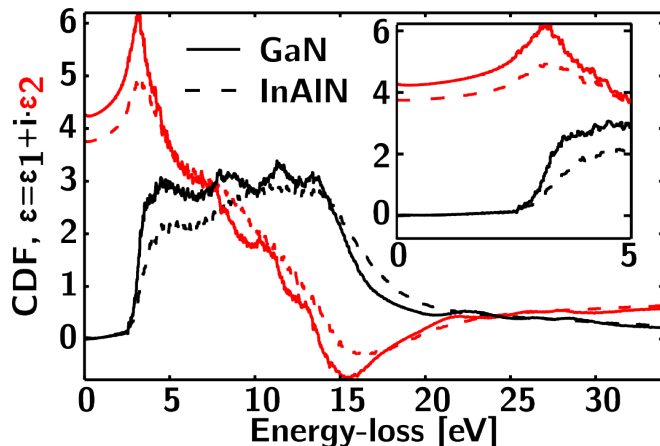


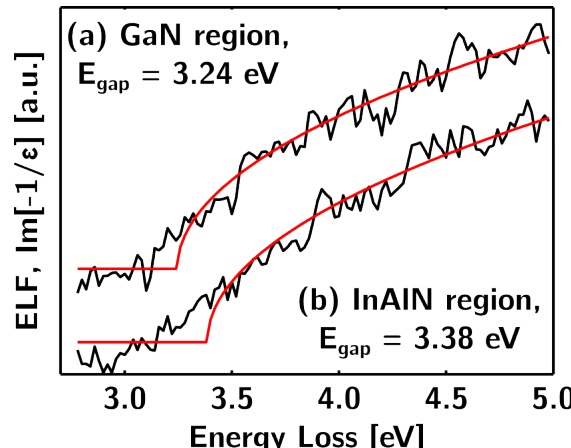
**Fig. 4.16** GaN and InAlN In-poor regions CDFs, the data correspond to 20 averaged CDFs from each of the indicated regions. The inset shows the lower energy-loss region in detail.

SNR and to obtain sufficiently clear functions, a square root model-based fit to the ELF was used to retrieve the band gap onset energy value. The normalized ELF that is recovered from KKA corresponds to the joint density of states (JDOS) of the conduction and valence bands. For a direct band gap transition<sup>50</sup>, a square root function of the shape  $A + (E - E_{gap})^{1/2}$  can be used for fitting the ELF band gap peak. In these fits, depicted in Fig. 4.17, parameter  $A$  is a step used to account for background level.

The result in both cases was found to be almost the same,  $E_{gap} \approx 3.2$  eV for GaN regions, and  $E_{gap} \approx 3.4$  eV for most of InAlN (spectra taken from the [In]  $\sim 15\%$  in the In concentration profile, the almost constant region in Fig. 4.15b), indicating that the lattice matched (LM) InAlN presents a band gap which is close to the one of GaN. Estimated error is  $\pm 0.2$  eV. As far as GaN is concerned, a band gap of 3.4 eV was expected for pure wurtzite GaN layers. However, the previous structural characterization had revealed the presence of zinc blende phase<sup>21</sup>; this cubic phase has a theoretical band gap of 3.2 – 3.3 eV. The two phases appeared to be mixed in the GaN semi-periods, and the electron beam was bound to cross (and excite) both wurtzite and zinc-blende regions. Indeed, the coexistence of these hexagonal and cubic phases could give rise to the lower band gap values determined after the EELS analysis. Nevertheless, the origin of the abnormal values for the band gap of InAlN remains elusive.

The experimental relationship between the [In] and the  $E_{gap}$  of InAlN were reviewed in Ref. 27. This study used spectroscopic ellipsometry on a series of samples grown by MOVPE, covering a wide compositional range, to determine an experimental dependence of InAlN bowing parameter on alloy composition. According to this study, a band gap value of  $E_{gap} \sim 4$  eV is predicted for an In

**Fig. 4.17** Square root fit individual examples from GaN region (top) and InAlN ( $In_{0.15}Al_{0.85}N$  region, bottom). Only the data in the intervals used for these fits has been plotted (from  $\sim 2.8$  to 5 eV). The added step accounts for the departure of the data from a square root shape at the baseline. The values of  $E_{gap}$  are indicated. Plots correspond to a 4 spectra average.



concentration of  $[In] \sim 18\%$ . In our case, since the In concentration is slightly lower in the considered region, we should expect a band gap value even higher than 4 eV, somewhat far from our measurement of 3.4 eV.

On the other hand, our measured value was in agreement with other experimental results, corresponding to different growth techniques, included in Ref. 27 and references therein. Our own DFT calculations for the (In, Al)N system, presented in Chapter 3, predict a band gap value close to 3.4 eV for an indium concentration of 18 %. Indeed, this system presents a strong band gap bowing and other theoretical studies have related it with the presence of In-clustering in the layer (understanding a cluster here as a nitrogen environment with a given indium coordination number)<sup>51</sup>. We could not disregard local In-clustering in the InAlN layer, as there was an excess of In at the first stages of InAlN growth, although no actual evidence was found.

Additionally, our measurements could also be affected by retardation losses, keeping in mind that our measurements were performed at 300 kV. This point will be addressed in Sec. 4.3.5.

### Effective electron number

As a sanity check on the data derived from KKA, a Bethe f-Sum Rule routine was designed; the results are shown in Fig. 4.18. The integrals of the CDF and ELF were performed using all channels of each of these data-sets. As expected, the integral of  $\varepsilon_2(E)$  showed greater or nearly equal values to the ELF integral (point-to-point). Also, from these integrals, the effective number of electrons taking part in the transitions (per unit cell),  $n_{eff}$ , could be derived, which seems to be  $\sim 3$ . The high dispersion of values in the middle region, which corresponds to the InAlN layer, reflects the lack of a good refractive index value for the InAlN region.

### Cole-Cole plots

With the obtained CDF, Cole-Cole plots were prepared to help identify characteristic transitions. The results are shown in Fig. 4.19 for GaN and InAlN, in panels (a) and (b), respectively. The one corresponding to InAlN shows no transition beyond the ribbon shape resulting from the convolved loops of band gap and plasmonic transitions. Conversely, the GaN Cole-Cole plot does show additional features.

According to the energy values reported in literature<sup>33</sup>, we can clearly distinguish a characteristic transition at  $\sim 7.8$  eV corresponding to pure h-GaN as highlighted in both the CDF and Cole-Cole plots in Fig. 4.19c and Fig. 4.19d. Additional transitions are also detected at energies  $\sim 10, 12.2, 23.6, 28.9$  eV, that can be attributed to both the h- and c-GaN phases. Moreover, at high energies

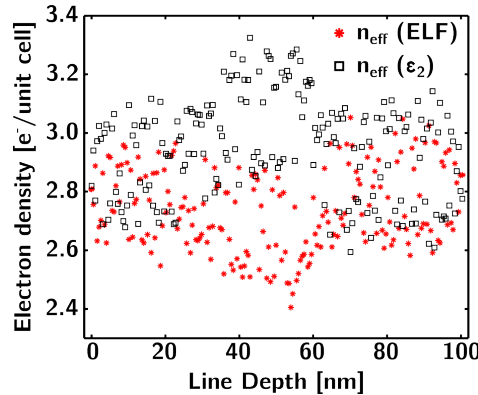


**Fig. 4.18** Effective electron numbers resulting from computing Bethe f-Sum rule, integrating the energy-loss function (ELF, red) or the real part of the CDF ( $\epsilon_2$ , blue) from zero to the highest recorded energy. As expected, ELF-calculated values are higher than CDF ones. They both tend to converge with increasing integration limits.

further small loops hint the presence of three transitions corresponding to energy values above the band gap (one of them at  $\sim 26.7 \text{ eV}$ , characteristic of pure c-GaN).

Looking back at the original low-loss spectra (the CDF depicted in Fig. 4.19c corresponds to the SSD of GaN in Fig. 4.13), we could correlate the intensity maxima (features A to F) with the corresponding transitions in the CDF plot. All of the features in Fig. 4.13, but for A and E, could be related to both c-GaN and h-GaN. Although slightly visible in the plot, the A-peak of pure h-GaN at  $7.8 \text{ eV}$  can be identified. Feature E, clearly discernible by naked eye, corresponds to the characteristic transition of c-GaN at  $\sim 26.7 \text{ eV}$ .

Summing up, our spectra show characteristic transitions from both h-GaN and c-GaN, in very good agreement with the previous HREM characterization. We thus show that energy-loss spectra can be used to detect the mixture of the two polytypes by identifying their distinctive features.

### 4.3.5 Assessing the impact of retardation losses

Retardation effects can significantly alter the shape of the obtained CDF<sup>45,52</sup>, as they can be important, depending on the experimental conditions. Similar conditions to the ones used here had been already considered in the work of Erni and Browning<sup>53</sup>, in which the impact of retardation losses on the single scattering distribution (SSD) was taken into account using the complete Kröger formulation<sup>54</sup>. In this sense, we calculated the difference between the experimentally obtained SSDs and the SSDs from the CDF in the complete Kröger formulation.

The calculation of the SSDs involved several steps. Starting from the CDFs that were obtained from KKA, the full-relativistic scattering was computed for each point of an angular grid representing the collection aperture. In this formulation, the scattering is divided in bulk- and surface-loss terms, both including

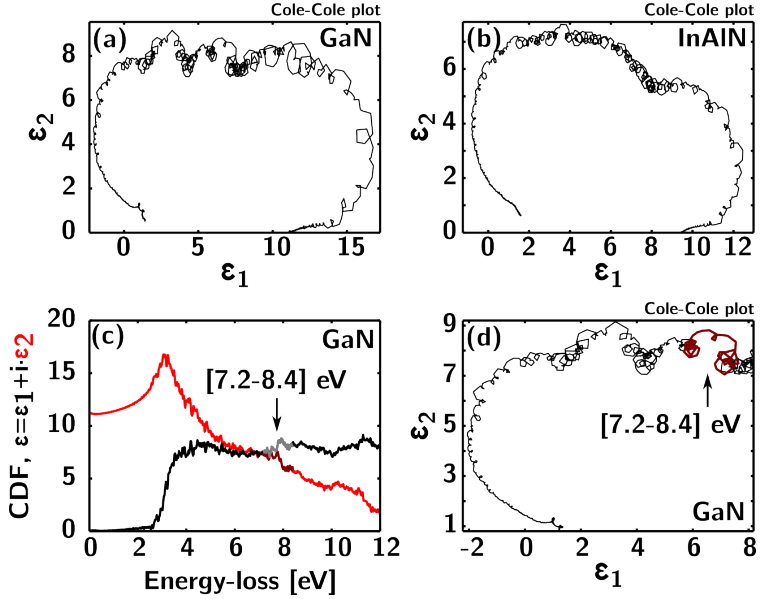


**Fig. 4.19** Panels (a) and (b) are examples of GaN and InAlN Cole-Cole plots from the obtained CDFs. Band gap transition (black, 0 – 6 eV) and plasmon excitation (green or light gray, 6 – 38 eV) regions are colored to allow an easy identification. Subtler transition regions of the CDF can be identified in the panels below. Panels (c) and (d) are detailed images of a CDF and its corresponding Cole-Cole plot, with the highlighted zone indicating an h-GaN transition ( $\sim 7.8$  eV, A in Fig. 4.13). Data corresponds to 20 averaged CDFs from each of the indicated regions.

retardation losses. A rather costly calculation integrates in the angular domain and the resulting data block contains the SSDs, then normalized to allow for a comparison with the, already normalized, experimental SSDs.

The results of this procedure are displayed in Fig. 4.20, showing the predicted analytical shape of the scattering which is not accounted for in a semi-relativistic bulk scattering formulation. These effects are present in most of the spectrum as a background signal, which is the registered signal present before the onset of the band gap. But, although the maximum of the retardation losses is located near the band gap onset, the overall shape of the spectrum is not changed, as a consequence, the fitting of the square root with constant background function will give us a measure of the band gap signal energy onset consistent with our error bars.

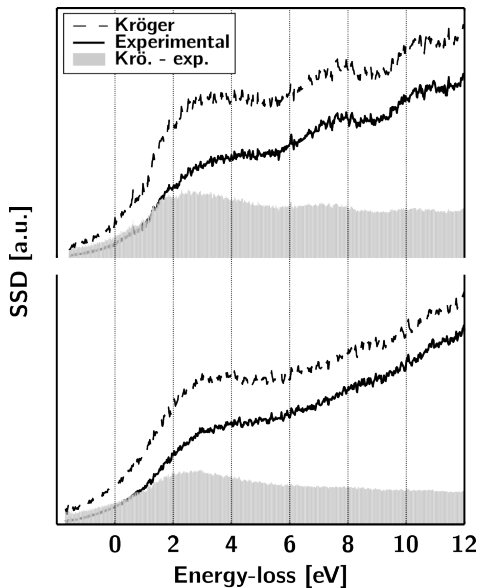


**Fig. 4.20** Expected complete scattering distribution for  $\varepsilon(E)$  deduced by KKA in the GaN and InAlN regions; experimental SSD and the difference between the two is also plotted. Data correspond to a 10 spectra average.

## 4.4 Conclusions

- We proposed quantitative methods for the characterization of materials using the combination of STEM-HAADF and low-loss EELS-SI mapping and we applied them to two group-III nitride DBR systems. Computational analyses were performed using home-made routines for automatic EELS-SI data processing.
- In both samples, plasmon energy shift was related to the composition of the ternary alloys (through Vegard law). This dependence was monitored by model-based fitting of the plasmon peak in the energy-loss spectrum, either using a simple Lorentzian peak shape or the more sophisticated Drude plasmon model.
- In the (AlN / GaN) $\times 20$  DBR, this property revealed the initially unknown composition of a repeating four-layer structure of AlGaN alloys. Furthermore, two dimensional mapping of this property using EELS-SI revealed the composition of anomalous segregations and metallic inclusions in the heterostructure. The linear dependence of plasmon energy with composition in these kind of alloys, predicted in the simulations, was additionally tested: we compared the experimental HAADF intensity profiles and images with HAADF simulations, constructed using atomistic models based

on the plasmon energy characterization.

- The low-loss EELS SIs from the localized anomalous segregation regions were studied through a detailed analysis. Plasmon width and relative thickness were measured, and compared to plasmon energy maps and HAADF images. Aluminum inclusions were found in the system. Plasmon broadening at abrupt interfaces and halo-like contrast surrounding these metallic inclusions were observed, evidencing the relationship between dielectric response and strain state.
- In the (InAlN / GaN)x10 DBR, we proposed a general method to adjust the parabolic composition dependence of the plasmon energy, given that the non-linear term (bowing) is unknown. The InAlN layers presented an In-rich segregation region, located just above the GaN layers. Using our method, we obtained the local composition from these regions, with sizes below 5 nm, and measured the value of the parabolic bowing parameter for this composition. This measurement indicates that bowing in this system is not well known, and may be better described by a higher order law, as hinted in our DFT simulations.
- An exhaustive optoelectronic and structural characterization was also carried out in this sample. CDFs were recovered by KKA, and used to assess the presence of polytypism in the GaN layers. Using the ELF, band gap energy onset values were also determined along the multilayer, finding values of 3.2 and 3.4 eV for the GaN and InAlN layers, respectively, with a  $\pm 0.2$  eV error.
- Finally, we carried out the calculation of the scattering distribution in the framework of a full-relativistic formulation in our band gap measurements. The impact of bulk Čerenkov losses needs to be taken into account because of the high voltage used ( $E_0 = 300$  keV). However, given the small thickness of the examined regions, always below 100 nm, we can estimate that the shape and position of the band gap signal is not affected and can be safely measured.

## Bibliography

- [1] S. Nakamura, S. Pearton, and G. Fasol. *The Blue Laser Diode. The Complete Story*. Springer New York, 1997.
- [2] M. Ikeda and S. Uchida. Blue-violet laser diodes suitable for blu-ray disk. *Physica Status Solidi A: Applications and Materials Science*, 194(2):407–413, 2002.

- [3] D. Brunner, H. Angerer, E. Bustarret, F. Freudenberg, R. Hopler, R. Dimitrov, O. Ambacher, and M. Stutzmann. Optical constants of epitaxial AlGaN films and their temperature dependence. *Journal of Applied Physics*, 82(10):5090–5097, 1997.
- [4] C. M. Wu, B. P. Zhang, J. Z. Shang, L. E. Cai, B. P. Zhang, J. Z. Yu, and Q. M. Wang. High-reflectivity AlN/GaN distributed Bragg reflectors grown on sapphire substrates by MOCVD. *Semiconductor Science and Technology*, 26:055013–055018, 2011.
- [5] I. Vurgaftman, J. R. Meyer, and L. R. Ram-Mohan. Band parameters for III-V compound semiconductors and their alloys. *Journal of Applied Physics*, 89(11):5815–5875, 2001.
- [6] T. Matsuoka. Calculation of unstable mixing region in wurtzite  $\text{In}_{1-x-y}\text{Ga}_x\text{Al}_y\text{N}$ . *Applied Physics Letters*, 71:105–107, 1997.
- [7] J. Kuzmik. InAlN/(In)GaN high electron mobility transistors: some aspects of the quantum well heterostructure proposal. *Semiconductor Science and Technology*, 17:540–544, 2002.
- [8] J. Kuzmik, P. Javorka, A. Alam, M. Marso, M. Heuken, and P. Kordos. Annealing of Schottky contacts deposited on dry etched AlGaN/GaN. *Semiconductor Science and Technology*, 17:L76–L78, 2002.
- [9] A. Vilalta-Clemente, M. A. Poisson, H. Behmenburg, C. Giesen, M. Heuken, and P. Ruterana. The structure of InAlN/GaN heterostructures for high electron mobility transistors. *Physica Status Solidi*, 207:1105–1108, 2010.
- [10] J.-F. Carlin and M. Illegems. High-quality AlInN for high index contrast Bragg mirrors lattice matched to GaN. *Applied Physics Letters*, 83:668–671, 2003.
- [11] J. Dorsaz, J.-F. Carlin, C. M. Zellweger, S. Gradecak, and M. Illegems. InGaN/GaN resonant-cavity LED including an AlInN/GaN Bragg mirror. *Phys. Stat. Sol.*, 201:2675–2678, 2004.
- [12] E. Feltin, R. Butté, J.-F. Carlin, J. Dorsaz, N. Grandjean, and M. Illegems. Lattice-matched distributed Bragg reflectors for nitride-based vertical cavity surface emitting lasers. *Electron. Lett.*, 41:94–95, 2005.
- [13] E. Feltin, G. Christmann, J. Dorsaz, A. Castiglia, J.-F. Carlin, R. Butté, N. Grandjean, S. Christopoulos, G. Baldassarri Höger von Högersthal, A. J. D. Grundy, P. G. Lagoudakis, and J. J. Baumberg. Blue lasing at room temperature in an optically pumped lattice-matched AlInN/GaN VCSEL structure. *Electronic Letters*, 43:924–926, 2007.

- [14] D. S. Katzer, D. F. Storm, S. C. Binari, B. V. Shanabrook, A. Torabi, L. Zhou, and D. J. Smith. Molecular beam epitaxy of InAlN/GaN heterostructures for high electron mobility transistors. *Journal of Vacuum Science and Technology B*, 23:1204–1208, 2005.
- [15] K. Jeganathan, M. Shimizu, H. Okumura, Y. Yano, and N. Akutsu. Lattice-matched InAlN/GaN two-dimensional electron gas with high mobility and sheet carrier density by plasma-assisted molecular beam epitaxy. *Journal of Crystal Growth*, 304:342–345, 2007.
- [16] S. Dasgupta, Nidhi, S. Choi, F. Wu, J. S. Speck, and M. K. Umesh. Growth, structural, and electrical characterizations of n-polar InAlN by plasma-assisted molecular beam epitaxy. *Applied Physics Express*, 4:045502–045505, 2011.
- [17] T. Ive, O. Brandt, X. Kong, A. Trampert, and K. H. Ploog. (Al,In)N layers and (Al,In)N/GaN heterostructures grown by plasma-assisted molecular beam epitaxy on 6H-SiC(0001). *Physical Review B*, 78:035311–035320, 2008.
- [18] S. Fernández-Garrido, Ž. Gačević, and E. Calleja. A comprehensive diagram to grow InAlN alloys by plasma-assisted molecular beam epitaxy. *Applied Physics Letters*, 93:191907–191910, 2008.
- [19] S. Schmult, T. Siegrist, A. M. Sergent, M. J. Manfra, and R. J. Molnar. Optimized growth of lattice-matched  $In_xAl_{1-x}N/GaN$  heterostructures by molecular beam epitaxy. *Applied Physics Letters*, 90:021922–021925, 2007.
- [20] Ž. Gačević, S. Fernández-Garrido, E. Calleja, E. Luna, and A. Trampert. Growth and characterization of lattice-matched InAlN/GaN Bragg reflectors grown by plasma-assisted molecular beam epitaxy. *Physica Status Solidi C: Conferences and Critical Reviews*, 6:S643–S645, 2009.
- [21] Ž. Gačević, S. Fernández-Garrido, D. Hosseini, S. Estradé, F. Peiró, and E. Calleja. InAlN/GaN Bragg reflectors grown by plasma-assisted molecular beam epitaxy. *Journal of Applied Physics*, 108:113117–113124, 2010.
- [22] M. Kariya, S. Nitta, S. Yamaguchi, H. Amano, and I. Akasaki. Structural properties of InN on GaN grown by metalorganic vapor-phase epitaxy. *Japanese Journal of Applied Physics*, 38:L984–L986, 1999.
- [23] Ž. Gačević, A. Eljarrat, F. Peiró, and E. Calleja. Insight into high-reflectivity AlN/GaN Bragg reflectors with spontaneously formed (Al, Ga)N transient layers at the interfaces. *Journal of Applied Physics*, 113:183106–7, 2013.

- [24] R. Erni and N. D. Browning. Valence electron energy-loss spectroscopy in monochromated scanning transmission electron microscopy. *Ultramicroscopy*, 104:176–192, 2005.
- [25] R. Erni and N. D. Browning. Local indium segregation and band gap variations in high efficiency green light emitting InGaN/GaN diodes. *Solid State Communications*, 137:230–234, 2006.
- [26] Z. Dridi, B. Bouhafs, and P. Ruterana. First-principles investigation of lattice constants and bowing parameters in wurtzite  $\text{Al}_x\text{Ga}_{1-x}\text{N}$ ,  $\text{In}_x\text{Ga}_{1-x}\text{N}$ ,  $\text{In}_x\text{Al}_{1-x}\text{N}$ . *Semiconductor science and technology*, 18(9):850, 2003.
- [27] E. Iliopoulos, A. Adikimenakis, C. Giesen, M. Heukens, and A. Georgakilas. Energy bandgap bowing of InAlN alloys studied by spectroscopic ellipsometry. *Applied Physics Letters*, 92:191907–191910, 2007.
- [28] H. Amari, H. Y. Zhang, L. Geelhaar, C. Chèze, M. J. Kappers, and T. Walther. Nanoscale EELS analysis of elemental distribution and band-gap properties in AlGaN epitaxial layers. In *Journal of Physics: Conference Series*, volume 326, page 012039. IOP Publishing, 2011.
- [29] G. S. Huang, T. C. Lu, H. H. Yao, H. C. Kuo, S. C. Wang, C.-W. Lin, and L. Chang. Crack-free GaN/AlN distributed Bragg reflectors incorporated with GaN/AlN superlattices grown by metalorganic chemical vapor deposition. *Applied Physics Letters*, 88(6), 2006. doi: <http://dx.doi.org/10.1063/1.2172007>.
- [30] O. Mitrofanov, S. Schmult, M. J. Manfra, T. Siegrist, N. G. Weimann, A. M. Sergent, and R. J. Molnar. High-reflectivity ultraviolet AlGaN/AlGaN distributed Bragg reflectors. *Applied Physics Letters*, 88(17):171101, 2006. doi: <http://dx.doi.org/10.1063/1.2195547>. URL <http://scitation.aip.org/content/aip/journal/apl/88/17/10.1063/1.2195547>.
- [31] A. D. Dorneich, R. H. French, H. Müllejans, S. Loughin, and M. Rühle. Quantitative analysis of valence electron energy-loss spectra of aluminium nitride. *Journal of Microscopy*, 191(3):286–296, 1998. ISSN 1365-2818. doi: [10.1046/j.1365-2818.1998.00370.x](https://doi.org/10.1046/j.1365-2818.1998.00370.x). URL <http://dx.doi.org/10.1046/j.1365-2818.1998.00370.x>.
- [32] G. Brockt and H. Lakner. Nanoscale EELS analysis of dielectric function and bandgap properties in GaN and related materials. *Micron*, 31(3):435–440, 2000.

- [33] S. Lazar, G. A. Bottom, C. M. Wu, F. D. Tichelaar, and H. W. Zandbergen. Materials science applications of HREELS in near edge structure analysis and low-energy loss spectroscopy. *Ultramicroscopy*, 96(3-4):535–546, 2003.
- [34] J. Arbiol, S. Estradé, J. D. Prades, A. Cirera, F. Furtmayr, C. Stark, A. Laufer, M. Stutzmann, M. Eickhoff, M. H. Gass, A. L. Bleloch, F. Peir'o, and Morante. Triple-twin domains in Mg doped GaN wurtzite nanowires: structural and electronic properties of this zinc-blende-like stacking. *Nanotechnology*, 20(14):145704–145713, 2009.
- [35] M. Benaissa, L. Gu, M. Korytov, T. Huault, P. A. van Aken, J. Brault, and P. Vennegues. Phase separation in GaN/AlGaN quantum dots. *Applied Physics Letters*, 95(14):141901,141904, 2009.
- [36] M. K. Kundmann. Study of semiconductor valence plasmon line shapes via electron energy-loss spectroscopy in the transmission electron microscope. Technical report, Lawrence Berkeley Lab., CA (USA), 1988.
- [37] A. M. Sánchez, R. Beanland, M. H. Gass, A. J. Papworth, P. J. Goodhew, and M. Hopkinson. Mapping quantum dot-in-well structures on the nanoscale using the plasmon peak in electron energy loss spectra. *Physical Review B*, 72:075339, Aug 2005. doi: 10.1103/PhysRevB.72.075339. URL <http://link.aps.org/doi/10.1103/PhysRevB.72.075339>.
- [38] R. F. Egerton. *Electron Energy-Loss Spectroscopy in the Electron Microscope*. Springer US, 3rd edition, 2011.
- [39] J. Palisaitis, C.-L. Hsiao, M. Junaid, J. Birch, L. Hultman, and P. O. Å. Persson. Effect of strain on low-loss electron energy loss spectra of group-III nitrides. *Physical Review B*, 84:245301, Dec 2011. doi: 10.1103/PhysRevB.84.245301. URL <http://link.aps.org/doi/10.1103/PhysRevB.84.245301>.
- [40] J. A. Perez-Omil. *Interpretación sistemática de imágenes de microscopía electrónica de alta resolución de materiales policristalinos. Estudio de catalizadores metálicos soportados*. PhD thesis, Universidad de Cadiz - Spain, 1994.
- [41] S. Bernal, F. J. Botana, J. J. Calvino, C. Lopez-Cartes, J. A. Perez-Omil, and J. M. Rodriguez-Izquierdo. The interpretation of HREM images of supported metal catalysts using image simulation: profile view images. *Ultramicroscopy*, 72(3-4):135–164, 1998.
- [42] E. J. Kirkland. *Advanced computing in electron microscopy*. Springer, 2010.

- [43] K. Iakoubovskii, K. Mitsuishi, Y. Nakayama, and K. Furuya. Mean free path of inelastic electron scattering in elemental solids and oxides using transmission electron microscopy: Atomic number dependent oscillatory behavior. *Physical Review B*, 77:104102(7), 2008.
- [44] T. Walther and H. Stegmann. Preliminary results from the first monochromated and aberration corrected 200-kV field-emission scanning transmission electron microscope. *Microscopy and Microanalysis*, 12:498–505, 2006.
- [45] M. Stöger-Pollach. Optical properties and bandgaps from low loss EELS: Pitfalls and solutions. *Micron*, 39(8):1092–1110, 2008.
- [46] P. Specht, J. C. Ho, X. Xu, R. Armitage, E. R. Weber, E. Erni, and C. Kisielowski. Zincblende and wurtzite phases in InN epilayers and their respective band transitions. *Journal of Crystal Growth*, 288:225–229, 2006.
- [47] J. C. Sánchez-López, L. Contreras, A. Fernández, A. R. González-Elipe, J. M. Martín, and B. Vacher. AlN thin films prepared by ion beam induced chemical vapour deposition. *Thin Solid Films*, 317, 1998.
- [48] S. Estradé. *Electron Energy Loss Spectroscopy Solutions for Nanoscale Materials Science Problems*. PhD thesis, Universitat de Barcelona, 2009.
- [49] R. F. Egerton. Electron energy-loss spectroscopy in the TEM. *Reports on Progress in Physics*, 72:016502–016527, 2009.
- [50] B. Rafferty and L. M. Brown. Direct and indirect transitions in the region of the band gap using electron-energy-loss spectroscopy. *Physical Review B*, 58:10326–10337, 1998.
- [51] I. Gorczyca, T. Suski, N. E. Christensen, and Svane. In-clustering induced anomalous behavior of band gap in InAlN and InGaN. *Physica Status Solidi C: Conferences and Critical Reviews*, 7:1283–1286, 2010.
- [52] P. L. Potapov, H.-J. Engelmann, E. Zschech, and M. Stöger-Pollach. Measuring the dielectric constant of materials from valence EELS. *Micron*, 40 (2):262–268, 2009.
- [53] R. Erni and N. D. Browning. The impact of surface and retardation losses on valence electron energy-loss spectroscopy. *Ultramicroscopy*, 108(2):84–99, 2008.
- [54] E. Kröger. Berechnung der Energieverluste schneller Elektronen in dünnen Schichten mit Retardierung. *Zeitschrift für Physik*, 216(2):115–135, 1968.





## Chapter 5

# Multiple InGaN QW heterostructure

“The ideal color scheme is unrealisable (...) A standard color scheme is not vital, but might be useful.”

---

R.F. Egerton, *Extract from presentation.*

This chapter presents a detailed examination of an  $\text{In}_x\text{Ga}_{1-x}\text{N}$  multilayer structure, composed of alternating In-rich quantum wells (QWs) and In-deficient barriers. The nominal widths of these semiconductor layers are 1.5 nm and 6 nm, for the QW and barrier layers, respectively. This is, thus, a structure with features in the nanometer size range, smaller than the two structures examined in the preceding Chapter. Again, our STEM examination consists in the simultaneous acquisition of HAADF images and spatially resolved low-loss EELS-SI, that are used in combination. However, this time, we also present a detailed analysis of high resolution HAADF images, that provides additional evidence of chemical and structural changes in the layers. Subtle changes in the valence properties of the materials, band gap energy, plasmon excitation and also elemental transitions are monitored by low-loss EELS. Kramers-Kronig analysis (KKA) of the energy-loss spectrum is used to extend the dielectric characterization. In this sense, we apply a method for the experimental characterization of the plasmon excitation in the CDF based on our findings in Chapter 3, consisting in the determination of  $E_{cut}$  in the CDF. Apart from this, we compute spatially localized electron effective mass values from our CDFs, as we expect some contrast in the QW region. Finally, we examine the intensity of the Ga 3d transition in a previously normalized SSD. We show how this can be carried out after KKA, revealing the gallium concentration distribution with an excellent spatial resolution.

## 5.1 Introduction

Devices based on a stacking of III-V semiconductor layers have led to a revolution in the optoelectronic research and industrial fields because of their ability to operate in a wide range of applications. Among these applications, high brightness light emitting diode (LED) devices based on multiple  $\text{In}_x\text{Ga}_{1-x}\text{N}$  quantum well (QW) active layers are important because of their high quantum efficiency<sup>1,2</sup>. There is a strong need to control the QW thickness down to the monolayer level while keeping a high indium composition, in order to achieve optimum operating properties.

The reduction of the QW size, down to nanometer range, is difficult to control because of the strain accumulation at the InGaN / GaN interfaces. It is also problematic to achieve a high indium content, given the tendency of  $\text{In}_x\text{Ga}_{1-x}\text{N}$  compounds to phase separation. For instance, indium mobility is an issue, as introduced in Chapter 4; other authors have reported coalescence during growth in similar systems<sup>3-9</sup>. In some of these works, the formation of segregated In-rich nanoclusters, with an In content of above 80 %, has been reported<sup>4-7</sup>. In other cases, a certain inhomogeneity inside the InGaN QW, and width variations have been observed<sup>8,9</sup>. Both variations in the local In composition and the QW width have been related to a carrier localization effect in the InGaN QW regions<sup>10</sup>. In these devices, carrier localization improves recombination rates, notwithstanding the typically high threading dislocation densities, which, in turn, act as light-quenching centers. Consequently, this effect could be responsible for the high emission rates obtained in  $\text{In}_x\text{Ga}_{1-x}\text{N}$  heterostructure-based laser devices<sup>11</sup>.

### 5.1.1 Structure growth and previous experiments

The multiple QW heterostructure under study was grown by the group of E. Calleja at the *Instituto de Sistemas Optoelectrónicos y Microtecnología* (ISOM). A RIBER Compact 21 molecular beam epitaxy (MBE) system was used, equipped with a radio-frequency plasma nitrogen source and standard Knudsen cells for Ga and In. The growth was carried out on commercial  $\sim 3.3 \mu\text{m}$  GaN-on-sapphire (0001) templates (Lumilog), grown by metal organic chemical vapor deposition. Prior to  $\text{In}_x\text{Ga}_{1-x}\text{N}$  quantum wells (QWs), a  $\sim 20 \text{ nm}$  thick  $\text{In}_{0.05}\text{Ga}_{0.95}\text{N}$  spacer was grown. Afterwards, six 1.5 nm thick InGaN QWs with nominal In content of 20 % were grown. The InGaN QWs are separated by 6 nm thick InGaN quantum barriers and covered with a 20 nm thick InGaN capping layer, both layers with a nominal 5 % In content. The entire growth was performed in intermediate metal-rich conditions and without interruptions, to facilitate good crystal quality and formation of flat and abrupt interfaces (for growth details see Ref. 12).

To get a preliminary insight into the layer structural properties, X-ray diffraction (XRD) was performed. The samples were probed with Cu-K $\alpha_1$  line ( $\lambda_X =$

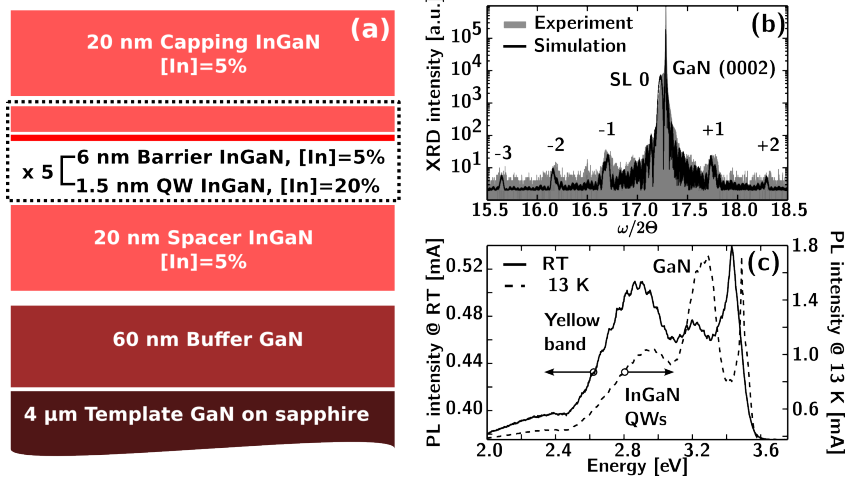


**Fig. 5.1** (a) Schematic depiction of the examined structure design. The active layer containing the QW and barrier structure is indicated by a dotted box. (b) XRD line-scan and simulated intensity, in gray filled area and solid line, respectively. The simulation confirms the growth of a superlattice structure. (c) PL spectra acquired at room temperature (RT) and at 13 K; in solid and dashed lines, respectively. The peaks are identified with the band gaps from the GaN substrate and the InGaN QW structure.

1.5406 Å), in a commercial Panalytical X’Pert Pro system, equipped with a Ge(220) hybrid monochromator.  $\omega/2\Theta$  XRD scans were acquired around the (0002) GaN Bragg reflection, see Fig. 5.1(b). The XRD spectrum reveals satellite peaks, resolved up to the third order. The satellite peak separation confirms a structure with a high periodicity, being the period thickness found at 7.5 nm, in excellent agreement with the nominal QW (1.5 nm) and barrier (6 nm) values.

Optical properties were assessed by photoluminescence (PL) measurements, exciting with a HeCd laser ( $\lambda = 325$  nm) with a power density of  $\sim 1 \text{ Wcm}^2$  at  $\sim 10 \text{ K}$  and room temperature (RT). These PL measurements, in Fig. 5.1(c), performed at 10 K, reveal three intense emission peaks, attributed to the underlying GaN, InGaN spacer/capping and InGaN QWs, respectively (from high to low energy). Temperature increase leads to a certain emission red shift and intensity drop, as expected. The relative intensity of InGaN QW emission is, nevertheless, higher at room temperature than at low temperature; this is attributed to enhanced photo-excited carriers mobility, which consequently reach the InGaN QWs (that is the lowest energy emission band) more easily. The energies of the InGaN QWs and the InGaN spacer/capping are found to be in good agreement with their nominal 20 and 5 % In contents, respectively.

After this characterization, thin lamella specimens were prepared for TEM observation by mechanical polishing, low angle Ar-ion milling (see Appendix A). The extremely small size of the structural features in this sample demands the use of the most advanced electron microscopy instruments for its characterization. Because of this, all the work in this sample was performed using the aberration corrected and monochromated FEI Titan STEM instrument, operated at 300 kV.

## 5.2 High resolution HAADF image analysis

Owing to the use of the Cs-corrector, the resolution of the HAADF images obtained allows to measure the lattice parameters of the crystalline layers. Z-contrast in these images means that the inclusion of the relatively large indium atoms will produce a more intense scattering at high angles, revealing the position of the InGaN QW layers. This information is used to assess the crystalline quality of the sample and to locate the position of the barrier and QW layers. Figure 5.2 shows an example of a high-resolution HAADF image; it corresponds to an InGaN QW. The width of the QW in this image is near the nominal value of 1.5 nm, with parallel and abrupt interfaces.

Figure 5.3 shows another high-resolution HAADF image, this time at a lower magnification, including several periods of the multilayer structure. In this image, we can still resolve the crystalline atomic columns and assess the location of the InGaN QW layers, identified by their brighter contrast. This allows to measure the width of the periods in the repeating QW and barrier multilayer structure, which is in excellent agreement with the nominal 7.5 nm. We can also assess the

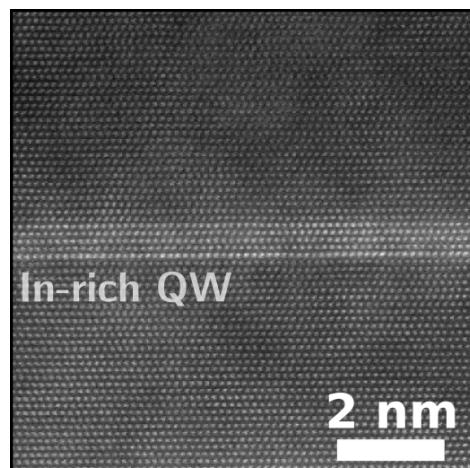


**Fig. 5.2** A high resolution HAADF image portraying an InGaN QW (bright contrast in the central region) and two barrier layers (dark contrast regions, above and below).

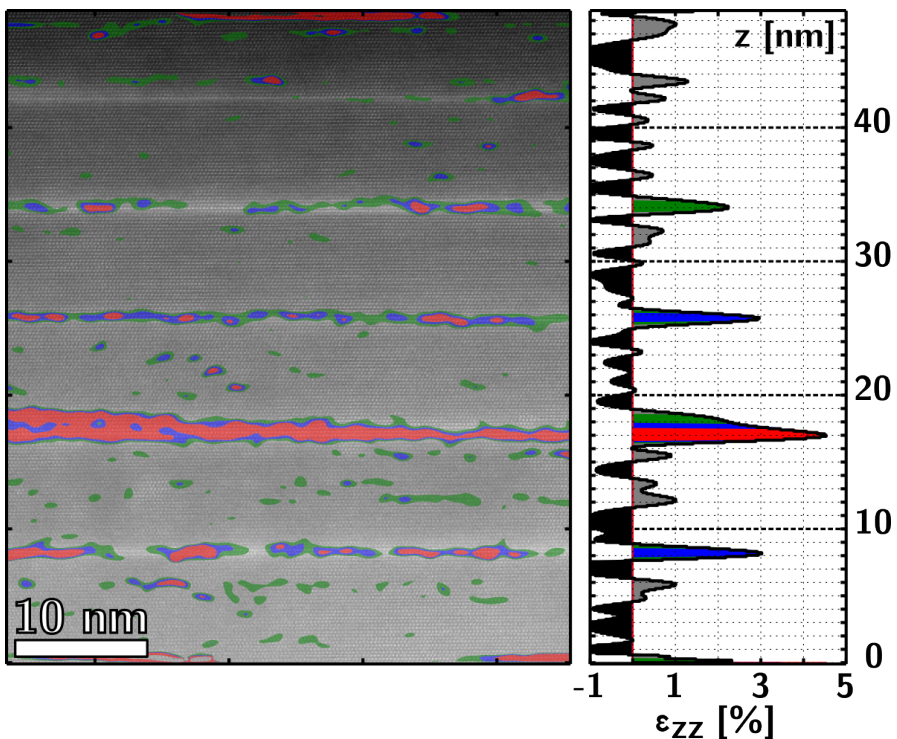


**Fig. 5.3** On the left hand side, a high resolution HAADF image with color filled contours showing the  $\epsilon_{zz}$  strain matrix element resulting from the GPA calculation. The average values of  $\epsilon_{zz}$  (along the horizontal direction) can be examined in the plot on the right-hand side.

inhomogeneity of the QW layers, with bulgings extending a few nanometers in some regions. The formation of these wider inhomogeneities is always detected in the upper QW interface, which is typically rougher than the lower one, in good agreement with previous observations of similar systems<sup>13–15</sup>.

In these images, the bright Z-contrast is indicative of the substitution of lighter gallium atoms for heavier indium ones. As the layers grow epitaxially, keeping the wurtzite structure, we expect a certain level of strain to be present<sup>8</sup>. In order to explore the strain distribution from HAADF images, we used geometrical phase analysis (GPA) software<sup>16</sup>. GPA calculates the relative spatial deformation maps from an image of a crystalline lattice using Fourier transforms. For this purpose, it is necessary to define a reference region in the image. The result of GPA is a map showing the spatial dependence of the elements of the strain matrix,  $\epsilon$ , that

measure the lattice deformation relative to the reference region.

In the GPA calculation, the lower region from the HAADF image, the InGaN spacer layer with a nominal In composition of 5 % (see Fig. 5.1a), which in principle should be more stable than the adjacent multilayer structure, was selected as a reference region. Results from GPA show no appreciable strain in any direction other than in the out-of-plane direction. This direction corresponds to the  $c$  lattice parameter in the wurtzite structure, which we are going to call  $z$  direction; thus, the lattice strain is expressed in the  $\epsilon_{zz}$  matrix term. This term is shown in Fig. 5.3 using green, blue and red filled contours for increasing values of strain. Additionally, the right-side graph in Fig. 5.3 shows the average strain along the vertical direction for the whole image. By looking at this graph (and the contours), we observe that the gradients of this  $\epsilon_{zz}$  term are located in the InGaN QW layers.

The inclusion of more indium atoms has been related to an increase of the out-of-plane lattice deformation ( $\epsilon_{zz} > 0$ ), in other studies of InGaN multilayer structures<sup>8,11,14,17,18</sup>. For this and other types of III-V semiconductor alloys, it is natural to associate this effect to Vegard Law. In this framework, a linear relationship is formulated between the measured lattice parameter of the alloy and the lattice parameter of the pure components, as a function of composition. If bi-axial strain is also taken into account in wurtzite  $\text{In}_x\text{Ga}_{1-x}\text{N}$ <sup>17</sup>, a cubic equation allows to extract  $x$  from experimentally determined  $a$  and  $c$  lattice parameters. Using this equation, we first calculated  $x$  for our measured lattice parameter in the spacer layer,  $(a, c) = (0.522, 0.319)$  nm. We obtained a concentration of  $x = 0.05$ , in excellent agreement with the nominal value. Considering this result, we continued using this equation to assess indium concentration through the strain map in Fig. 5.3. Consequently, the detected strain values above 2.5 % correspond to an indium content above the nominal indium composition of 20 % in the  $\text{In}_x\text{Ga}_{1-x}\text{N}$  QW layers. Lattice deformations of around 5 % correspond to an indium content of  $\sim 35$  %. Such large lattice deformations are consistently detected in our HAADF images, in the regions showing a wider bulging of the QW. Conversely, more moderate strain values (below 2 %) are detected for the QW layers of width closer to the nominal 1.5 nm.

Other authors have reported deformations above 10 %, indicating indium content  $\sim 80$  %, for similar systems in which In-clustering had been observed<sup>4–7</sup>. Our results, and the homogeneous Z-contrast of the HAADF images indicate that, if present, a more moderate degree of indium diffusion is occurring in this particular system. Anyway, when preparing this work we were aware of the reports stating that In-cluster formation may be induced by the high irradiation damage in typical high-energy HRTEM experiments<sup>8,11</sup>. In these cases, InGaN samples containing similar QW heterostructures present an indium segregation and separation of phases that is detectable by examination of time series images.

However, recent works have postulated that a comparatively small irradiation damage is suffered by InGaN in a typical HR-STEM observation<sup>18</sup>. Moreover, this adds to the fact that no particular In-cluster formation was detected during our STEM acquisition, for example through salt-and-pepper or dot-like contrasts, which we surveyed by acquiring images of the same regions through the whole experimental process. Because of this, we relate the detected  $\epsilon_{zz}$  gradients to the natural lattice deformation induced during the growth process.

### 5.3 Band gap and plasmon analysis

The low-loss EELS-SI were treated using computational tools developed in collaboration with the Hyperspy Python project<sup>19</sup>, available open-source to the public. To improve the spectral signal-to-noise ratio (SNR), we used a spatial filtering approach (see Fig. 5.4). First, cross-correlation of the ZLP was used to calibrate the energy axis. After that, averaging and deconvolution methods were used in order to subtract the tails of the ZLP and to effectively improve SNR. To perform the averaging, we applied a square uniform spatial filter (3x3 pixel size). At the same time, we used Richardson-Lucy deconvolution (RLD), a Bayesian algorithm that uses a ZLP model to increase spectral resolution<sup>20</sup>. Using this method, we obtain an improvement in spectral resolution from  $\sim 0.3$  eV to  $\sim 0.16$  eV, measured by the FWHM of the ZLP. Additionally, RLD also reduced the tail of the ZLP, that masks low-energy features like the band gap onset. Finally, ZLP and plural scattering were suppressed by Fourier-log deconvolution (FLD)<sup>21</sup>.

This data processing improves SNR at the expense of spatial resolution of the datasets, originally below the nm. Here, we have taken into account that we are examining electronic properties with a certain delocalization length, *e.g.* in the order of 1 nm for the plasmon. By repeating all the following calculations with unfiltered datasets, we made sure that no important information was lost

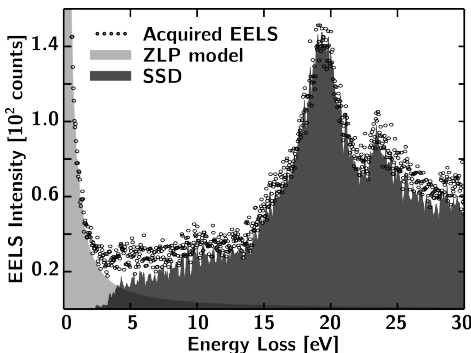


**Fig. 5.4** An example energy-loss spectrum of  $\text{In}_x\text{Ga}_{1-x}\text{N}$ . This panel shows the effect of our data treatment as it depicts the ZLP model (light gray) subtracted by deconvolution from the original spectrum (circles) to obtain the SSD (dark gray). The features analyzed in this work are: the band gap, which is expected at  $\sim 3$  eV; the plasmon, the most intense peak at  $\sim 19$  eV; and the Ga 3d transition, at  $\sim 22.5$  eV.

when increasing SNR and removing artifacts from the spectra in this manner. After the processing, we obtained a pixel-by-pixel map of the single scattering distribution (SSD).

The low-loss EELS from In-poor  $\text{In}_x\text{Ga}_{1-x}\text{N}$  features a number of interband transitions in the vicinity of the plasmon peak<sup>8,22–24</sup>, prominently from the Ga 3d band (see Fig. 5.4). Additional effects exist; for instance, a plasmon shift in response to deformation in strained structures has been reported<sup>25</sup>; or a plasmon broadening in response to strain and the presence of interfaces and defects, as seen in Chapter 4. These changes indicate an enhancement of the de-excitation processes through structural and chemical inhomogeneities which has yet to be fully understood.

### 5.3.1 Low-loss EELS in nanometer-sized structures

For band gap and also for plasmon energies, a size dependent shift is expected in very small structures, such as these QWs. As the size of the QW shrinks it is customary to consider a quantum confinement model to assess the band structure related properties. One of such models is presented in Ref. 26, for a free particle with effective mass,  $m^*$ , confined in one direction by impenetrable barriers with a separation,  $L$ . In this simple case, the increase in ground state energy for the particle,  $\Delta E$ , is,

$$\Delta E = \frac{1}{2m^*} \left( \frac{\hbar\pi}{L} \right)^2 \quad (5.1)$$

Finally, delocalization of inelastic scattering, see Sec. 1.2.5, at these energy ranges is important and can be the leading cause for plasmon broadening in the vicinity of some interfaces. The electron probe in a STEM-EELS experiment can be as small as a few Å, and one may expect low-loss spectra to be originated from interactions with an atomic-sized volume of the sample material. However, it is generally accepted that this realization is far from reality due to the finite range of electron interaction and the extended nature of these excitations<sup>27</sup>. Because the threshold energy for the transitions in valence EELS is low, the characteristic Coulomb delocalization is high. Importantly, for band gap and other low-lying features, but also for the plasmon excitation, the effective characteristic length may become several times above the probe size<sup>28</sup>.

### 5.3.2 Band gap energy

Using the data treatment mentioned above, the SSD are retrieved after deconvolution of the ZLP from the original spectra, as is depicted in detail in Fig. 5.5(a), and the features at low energy losses are revealed. We assume that the band gap

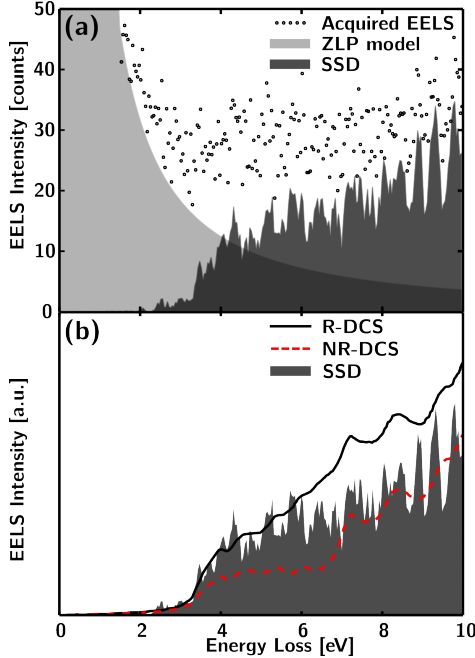


**Fig. 5.5** (a) Detail from the 0 – 10 eV energy-loss region depicted as in Fig. 5.4. (b) The same SSD is compared with the results from a full-relativistic calculation, performed with optical data<sup>29</sup>. These results are the relativistic differential cross section (DCS), black solid line, and the non-relativistic DCS, red dashed line.

signal is the first signal in the low-loss spectrum, detected at the lowest energy (here  $\sim 3$  eV). The validity of this assumption was assessed by the simulation of the EELoS intensity using a full-relativistic inelastic scattering calculation for an 80 nm GaN thin TEM lamella (the measured relative thickness,  $t/\lambda$ , is below 0.9 for the examined regions). This calculation was carried out as explained in Sec. 4.3.5, with the difference that this time optical data was used as an input for the calculation. Results are shown in Fig. 5.5(b).

We first notice that the experimental and simulated intensities near the signal onset are in good agreement up to  $\sim 6$  eV (see Fig. 5.5(b), black solid line). Above that energy both intensities diverge a little, as the simulation predicts an increase of the relativistic contribution. The origin of this divergence is in the relativistic surface-loss term of the calculation, rather than in the bulk radiative-loss. Hence, the departure can be related either with a failure to estimate the surface effects, or, rather, a failure in the optical data (from Ref. 29) to predict high-energy dielectric behavior. Nevertheless, the result confirms that the characteristic square root shape for the direct band gap transition is the dominant contribution to the spectral intensity below 10 eV. Moreover, we are now convinced that, for our experimental thickness and beam energy, the contributions from surface and radiative losses are not intense enough as to mask the other

low-energy features.

The three panels in Fig. 5.6(b) depict two QW periods, both with suspected In-diffusion regions. The InGaN QW layers are apparent in the HAADF image, thanks to Z-contrast. This image confirms that acquisition did not suffer much from spatial drift. Spatially resolved band gap onset energy values were obtained from a series of EELS-SI, looking at the low energy onset (between 1 and 10 eV). The first procedure to determine band gap energy is based on inflection point detection using a normalized and smoothed derivative of the spectrum, obtained from a Savitzky-Golay filter. This procedure results in energy values around  $3.1 \pm 0.1$  eV, as depicted in the histogram in Fig. 5.6(a). The band gap onset energy for  $\text{In}_x\text{Ga}_{1-x}\text{N}$ , on a first approximation, is linearly related to the band gap energy of the pure compounds. The generally accepted values for these energies are 3.44 eV and 0.77 eV<sup>30,31</sup>, for pure bulk GaN and InN, respectively. Following Vegard law, our average band gap energy value corresponds to an indium concentration,  $x$ , of around 12.7 %. Remarkably, these band gap energy / concentration values are between, and close to the mean of the nominal values for the barrier and QW layers, of 3.3 eV / 5 % and 2.9 eV / 20 %, respectively.

In the pure compounds, both band gaps are direct transitions<sup>22,23,26,32</sup>. In EELS, the energy dependence of the signal in direct transitions goes as  $\text{SSD} \propto \sqrt{E - E_g}$  near the signal onset. As a second procedure, a fit based on a model

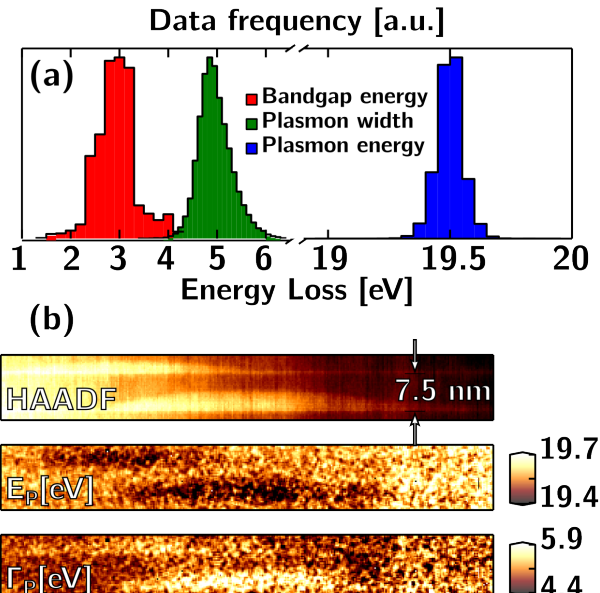


**Fig. 5.6** (a) An histogram showing the dispersion of the band gap energy (bin size 0.2 eV),  $\Gamma_P$  and  $E_P$  (bin size 0.1 eV); in red, green and blue color filled areas, respectively. The band gap energy was measured using the inflection method, as explained in the text. (b) From top to bottom, HAADF image and maps for  $E_P$  and  $\Gamma_P$ , from the same region. The spatial resolution is  $\sim 0.3$  nm.

containing this square root function confirmed this type of band gap in our spectra. This fitting procedure could be carried out throughout the whole EELS-SI, giving an equivalent result to that obtained above for the onset energy. However, the inflection-point procedure proved to be more reliable, giving a much smaller dispersion of values.

No spatial correlation with the QW position was found, neither with the inflection point procedure nor using the model-based fit. We have to consider that spatial delocalization for this interaction is larger than the dimensions of the multilayer structure constituents<sup>22,33</sup>. Hence, these extremely thin InGaN QW layers are effectively rendered invisible to the direct detection of their band gap properties using a fast electron beam. Given the beam spreading and delocalization lengths for the band gap signal it is reasonable to think that the electron beam interacts with both barrier and QW layers as a whole<sup>34</sup>. Arguably, the band gap energy that has been observed is related to an average band gap signal of the layered system. This is in contrast with the results obtained by similar studies<sup>8</sup>, in which In-clusters of around 3 nm in size presented a sizable band gap onset energy redshift to around 2.65 eV. This result could be related to a bigger size and higher indium concentration of the In-clusters in the samples analyzed in that work.

Finally, taking into account the reduced size of the InGaN QW layers, we have to consider that quantum confinement effects could be taking place. Because of that, an increase of the band gap energy, of  $\lesssim 1$  eV for a 1.5 nm wide QW (see Eq. 5.1), could be expected in these layers, which is not detected. Following the discussion in the last paragraph, trying to assess the impact of this effect by monitoring the band gap alone seems hopeless given the large delocalization of this signal.

### 5.3.3 Plasmon analysis

Our interest now is in the plasmon peak and the interband transitions, appearing in EELS at higher energies than the band gap. After a Drude model-based fit procedure (see Eq. (3.1)) is applied pixel-by-pixel to our EELS-SI, plasmon energy ( $E_P$ ) and width ( $\Gamma_P$ ) values are measured. Figure 5.6(b) presents these results as histograms and as maps, compared with the simultaneously acquired map of the HAADF intensity. From the examination of the histograms, in panel (a), it becomes apparent that the dispersion of the plasmon energy and width values is smaller than for the inflection energy values resulting from the study of the band gap region. From the maps, we see that the spatial distribution of the plasmon energy and width shows some contrast in the QW region.

Across the whole region, plasmon energy measurements yield quite constant values. Only a slight variation of 0.2 eV is found, between the wider QW regions

and the barrier layers, at about 19.4 eV and 19.6 eV, respectively. Additionally, a localized broadening of the plasmon peak in the InGaN QW layers is detected.  $\Gamma_P$  shows a strong variation between QW and barrier regions of around 1 eV.

Parts of the InGaN QW structures are almost invisible by looking at the plasmon energy distribution. As for the band gap, delocalization of the plasmon interaction is an important factor that needs to be addressed. In this sense, we have to take into account that the delocalization length for the plasmon interaction is  $\sim 1$  nm. The nominal size of the QW structure, 1.5 nm, is in the order of this length. On the contrary, localized QW regions with larger sizes, well above 3 nm at their most prominent bulgings, are detected. A consistent plasmon energy and width contrast is apparent for these regions, and it is reasonable to conclude that the measures correspond to characteristic properties of these layers.

The determination of the indium concentration in the multilayer structure from these plasmon measurements is a controversial matter. For instance, following a linear Vegard Law, considering that for the pure compounds,  $E_P^{GaN} = 19.7$  eV and  $E_P^{InN} = 15.7$  eV, the obtained  $E_P^{In_x Ga_{1-x} N}$  in the barrier layers would be of  $x \simeq 2.5\%$ , an indium content of half the nominal value. This result would indicate that the barriers have been partially depleted from indium, contributing to the formation of the wider QW regions with an indium content above the nominal 20 %. However, the  $In_x Ga_{1-x} N$  system has been reported to follow a parabolic version of Vegard's Law with a negative bowing parameter, as in Ref. 31 for the band gap ( $b = -1.43$  eV). In this sense, a bowing parameter of around  $-2.1$  eV would suffice to get the nominal In composition of 5 % in the barrier layers. Notice that even higher bowing parameters have been recently reported for the system, e.g.  $b = -2.55$  eV in Ref. 9. This last result would indicate that In content in the barrier layers is higher than the nominal value and that diffusion from the QW layers has increased the In content. This relative divergence in the  $In_x Ga_{1-x} N$  bowing can be related to a non-parabolic composition dependence, as indicated by our simulations in Chapter 3.

The measured plasmon energy for the InGaN QW layers, around 19.4 eV, deserves a final comment, as it is far too large for  $In_{0.2} Ga_{0.8} N$ . In a hypothetic system of broader layers with the same nominal composition, a larger negative gradient of the plasmon energy in the In-rich regions, of several eV, would be expected<sup>9</sup>. Again, one has to consider the impact of nanometer size effects, increasing the ground energy by an amount, termed confinement energy, proportional to the inverse square of the barrier separation (see Eq. (5.1)). As a consequence, both the band gap and the plasmon energies may experience an increase, of  $\Delta E \lesssim 1$  eV for barriers separated by  $L \lesssim 1.5$  nm.

With the available information, it is difficult to determine which effect is responsible for the broadening of the plasmon peak. So far we have showed that the plasmon broadening is sizable in the thin InGaN QW regions, whereas the plas-

mon energy shift is undetectable at these regions. Other works showed plasmon broadening independent of the energy shift in similar systems with strained layers<sup>35</sup>. It thus seems that these two facts support the evidence of a strain driven broadening at a scale similar to the plasmon delocalization length, through interband transition de-excitation processes. Nevertheless, QC effect has also been related to a significant broadening of the plasmon<sup>36,37</sup>, as well as the already considered delocalization and strain effects.

## 5.4 KKA and electronic properties

Kramers-Kronig analysis (KKA) was carried out on the SSD spectrum images, in order to further explore the electronic properties of the InGaN structure. Before using the KKA algorithm, a standard pretreatment procedure was used to taper the SSD intensity at high and low energies, as explained in Sec. 2.1.2. This procedure is important for the numerical stability of the KKA algorithm, that uses fast Fourier transforms (FFT). These are prone to errors when the spectral intensity at the energy extrema does not decay smoothly down to zero. Care was taken to suppress only the intensity at low energies (below the band gap) proceeding from the remaining signal after ZLP tail subtraction, which is mostly noise without any specific physical meaning. This is dealt with using a Hanning taper to filter the data in this region along the energy dimension. The intensity at high energy comes from the plasmon tail and the limited energy range used to acquire it. We use a power law fit to smoothly extend this decaying tail up to the next power of two, another important factor in the success of the KKA algorithm.

Once the SSD spectrum image was treated, the standard KKA algorithm was used to calculate the complex dielectric function (CDF), as explained in Sec. 2.1.2 also. This calculation relays on prior knowledge of the refraction index,  $n$ , of the material under observation. A precise knowledge of  $n$  in a nanostructure such as this one is unlikely, except for notable exceptions<sup>38,39</sup>. For our relatively In-poor InGaN multilayer structure we lacked this knowledge, but we assumed we could approximate the CDF by using the known refractive index of pure GaN,  $n_{GaN} = 2.4^{22}$ . This assumption is supported by the fact that EELS measurements in these regions show only quite subtle variations from those obtained in the barrier regions. In doing this we assume that In-rich QW layers do not depart strongly in their optoelectronic properties from the rest of the barrier layers. A complex dielectric function (CDF),  $\varepsilon(E)$ , is obtained from each energy-loss spectrum in the EELS-SI. Additionally, an estimation of the absolute thickness,  $t$ , of the sampled region is obtained, yielding  $\sim 80$  nm, in good agreement with the estimation from  $t/\lambda$ . A  $t$  map was also obtained, which is presented later in this section. Before this, we describe the results obtained from the examination of (a) plasmon

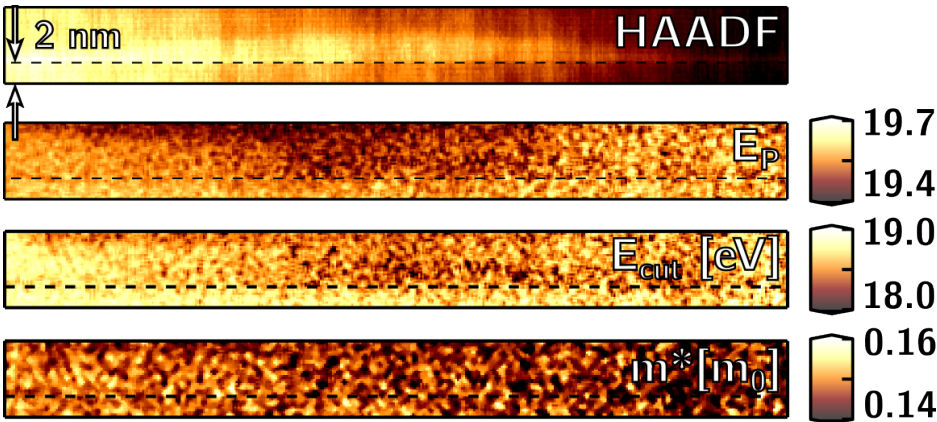


**Fig. 5.7** From top to bottom, HAADF image,  $E_P$ ,  $E_{cut}$  and  $m^*$  maps, from an InGaN QW layer. Notice that the growth direction is from bottom to top, and a dashed line is included in all images to indicate the start of the QW deposition. All images are the result of the same STEM-EELS acquisition, for which the spatial resolution was  $\lesssim 0.2$  nm.

excitation properties,  $E_P$  in low-loss EELS and  $E_{cut}$  in the CDF, and (b) the calculation of the electron effective mass from the CDF.

Results were obtained from an acquisition with greater spatial resolution, as presented in Fig. 5.7. A small bulging, of about  $\sim 3$  nm at its widest part, is visible in the HAADF image. The contrast from this InGaN QW region is also apparent in the  $E_P$  map. The contrast in this map is faint, yet an additional region of lower  $E_P$  values appears at the top of the image. Because of its position, we know that this region is not part of the next multilayer period, but rather some inhomogeneity in a localized spot inside the adjacent barrier. In the  $\Gamma_P$  map, in Fig. 5.8, a broadening of the plasmon is observed, localized around the same regions. Moreover, the contrast in this map extends along most of the QW, even through thinner parts (see dashed line).

#### 5.4.1 Zero-cut energy

After the KKA of this spectrum image was performed, we explored the calculation of spatially resolved properties. For instance, the zero-cut energy of the CDF,  $E_{cut}$ , was determined through a linear fit of the real part of the CDF in the 17 – 20 eV energy region, as depicted in Fig. 5.7. This figure shows a map of  $E_{cut}$  together with a map of  $E_P$ , for comparison. The  $E_P$  map was obtained through the model based fit procedure explained above. These plasmon energy

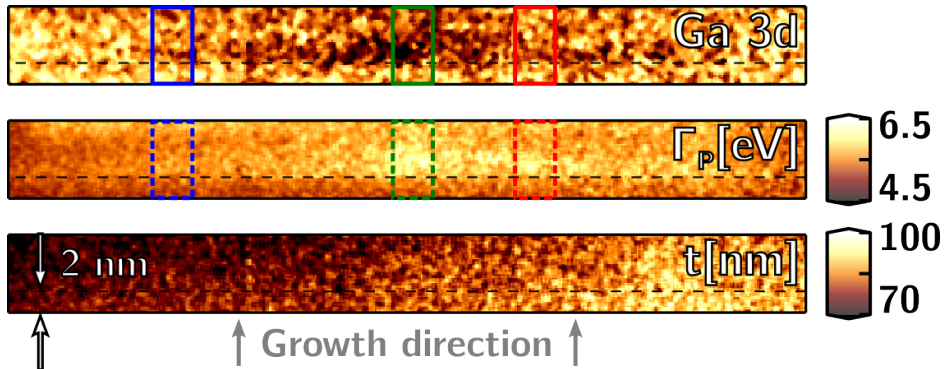


**Fig. 5.8** From top to bottom, the Ga 3d intensity,  $\Gamma_P$  and  $t$  maps from the same region as in Fig. 5.7. Ga 3d is an integral mapping, subject to normalization; hence, in this case no intensity bar is given. Additionally, three color squares over the Ga 3d and  $\Gamma_P$  maps are used to indicate the regions from which the averages in Fig. 5.9 were taken.

maps show a contrast along the QW and in the indium diffusion region above it. Additionally,  $E_{cut}$  seems to have an amplified contrast of  $\sim 1$  eV, greater than the  $\sim 0.3$  eV one that we can see in the  $E_P$  map.

The good agreement between  $E_{cut}$  and  $E_P$  was already expected, as both properties are related to the collective mode excitation. On one hand, the determination of  $E_P$  from the SSD, through model based fitting, relies on the quasi-free particle approximation in Eq. (3.1). This model can fail to predict the true shape of the plasmon peak in EELS to some extent, because of the presence of interband transitions (see Eq. (1.33)). On the other hand, plasmon energy determination through  $E_{cut}$  does not rely on a model and still gives a measure of the energy for collective transitions, as discussed in the previous chapters.

### 5.4.2 Electron effective mass

From the obtained CDFs, we also calculated the electron effective masses for conduction electrons,  $m^*$ , related to charge mobility<sup>40</sup>, following a free-electron plasmon model similar to the one leading to Eq. (1.36). This analysis is based on the relationship between  $E_P$ , the electron concentration at this energy,  $n_{eff}$ , and the high frequency dielectric constant,  $\varepsilon_\infty$ <sup>41,42</sup>,

$$m^* = \frac{n_e}{\varepsilon_0 \varepsilon_\infty} \left( \frac{e \hbar}{E_P} \right)^2 \quad (5.2)$$

where  $\varepsilon_0$  is the permittivity of free space and  $e$  the electron charge.  $n_e$  and

$\varepsilon_\infty$  can be obtained from the CDF<sup>28</sup>, as has been done for similar systems<sup>40</sup>. We mapped the electron effective mass,  $m^*$ , using the  $E_P$  maps and the CDFs, through Eq. (5.2).

The obtained  $m^*$  map for the EELS-SI, also in Fig. 5.7, shows values between  $0.16 \cdot m_0$  and  $0.14 \cdot m_0$ . The effective masses for the conduction of electrons for the binary compounds are  $m_{GaN}^* \sim 0.2 \cdot m_0$  and  $m_{InN}^* \sim 0.11 \cdot m_0$ , where  $m_0$  is the electron rest mass<sup>26</sup>. For an  $In_x Ga_{1-x} N$  compound, we expect the  $m_{In_x Ga_{1-x} N}^*$  value to typically lie between  $0.2 \cdot m_0$  and  $0.11 \cdot m_0$ . In terms of absolute values, the agreement of our calculations with the theoretically expected values is good. We detect somehow lower values associated with the presence of wider In-rich regions in the QW at the center of the image, but there is not enough information to confirm a consistent spatial distribution of this effect.

#### 5.4.3 Ga 3d intensity

In addition to the characterization of the plasmon, we also examined the Ga 3d transition intensity. Before this could be done, we needed a method to normalize the spectral intensity, so that it could be used for approximate elemental quantification. In the developed method, we take advantage of the absolute thickness,  $t$ , map obtained from KKA. This map is included at the bottom in Fig. 5.8, and portrays the thickness gradient in the region. Using this knowledge and the ZLP total intensity,  $I_0$ , we can normalize the SSD following Eq. (1.47). Because in this equation the angular term varies slowly for energies above  $\sim 10$  mrad, this procedure ensures that the intensity in a normalized SSD is proportional to  $\text{Im}(-1/\varepsilon)$ . Notice that the angular factor can be calculated and added if necessary, for instance, if using a wider integration energy window. We expect the integral of the intensity below the Ga 3d transition to be proportional to the gallium concentration, following the Bethe f-sum rule<sup>28,43</sup>.

To extract the spectral intensity of the Ga 3d transition, routine background subtraction on the normalized SSD-SI was performed, using a power-law fit before  $\sim 21.5$  eV. The Ga 3d intensity is found in the  $22 - 25$  eV spectral range. The intensity integral in this range is shown in the top panel of Fig. 5.8. To calibrate the image we used the average over the first nm in the growth direction (see arrow in the left hand side), that presented a relatively homogeneous intensity distribution. Hence, this region was normalized to 95 % gallium, the nominal composition of the barrier. Square regions are marked in Fig. 5.8, using color-coded rectangles. Average line profiles in these regions, through the in-plane direction, were taken from the  $m^*$  and  $\Gamma_P$  maps. These profiles are portrayed in Fig. 5.9 with solid and dashed lines, respectively.

The maps and profiles of the Ga 3d intensity inform us of the composition of the examined  $In_x Ga_{1-x} N$  region. Panels (a) and (b) in Fig. 5.9 (solid lines),

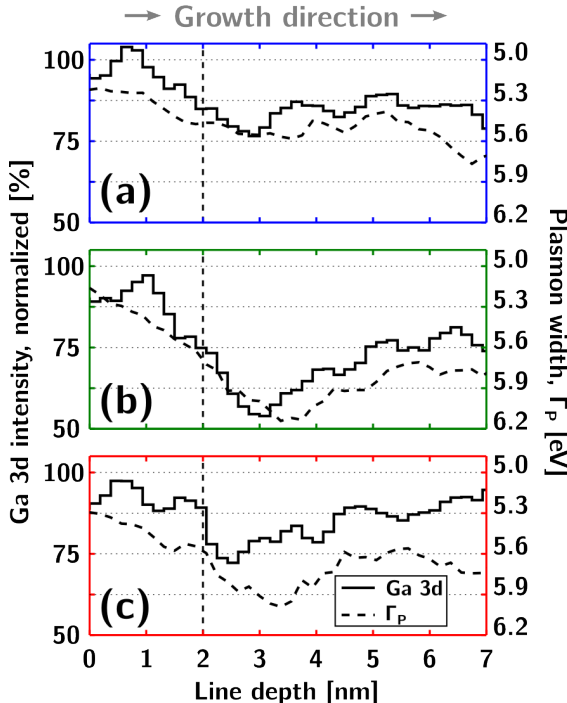


**Fig. 5.9** In panels (a), (b) and (c), Ga 3d intensity (solid lines) and  $\Gamma_P$  (dashed lines) averaged from the blue, green and red rectangular regions highlighted in Fig. 5.8. As in that figure, an arrow indicates the growth direction, from left to right, and the dashed line indicates the beginning of the QW.

showcase the left-hand side and central regions of the InGaN QW bulging. Both profiles indicate the depletion of gallium where the QW was deposited, with a width of  $\sim 1.5$  nm in (a) and  $\sim 3$  nm in (b). In the central region the depletion is deeper, the Ga 3d intensity drops to almost 50 % of its value, at the wider part of the bulging. The profiles indicate some localized diffusion region above the QW: gallium concentration in the region *after* the deposition of the QW is much smaller than in the region *before*. To the contrary, panel (c) from the right-hand side region shows an abrupt start of the QW valley, 1.5 nm wide, and a lower degree of indium diffusion. The quantification of the profiles indicates that  $\text{In}_x\text{Ga}_{1-x}\text{N}$  composition at the sides of the QW is close to  $x = 0.2$  (gallium concentration of 80 %), and in the central part of the bulging is closer to  $x = 0.5$ . It seems that the right-hand side region returns somewhat to the Ga 3d intensity level at the beginning of the next period. Meanwhile, the other regions keep a low Ga 3d intensity, indicative of the gradual diffusion. Finally, a region further above the QW shows a compositional inhomogeneity according to the Ga 3d intensity. Notice that this region is a localized spot inside the barrier region, not visible in the HAADF image.

As a final note, consider that the examination of the Ga 3d transition was initially proposed in Ref. 43, in similar samples, characterizing also the  $\varepsilon_1$  shift and intensity. In our work, the possibilities of using  $\varepsilon_1$  were naturally explored, as we performed KKA. As expected, we obtained similar maps as for the normalized SSD intensity ones, but with increased numerical noise which we were not able to improve. Indeed, the analysis of SSD is advantageous in the sense that it is performed directly from EELS measurements without the need of a model-based fitting to  $\varepsilon_1$ . Anyway, the success of this method relies on our ability to normalize the SSD to produce spectra effectively proportional to  $\text{Im}(-1/\varepsilon)$ . This is only possible if the thickness gradient is small (or better, negligible), as was our case. In cases where thickness gradients are important, using  $\varepsilon_1$  may be advantageous, if KKA is still feasible.

In summary, for the InGaN QWs and some localized spots inside the barriers, we have measured the shift and broadening of the plasmon. See for instance  $E_{cut}$  in Fig. 5.7, in which a consistent plasmon energy shift is detected for the QW, and also at a separate spot on top of the image, in the barrier region. Meanwhile, the  $\Gamma_P$  map in Fig. 5.8 and profiles in Fig. 5.9 (dashed lines), show broadening of the plasmon peak in these two regions. These measurements follow a similar trend to the Ga 3d intensity (solid lines), indicative of a gradual indium diffusion from the QW, as already commented. Notice that this analysis is in overall good agreement with the strain analysis carried out by GPA. It has been suggested that broadening of the plasmon peak may serve as an indicator of strain in nanoscaled systems<sup>44</sup>. Indeed, out-of-plane deformation has been related to the broadening of the plasmon peak before<sup>25</sup>. Following this reasoning, it is natural to relate the shift and broadening of the plasmon peak to the structural and chemical inhomogeneities in the layer, appearing because of the high diffusivity of In.

It is hard to give a precise account of the magnitude of indium diffusion to the barriers, although evidence from the Ga 3d intensity distribution and Z-contrast in the HAADF images suggests that it is small and constrained to localized spots. In the localized region in Fig. 5.7, the HAADF contrast is not as bright as for the QW. Additionally, the strain analysis from GPA shows that the overall structural inhomogeneity inside the barriers is negligible.

## 5.5 Conclusions

- An  $\text{In}_x\text{Ga}_{1-x}\text{N}$  multiple QW structure was studied. As a starting point, high resolution HAADF imaging revealed chemical and structural inhomogeneities in the multilayer. Z-contrast and GPA mappings gave a qualitative account of the compositional and strain gradients, respectively, at

sub-nanometer scale. It, thus, became relevant to examine low-loss EELS, since such changes are expected to alter the electronic properties of the materials. We combined model-based analyses in the dielectric formulation with the appropriate data treatments to perform a quantitative characterization.

- In this framework, the features in low-loss EELS were identified with single-electron or with collective excitations. We confirmed their strong spatial delocalization, at the nanometer range, higher for lower energy thresholds. Hence, the more delocalized one is the band gap signal which has the lower energy threshold. For this signal, the QW features are virtually undetectable and no spatial distribution was found. We compared our measurements with optical data using a full-relativistic calculation of the EELS intensity. The average  $E_g$  value was related to the mean indium content in these layers through Vegard Law.
- We analyzed the plasmon peak using model-based fitting. Consistent shift and broadening of this peak in the InGaN QW layers was found, with a spatial resolution close to the QW size range. However, the obtained  $E_P$  values are well above the expected ones for the suspected QW composition, which is proposed to be related to quantum confinement effects. Moreover,  $\Gamma_P$  maps exhibit a contrast that can also be related to the structural and chemical inhomogeneities in the layers.
- In addition, we mapped other quantitative parameters that can be accessed after KKA using the same EELS data. For instance, the direct determination of the collective mode energy threshold as  $E_{cut}$  in  $\varepsilon(E_{cut}) = 0$  was applied. The results from this procedure seem to improve the plasmon energy contrast in the QW, in comparison with model-based plasmon shift measurements. Electron effective mass ( $m^*$ ) and absolute thickness ( $t$ ), were also mapped. The  $m^*$  measurements were related to the expected values for the pure binaries.
- Finally, we showed how, after normalization of the SSD, chemical information can be obtained by examination of the Ga 3d transition. Intensity maps for this transition were obtained with a strong contrast in the QW regions. These gradients can be related to gallium depletion in the InGaN QW layers. They confirm the chemical information extracted from HAADF and plasmon measurements.

## Bibliography

- [1] S. Nakamura. The roles of structural imperfections in InGaN-based blue light-emitting diodes and laser diodes. *Science*, 281(5379):956–961, 1998.
- [2] S. Nakamura, M. Senoh, N. Iwasa, and S. Nagahama. High-brightness InGaN blue, green and yellow light-emitting diodes with quantum well structures. *Japanese Journal of Applied Physics*, 34(7A):L797, 1995.
- [3] I.-H. Ho and G. B. Stringfellow. Solid phase immiscibility in GaInN. *Applied Physics Letters*, 69(18):2701–2703, 1996. doi: 10.1063/1.117683.
- [4] C. Kisielowski, Z. Liliental-Weber, and S. Nakamura. Atomic scale indium distribution in a GaN /  $\text{In}_{0.43}\text{Ga}_{0.57}\text{N}$  /  $\text{Al}_{0.1}\text{Ga}_{0.9}\text{N}$  quantum well structure. *Japanese Journal of Applied Physics*, 36(11R):6932, 1997.
- [5] D. Gerthsen, E. Hahn, B. Neubauer, A. Rosenauer, O. Schön, M. Heuken, and A. Rizzi. Composition fluctuations in InGaN analyzed by transmission electron microscopy. *Physica Status Solidi (a)*, 177(1):145–155, 2000.
- [6] D. Gerthsen, E. Hahn, B. Neubauer, V. Potin, A. Rosenauer, and M. Schowalter. Indium distribution in epitaxially grown InGaN layers analyzed by transmission electron microscopy. *Physica Status Solidi (c)*, (6): 1668–1683, 2003.
- [7] Y.-C. Cheng, E.-C. Lin, C.-M. Wu, C. C. Yang, J.-R. Yang, A. Rosenauer, K.-J. Ma, S.-C. Shi, L. C. Chen, C.-C. Pan, et al. Nanostructures and carrier localization behaviors of green-luminescence InGaN/GaN quantum-well structures of various silicon-doping conditions. *Applied Physics Letters*, 84(14):2506–2508, 2004.
- [8] J. R. Jinschek, R. Erni, N. F. Gardner, A. Y. Kim, and C. Kisielowski. Local indium segregation and band gap variations in high efficiency green light emitting InGaN/GaN diodes. *Solid state communications*, 137(4):230–234, 2006.
- [9] K. H. Baloch, A. C. Johnston-Peck, K. Kisslinger, E. A. Stach, and S. Gradečák. Revisiting the “In-clustering” question in InGaN through the use of aberration-corrected electron microscopy below the knock-on threshold. *Applied Physics Letters*, 102(19):191910, 2013.
- [10] Z. Li, J. Kang, B. Wei Wang, H. Li, Y. Hsiang Weng, Y.-C. Lee, Z. Liu, X. Yi, Z. Chuan Feng, and G. Wang. Two distinct carrier localization in green light-emitting diodes with InGaN/ GaN multiple quantum wells. *Journal of Applied Physics*, 115(8):083112, 2014. doi: <http://dx.doi.org/10.1063/1>.

4866815. URL <http://scitation.aip.org/content/aip/journal/jap/115/8/10.1063/1.4866815>.
- [11] C. J. Humphreys. Does In form In-rich clusters in InGaN quantum wells? *Philosophical Magazine*, 87(13):1971–1982, 2007.
  - [12] Ž. Gačević, V.J. Gómez, N. García-Lepetit, P.E.D. Soto-Rodríguez, A. Ben-goechea, S. Fernández-Garrido, R. Nötzel, and E. Calleja. A comprehensive diagram to grow (0001) InGaN alloys by molecular beam epitaxy. *Journal of Crystal Growth*, 364(0):123 – 127, 2013.
  - [13] G. H. Gu, D. H. Jang, K. B. Nam, and C. G. Park. Composition fluctuation of in and well-width fluctuation in InGaN/GaN multiple quantum wells in light-emitting diode devices. *Microscopy and Microanalysis*, 19(S5):99–104, 2013.
  - [14] C. Bazioti, E. Papadomanolaki, Th. Kehagias, M. Androulidaki, G. P. Dimitrakopoulos, and E. Iliopoulos. Structure and strain variation in InGaN interlayers grown by PAMBE at low substrate temperatures. *Physica Status Solidi (b)*, 252(5):1155–1162, 2015. ISSN 1521-3951. doi: 10.1002/pssb.201451597. URL <http://dx.doi.org/10.1002/pssb.201451597>.
  - [15] J. Palisaitis, A. Lundskog, U. Forsberg, E. Janzén, J. Birch, L. Hultman, and P. O. Å. Persson. Characterization of InGaN/GaN quantum well growth using monochromated valence electron energy loss spectroscopy. *Journal of Applied Physics*, 115(3):034302, 2014. doi: <http://dx.doi.org/10.1063/1.4861179>. URL <http://scitation.aip.org/content/aip/journal/jap/115/3/10.1063/1.4861179>.
  - [16] M. J. Hýtch, E. Snoeck, and R. Kilaas. Quantitative measurement of displacement and strain fields from HREM micrographs. *Ultramicroscopy*, 74 (3):131–146, 1998.
  - [17] F. M. Morales, D. González, J. G. Lozano, R. García, S. Hauguth-Frank, V. Lebedev, V. Cimalla, and O. Ambacher. Determination of the composition of  $\text{In}_x\text{Ga}_{1-x}\text{N}$  from strain measurements. *Acta Materialia*, 57(19): 5681–5692, 2009.
  - [18] A. Rosenauer, T. Mehrtens, K. Müller, K. Gries, M. Schowalter, P. V. Satyam, S. Bley, C. Tessarek, D. Hommel, K. Sebald, et al. Composition mapping in InGaN by scanning transmission electron microscopy. *Ultramicroscopy*, 111(8):1316–1327, 2011.
  - [19] F. de la Peña, P. Burdet, M. Sarahan, M. Nord, T. Ostasevicius, J. Taillon, A. Eljarrat, S. Mazzucco, V. T. Fauske, G. Donval, L. F. Zagonel, I. Iyengar,

- and M. Walls. Hyperspy 0.8, April 2015. URL <http://dx.doi.org/10.5281/zenodo.16850>.
- [20] A. Gloter, A. Douiri, M. Tencé, and C. Colliex. Improving energy resolution of EELS spectra: an alternative to the monochromator solution. *Ultramicroscopy*, 96(3–4):385 – 400, 2003. ISSN 0304-3991. doi: [http://dx.doi.org/10.1016/S0304-3991\(03\)00103-7](http://dx.doi.org/10.1016/S0304-3991(03)00103-7). URL <http://www.sciencedirect.com/science/article/pii/S0304399103001037>. Proceedings of the International Workshop on Strategies and Advances in Atomic Level Spectroscopy and Analysis.
- [21] A. Eljarrat, S. Estradé, Ž. Gačević, S. Fernández-Garrido, E. Calleja, C. Magén, and F. Peiró. Optoelectronic properties of InAlN/GaN distributed Bragg reflector heterostructure examined by valence electron energy loss spectroscopy. *Microscopy and Microanalysis*, 18:1143–1154, 10 2012. ISSN 1435-8115. doi: 10.1017/S1431927612001328. URL [http://journals.cambridge.org/article\\_S1431927612001328](http://journals.cambridge.org/article_S1431927612001328).
- [22] V. J. Keast, A. J. Scott, M. J. Kappers, C. T. Foxon, and C. J. Humphreys. Electronic structure of GaN and  $\text{In}_x\text{Ga}_{1-x}\text{N}$  measured with electron energy-loss spectroscopy. *Physical Review B*, 66(12):125319, 2002.
- [23] K. A. Mkhoyan, J. Silcox, E. S. Alldredge, N. W. Ashcroft, H. Lu, W. J. Schaff, and L. F. Eastman. Measuring electronic structure of wurtzite InN using electron energy loss spectroscopy. *Applied physics letters*, 82(9):1407–1409, 2003.
- [24] R. Erni, S. Lazar, and N. D. Browning. Prospects for analyzing the electronic properties in nanoscale systems by VEELS. *Ultramicroscopy*, 108(3):270–276, 2008.
- [25] J. Palisaitis, C.-L. Hsiao, M. Junaid, J. Birch, L. Hultman, and P. O. Å. Persson. Effect of strain on low-loss electron energy loss spectra of group-III nitrides. *Physical Review B*, 84:245301, Dec 2011. doi: 10.1103/PhysRevB.84.245301. URL <http://link.aps.org/doi/10.1103/PhysRevB.84.245301>.
- [26] P. Yu and M. Cardona. *Fundamentals of Semiconductors: Physics and Materials Properties*. Graduate Texts in Physics. Springer, 2010. ISBN 9783642007101. URL [http://books.google.es/books?id=5aBuKYBT\\_hsC](http://books.google.es/books?id=5aBuKYBT_hsC).
- [27] F. J. García de Abajo. Optical excitations in electron microscopy. *Reviews on Modern Physics*, 82:209–275, Feb 2010. doi: 10.1103/RevModPhys.82.209. URL <http://link.aps.org/doi/10.1103/RevModPhys.82.209>.

- [28] R. F. Egerton. *Electron Energy-Loss Spectroscopy in the Electron Microscope*. Springer US, 3rd edition, 2011.
- [29] L. X. Benedict, T. Wethkamp, K. Wilmers, C. Cobet, N. Esser, E. L. Shirley, W. Richter, and Cardona. Dielectric function of wurtzite GaN and AlN thin films. *Solid State Communications*, 112(3):129 – 133, 1999. ISSN 0038-1098. doi: [http://dx.doi.org/10.1016/S0038-1098\(99\)00323-3](http://dx.doi.org/10.1016/S0038-1098(99)00323-3). URL <http://www.sciencedirect.com/science/article/pii/S0038109899003233>.
- [30] V. Y. Davydov, A. A. Klochikhin, R. P. Seisyan, V. V. Emtsev, S. V. Ivanov, F. Bechstedt, J. Furthmüller, H. Harima, A. V. Mudryi, J. Aderhold, et al. Absorption and emission of hexagonal InN. evidence of narrow fundamental band gap. *Physica Status Solidi (b)*, 229(3):r1–r3, 2002.
- [31] J. Wu, W. Walukiewicz, K. M. Yu, J. W. Ager III, E. E. Haller, H. Lu, W. J. Schaff, Y. Saito, and Y. Nanishi. Unusual properties of the fundamental band gap of InN. *Applied Physics Letters*, 80(21):3967–3969, 2002.
- [32] P. Schley, R. Goldhahn, A. T. Winzer, G. Gobsch, V. Cimalla, O. Ambacher, H. Lu, W. J. Schaff, M. Kurouchi, Y. Nanishi, M. Rakel, C. Cobet, and N. Esser. Dielectric function and Van Hove singularities for In-rich  $\text{In}_x\text{Ga}_{1-x}\text{N}$  alloys: Comparison of N- and metal-face materials. *Physica Review B*, 75:205204, May 2007. doi: 10.1103/PhysRevB.75.205204. URL <http://link.aps.org/doi/10.1103/PhysRevB.75.205204>.
- [33] V. J. Keast and M. Bosman. Applications and theoretical simulation of low-loss electron energy-loss spectra. *Materials Science and Technology*, 24(6):651–659, 2008.
- [34] R. Erni and N. D. Browning. The impact of surface and retardation losses on valence electron energy-loss spectroscopy. *Ultramicroscopy*, 108(2):84–99, 2008.
- [35] A. Eljarrat, L. López-Conesa, C. Magén, Ž. Gačević, S. Fernández-Garrido, E. Calleja, S. Estradé, and F. Peiró. Insight into the compositional and structural nano features of AlN/GaN DBRs by EELS-HAADF. *Microscopy and Microanalysis*, 19(03):698–705, 2013.
- [36] P. D. Nguyen, D. M. Kepaptsoglou, Q. M. Ramasse, and A. Olsen. Direct observation of quantum confinement of Si nanocrystals in Si-rich nitrides. *Physical Review B*, 85:085315, Feb 2012. doi: 10.1103/PhysRevB.85.085315. URL <http://link.aps.org/doi/10.1103/PhysRevB.85.085315>.
- [37] P. D. Nguyen, D. M. Kepaptsoglou, R. Erni, Q. M. Ramasse, and A. Olsen. Quantum confinement of volume plasmons and interband transitions in

- germanium nanocrystals. *Physical Review B*, 86:245316, Dec 2012. doi: 10.1103/PhysRevB.86.245316. URL <http://link.aps.org/doi/10.1103/PhysRevB.86.245316>.
- [38] M. M. Y. Leung, A. B. Djurišić, and E. H. Li. Refractive index of InGaN/GaN quantum well. *Journal of Applied Physics*, 84(11):6312–6317, 1998.
  - [39] G. M. Laws, E. C. Larkins, I. Harrison, C. Molloy, and D. Somerford. Improved refractive index formulas for the  $\text{Al}_x\text{Ga}_{1-x}\text{N}$  and  $\text{In}_y\text{Ga}_{1-y}\text{N}$ . *Journal of Applied Physics*, 89(2):1108–1115, 2001.
  - [40] M. H. Gass, A. J. Papworth, R. Beanland, T. J. Bullough, and P. R. Chalker. Mapping the effective mass of electrons in III-V semiconductor quantum confined structures. *Physical Review B*, 73(3):035312, 2006.
  - [41] W. G. Spitzer and H. Y. Fan. Determination of optical constants and carrier effective mass of semiconductors. *Physical Review*, 106:882–890, Jun 1957. doi: 10.1103/PhysRev.106.882. URL <http://link.aps.org/doi/10.1103/PhysRev.106.882>.
  - [42] H. R. Chandrasekhar and A. K. Ramdas. Nonparabolicity of the conduction band and the coupled plasmon-phonon modes in n-GaAs. *Physical Review B*, 21:1511–1515, Feb 1980. doi: 10.1103/PhysRevB.21.1511. URL <http://link.aps.org/doi/10.1103/PhysRevB.21.1511>.
  - [43] A. M. Sánchez, M. Gass, A. J. Papworth, P. J. Goodhew, and P. Ruterana. Nanoscale EELS analysis of InGaN/GaN heterostructures. *Physical Review B*, 70(3):035325, 2004.
  - [44] A. M. Sánchez, R. Beanland, M. H. Gass, A. J. Papworth, P. J. Goodhew, and M. Hopkinson. Mapping quantum dot-in-well structures on the nanoscale using the plasmon peak in electron energy loss spectra. *Physical Review B*, 72:075339, Aug 2005. doi: 10.1103/PhysRevB.72.075339. URL <http://link.aps.org/doi/10.1103/PhysRevB.72.075339>.





# Chapter 6

## Er-doped Si-nc/SiO<sub>2</sub> multilayer

“Size matters not. Look at me. Judge me by my size, do you?”

---

Yoda, *The Empire Strikes Back*.

In this chapter (and the next one), we turn our attention to silicon-based electronic devices. In particular, we present here the characterization of an active layer stack for novel optoelectronic devices consisting of alternate thin layers of pure silica (SiO<sub>2</sub>) and silicon-rich silicon oxide (SRO, SiO<sub>x</sub>). Upon high temperature annealing the SRO sublayer segregates into a Si nanocluster (Si-nc) precipitate phase and a SiO<sub>2</sub> matrix. Additionally, erbium (Er) ions were implanted and used as luminescent centres in order to obtain a narrow emission at 1.54 µm. By means of the combination of HAADF and EELS techniques, structural and chemical information from the embedded Si-ncs is revealed. The analyzed energy-loss spectra contain contributions from the Si-ncs and the surrounding SiO<sub>2</sub>. By performing a double plasmon fit, the spatial distribution of the Si-ncs and the SiO<sub>2</sub> barriers is accurately determined in the multilayer. Additionally, the quality of the studied multilayer in terms of composition, roughness and defects is analysed and discussed. Er clusterization was not observed, neither by HAADF-EELS nor EDX. Blue-shifted plasmon and interband transition energies for silica are measured, in the presence of Er ions and sizable quantum confinement effects.

## 6.1 Introduction

Design and characterization of new complementary-metal-oxide-semiconductor (CMOS) silicon-based light emitting devices is an important driving force for the functional integration of photonics and electronics in the same chip, as well as the development and mass manufacturing of a vast variety of products<sup>1</sup>. Indeed, silicon is the most appropriate material for optoelectronic and photonic applications, as it is transparent in the third telecommunication window at 1.5 μm, CMOS compatible, extremely low-cost, and presents a high refractive index contrast with its natural oxide. However, as a bulk material, silicon exhibits some unsuitable optical properties for the development of light emitting devices (LEDs)<sup>2</sup>. For instance, the indirect nature of its band gap leads to a poor radiative recombination rate, causing long radiative lifetimes in pure bulk silicon and hindering the efficient emission of light.

Overcoming these limitations is the key challenge for the material scientist working on this field. Some solutions have been proposed in the literature: (i) the incorporation of silicon nanoclusters (Si-ncs) embedded in either SiO<sub>2</sub> or Si<sub>3</sub>N<sub>4</sub> dielectric matrices to achieve the spatial confinement of the electrons and holes, which allows relaxing the momentum conservation in the recombination process (intrinsic emission), and (ii) the introduction of rare earth impurities such as erbium (Er) ions that act as optically active dopants (extrinsic emission). In particular, Er-doped silicon-rich silicon oxide (SRO, SiO<sub>x</sub>) has been extensively used and characterized<sup>3</sup>. The reported results have shown that the Si-ncs inclusion may allow for a larger photoluminescence (PL) if efficient coupling between Si-ncs and Er ions occur, thus increasing the absorption cross-section of Er by orders of magnitude<sup>4</sup>. Equally, Si-ncs are also beneficial for the electrical conductivity because they promote the modulation of the electrode-active layer barrier height providing better injection of carriers or just an increase of the bulk conductivity of the composite material<sup>5</sup>. Additionally, the role of Er ions is crucial for luminescent applications. Therefore, special attention must be paid to the ratio between the total Er ion concentration and the Er ions that can emit (*i.e.* that are optically active) for boosting the emission at 1.5 μm and also to avoid the Er clustering. Undoubtedly, to better understand and control the structural and compositional properties of the material, an in-depth analysis at the nanoscale is required.

In the past, the spatial resolution obtained by electron microscopy methods has been critical for the detection of Er ion clustering and assessment of its impact on efficient light emission by the dopant<sup>6</sup>. In particular, electron energy loss spectroscopy (EELS) in the low-loss regime has been a valuable tool for the characterization of materials involved in the configuration of these photonic devices. As an example, Si excess in oxide-nitride-oxide structures and quantum con-

finement at the nanometer scale have been detected early-on by examination of low-loss EELS data<sup>7,8</sup>. With the development of new powerful instrumentation (aberration correctors and monochromators to improve the spatial and energy resolution of EELS), the usefulness of low-loss EELS increases. Henceforth, the analysis of the plasmon peak has allowed the mapping of a number of materials properties with unprecedented spatial and energy resolution<sup>9–11</sup>. It is now possible to directly examine critical nanoscale features of silicon-based photonic devices such as Er cluster formation or quantum confinement in Si-ncs<sup>12,13</sup>.

This chapter presents the structural and chemical characterization of a multilayer structure, that acts as an active layer for optoelectronic devices. Our aim is to assess the morphology of the interfaces, check for the occurrence of Er clusterization and detect the distribution of Si-ncs with high spatial resolution. In this sense, we test the ability of the STEM HAADF and EELS techniques to extend the information provided by EFTEM, HRTEM and EDX. Additionally, we measure electronic properties with high energy and spatial resolution, a feat that can only be achieved by using EELS.

### 6.1.1 Sample details and preliminary examination

We examine a  $\sim 50$  nm wide active multilayer of Er-doped  $\text{SiO}_2/\text{SRO}$  in an electro-optical active slot waveguide<sup>14</sup>, as shown in Fig. 6.1. These kinds of multilayers can also be used as electroluminiscent layers in other photonic devices, such as ring resonators and LEDs. The examined device was provided by the group of Prof Blas Garrido, from the *Departament d'Electrònica* at *Universitat de Barcelona*.

The multilayer was deposited on a [001] crystalline silicon (c-Si) substrate, with a highly doped poly-Si contact on top (to provide the electron injection). The stacking is composed by alternate 2 nm wide  $\text{SiO}_2$  layers and 3 nm wide SRO layers. The Si excess in each SRO sublayer is around of 20 %, thus being the averaged Si excess in the whole layer equal to 12 %. The layers were deposited by plasma enhanced chemical vapour deposition (PECVD), over a c-Si substrate in [100] orientation. Conventional annealing at 900°C for 1 hour was performed, in order to induce the Si phase separation and precipitate the Si-ncs. In addition, the multilayer structure was implanted with Er ions which measured concentration was roughly of  $2 \times 10^{20} \text{ atm}/\text{cm}^3$  at the centre of the implanted profile. A post-annealing at 800°C for 6 hours was also performed in all samples in order to optically activate the Er ions and additionally to recover the multilayer from defects caused by the implantation.

Since the active layer is specifically localized in the device, a thin lamella was prepared for STEM-EELS observation by focused ion beam (FIB) lift-out procedure (see Appendix A), as illustrated in successive panels, (a)-(c), in Fig. 6.1.

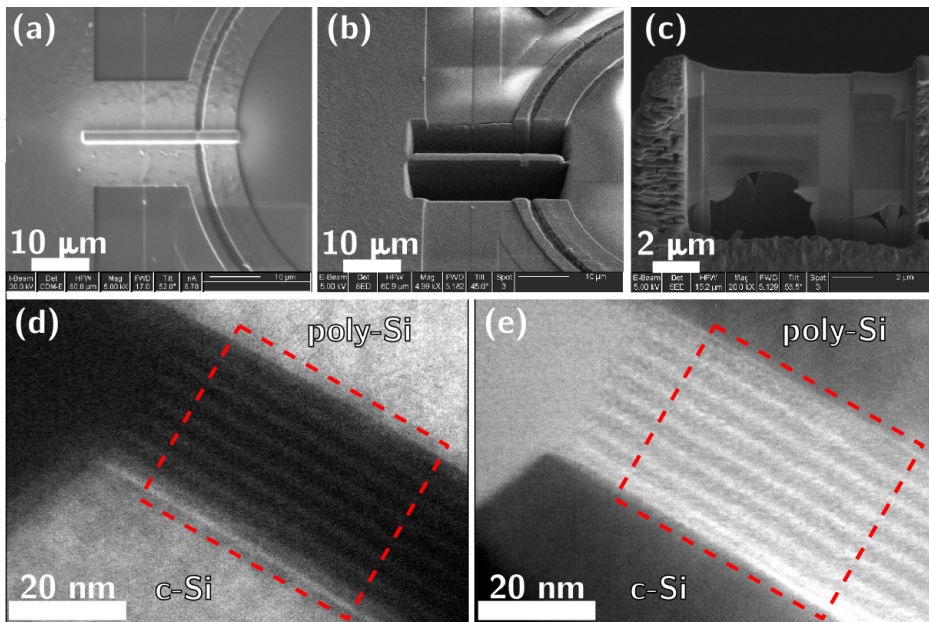


**Fig. 6.1** Upper panels: scanning electron microscopy (SEM) images of the sample preparation process, from an electro-optical active slot waveguide integrated photonic device. Each panel corresponds to a specific stage of the FIB lift-out preparation process: The protective Pt deposition, panel (a), the ion beam-carved trenches, panel (b), and the final thinning of the extracted lamella, panel (c). Lower panels: Two EFTEM images of the sample. Left image, (d), was acquired filtering the silicon plasmon peak; right image, (e), filtering the silica plasmon peak. The comparison of these two images reveals the alternative presence of silicon and silica in the multilayer. In both images, a red dashed square highlights the active layer region, explored in this work.

A preliminary HRTEM characterisation and energy filtered TEM (EFTEM) observation was performed using a JEOL J2010 F (S)TEM. Figures 6.1(d) and (e) correspond to the EFTEM images acquired by filtering the plasmon peak of Si (at  $\sim 17$  eV) and of SiO<sub>2</sub> (at  $\sim 24$  eV), respectively. These images illustrate the general configuration of the stack and allow for an initial assessment of the quality of the fabrication process, showing the expected morphology of the active multilayer. Besides the conventional evaluation of the quality of the fabricated multilayers for the validation of the growth procedure (relative layer thicknesses, abruptness and homogeneity of the layers through the stack), this preliminary analysis was already focused on the detection of Er and Si clusterization signs and on the phase separation between Si-ncs and SiO<sub>2</sub> host matrix<sup>6,15</sup>.

However, the small size of the features in this multilayer structure demands a spatial resolution beyond that of a conventional electron microscope. In addition, the use of a low energy beam to avoid damaging the sampled region is required. Subsequently, a probe-corrected FEI Titan (S)TEM, operated at 80 kV, was used to obtain the data from the sample at great spatial resolution. Notice that a precise evaluation of the configuration of the multilayer stack requires spatially resolved information, to appropriately correlate the EELS-HAADF data to the material properties. For this reason, hyperspectral low-loss EELS data-sets and HAADF images covering the whole active multilayer were simultaneously acquired using this instrument. Additionally, energy dispersive X-ray (EDX) analysis was performed on the sample using EDAX X-rays microanalysis.

The STEM-EELS experiment was carried out on the active region of the sample, indicated with a red square in the EFTEM images in Fig. 6.1. Hyperspectral acquisition was performed, consisting in HAADF-EELS data-sets with up to 100x100 spatially localized spectra, acquired with a  $\sim 0.5$  nm spatial resolution, with  $\beta \sim 14.3$  mrad and  $\alpha \sim 7$  mrad. These data were processed using the standard tools explained in Sec. 2.1. The energy axis was calibrated using the zero-loss peak (ZLP), and Fourier-log deconvolution was performed. The symmetry of the sampled area along the growth direction allowed us to perform an initial perpendicular binning of the spectra in the EELS-SI to increase statistics. Because of this averaging, the spatial sampling in the growth direction is of  $\sim 0.5$  nm while for the perpendicular direction it was reduced to  $\sim 1$  nm. Even if the probe in the Titan microscope is of sub-nanometer size, the actual sampling resolution is above 1 nm due to volume plasmon delocalization, see Sec. 1.2.5.

The following sections present the analysis of one of the acquired data-sets, containing a low-loss EELS-SI plus a HAADF image. Two-dimensional maps of properties in low-loss EELS were calculated from the spatially localized energy-loss spectra. To help identify the different parts of the structure, all these maps follow the same alignment: the top and bottom ends correspond to the contact and substrate sides respectively, while the central part corresponds to the active multilayer.

## 6.2 HAADF and relative thickness analysis

Figure 6.2(a) shows the HAADF image recorded simultaneously with the EELS-SI. As already discussed, in HAADF images heavier atoms appear brighter. From the examination of the contrast in Fig. 6.2(a), we can see that the first two layers present a much brighter contrast. Also, we can appreciate localized areas of increased intensity, roughly circular spots, usually over the bright layers. These areas should correspond to a difference in the local composition or thickness. EDX analysis was performed on this region, finding no evidence of the presence

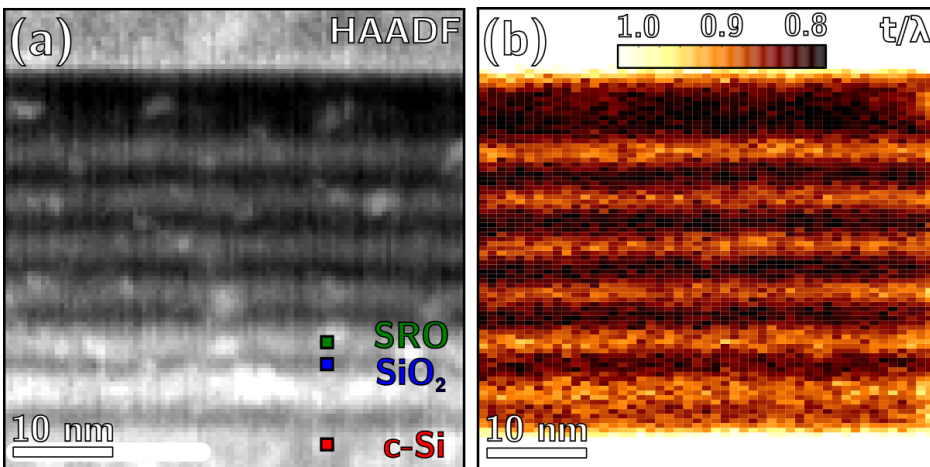


**Fig. 6.2** Panel (a) shows a HAADF image of the examined region, acquired simultaneously to the EELS-SI. Panel (b) shows the relative thickness map calculated from the EELS-SI. In these and all further maps: c-Si substrate and poly-Si contact are located at bottom and top sides, respectively, while the central part of the map shows the multilayer structure.

of erbium in these spots, neither copper nor gallium from the sample preparation process. Three color-coded marks have been added to this image: silicon (red), silica (blue) and SRO (green) regions. This color code will be used to identify these regions in the figures.

We can have an indirect insight into the thickness of the sampled area through the examination of the relative thickness,  $t/\lambda$ , as measured using low-loss EELS. This parameter is mapped in Fig. 6.2(b) using the spatially localized spectra in the EELS-SI. As explained in Sec. 1.2.4,  $t/\lambda$  is equal to the ratio between the thickness,  $t$ , and the inelastic electron mean free path ( $\lambda$ ) of the material. As the FIB lift-out sample preparation method minimizes thickness variations, we expect the  $t/\lambda$  profiles to have a great stability and contrast, and that they may also be used as a fingerprinting tool.

In Fig. 6.2(b), the measured value for the pure silicon regions (substrate at the bottom of the image, and contact at the top) is very homogeneous,  $t/\lambda(\text{Si}) \sim 1.2$ , at both sides. This confirms that we are sampling a constant thickness region, owing to the FIB preparation of the sample. Moreover, high contrast between the pure silicon and the active multilayer ( $t/\lambda \sim 0.8$ ) is found. This  $\sim 1.5$  measured ratio is greater than the theoretically expected ratio between mean free paths for silica and silicon,  $\sim 1.1$  (calculated for a 80 kV incident energy and an effective collection angle of 14 mrad)<sup>16,17</sup>. As the value for the pure Si layers is reliable,

we estimate that this departure from the theoretical values is due to an increase in the  $\lambda$  values in the silica. This can be related to the effect of Er doping and the nanoscaled multilayer staking on promoting the contribution of low-energy excitations in the plasmon region<sup>10,13,18</sup>. Meanwhile, in the active multilayer, the Si excess in the SRO yields a lower but still appreciable contrast,  $t/\lambda(\text{SRO}) \sim 0.9$ . The contrast in  $t/\lambda$  is enough to sharply differentiate the periodic structure, giving also the first quantitative information about the material properties and providing additional insight into the morphology observed in Fig. 6.1 (d) and (c).

In summary, the sampled region presents a negligible thickness variation, while Z-contrast imaging suggests the presence of localized higher density particles. To further understand the structure of the layers, the analysis of the plasmon peak in the energy-loss spectra was carried out.

### 6.3 Measuring the Si-ncs plasmon energy

We could accurately measure both bulk plasmon energy and width using non-linear fitting techniques. Notice that, with this application in mind, plural scattering was previously suppressed using Fourier-log deconvolution. As in the previous chapters, a Drude plasmon model (DPM) was used to fit the plasmon peaks, following Eq. (3.1). In this model, the  $E_P$  parameter does not correspond directly to the plasmon peak maximum intensity energy position,  $E_{max}$ , but is a function of this parameter and  $\Gamma_P$  (see *Plasmon profiling* in Sec. 4.2.2).

In Fig. 6.3 (a), we observe examples of individual spectra acquired in the c-Si substrate, a  $\text{SiO}_2$  layer and a SRO layer. The c-Si energy-loss spectrum in this image shows a narrow bulk plasmon at an energy  $E_P \sim 17$  eV, as expected for this material ( $E_{max} \sim 16.8$  eV). For the  $\text{SiO}_2$  plasmon, the middle spectrum in Fig. 6.3(a), we observe a blue shift from the expected  $E_P$  value, 22.3 eV for pure silica, to 23.7 eV and above. Apart from this blue shift, we acknowledge the presence of a secondary peak at  $\sim 15$  eV corresponding to a  $\text{SiO}_2$  interband transition. For the SRO plasmon, the top spectrum in Fig. 6.3(a), a similar blue shift is also evident, towards higher  $E_P$  values in the order of 24 eV. In this case, a secondary peak observed at 18 eV can be identified with the Si-ncs.

An EELS-SI across the entire active multilayer was acquired and the plasmon peak energies were determined according to a DPM fit. The appropriateness of this procedure was assessed by examination of the sum of the squared residuals in the fitting region. The resulting distribution of plasmon energies,  $E_P$ , in the analyzed EELS-SI is presented as an histogram in Fig. 6.3(b). Plasmon energies are indicated in the energy axis. A clear separation in the plasmon energy of the c-Si substrate and poly-Si on top (both at  $\sim 17$  eV) from the dielectric material in the multilayer ( $\sim 23.5$  eV) is found. Moreover, the  $E_P$  values for the multilayer appear to be somewhat spread (the energy resolution is around 0.2 eV), because

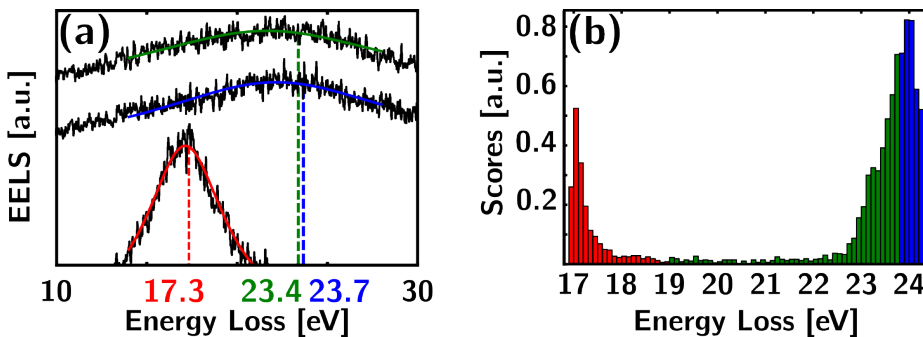


**Fig. 6.3** (a) experimental energy-loss spectra (black lines) from the three distinctive material regions highlighted in Fig. 6.2(a), showing their Drude plasmon fits (solid color lines). The dashed color lines correspond to the plasmon energy from the corresponding fit. (b) histograms of the fitted plasmon energies, calculated from the whole dataset (including Si substrate and upper contact). The bars have been color coded according to the identifiable characteristics from silicon, SiO<sub>2</sub> and SRO regions.

the plasmon energy values are red shifted (to lower energies) in the SRO layers with respect to the ones in the SiO<sub>2</sub> layers.

### 6.3.1 Double plasmon fit

The energy-loss spectra in Fig. 6.4(a), top and bottom, correspond to SRO and SiO<sub>2</sub> layers, respectively. Looking carefully, we can identify secondary peaks, at lower energies compared to the bulk plasmon of silica at  $\sim 24$  eV. They correspond to the Si-nc at  $\sim 18$  eV, for SRO, and to the interband transition at  $\sim 15$  eV, for SiO<sub>2</sub>. According to these observations, fingerprinting should be performed by using a model containing two DPM peaks instead of a single one. This procedure implies that when the model is applied to an EELS spectrum acquired on the active region, two peaks are fitted at the same time. Taking the observed silica plasmon energy as a reference, our average fitting results in a slightly blue shifted SiO<sub>2</sub> plasmon ( $\sim 24$  eV) in addition to a lower energy and lower intensity peak. This “low energy” peak will correspond to the SiO<sub>2</sub> interband transition or to the Si-nc plasmon, depending on the region. Figure 6.4(b) shows the histogram of the distribution of the “low energy” plasmon energies in the active multilayer region, which undoubtedly reveals the existence of these two overlapped but apparent plasmon peaks. Also, the good accord of the double plasmon fits with the experimental shape of the plasmon can be assessed by examination of the energy-loss spectra and color lines in Fig. 6.4(a).

The raw plasmon energies obtained from the application of these procedures

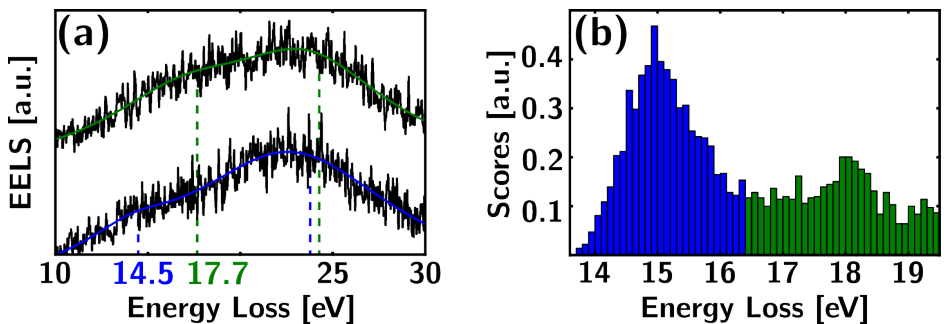


**Fig. 6.4** (a) experimental energy-loss spectra (black lines) from SRO (top) and SiO<sub>2</sub> (bottom) regions, showing their Double plasmon fits (solid colored lines). The dashed color lines correspond to the plasmon energy from the Drude components involved in the corresponding fit. (b) histogram plots for the “low-energy” component of the double plasmon fits, containing only data from the spectra within the multilayer region. The bars have been color coded according to the identifiable characteristics from silicon, SiO<sub>2</sub> and SRO regions.

to the analysis of the plasmon peak in each individual EEL spectrum in our dataset are depicted in Fig. 6.5 (a) and (b). Particularly, Fig. 6.5(a) corresponds to the plasmon energy according to the single plasmon model. In this image, The measured plasmon energy on the dark zones at the bottom (Si substrate) and the top (poly-Si electrode) was around  $\sim 16.9$  eV, as expected for this material<sup>16</sup>. Likewise, the central region, corresponding to the multilayer structure yielded a plasmon energy value in the range of  $23 - 24$  eV. This value is slightly shifted approximately 1 eV to higher energies with respect to the pure silica plasmon (22.3 eV), in well-defined regions: blue shifted silica plasmon corresponds to the layers observed in the EFTEM, HAADF and  $t/\lambda$  maps.

Figure 6.5(b) corresponds to the energy position of the “low energy” plasmon after fitting the spectra with the double plasmon model. In the SRO layers, the double plasmon fit detects a “low energy” plasmon identified as the Si-ncs signature. We expect the Si-ncs plasmon energy to be above 16.3 eV or 16.7 eV, which are the values for a-Si and c-Si respectively, due to quantum confinement effects<sup>9,18</sup>. A wide distribution of plasmon energies around  $\sim 18$  eV can be identified in Fig. 6.4(b), which can be attributed to the size variation of Si-ncs. Finally, the bright regions in Fig. 6.5(a) correspond to dark areas in Fig. 6.5(b) in which a less energetic “low energy” plasmon was detected through the double plasmon fit. This peak is identified as the SiO<sub>2</sub> interband transition at  $\sim 15$  eV.

The threshold energies in the histograms in Fig. 6.3(b) and Fig. 6.4(b) were used as a color scale to better map the plasmon energy distribution. The resulting

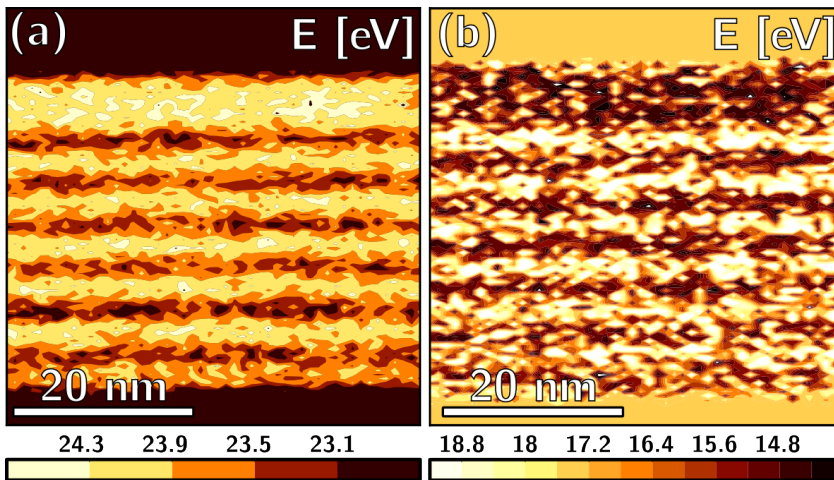


**Fig. 6.5** (a) Energies from the single plasmon model; (b) “low energy” component of the double plasmon model in the same EELS-SI.

color plots are presented in Fig. 6.6 (a) and (b), in which red, green and blue are used to indicate Si, SiO<sub>2</sub> and SRO/Si-ncs regions, respectively. Figure 6.7 shows an averaging through the the whole set of presented results. The plasmon energies were averaged in a direction perpendicular to the growth direction, indicated with an arrow in Fig. 6.6(b), from the c-Si substrate (left) to the poly-Si contact (right). The dotted blue line, indicating the position of the “low energy secondary plasmon” alternates between the SiO<sub>2</sub> interband transition ( $\sim 15$  eV) and the Si-nc ( $\sim 18$  eV) values. The black triangles line indicates the “high energy” plasmon in the double fitting model. The red triangles line, corresponding to the single plasmon model fit, oscillates between higher ( $\sim 24$  eV) lower ( $\sim 23$  eV) values.

Figure 6.7 corroborates the good agreement between single and double plasmon fits: when a SiO<sub>2</sub> interband transition is detected in the “low energy” plasmon (minima of the blue line oscillation), the “high energy” plasmon (black line) and the maximum of the single plasmon fit (maxima of the red line oscillation) are both found at  $\sim 24$  eV. Conversely, when the Si-nc plasmon is detected (maxima of the blue line oscillation), the “high energy” plasmon remains at the same energy value as it had for the silica,  $\sim 24$  eV, whereas the minima of the single plasmon fit shift about  $\sim 1$  eV towards lower energies. The average profile allows us to establish the period for each SRO/SiO<sub>2</sub> repetition at  $\sim 5$  nm, as is expected from the deposition process, with an extra silica layer on top (below the upper poly-Si contact). As expected also, the average width of each SRO layer is about 2.5–3 nm. In this profile, as in the histograms, the plasmon energy for the Si-ncs

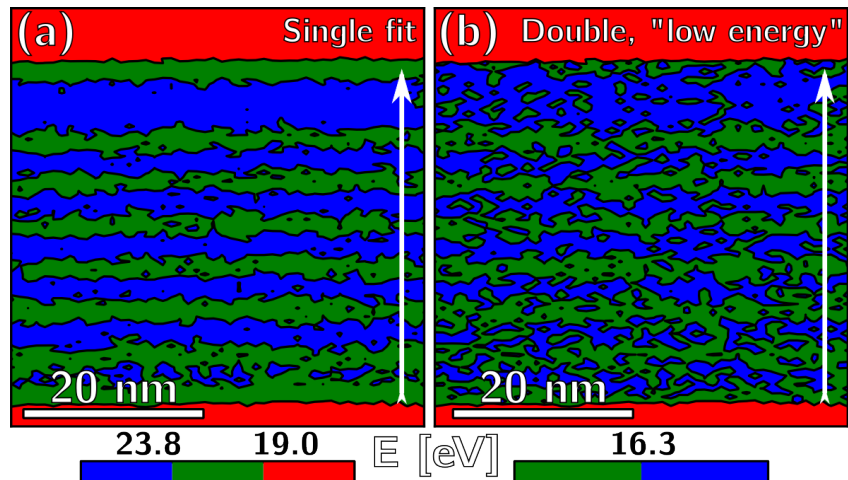


**Fig. 6.6** Color filled contour maps of the plasmon energies in Fig. 6.5, for (a) the single plasmon fit, and (b) the “low-energy” component from the double plasmon fit.

is found to be spread around  $\sim 18$  eV, but the profile allows detecting an increase in the average energies of the Si-ncs as the periods are sequentially deposited.

Notice that the profiles in Fig. 6.7 are averages from the EELS signals in the spectrum image, and the fact that smooth outlines are observed reflects both the expected delocalization effects and the statistical nature of the study.

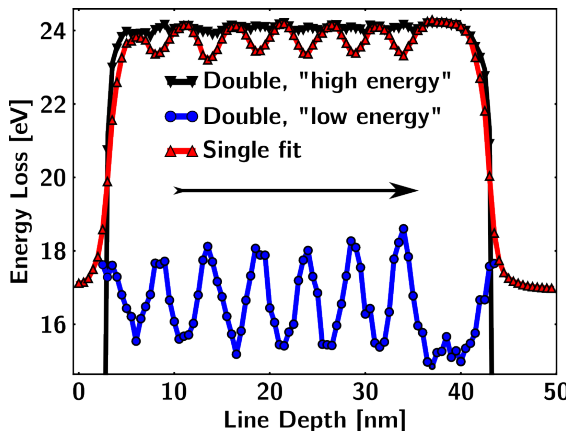


**Fig. 6.7** Plasmon energies from the double model (the “low energy” and the “high energy” components in blue and black, respectively); and the single model (red). Data were averaged in the direction perpendicular to the growth (the latter is indicated with a white arrow in Fig. 6.6)

### 6.3.2 Discussion

For Si-ncs embedded in a Si-rich nitride matrix, for which quantum confinement (QC) takes place, a direct relationship between the size of the particles and the blue shift of the Si plasmon energy can be established through an empirical formula<sup>13</sup>. For instance, a measured energy of  $\sim 18$  eV should correspond to plasmons in crystalline particles with a typical size of  $\sim 4$  nm, bigger than the width of our layers. This result does not apply directly to our Si-ncs, although we expect the QC to be the main reason for the plasmon blue shift. Additionally, we observe an increase in plasmon energy in subsequently deposited sublayers of the multilayer (see “high energy” component in Fig. 6.7). In the framework of QC effects, this is related to an increase of the crystalline quality of the Si-ncs and/or to a shrinkage of the Si-ncs after few sublayer depositions of the multilayer.

No traces of Er clusterization were found, probably because the rare-earth dopant distribution cannot be observed at the resolution at which experiments were carried out. Based on the assumption that clusterization takes place in the form of Er oxide, we could expect to measure a contribution from the Er O<sub>2,3</sub> absorption edge. This edge is at 29 eV, within the energy range of our energy-loss spectra, and has been reported in similar systems, where Er clusters were detected<sup>12</sup>. If optically active Er (not in clusters) is present in the sample, we expect the dopant to introduce intermediate energy levels in the band structure. Namely, 1.54  $\mu$ m emission is produced via interband transitions of the 4f shell. When inter-band transitions occur at a lower energy than that of the Drude plasmon peak, a shift to higher energies of the plasmon peak is produced<sup>16</sup>. The observed shift of the plasmon energy to higher values in the SiO<sub>2</sub> layers would then indicate the presence of optically active Er.

If a Vegard law-like linear relationship existed between the SiO<sub>2</sub> matrix measured plasmon energy ( $\sim 24$  eV) and the plasmon energy from the Si-ncs (average plasmon energy  $\sim 18$  eV), this should allow us to calculate the Si excess for each value of the plasmon energy. In spite of the problematic nature of this assumption, the  $\sim 1$  eV measured redshift of the plasmon maxima from Silica to SRO would be associated with a 16.6 % Si-excess, not far from the 20 % nominal concentration.

From the examination of the maps and profiles in Figures 6.3-6.7 we can conclude that the silicon excess from the two first periods suffered some intermixing after the annealing. In these two layers Si-ncs are detected outside the targeted periodic structure, thus blurring the multilayer boundaries and increasing high-angle scattering (brighter HAADF contrast). In spite of this initial instability, the successive periodic growth and formation of the multilayers was successfully achieved for the next layers.

## 6.4 Conclusions

- A multilayer structure, made of Er-doped alternating layers of  $\text{SiO}_2$  and SRO, was examined. In this structure, an annealing process has been carried out to obtain Si-ncs in the SRO region. This embedded nanoparticle system was characterized using a combination of HAADF and EELS-SI. Such a study is unavoidably difficult because of the overlapping of Si-ncs and silica contributions to the EELS signal.
- In this sense, HAADF and  $t/\lambda$  maps (obtained from EELS), were used for a preliminary assessment of thickness and stack homogeneity of the sample. In the HAADF images, we detected some brighter spots on the SRO layers, and also on the last silica layer, that could be hinting the presence of more massive localized regions. The  $t/\lambda$  maps confirmed that as the specimen for TEM observation was prepared by focused-ion beam (FIB), it presented a negligible thickness gradient. This allowed to use the contrast in the  $t/\lambda$  maps and the Z-contrast in the HAADF images to identify the Si-ncs regions.
- Plasmon energy maps were obtained from low-loss EELS-SIs, with great spatial and energy resolution. We demonstrated a double plasmon model-based fit, adjusting the energy-loss spectra according to the presence of two distinct plasmon peaks. In our example, a “high-energy” plasmon model is always used to fit the  $\text{SiO}_2$  peak (23.7 eV); conversely, a “low energy” plasmon model is used to tell the Si-ncs peak from the  $\text{SiO}_2$  interband transition. This strategy allowed us to locate the Si-ncs in the multilayer, in which they appear scattered, with a relatively low concentration, and have a subtle impact on the low-loss EELS data.
- No evidences of Er clusterization were found. The presence of optically active Er is suggested by blue-shifted interband transition and plasmon energies in silica.
- The obtained maps and profiles confirmed the good quality of the fabricated multilayer. Our results indicate that the Si-ncs formation can be effectively controlled by adjusting the distance between  $\text{SiO}_2$  barrier layers, hence providing an ordered array of Si-ncs of very similar sizes. Moreover, this multilayer approach offers an additional benefit when compared to single layers with the same fabrication parameters because of the apparent absence of Er clusterization<sup>6,19</sup>.

## Bibliography

- [1] B. Jalali, M. Paniccia, and G. Reed. Silicon photonics. *IEEE Microwave Magazine*, pages 55–68, 2006.
- [2] L. Pavesi and G. Guillot. *Optical Interconnects: The Silicon Approach*. Springer Series in Optical Sciences. Springer, New York, 2006.
- [3] D. Pacifici, A. Irrera, G. Franzo, M. Miritello, G. Iacona, and F. Priolo. Erbium-doped Si nanocrystals: Optical properties and electroluminiscent devices. *Physica*, E16:331–340, 2003.
- [4] B. Garrido, C. García, S.-Y. Seo, P. Pellegrino, D. Navarro-Urrios, N. Daldoso, L. Pavesi, F. Gourbilleau, and R. Rizk. Excitable Er fraction and quenching phenomena in Er-doped  $\text{SiO}_2$  layers containing Si nanoclusters. *Physical Review B*, 76:245308, 2007.
- [5] J. M. Ramírez, F. Ferrarese-Lupi, O. Jambois, Y. Berencén, D. Navarro-Urios, A. Anopchenko, A. Marconi, N. Prtljaga, L. Pavesi, J. P. Colonna, J. M. Fedeli, and B. Garrido. Erbium emission in MOS light emitting devices: from energy transfer to direct impact excitation. *Nanotechnology*, 23:125203, 2012.
- [6] N. Prtljaga, D. Navarro-Urrios, A. Tengantini, A. Anopchenko, J. M. Ramírez, J. M. Rebled, S. Estradé, J. P. Colonna, J. M. Fedeli, B. Garrido, and L. Pavesi. Limit to the erbium ions emission in silicon-rich oxide films by erbium ion clustering. *Optical Materials Express*, 2:1278, 2012.
- [7] V. A. Gritsenko, H. Wong, J. Xu, R. Kwok, I. Petrenko, B. Zaitsev, Y. Moroko, and Y. Novikov. Excess silicon at the silicon nitride/thermal oxide interface in oxide-nitride-oxide structures. *Journal of Applied Physics*, 86: 3234–3240, 1999.
- [8] B. W. Reed, J. M. Chen, N. C. MacDonald, J. Silcox, and G. F. Bertsch. Fabrication and STEM/EELS measurement of nanometer-scale silicon tips and filaments. *Physical Review B*, 60:5641–5652, 1999.
- [9] A. M. Sánchez, R. Beanland, M. H. Gass, A. J. Papworth, P. J. Goodhew, and M. Hopkinson. Mapping quantum dot-in-well structures on the nanoscale using the plasmon peak in electron energy loss spectra. *Physical Review B*, 72:075339, Aug 2005. doi: 10.1103/PhysRevB.72.075339. URL <http://link.aps.org/doi/10.1103/PhysRevB.72.075339>.

- [10] K. Iakoubovskii, K. Mitsuishi, Y. Nakayama, and K. Furuya. Mean free path of inelastic electron scattering in elemental solids and oxides using transmission electron microscopy: Atomic number dependent oscillatory behavior. *Physical Review B*, 77:104102(7), 2008.
- [11] R. F. Egerton. Electron energy-loss spectroscopy in the TEM. *Reports on Progress in Physics*, 72:016502–016527, 2009.
- [12] R. Kashtiban, U. Bangert, I. Crowe, M. P. Halsall, B. Sherliker, A. J. Harvey, J. Eccles, A. Knights, R. Gwilliam, and M. Gass. Structural and compositional study of erbium-doped silicon nanocrystals by HAADF, EELS and HRTEM techniques in an aberration corrected STEM. *Journal of Physics: Conference Series*, 2010.
- [13] P. D. Nguyen, D. M. Kepaptsoglou, Q. M. Ramasse, and A. Olsen. Direct observation of quantum confinement of Si nanocrystals in Si-rich nitrides. *Physical Review B*, 85:085315, Feb 2012. doi: 10.1103/PhysRevB.85.085315. URL <http://link.aps.org/doi/10.1103/PhysRevB.85.085315>.
- [14] J. M. Ramírez, Y. Berencén, L. López-Conesa, J. M. Rebled, A. Eljarrat, S. Estradé, F. Peiró, J. M. Fedeli, and B. Garrido. (invited) optimizing er-doped layer stacks for integrated light emitting devices. *ECS Transactions*, 53(4):81–84, 2013.
- [15] Y. Berencén, O. Jambois, J. M. Ramírez, J. M. Rebled, S. Estradé, F. Peiró, C. Domínguez, J. A. Rodríguez, and B. Garrido. Blue-green to near-IR switching electroluminescence from si-rich silicon oxide/nitride bilayer structures. *Optics Letters*, 14:2617–2619, 2011.
- [16] R. F. Egerton. *Electron Energy-Loss Spectroscopy in the Electron Microscope*. Springer US, 3rd edition, 2011.
- [17] C.-W. Lee, Y. Ikematsu, and D. Shindo. Measurement of mean free paths for inelastic electron scattering of si and sio<sub>2</sub>. *Journal of Electron Microscopy*, 51:143–148, 2002.
- [18] S. Ossicini. Optical properties of confined Si structures. *Physica Status Solidi A*, 140:377–390, 1998.
- [19] E. Talbot, R. Lardé, P. Pareige, L. Khomenkova, K. Hijazi, and F. Gourbillau. Nanoscale evidence of erbium clustering in Er-doped silicon rich silica. *Nanoscale Research Letters*, 8:331–340, 2013.



## Chapter 7

# Si-NCs embedded in dielectric matrices

“Any sufficiently advanced technology is indistinguishable from magic.”

---

Arthur C. Clarke, *Profiles of the Future.*

In this chapter, we present a novel analytical strategy, useful in order to probe structural and electronic properties of single silicon nanocrystals (NCs) embedded in a dielectric matrix. We tested this strategy in three systems with different embedding dielectric matrices ( $\text{SiO}_2$ , SiC and  $\text{Si}_3\text{N}_4$ ). Experiments were performed using a monochromated and aberration corrected Titan low-base microscope, operated at 80 kV to avoid sample damage and to reduce the impact of radiative losses. Then, a novel analysis approach allowed to disentangle the electronic features corresponding to pure Si-NCs from the spectral contribution of the surrounding dielectric materials, through an appropriate computational treatment of hyperspectral datasets. First, the different materials were identified by measuring the plasmon energy. Notice that due to the overlapping of Si-NCs and dielectric matrix information, the variable shape and position of mixed plasmonic features increases the difficulty for non-linear fitting methods to identify and separate the components in the EELS signal. We managed to solve this problem for the silicon oxide and silicon nitride systems by applying multivariate analysis (MVA) methods that can factorize the hyperspectral datacubes in selected regions. By doing so, the EELS spectra are re-expressed as a function of abundance of Si-NC and dielectric signal components. EELS contributions from the embedded nanoparticles as well as their dielectric surroundings are thus separated, studied, and compared with the crystalline silicon from the substrate and with the dielectric material in the matrix.

## 7.1 Introduction

Silicon-based devices represent the dominant technology for photovoltaic applications both at research and production stages. As discussed in the previous chapter for photonic applications, the reason for this is the maturity, high availability and low cost of the technological processes involved. Theoretically, the efficiency of a bulk silicon solar cell is limited by the fixed band gap energy of this material<sup>1</sup>. In order to overcome this limitation, alternative structures such as tandem solar cells have been proposed<sup>2,3</sup>. In this tandem configuration, the bulk silicon is complemented with one or more solar cells presenting different band gap energies.

A suitable approach is a superlattice (SL) layer composed of ordered silicon nanocrystals (Si-NCs) embedded in a dielectric medium<sup>4</sup>. The functionality in this type of nanostructure is related to the Si-NC band gap energy, higher than that of bulk silicon. The size and spatial distribution of the Si-NCs and the surrounding dielectric media greatly influence the performance of the final photovoltaic device. For instance, the quantum confinement of charge carriers (QC)<sup>5</sup> is a size-dependent effect. Due to the QC effect, band gap energy is inversely proportional to NC size.

Most of the experimental techniques that are commonly used for the assessment of performance in these systems – photo- and electro-luminescence, charge transport measurements, Raman scattering spectroscopy, to name a few – do not allow a direct characterization of the individual NCs. However, different techniques available in transmission electron microscopy (TEM) do access these properties at high spatial resolution. In particular, high resolution (HR-) and energy filtered (EF-) TEM are the most commonly employed techniques. As a combination of structural and chemical characterization, EFTEM has been intensively used in the evaluation of the Si-NCs size after deposition<sup>3,6,7</sup>.

Among the electron microscopy techniques, EELS performed in an aberration corrected STEM instrument using a monochromated probe offers best spatial and energy resolution. In this chapter, we propose a low-loss EELS examination, appropriate for the individual characterization of the Si-NCs.

### 7.1.1 Sample details and preliminary examinations

The systems considered for the present study, designed as active layers for tandem solar cells, consist of silicon-based multilayer stacks combining stoichiometric- and Si-rich-based dielectric layers. Three dielectric materials were used as a barrier:  $\text{SiO}_2$ ,  $\text{SiC}$  and  $\text{Si}_3\text{N}_4$ . The respective non-stoichiometric layers were: silicon rich oxynitride, carbide and nitride (SRON, SRC and SRN). The layers were deposited by plasma-enhanced chemical-vapor deposition (PECVD) with thicknesses below 5 nm. After the deposition process, the Si excess was precipitated,

and phase separation was induced in order to achieve the Si-NC formation. For this purpose, different accumulative annealing treatments were used, with temperatures ranging from 1100°C to 1150°C depending on the compound and, in the SiC sample, a previous annealing step at 600°C. The final goal is the formation of a silicon quantum dot superlattice, on top of a bulk silicon solar cell (see Fig. 7.1 for a diagram of the structure). These systems were grown in the context of the European 7th framework project “silicon NAnodots for Solar Cell Tandem” (NASCEnT). More information regarding the NC superlattice growth can be found in Ref. 3 for the  $\text{SiO}_2$  sample, in Ref. 3 for the SiC system and in Ref. 6 for the  $\text{Si}_3\text{N}_4$  system.

Electro-transparent specimens for STEM observation were prepared by mechanical polishing followed by an  $\text{Ar}^+$  attack, as explained in Appendix A, and preliminary observations were performed in a JEOL J2010 F (S)TEM. Figure 7.2 (a) and (b) correspond to these observations, for the  $\text{SiO}_2$  and  $\text{Si}_3\text{N}_4$  samples, respectively. HRTEM and EFTEM measurements in the J2010 were used to evaluate the quality of the fabricated multilayers, measuring abruptness and homogeneity of the layers<sup>3,6,8</sup>. The EFTEM experiments confirmed the formation of Si-NCs within alternative layers in the stack, and were used to measure an average crystal size. As expected, crystal sizes were found to be related to the silicon-rich layer thickness, in all studied cases cases around or below 5 nm. From these first observations, it was clear that conventional electron microscopy would not suffice for the individual characterization of the Si-NCs and their environment.

As in the previous chapter, some preliminary experiments indicated that

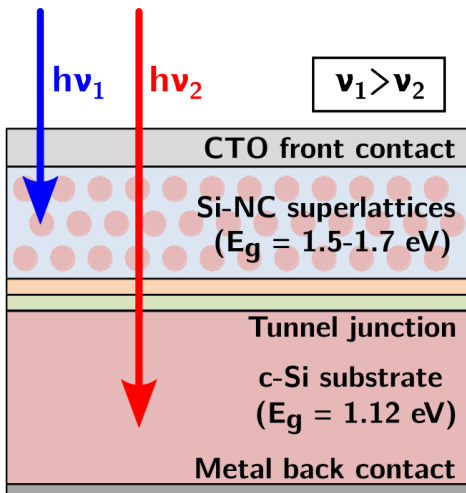


**Fig. 7.1** Schematic diagram for a tandem solar cell, showing the arrangement of the Si-NC superlattices on top of the c-Si solar cell. Arrows represent the incoming solar radiation, the high-energy photons (blue arrow) are absorbed by the higher band gap energy material, whereas the low-energy ones (red arrow) are absorbed within the c-Si bottom cell. CTO stands for conductive transparent oxide.

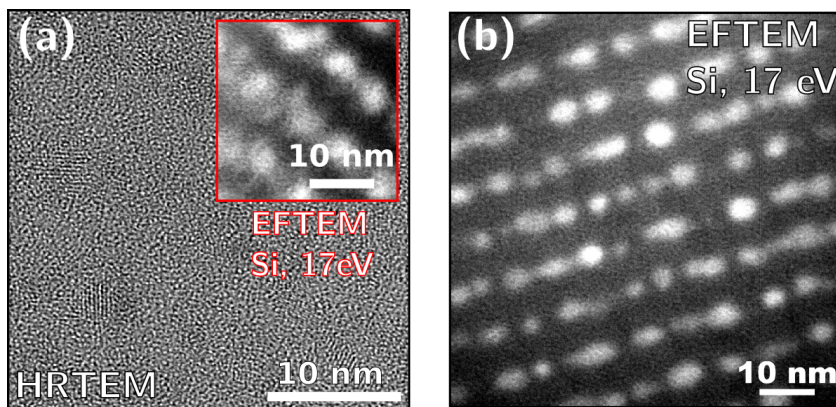


**Fig. 7.2** (a) HRTEM image of the  $\text{SiO}_2$  based sample showing crystalline lattice planes from the Si-NCs. The inset shows an EFTEM image of the same sample, where the bright contrast corresponds to Si-NCs. (b) EFTEM image of the  $\text{Si}_3\text{N}_4$  sample, with an analogous contrast.

higher voltages in STEM mode (*i.e.* 300 keV) and/or larger acquisition times could damage the Si-NCs and their environment, modifying or even destroying the studied structures in the process. Given the beam sensitivity of the Si-NCs, low accelerating voltages were used in the experiment. As the experiment is usually designed to minimize radiation dosage by maximizing acquisition speed and reducing beam current density, the acquired spectral data could present low signal-to-noise ratios (SNRs). Nevertheless, since the plasmon signal is the strongest one in the EELS spectrum but for the zero-loss peak, the acquisition of low-loss EELS at low accelerating voltages and short acquisition times is feasible, in terms of SNR, when probing beam-sensitive materials. A probe-corrected FEI Titan (S)TEM, operated at 80 kV, was used to obtain the EELS data at high spatial resolution.

Three sets of low-loss EELS-SI and simultaneously acquired high-angle annular dark field (HAADF) images were obtained, from the  $\text{SiO}_2$ ,  $\text{SiC}$  and  $\text{Si}_3\text{N}_4$  systems, respectively. A collection angle of  $\sim 2.5$  mrad, a convergence angle of  $\sim 26$  mrad, and an acquisition time of 0.03 s per spectrum were employed in the acquisition. Pixel sizes between 0.2 – 0.6 nm were selected for the EELS-SIs. The microscope conditions were thus adjusted to acquire HAADF-EELS datasets containing a few Si-NCs and a portion of the barrier layer. Exceptionally, for the silicon carbide sample, bigger datasets were acquired containing more than one period to portray wider scale structural phenomena. Large areas of the specimens in relation to pixel size were covered in this way with no apparent beam damage.

According to the full width at half maximum (FWHM) measured from the ZLP of the EELS-SI, energy resolution was kept below 0.2 eV in all experiments.

## 7.2 Phase identification and MVA analysis

We developed an original methodological approach for EELS data treatment to elucidate the individual properties of the Si-NCs. The reasons to propose this strategy stem from the nature of the analyzed samples: multilayer stacks combining dielectric barriers and Si-enriched layers that contain Si-NCs (precipitated during the post-deposition annealing treatment). In this configuration, the Si-NCs are completely surrounded by the dielectric material, and it is unlikely to prepare an electro-transparent TEM specimen that will give a direct and pure Si-NC low-loss EELS measurement in a STEM experiment. In other words, surrounding material will be present over and/or under the NC in the TEM lamella, so that the incident  $e^-$  will go through it and it will contribute to the EEL spectra in the NC region. The reason for this limitation is the size of the NCs, below 5 nm in diameter, and the geometry of the embedded particle and matrix system. As in the preceding chapter, and in the related literature<sup>9,10</sup>, all measured spectra present a mixture of nanoparticle and matrix contributions, at least. Nevertheless, in this work we show that indirect low-loss EELS calculations revealing the electronic and structural properties of the individual Si-NCs are feasible by the appropriate use of computational methods.

### 7.2.1 Analytical methodology

The large amount of raw data acquired for each system further motivated the development of a simple, yet fast and powerful, computational treatment based on the prior identification of phase compositions through model-based fitting and segmentation of the datasets by mathematical morphology techniques. Moreover, factorization of the EELS-SI is achieved using multivariate analysis (MVA) algorithms, allowing us to separate the contribution of the Si-NC to the EELS spectra. In this way we could analyze a collection of several EELS-SI with hundreds of pixels and 2048 spectral channels each.

#### Identification and segmentation of data regions

The first part of the applied treatment is based on the experiences gathered through the several studies of the low-loss EELS of semiconducting devices, presented in this thesis, in which the characterization of the plasmon peak revealed structural and compositional information from the examined materials. Following a standard low-loss analysis scheme, all spectra had their energy axis calibrated

using the ZLP and a measure of their relative thickness,  $t/\lambda$ , was obtained, from which the absolute thickness of the material can be estimated. Additionally, a Fourier-log algorithm was used to produce single scattering distribution (SSD) spectra that can be compared to the original spectra to assess the impact of plural scattering. This is important because plural scattering contribution to the spectra from thicker specimens can pose a problem to further analyses of the data.

The plasmon peak in bulk c-Si has an energy of  $\sim 16.7$  eV, while the dielectric materials studied in this work have higher energy plasmons,  $\sim 22.5$  eV for  $\text{SiO}_2$ ,  $\sim 23.7$  eV for  $\text{Si}_3\text{N}_4$  and  $\sim 21.5$  eV for SiC. This difference is large enough to distinguish each material by their characteristic plasmonic signature in the EELS spectra. An example of this, illustrated with EELS spectra from the  $\text{SiO}_2$  sample, is given in Fig. 7.3(b) and (c). These spectra contain all the features examined in this work: the ZLP, the onset of valence transitions at low energies, and the plasmon peaks. Plasmon peaks were fitted, using a simple Lorentz model, with 2 fitting regions. These regions were selected according to the position of the low-loss maxima. In some regions, the Si-NC plasmon became apparent over a background signal similar to the one measured in the regions of “pure dielectric” expected composition. Hence, the fit energy window was modified to adjust only the area around the Si-NCs plasmon. For each spectrum the fit window is centered on its intensity maximum, which is also a fitting parameter.

From the analysis of a given EELS-SI with this method, a plasmon energy,  $E_P$ , map is produced which we then analyze through a histogram thresholding approach. Our aim here is to identify regions of the dataset where the spectra and their neighbors show “dominant Si-NC” or “pure dielectric” plasmonic features according to a defined threshold depending on the material. For this plasmon fingerprinting we impose the condition that a certain pixel of the  $E_P$  map (corresponding to a spectrum in the EELS-SI) is labeled as belonging to one of these two classes: the dominant Si-NCs (in fact a mixture of Si-NCs and the surrounding matrix) or the dielectric phase. However, the allocation of each pixel to a specific class (technically, Boolean masks, at this stage) generated by this approach alone may not be useful for several reasons. First, thresholding alone applied to an image may generate a mask that includes small disconnected spatial features, such as Fig. 7.3(d), like separate regions containing only a single or a few pixels without physical meaning. Also, spatial features may appear to be connected, and identified as one even if only joined by few pixels. Finally, it is desirable to identify big enough, yet separate, spatial features in the EELS-SI no matter what shape they may have. For this purpose, we developed an application in the framework of the Hyperspy toolbox<sup>11</sup> that takes advantages of the computer vision tools included in the n-dimensional image analysis library of scientific Python (ndimage in SciPy). Operating over the binary identification

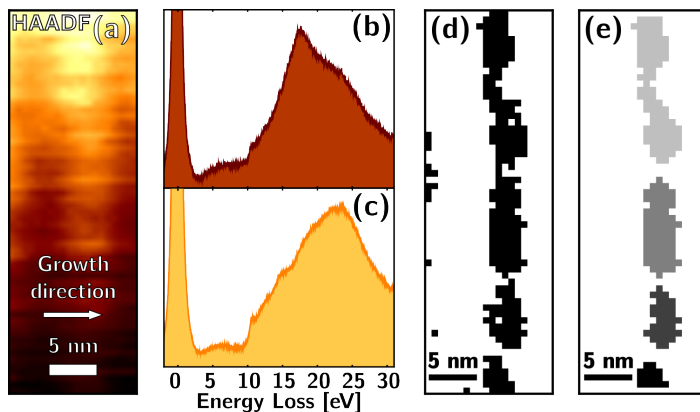


**Fig. 7.3** Typical HAADF-EELS data from the  $\text{SiO}_2$  sample. (a) displays the HAADF intensity (the image is rotated as indicated). (b) and (c) contain typical energy-loss spectra, acquired at the Si-rich and barrier regions, respectively. (d) shows a binary mask resulting from the thresholding of the corresponding EELS-SI. In this case, the pixels portrayed in black color have been found to contain spectra with  $E_P < 19$  eV. (e) shows the map of individual elements labeled as “dominant Si-NC” regions generated from the previous mask after selecting connected regions only.

maps, mathematical morphology operations act like a fast and powerful filter on the mask, allowing to select the degree of connectivity required from the regions to be labeled. Namely, the  $E_P$  map is filtered using binary opening and closing operations, with a structural element that selects connected regions only. Once a filtered mask has been produced, see Fig. 7.3(e), the labels are assigned in a simple and straightforward step. As a result, there exist the possibility to locate a spatial region of the original EELS-SI which spectra fulfill a certain requirement, then access it regardless of its shape, and operate with it as a separate sub-dataset with the same number of dimensions as the original dataset. Additionally, the size of the identified region is automatically measured as the number of pixels that fulfill the imposed condition.

After this procedure, a collection of sub-datasets allocated to the class of “dominant Si-NCs” or “pure dielectric” regions was generated. All the results presented in this work were achieved taking those regions as a starting point. For example, by averaging the spectra within a given region, noise-free spectra can be obtained that reveal its characteristic EELS features. Indeed, using this strategy one can obtain material information or, depending on the case and region, get close estimates of the pure Si-NC or pure dielectric EELS data.

Figure 7.4 shows some examples of energy-loss spectra for the three systems with different dielectric matrices ( $\text{SiO}_2$ ,  $\text{SiC}$  and  $\text{Si}_3\text{N}_4$  as labeled in the figure).

For each matrix, a pair of spectra representative of the classes “Si-NCs” or “pure dielectric” (labeled as barrier) are drawn. In these plots, the raw spectra are presented as color-filled areas, and the black lines define the averaged spectra of a specific sub-data set of each class, identified following the segmentation procedure explained above. In the figure, the improvement of the SNR from raw to average spectra is evidenced. But, interestingly enough, it is also clear that the spectra from the class “dominant Si-NC regions” present significant differences depending on the matrix, revealing the impact of the different dielectric backgrounds.

Although this mixing will increase the difficulty in analyzing and interpreting results from the spectra, EELS may be the less problematic (S)TEM technique for extracting information arising solely from the Si-NCs. Other methods were found to be not a reliable source of structural and chemical information regarding the Si-NCs (EFTEM, HAADF, or  $t/\lambda$  imaging)<sup>9</sup>.

### MVA factorization

Our analysis continued by focusing on the factorization of the low-loss EELS spectra by MVA within the detached subsets of data of the class “dominant Si-NCs” features. As explained in Sec. 2.2.1, MVA factorization is performed by using computational tools that analyze a given matrix of spectral data and decompose it into a number of components. These components constitute additive

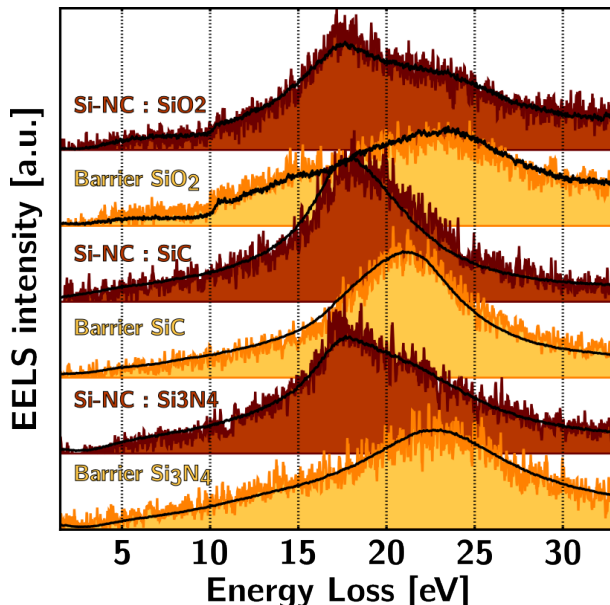


**Fig. 7.4** Raw (color-filled areas) and average (black lines) energy-loss spectra from the three examined samples. The spectra are averaged or extracted from regions identified as belonging to the class of “dominant Si-NCs” or to the class of “dielectric” region using threshold values of the  $E_P$  plasmon distribution.

contributions to a model of the EELS data, which is expressed as the product of the corresponding factors and abundance maps. Factors have the same number of channels as the input EELS spectra and an associated abundance map indicating its spatial distribution, with the same number of pixels as the original EELS-SI, can be obtained. A legitimate guess is that it might be possible to retrieve the contribution corresponding to the Si-NCs by performing a factorization of the whole EELS-SI by using MVA algorithms. It turns out that for most cases this is a difficult task because low-loss EELS is not always optimized as a direct input for MVA. The major reason for this is the fact that, in many cases, the presence of different phases in the examined materials translates into an energy shift of the plasmon peaks. This peak shift, which is usually an interesting subject of study, increases the number of dimensions for the factorization. As a result, multiple factors appear associated to a single shifting feature, hindering the interpretation of the results. With these limitations in mind, MVA factorization was performed on the aforementioned sub-datasets, which are given by the mixture of two competing contributions, the Si-NC plasmon peak and a dielectric-type background peak.

MVA factorization is generally performed in the EELS community using decomposition by principal component analysis (PCA), followed by blind source separation (BSS) by independent component analysis (ICA)<sup>12–16</sup>. The application of such an approach to low-loss EELS presents an additional difficulty because the mutually independent sources assumption in ICA may not be necessarily fulfilled in the hyperspectral data. In this work, two different methods were used, the non-negative matrix factorization (NMF, included in Hyperspy)<sup>17</sup>, and the Bayesian linear unmixing (BLU, available as a Matlab code)<sup>18,19</sup>. These two algorithms have in common the so-called positivity assumption, *i.e.* sources are supposed to be positive. This constrain fits well to the nature of EELS spectra, as no negative contribution is expected. The BLU algorithm imposes an extra additivity constrain to the sources, meaning that the sum of all contributions should be equal from pixel to pixel. Additionally, as this algorithm is initialized by a set of factors determined from a geometrical algorithm (N-FINDR in this work), the resulting set of factors is expected to be related to the possibility to find pixels containing spectral components as pure as possible (least mixed pixels). Gaussian statistical distribution of the noise is also required for BLU.

We added spike removal and Poisson normalization steps to the data treatments prior to the application of any of these MVA algorithms<sup>20</sup>. In the first step, spikes are detected by thresholding the first derivative of the spectral data and removed by spline interpolation. In the second one, the Poissonian nature of the statistical distribution in EELS is taken into account, and data are normalized to approach a Gaussian distribution. With this normalization we expect to improve the suitability of the input data for the BLU algorithm. Both methods

are included in Hyperspy, and a Matlab application was developed in order to use the Poisson-normalized data-cubes together with the available BLU program.

### 7.2.2 System I: silicon oxide barriers

Figure 7.5 presents some results from one of the HAADF-EELS datasets corresponding to the  $\text{SiO}_2$  system. Fig. 7.5(a) shows the HAADF-STEM image obtained in a region that contains both silicon enriched  $\text{SiO}_2$  layer and a  $\text{SiO}_2$  barrier, and Figs. 7.5(b) and (c) show the  $t/\lambda$  ratio and the  $E_P$  maps, respectively, as calculated from the corresponding EELS-SI. The faint contrast through the center of both HAADF and  $t/\lambda$  maps indicates the presence of the Si-rich layer. Also, a  $t/\lambda$  value around 0.25 tells us that this is a very thin sample and that the impact of plural scattering should be low. An alternative to the  $E_P$  map is to represent the values of  $E_P$  as a histogram of frequencies as shown in Fig. 7.5(d). The latter is useful to understand the color code in the map and to assess the  $E_P$  distribution. The two significant classes are easily distinguished in the histogram where  $E_P$  thresholds of 19 eV and 22.3 eV, indicated by lines in Fig. 7.5(d) and by region contours in Fig. 7.5(c), were selected to define the class of “dominant Si-NC” or “pure dielectric” features. Notice also that the energy resolution of the experiment, indicated by the ZLP, is below 0.2 eV, the size of one bin in the histogram.

The barriers and the Si-rich region seem to be well defined, with little variation of  $E_P$  through consistent areas. While  $E_P$  for the barriers is below 23 eV, the corresponding plasmon maximum is  $\sim 23.7$  eV, due to the asymmetric shape of this peak. It is now clear that the examined area contains a full dielectric barrier, on the left-hand side of the image, a total of 4 Si-NC regions, featured at the center, and part of a second barrier, on the right-hand side. The image also shows that the width of the dielectric layer and Si-rich layers remained unchanged after annealing, both layers being  $\sim 5$  nm in width. The Si-NCs appear to be confined inside the Si-rich layer. Other areas of this  $\text{SiO}_2$  multilayer were scanned, showing similar results along the different periods.

Once the regions are defined, average spectra may be obtained from the pixels within. Two of these spectra, from the “dominant Si-NC” region at the center of the image and the “pure dielectric” barrier on the left-hand side, are shown as black lines in the first two panels of Fig. 7.4. The raw spectra that are shown below the lines as color-filled areas were hand picked from a single pixel within these two regions. Some features evidence the presence of a contribution from a dielectric-like inelastic scattering to the EELS signal in the Si-NC region. The main one is the presence of a shoulder at  $\sim 24$  eV that can be related to the  $\text{SiO}_2$  plasmon, present at this energy. Also, a strong peak onset at  $\sim 9.5$  eV and spanning several more eVs is detected, related to the band gap of  $\text{SiO}_2$ . This

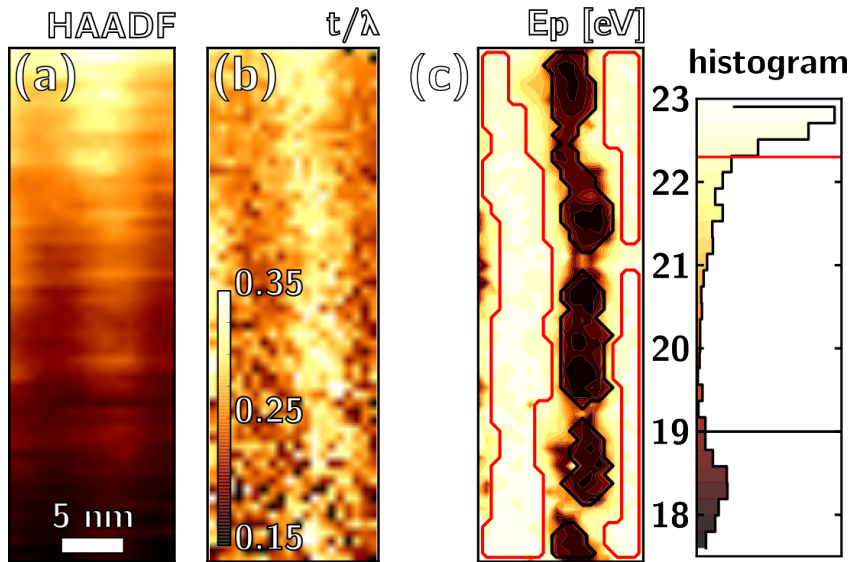


**Fig. 7.5** Panel (a) displays the HAADF intensity while (b) and (c) show the  $t/\lambda$  and  $E_P$ , respectively, of the simultaneously acquired EELS-SI from a  $\text{SiO}_2$  sample. (d) shows the histogram corresponding to the  $E_P$  map in (c). In both last panels black and red lines indicate the threshold of the "dominant Si-NC" and "pure dielectric" regions. The process to identify the very same "dominant Si-NC" regions was illustrated in Fig. 7.3.

is in good agreement with our picture of crystalline silicon particles embedded in a dielectric medium giving overlapped contribution to EELS, but does not constitute a direct confirmation.

MVA factorization by the NMF method did prove to be useful as an indirect method to confirm it. Let us focus on the specific "dominant Si-NC" region highlighted on top of Fig. 7.5(c). Fig. 7.6(a) shows the three main factors extracted from NMF. The contributions to the EELS data from both dielectric and Si-NC phases are identified with the first two components. Using a RGB code, we assign green color to the C1 component, corresponding to the Si-NCs, red one to the C2 component corresponding to the dielectric contribution, and blue color to C3, that reveals a sudden change in sensibility in the detector at mid-channel scale.

The number of factors used for NMF was chosen by examination of the *scree* plot after PCA. A sanity check was performed, by comparing the decomposition reconstructed signal with raw spectra (residuals method). The plot in Fig. 7.6(b) illustrates this method; two NMF reconstructed spectra (lines) and two raw spectra, one from each representative region, are shown to be in good agreement.

Panels (c)-(e) in Fig. 7.6 show the abundance maps corresponding to these

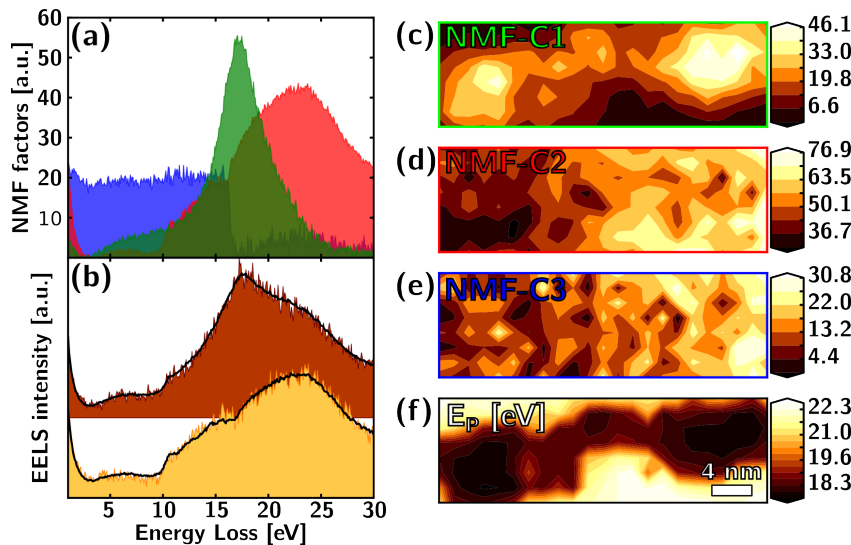


**Fig. 7.6** MVA analysis by NMF of Si-NCs in the oxide sample. (a) main factors, corresponding to the Si-NCs (green), the dielectric barrier (red) and a detector artifact (blue). (b) shows the reconstruction of the EELS data from the decomposition model vs the raw model data. (c)-(e) show the corresponding abundance maps of these factors, using the same RGB color coding. Notice the 90° rotation with respect to Fig. 7.5; (f) shows the plasmon energy map for the same area and can be used as visual reference.

three factors. Notice that these plots are rotated 90° clockwise with respect to the map in Fig. 7.5(c). Additionally, a rotated  $E_P$  map is included, in Fig. 7.6(f), and can be used as a reference. The spatial distribution of these components evidences two Si-NCs (in good agreement with the  $E_P$  map) with a  $\text{SiO}_2$  background. The detector artifact component (blue) presents a rather random spatial distribution and a smaller abundance than the other two.

The factorization reveals that the EELS contributions corresponding to the Si-NC and the  $\text{SiO}_2$  matrix present plasmon maxima at  $\sim 17.3$  eV and  $\sim 22.7$  eV, respectively. The 1-eV energy shift between the  $\text{SiO}_2$  in the barrier ( $\sim 23.7$  eV, plasmon maximum) and in the particle surroundings indicates the probable formation of a nitrogen oxide in the matrix from the SRON. The absence of further plasmon shifting within the barrier indicates a low and homogeneous diffusion of nitrogen through the dielectric.

### 7.2.3 System II: silicon carbide barriers

For the SiC sample we succeeded in acquiring and analyzing large EELS-SI, with sizes up to more than  $120 \times 120$  pixels. The resulting  $t/\lambda$  and  $E_P$  maps are shown in Fig. 7.7. The area covered in this image spans over 3 periods of the multi-layer (more than  $40 \times 40 \text{ nm}^2$ ), with a pixel-to-pixel resolution better than 0.4 nm. Smaller EELS-SI were also acquired and analyzed, as for oxide samples, but the use of a wider region was necessary to study a larger scale structural phenomenon in this sample using the chemical sensitivity of low-loss EELS. Again,  $t/\lambda$  confirms that the TEM sample is particularly thin at the examined region, around 0.25 times the electron inelastic mean free path,  $\lambda$ . No contrast related with the difference in  $\lambda$  between Si-NC and the dielectric region is found, Fig. 7.7(a). Nevertheless, some faint fringes can be distinguished at the center of the image,

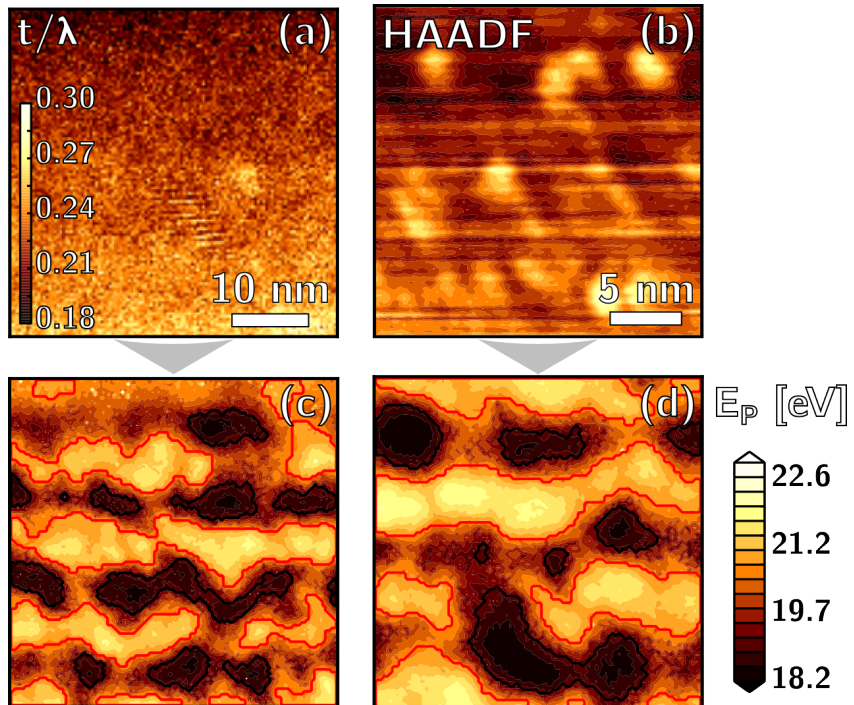


**Fig. 7.7** (a) and (c) display the  $t/\lambda$  and  $E_P$  maps, respectively, calculated from the same EELS-SI covering a 3-period wide region of the carbide sample. (b) and (c) show a HAADF image and  $E_P$  map, respectively, from an acquisition covering a smaller region. In the  $E_P$  maps, black and red lines are used, as in Fig. 7.5(c), as region boundaries.

coming from the elastic scattering contrast in the ZLP intensity (equivalent to bright-field imaging), which are indicative of the presence of a crystalline particle. The simultaneously acquired HAADF images, see Fig. 7.7(b), show a weak contrast of the silicon particles in the carbide medium, not useful for the characterization of neither particles nor barriers.

Figure 7.7(c) and (d) display the  $E_P$  map with thresholds at 18.5 eV (red line) and 20.3 eV (black line). A procedure similar to the one used for the oxide system was used to discriminate the “dominant Si-NC” and “pure dielectric” regions. c-Si and SiC plasmons are much closer than in the case of  $\text{SiO}_2$ , for which the thresholds were 19 eV and 22.3 eV, respectively, as evidenced by the energy-loss spectra in the middle of Fig. 7.4, taken from Si-NC and SiC regions. When averaging inside these “dominant Si-NC” and “pure dielectric” regions, it seems that the EELS low-loss features are sharp and differentiated. This indicates that the EELS contribution measured in the “dominant Si-NC” region has a much smaller impact from SiC than in the case of  $\text{SiO}_2$ , owing probably to the bigger size of the formed Si-NCs. Taking these considerations into account, we generated spatially averaged energy-loss spectra and examined them in order to identify both band gap and plasmon features. In these spectra a strong signal with an onset at  $\sim 2.5$  eV is evident, corresponding to the band gap energy of the SiC. No signal at lower energies could be consistently detected in this case. This indicates that the band gap signal of the Si-NCs, if present, is faint over the delocalized band gap signal of the surrounding SiC. For the plasmon peak, the contrast between regions is clear in both energy and width. The barrier material from the center of the “pure dielectric” regions presents a broad plasmon peak at  $\sim 21.5$  eV. This peak shifts smoothly to lower energies as we examine regions farther away, down to a sharp peak at  $\sim 17.5$  eV at the center of the “dominant Si-NCs” regions.

From the examination of the  $E_P$  maps in Fig. 7.7, we can tell that the dielectric barriers and silicon rich layers underwent some kind of segregation process. The inhomogeneity of the interfaces is apparent, and, although the dielectric and silicon rich multilayer structure is preserved, the gradient of  $E_P$  values through the map evidences an unintended inter-diffusion in the growth direction. The plasmon energies detected in the sample are only spatially consistent (meaning  $E_P$  values close to one of the two expected values) in small areas. In fact, the dielectric barriers do not always show a plasmon energy corresponding to pure SiC, indicating that the diffusion from the silicon-rich layer modifies the chemical composition of the barrier layer. Finally, the inhomogeneity of the Si-NCs size is greater than in the  $\text{SiO}_2$  system, with coalescence and vertical growth.

MVA factorization was also carried out in this EELS data-set, and the separation of a component related to the Si-NCs plasmon was achieved. However, it was difficult or impossible to obtain a consistent component associated with

the silicon carbide background. We suspect the reasons for this are a continuous change in the energy of the silicon carbide plasmon, caused by the composition gradient, and an imperfect phases separation in this structure. Thus, no MVA results are shown in this case.

#### 7.2.4 System III: silicon nitride barriers

As for the previous two systems, the silicon nitride multilayer was probed by HAADF-EELS and data were analyzed using a similar methodology. Fig. 7.8 presents three plasmon energy maps for this sample obtained in different regions of the multilayer stack. Black and red lines show the nature of the EELS plasmon in the enclosed regions, “dominant Si-NC” and “pure dielectric”, respectively. The same energy thresholds as for  $\text{SiO}_2$ , 19 eV and 22.3 eV, were used since  $\text{Si}_3\text{N}_4$  plasmon energy is similar to that of  $\text{SiO}_2$ . Concerning the morphology, the configuration of barriers and Si-rich layers is preserved, as in the case of  $\text{SiO}_2$ . However, the contribution of the dielectric plasmon as a background to the EELS data in “dominant Si-NC” regions is not as evident as in the oxide case. This is because silicon nitride lacks the strong and characteristic low-energy peaks of the silicon oxide EELS features.

Yet, MVA was able to separate the contributions of the Si-NC and the dielectric background to the EELS data in the “dominant Si-NC” region. Fig. 7.9 shows an example of MVA analysis, corresponding to the particle at the right-hand side of Fig. 7.8(c). In this case, we used a BLU algorithm with three components and a wider spatial crop in order to include the dielectric regions on top and bottom of the particle also. The resulting components show an analogous re-

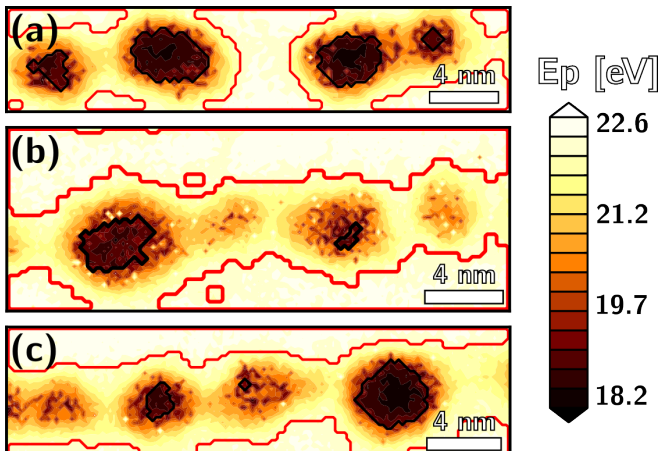


**Fig. 7.8** Panels (a)-(c) feature plasmon energy maps from different EELS-SI acquired in the nitride sample. Black and red lines are used, as in Fig. 7.5(c) and 7.7(b), as region boundaries.

sult to that of the NMF applied to  $\text{SiO}_2$ . Figure. 7.9(a), shows one of these components (green factor), corresponding to the Si-NC with an abundance map located within the particle. The other two components correspond to the dielectric background plasmon convolved with a small positive or negative intensity step from the detector. When added, these contributions cancel out, leaving only the background peak, also in Fig. 7.9(a) (red factor). We also observe a good agreement between the modeled spectra after decomposition and the raw spectra, as depicted in Fig. 7.9(b). The contribution from the Si-NC particle in Fig. 7.9 corresponds to a plasmon energy of  $\sim 17.8$  eV. The barrier and matrix dielectric plasmon energies determined from averaging and factorization were found to lie at  $\sim 22.7$  eV. It is, thus, strongly suggested that the dielectric material from the barrier and the particle surroundings have a similar composition, altered in the nearest vicinity of the Si-NC only. Indeed, “pure dielectric” regions are found in

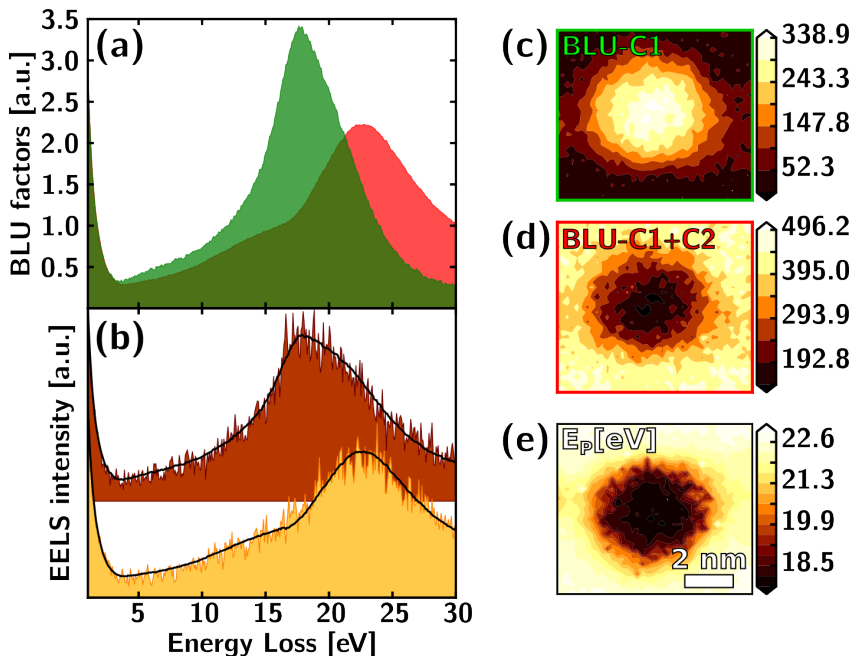


**Fig. 7.9** MVA analysis of Si-NCs in the nitride sample by BLU. Panel (a) shows estimated main factors related to Si-NCs (green) and a mixture of dielectric and instrument-related components (red). (c) and (d) show the abundance of the factors in panel (a), using the same red-green color coding. Meanwhile, a reconstruction of the EELS signal from the decomposition model vs the raw EELS data is shown in panel (b). Panel (c) gives the plasmon energy map the same area.

the silicon-rich layer, between Si-NCs, see Fig. 7.8(a).

From the  $E_P$  maps in Fig. 7.8 and the BLU abundance maps in Fig. 7.9, it seems that the particles in the silicon nitride matrix are rounder than the ones in silicon oxide (and, of course, in silicon carbide). Other authors have found the Si-NCs formed in  $\text{SiO}_2$  to occupy irregular volumes<sup>9</sup>. Conversely, some of the Si-NCs in  $\text{Si}_3\text{N}_4$  are not completely formed while Si-NCs in  $\text{SiO}_2$  appear to have a very homogeneous distribution of sizes.

In these spectra, a strong signal with an onset at  $\sim 4$  eV is observed, near the band gap energy of  $\text{Si}_3\text{N}_4$ , at  $\sim 5$ eV. In the regions with a presence of Si-NCs, a lower band gap onset energy, at  $\sim 3.5$  eV, is observed.

### 7.2.5 Discussion and remarks

The separation between particle and surrounding material, in terms of EELS signal, has been proven feasible. One of the main reasons for this is the smaller delocalization distance for the quantum-confined Si-NC plasmon than for the band gap. Also, the relatively small expected difference between the dielectric functions of the Si-NCs and surrounding materials means the effects of interface plasmons can be considered negligible<sup>21</sup>. We should also mention that for any MVA technique, peak energy shifting and the existence of an intense background signal would negatively affect the final result<sup>22</sup>. In low-loss EELS we easily get both effects, the shifting of the plasmons linked to gradients in concentration or strain being a well-known feature in a wide range of systems. To complete the list, ZLP intensity is typically several orders of magnitude more intense than any other feature in low-loss EELS data. This means that MVA techniques are unsuitable to solve problems in which a continuous plasmon shift is a dominant characteristic or in which the ZLP masks out the relevant feature, as in low-lying band gap energies. In our case, the energy stability of the plasmons in selected areas and the correct alignment of the ZLP and energy windows before the MVA have been critical to enable the successful NMF and BLU analyses.

Our plasmon energy measurements have to be interpreted in the context of QC theory (as in Chapters 5 and 6), in which the plasmon peaks of Si-NCs are expected to show higher plasmon energies than those measured for c-Si ( $\sim 16.9$  eV). Ref. 10 proposes a phenomenological formula to relate plasmon energy with particle size in similar systems. Following this formula, a plasmon energy of 17.8 eV corresponds to cristallyne Si nanoparticles with diameters around 5.1 nm, which is in excellent agreement with the obtained results.

Yet, regarding the measured Si-NC plasmon energies for all systems, no consistent shift related to (apparent) particle size was found. Bearing in mind that QC effect implies an inverse relationship between particle diameter and plasmon energy, this is a surprising result. For instance, much smaller Si-NCs are formed

in  $\text{Si}_3\text{N}_4$  in comparison to the other systems. Nevertheless, no plasmon shift associated with the smaller size of these particles was found. This might indicate that the smallest particles are not fully crystalline.

To summarize, we have presented three different cases where the analysis of EELS maps is an advantageous technique when compared to other TEM-based approaches, although convolution of the interesting features is an inherent difficulty. In the previous chapter, a Drude model containing two plasmons also proved reliable. Nevertheless, when applied to carbide and nitride systems, it failed to give consistent measurements of neither  $E_P$  nor plasmon width. Our present experience indicates that this double plasmon model will only be reliable when the fitted features are well separated in energy and exhibit significant differences in FWHM, *i.e.* low energy narrow peak vs high energy wide peak (as in the case of Si-NCs in a  $\text{SiO}_2$  matrix). Conversely, when analyzing plasmonic features that are very close in energy and width, this method may not be reliable and may lead to uninterpretable or wrong results (as in Si-NCs in SiC and  $\text{Si}_3\text{N}_4$  matrices). Other works have examined Si-NCs in a silicon nitride matrix using a model-based fit analysis of EELS data found much higher variability of the calculated plasmon energies for the background<sup>10</sup>. Moreover, an additional disadvantage regarding model-based procedures is that EELS data acquired from thin specimens will be naturally noisy, as the inelastic scattering signal is diminished. Our phase identification and segmentation technique, followed by factorization by NMF and BLU algorithms, has proved to be capable of extracting relevant information from EELS data. More complex aspects of the low-loss EELS analysis are addressed in the following section.

### 7.3 Optoelectronic properties of the Si-NCs

Kramers-Kronig analysis (KKA) was carried out on the spectra to extract the complex dielectric function (CDF) from the Si-NCs and barrier dielectric. This analysis is based on the relationship between the energy-loss spectrum and the CDF of a given bulk material following the semi-classical formula for the single scattering distribution (SSD), see Sec. 2.1.2,

$$\text{SSD}(E) = \frac{I_0 t}{\pi a_0 m_0 v^2} \cdot \log [1 + \beta/\theta_E] \cdot \text{Im} [-1/\varepsilon(E)] \quad (7.1)$$

Where  $I_0$  is the elastic scattering (ZLP) intensity,  $t$  is the sample thickness,  $a_0$  is the Bohr radius,  $m_0$  is the electron rest mass,  $v$  is the electron velocity,  $\beta$  is the collection angle,  $\theta_E$  is the characteristic angle for inelastic scattering at a given energy loss  $E$ , and  $\varepsilon$  is the energy dependent CDF. Thus the pre-logarithmic factor, which will be called  $K$ , depends only on the ZLP intensity and the electron

kinetic energy  $T$ . The logarithmic factor will be called the angular correction,  $\Theta(\beta, E)$ .

The first step in KKA is to normalize the SSD. For the normalization step of KKA we have used two main approaches depending on the availability of refractive index values. If this value is available, the sum-rule of the Kramers-Kronig relations allows us to calculate  $K$ ,

$$K = \left(1 - \frac{1}{n^2}\right)^{-1} \frac{2}{\pi} \int_0^\infty \frac{\text{SSD}}{\Theta(\beta, E)} \frac{dE}{E} \quad (7.2)$$

Also, this approach allows measuring the thickness of the sampled region from the expression of  $K$  in eq. 7.1. The refractive indices of all the bulk materials involved in this samples are well known, so this approach may be used for spectra from the dielectric barriers or the crystalline silicon substrate. However, the values to be used for the Si-NCs MVA factors are not clearly known, since  $n$  depends on particle size<sup>23</sup>. For this reason, we have developed an alternative approach for the normalization step that rests on the previous estimation of the absolute thickness of the sampled region<sup>24</sup>. In this thickness normalization step, we use the value of  $t$  calculated in an adjacent region, of known  $n$ ,

$$K = \frac{I_0 t}{\pi a_0 m_0 v^2} = \frac{I_0 t}{T \cdot 332.5} \left[ \frac{\text{nm}}{\text{keV}} \right] \quad (7.3)$$

Also, for each KKA, a measure of the intensity (sum of channel values) of the ZLP is necessary. In the case of the MVA factors, this value is not directly available because the ZLP has to be cropped off or subtracted before MVA factorization. We measured and stored the  $t/\lambda$  values using the total and ZLP intensities,  $I_T$  and  $I_0$ , respectively, for each pixel. Using this value we can relate the integral of a given EELS signal,  $I_S$ , to the value of the ZLP intensity to which it would theoretically correspond using the following formula,

$$t/\lambda = \log(I_T/I_0) = \log(1 + I_S/I_0) \quad (7.4)$$

Hence, the ZLP intensity values that are needed for the normalization step in the KKA of MVA factors can be estimated from the  $t/\lambda$  mean value in a region where the factor is the dominant spectral feature (highest abundance). This KKA algorithm, including the two normalization options, was implemented for Hyperspy<sup>11</sup>, and is freely available. Also using this toolbox, a measurement of the atomic (molecular) density of electrons involved in the valence plasmon excitation,  $n_{eff}$ , was obtained, using the procedures explained in Sec. 2.1.2. Finally, electron effective mass values,  $m^*$ , were calculated as well, using the same procedure as in Sec. 5.4.2.

### 7.3.1 KKA in the Si-NCs and dielectric regions

KKA was used to calculate the CDF from the available spectra, namely, the “pure dielectric” region averaged spectra, the Si-NC and dielectric background spectra from MVA factors, and crystalline silicon (c-Si) single spectra acquired from the substrate (see Fig. 7.10).

On both silicon oxide and nitride cases, the first step was to perform KKA on the spectra identified as dielectric signals, using the corresponding refractive index for each material<sup>25</sup>,  $n_{\text{SiO}_2} = 1.5$  and,  $n_{\text{Si}_3\text{N}_4} = 2$ . For the MVA factors, the ZLP intensities were calculated from the signal integral and a mean of the calculated  $t/\lambda$  from a selected “pure dielectric” region of the EELS dataset.

These CDFs are depicted in Fig. 7.10(a) and (b); notice that, for silicon nitride, both dielectric CDFs, from MVA factor and averaged spectra, are found to be in excellent agreement with one another. On the other hand, CDFs for the silicon oxide differ in intensity and plasmon position. This is not unexpected, as the EELS average spectrum from the barrier region ( $\text{SiO}_2$ ) differs in plasmon position and width from the EELS contribution from the dielectric surrounding the Si-NC (SRON). Sample thicknesses were obtained from  $t/\lambda$  values. Both samples were confirmed to be particularly thin at the examined regions, with  $t \sim 48 \text{ nm}$  and  $t \sim 18 \text{ nm}$  for the silicon oxide and nitride matrices, respectively. These values were used for the normalization step in the KKA of the MVA factors identified as Si-NC signals. The  $t/\lambda$  mean values for the dominant Si-NC regions were used to determine ZLP intensity from the signal integral (Eq. (7.4)). The  $t/\lambda$  values are typically higher than in the dielectric region, indicating a decrease in the electron mean free path,  $\lambda$ , associated with the presence of the Si-NC. The Si-NC CDFs were then calculated, Fig. 7.10(c), showing a good agreement for particles within the silicon oxide and nitride matrices. For the sake of completeness, KKA was also applied to retrieve the CDF from a single spectrum acquired at the c-Si substrate in the silicon nitride system, see Fig. 7.10(c).

### 7.3.2 Band gap measurements

We measured band gap energies to add this information to our derived CDF. These results are summarized in Table 7.1. For the silicon oxide barrier, the band gap of  $\text{SiO}_2$  was observed at  $\sim 10 \text{ eV}$ , in good agreement with the literature<sup>26</sup>. This suggests, again, a very limited nitrogen diffusion from the silicon rich layer (SRON) to the  $\text{SiO}_2$  in the barrier.

The band gap of  $\text{Si}_3\text{N}_4$ , measured at  $\sim 4 \text{ eV}$ , is lower than the  $5 \text{ eV}$  value expected for the pure dielectric material. This is in good agreement with the measured plasmon energy shift in the barriers from the expected  $23.7 \text{ eV}$  to the obtained  $22.7 \text{ eV}$  (the measured  $E_P$  values are also included in Table 7.1). We thus propose the formation of a  $\text{SiN}_x$  ( $x < 1$ ) type matrix, and a growth mecha-

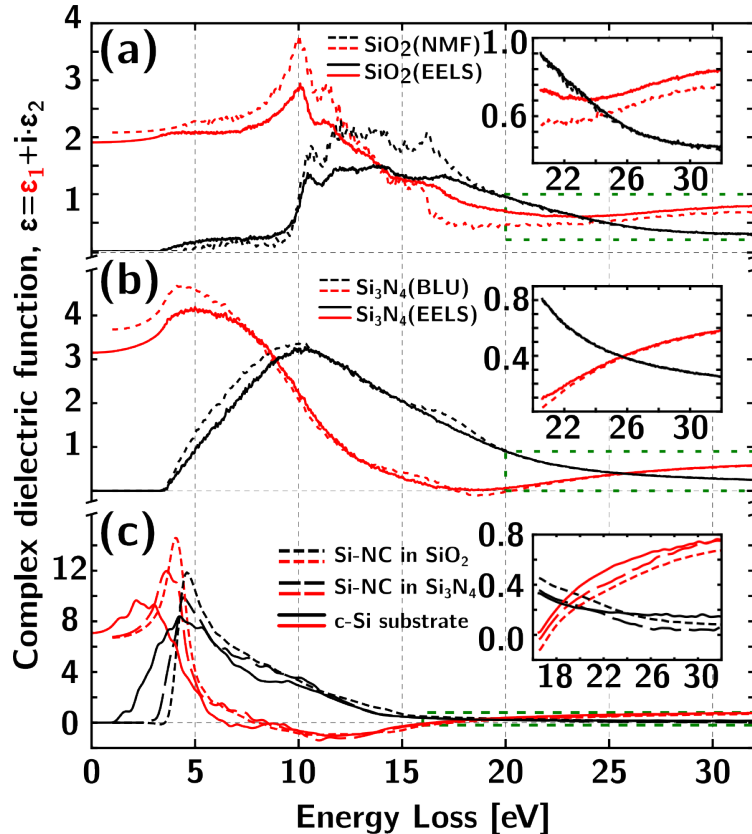


**Fig. 7.10** This figure shows the CDFs calculated from the KKA of experimental EELS spectra and MVA factors. In all of them, the real and imaginary parts of the CDF are indicated with red and black colors, respectively. Panels (a) and (b) display the CDFs calculated from silicon oxide and silicon nitride, respectively; energy-loss spectra from the different regions (solid lines) and NMF and BLU factors (dashed lines). Panel (c) displays the Si-NCs CDFs calculated from NMF and BLU, in the oxide and nitride samples, respectively, in dashed lines. Also in this panel is the CDF calculated from an energy-loss spectrum obtained in the c-Si substrate, in solid lines. The insets show in greater detail the regions of the CDFs highlighted using dashed line squares.

**Table 7.1** Summary of the band gap and plasmon energies and the electron effective masses, obtained for the three different systems in regions of interest. Notice that, for  $\text{SiO}_2$  and  $\text{Si}_3\text{N}_4$ , the values obtained from the barrier regions are obtained by averaging, while the ones from the matrix and the Si-NC regions are obtained by MVA. For SiC, only averaging is used, as explained in the text.

		$E_B/\text{eV}$	$E_P/\text{eV}$	$m^*/m_0$
$\text{SiO}_2$	Barrier	9.5	23.7	—
	Matrix	9.5	22.7	0.188
	Si-NC	3.0	17.3	0.129
SiC	Barrier	2.5	21.5	—
	Si-NC	—	17.5	—
$\text{Si}_3\text{N}_4$	Barrier	4.0	22.7	—
	Matrix	4.0	22.7	0.160
	Si-NC	3.5	17.8	0.133
c-Si substrate		1.3	16.9	0.1

nism for the Si-NCs from nucleation up to a critical size after which coalescence takes over, as in Refs. 27, 28, 10. The authors of those works attributed the decrease in plasmon energy to an increase of Si-Si bonds concentration in the material. Our measurements of both plasmon and band gap energies exhibit a solidary redshift of  $\sim 1$  eV, indicating a consistent energy shift of the whole band structure or the addition of new levels<sup>29–31</sup>. Additionally, other works on similar samples characterized by EFTEM<sup>6</sup>, estimated that 15% of the volume of the dielectric barrier is distributed around the Si-rich layer between the Si-NC. This measurement is in good agreement with our observations, *e.g.* a pure dielectric region between particles in Fig. 7.8(a).

The indirect band gap for c-Si is found at energies between 1.2-1.4 eV, and it is possible to measure this signal in the EELS spectra from bulk samples<sup>32</sup>. We confirmed the possibility to obtain this measurement using c-Si spectra acquired at the substrate level. The CDF from the c-Si substrate is shown in Fig. 7.10(c) (the onset of the imaginary part is clearly visible). It can be expected to detect a similar indirect band gap signal also in the case of embedded particles. In the case of the Si-NC, we would expect this signal to appear at higher energies, owing to QC effects<sup>23</sup>, but still below 2-3 eV. However, no such feature was found in any of the Si-NC regions in the  $\text{SiO}_2$  or  $\text{Si}_3\text{N}_4$  systems. It was also impossible to measure any consistent contribution to the spectral intensity levels below  $\sim 3$  eV for the Si-NC MVA factors or average spectra from the “dominant Si-NC” regions. We believe that the lack of a silicon indirect band gap signal in

these embedded-particle systems should be attributed to the fact that particle dimensions are comparable to the electron delocalization distance,  $\sim 10$  nm for the spectrum at low energy losses<sup>13,33</sup>, as explained in Sec. 1.2.5.

Arguably, this does not exclude the possibility that a contribution from the indirect band gap may be present in our low-loss EELS data. On one hand, this contribution would be among the less intense features in the low-loss range, making it difficult to detect it above the tail of the ZLP, the band gap signal from the surrounding material, and the noise level. On the other hand, we cannot neglect the possibility that electron energy losses different from the ones related with the semi-classical interpretation of inelastic scattering may have an impact in the measured EELS spectra (see Sec. 1.3.2). García de Abajo considered many of these losses<sup>34</sup>; among them, the excitation of Čerenkov radiation, and the case of a composite material in which the grain size affects the interface-to-volume loss ratio. Although we are not able to consistently measure such contributions and the use of a low energy beam (80 keV) makes Čerenkov radiation excitations less probable, we cannot discard the possibility that a mixture of spurious losses could be affecting the measurement of the indirect band gap. Surface losses, which relative importance increases as sample thickness decreases, were subtracted in the usual manner in the KKA algorithm<sup>33</sup>. The fact that the surface loss contribution is relatively more important in the thinner  $\text{Si}_3\text{N}_4$  sample meant that KKA algorithm required more iterations (10 instead of 5 in the case of the Si-NC CDF) to reach proper convergence. Finally, the shape and energy of the features detected at  $\sim 3\text{-}3.5$  eV allows us to relate this measurement to the Tauc optical absorption gap, the direct band gap feature of the Si-NC<sup>23,35,36</sup>.

Again, these results are in good agreement with the QC model for Si-NCs in this size range. Although recent reports have stated that small Si-NCs could exhibit smaller band gaps than the ones predicted in the QC model<sup>37</sup>, this correction will only be important for Si-NCs which size is around or below the 1 nm range. In this case it would be troublesome to characterize the optoelectronic properties of the Si-NC, as the low-loss EELS from particles of so small a size would be very strongly affected by delocalized scattering from the surrounding material.

### 7.3.3 Electron effective mass

The electron effective mass,  $m^*$ , related to carrier mobility can be derived from the CDF<sup>38</sup>. These results are also summarized in Table 7.1. For the Si-NC in silicon oxide and nitride matrices,  $m^*$  values of  $0.129m_0$  and  $0.133m_0$  ( $m_0 = 9.11 \cdot 10^{-31}$  kg) were obtained, respectively. Meanwhile, for the c-Si substrate, a value of  $0.1m_0$  was obtained. By supposing an equal atomic density for c-Si and Si-NC of  $50.2 \text{ nm}^{-3}$ , an atomic density of electrons,  $n_{\text{eff}}$ , of  $\sim 3$  electrons

was obtained, actually higher for the Si-NCs, up to 3.5, in  $\text{Si}_3\text{N}_4$ . In the case of crystalline silicon, as the k-space surfaces of constant energy are ellipsoids, this quantity consists of a combination of the transversal and longitudinal electron effective masses. The generally accepted value of  $m^*$  for c-Si is  $0.26m_0$ , with a valence electron density of 4 electrons per atom<sup>39</sup>. Notice that the obtained  $m^*$  and  $n_{eff}$  values are below the expected ones. This appears to be a general trend for EELS measurements, as in the work in Ref. 38, or in Chapter 5, where the  $m^*$  and  $n_{eff}$  calculated values for III-V nitride samples were smaller than the theoretically expected ones. However, the possibility to combine the chemical information also present in the spectra justify the use of EELS for the calculation of  $m^*$  values<sup>10,40</sup>. Moreover, our calculation indicates an approximate correspondence of the values for c-Si and the Si-NCs, with an increase of the  $m^*$  and  $n_{eff}$  in the Si-NCs.

## 7.4 Conclusions

- Three systems were examined, made of alternating pure dielectric and silicon rich layers (SRON, SRC and SRN respectively); Si-NCs are formed in the Si-rich layer after annealing. As in Chapter 6, the mixed nature of the energy-loss spectra from the embedded nanoparticle systems poses a problem to the analyst. We proposed a novel approach for this analysis, based on phase identification by plasmon energy, followed by segmentation of the EELS data-cubes by MVA. These procedures were tested on the three systems.
- Our phase identification and segmentation technique proved that a selective averaging of spectra from regions allocated to a specific “dominant Si-NC” or “pure dielectric” class, can enhance the SNR, thus preserving the features of the EELS spectrum containing valuable information about the probed regions. We showed how MVA can be used to disentangle the individual spectral contributions to the characteristic EELS spectrum of the embedded particle system: the Si-NC and background dielectric signals.
- The plasmon energies measured in the  $\text{SiO}_2$  barriers are consistent with the literature, indicating the growth of mostly pure dielectric barriers that do not suffer from such effects as inhomogeneous silicon or nitrogen diffusion. Conversely, in the case of the SiC and  $\text{Si}_3\text{N}_4$  barriers, the significant shifts of the plasmon energy indicate an overall inhomogeneity in composition that can be related to the diffusion of silicon from the Si-rich layer. Moreover, the inhomogeneous shape and distribution of Si-NC in the SiC system as compared with the other two systems indicates that diffusion severely

affected the shape of the multilayer structure, with generalized coalescence of the Si-NCs and deformation of the barrier interfaces.

- In the  $\text{SiO}_2$  case, NMF allowed separating a spurious intensity step in the detector and recovering each contribution in the SRON layer as a separate component. This was not possible in the SRN case, in which we showed that BLU allowed for the separation of the Si-NC contribution in one component whereas two other components contained the mixed contributions from dielectric plasmon and intensity step. The different results after applying NMF or BLU highlight the differences between both approaches, in particular the geometrical initialization and additivity constrain of BLU. Both analyses were enabled by the previous use of spike removal and Poisson normalization steps.
- A detailed report on the electronic analysis of the EELS data and the derived MVA factors was given. Different KKA normalization steps were employed, using the refractive index or the thickness as an input, depending on the available data. The derived CDFs of the dielectric material in the barriers, the dielectric material surrounding the Si-NCs, and the Si-NCs themselves provided a valuable insight into the structural properties of the systems after the growth process. The Si-NC CDFs were compared to the CDF from a c-Si substrate area. Band gap energies were also determined. Finally, electron effective masses and an approximate density of electrons for c-Si and the Si-NCs were calculated. Results are found to be in good agreement with QC theory.

## Bibliography

- [1] F. Meillaud, A. Shah, C. Droz, E. Vallat-Sauvain, and C. Mazzia. Efficiency limits for single-junction and tandem solar cells. *Solar Energy Materials and Solar Cells*, 90(18-19):2952–2959, 2006. ISSN 0927-0248. doi: <http://dx.doi.org/10.1016/j.solmat.2006.06.002>. URL <http://www.sciencedirect.com/science/article/pii/S0927024806002029>. 14th International Photovoltaic Science and Engineering Conference 14th International Photovoltaic Science and Engineering Conference.
- [2] G. Conibeer, M. Green, E.-C. Cho, D. König, Y.-H. Cho, T. Fangsuwan-narak, G. Scardera, E. Pink, Y. Huang, T. Puzzer, S. Huang, D. Song, C. Flynn, S. Park, X. Hao, and D. Mansfield. Silicon quantum dot nanostructures for tandem photovoltaic cells. *Thin Solid Films*, 516(20): 6748 – 6756, 2008. ISSN 0040-6090. doi: <http://dx.doi.org/10.1016/j.tsf.2007.12.096>. URL <http://www.sciencedirect.com/science/article/>

- pii/S0040609007020081. Proceedings on Advanced Materials and Concepts for Photovoltaics {EMRS} 2007 Conference, Strasbourg, France.
- [3] J. López-Vidrier, S. Hernández, J. Samà, M. Canino, M. Allegrezza, M. Bellettato, R. Shukla, M. Schnabel, P. Löper, L. López-Conesa, S. Estradé, F. Peiró, S. Janz, and B. Garrido. Structural, optical and electrical properties of silicon nanocrystals embedded in  $\text{Si}_x\text{C}_{1-x}/\text{SiC}$  multilayer systems for photovoltaic applications. *Materials Science and Engineering: B*, 178(9):639 – 644, 2013. ISSN 0921-5107. doi: <http://dx.doi.org/10.1016/j.mseb.2012.10.015>. URL <http://www.sciencedirect.com/science/article/pii/S0921510712004965>. Advanced materials and characterization techniques for solar cells.
  - [4] M. Zacharias, J. Heitmann, R. Scholz, U. Kahler, M. Schmidt, and J. Bläsing. Size-controlled highly luminescent silicon nanocrystals: A  $\text{SiO}/\text{SiO}_2$  superlattice approach. *Applied Physics Letters*, 80(4):661–663, 2002. doi: <http://dx.doi.org/10.1063/1.1433906>. URL <http://scitation.aip.org/content/aip/journal/apl/80/4/10.1063/1.1433906>.
  - [5] L. T. Canham. Silicon quantum wire array fabrication by electrochemical and chemical dissolution of wafers. *Applied Physics Letters*, 57(10):1046–1048, 1990. doi: <http://dx.doi.org/10.1063/1.103561>. URL <http://scitation.aip.org/content/aip/journal/apl/57/10/10.1063/1.103561>.
  - [6] A. Zelenina, S. A. Dyakov, D. Hiller, S. Gutsch, V. Trouillet, M. Bruns, S. Mirabella, P. Löper, L. López-Conesa, J. López-Vidrier, S. Estradé, F. Peiró, B. Garrido, J. Bläsing, A. Krost, D. M. Zhigunov, and M. Zacharias. Structural and optical properties of size controlled Si nanocrystals in  $\text{Si}_3\text{N}_4$  matrix: The nature of photoluminescence peak shift. *Journal of Applied Physics*, 114(18):184311, 2013. doi: <http://dx.doi.org/10.1063/1.4830026>. URL <http://scitation.aip.org/content/aip/journal/jap/114/18/10.1063/1.4830026>.
  - [7] S. Hernández, J. López-Vidrier, L. López-Conesa, D. Hiller, S. Gutsch, J. Ibáñez, S. Estradé, F. Peiró, M. Zacharias, and B. Garrido. Determining the crystalline degree of silicon nanoclusters/ $\text{SiO}_2$  multilayers by Raman scattering. *Journal of Applied Physics*, 115(20):203504, 2014. doi: <http://dx.doi.org/10.1063/1.4878175>. URL <http://scitation.aip.org/content/aip/journal/jap/115/20/10.1063/1.4878175>.
  - [8] C. Summonte, M. Allegrezza, M. Bellettato, F. Liscio, M. Canino, A. Desalvo, J. López-Vidrier, S. Hernández, L. López-Conesa, S. Estradé, F. Peiró, B. Garrido, P. Löper, M. Schnabel, S. Janz, R. Guerra, and S. Ossicini.

- Silicon nanocrystals in carbide matrix. *Solar Energy Materials and Solar Cells*, 128(0):138 – 149, 2014. ISSN 0927-0248. doi: <http://dx.doi.org/10.1016/j.solmat.2014.05.003>. URL <http://www.sciencedirect.com/science/article/pii/S0927024814002451>.
- [9] A. Yurtsever, M. Weyland, and D. A. Muller. Three-dimensional imaging of nonspherical silicon nanoparticles embedded in silicon oxide by plasmon tomography. *Applied Physics Letters*, 89(15):151920, 2006. doi: <http://dx.doi.org/10.1063/1.2360906>. URL <http://scitation.aip.org/content/aip/journal/apl/89/15/10.1063/1.2360906>.
  - [10] P. D. Nguyen, D. M. Kepaptsoglou, Q. M. Ramasse, and A. Olsen. Direct observation of quantum confinement of Si nanocrystals in Si-rich nitrides. *Physical Review B*, 85:085315, Feb 2012. doi: 10.1103/PhysRevB.85.085315. URL <http://link.aps.org/doi/10.1103/PhysRevB.85.085315>.
  - [11] F. de la Peña, P. Burdet, M. Sarahan, M. Nord, T. Ostasevicius, J. Taillon, A. Eljarrat, S. Mazzucco, V. T. Fauske, G. Donval, L. F. Zagonel, I. Iyengar, and M. Walls. Hyperspy 0.8, April 2015. URL <http://dx.doi.org/10.5281/zenodo.16850>.
  - [12] A. Hyvärinen and E. Oja. Independent component analysis: algorithms and applications. *Neural networks*, 13(4):411–430, 2000.
  - [13] M. Bosman, L. J. Tang, J. D. Ye, S. T. Tan, Y. Zhang, and V. J. Keast. Nanoscale band gap spectroscopy on ZnO and GaN-based compounds with a monochromated electron microscope. *Applied Physics Letters*, 95(10):101110, 2009.
  - [14] F. de la Peña, M.-H. Berger, J.-F. Hochepied, F. Dynys, O. Stephan, and M. Walls. Mapping titanium and tin oxide phases using EELS: An application of independent component analysis. *Ultramicroscopy*, 111(2):169–176, 2011.
  - [15] T. Yamazaki, Y. Kotaka, and Y. Kataoka. Analysis of EEL spectrum of low-loss region using the  $C_s$ -corrected STEM-EELS method and multivariate analysis. *Ultramicroscopy*, 111(5):303 – 308, 2011. ISSN 0304-3991. doi: <http://dx.doi.org/10.1016/j.ultramic.2011.01.005>. URL <http://www.sciencedirect.com/science/article/pii/S0304399111000209>.
  - [16] J. M. Bioucas-Dias, A. Plaza, N. Dobigeon, M. Parente, Q. Du, P. Gader, and J. Chanussot. Hyperspectral unmixing overview: Geometrical, statistical, and sparse regression-based approaches. *Selected Topics in Applied Earth Observations and Remote Sensing, IEEE Journal of*, 5(2):354–379, 2012.

- [17] O. Nicoletti, F. de La Peña, R. K. Leary, D. J. Holland, C. Ducati, and P. A. Midgley. Three-dimensional imaging of localized surface plasmon resonances of metal nanoparticles. *Nature*, 502(7469):80–84, 2013.
- [18] N. Dobigeon, S. Moussaoui, M. Coulon, J.-Y. Tourneret, and A. O. Hero. Joint bayesian endmember extraction and linear unmixing for hyperspectral imagery. *Signal Processing, IEEE Transactions on*, 57(11):4355–4368, 2009. ISSN 1053-587X. doi: 10.1109/TSP.2009.2025797.
- [19] N. Dobigeon and N. Brun. Spectral mixture analysis of EELS spectrum-images. *Ultramicroscopy*, 120(0):25 – 34, 2012. ISSN 0304-3991. doi: <http://dx.doi.org/10.1016/j.ultramic.2012.05.006>. URL <http://www.sciencedirect.com/science/article/pii/S0304399112001088>.
- [20] M. R. Keenan and P. G. Kotula. Accounting for poisson noise in the multivariate analysis of ToF-SIMS spectrum images. *Surface and Interface Analysis*, 36(3):203–212, 2004.
- [21] V. J. Keast and M. Bosman. Applications and theoretical simulation of low-loss electron energy-loss spectra. *Materials Science and Technology*, 24(6):651–659, 2008.
- [22] M. Bosman, M. Watanabe, D. T. L. Alexander, and V. J. Keast. Mapping chemical and bonding information using multivariate analysis of electron energy-loss spectrum images. *Ultramicroscopy*, 106(11–12):1024 – 1032, 2006. ISSN 0304-3991. doi: <http://dx.doi.org/10.1016/j.ultramic.2006.04.016>. URL <http://www.sciencedirect.com/science/article/pii/S0304399106001021>. Proceedings of the International Workshop on Enhanced Data Generated by Electrons.
- [23] R. Guerra, F. Cigarini, and S. Ossicini. Optical absorption and emission of silicon nanocrystals: From single to collective response. *Journal of Applied Physics*, 113(14):143505, 2013. doi: <http://dx.doi.org/10.1063/1.4799394>. URL <http://scitation.aip.org/content/aip/journal/jap/113/14/10.1063/1.4799394>.
- [24] D. T. L. Alexander, P. A. Crozier, and J. R. Anderson. Brown carbon spheres in east asian outflow and their optical properties. *Science*, 321(5890):833–836, 2008. doi: 10.1126/science.1155296. URL <http://www.sciencemag.org/content/321/5890/833.abstract>.
- [25] E. D. Palik. *Handbook of optical constants of solids*, volume 3. Academic press, 1998.

- [26] M. Couillard, A. Yurtsever, and D. A. Muller. Competition between bulk and interface plasmonic modes in valence electron energy-loss spectroscopy of ultrathin  $\text{SiO}_2$  gate stacks. *Physical Review B*, 77:085318, Feb 2008. doi: 10.1103/PhysRevB.77.085318. URL <http://link.aps.org/doi/10.1103/PhysRevB.77.085318>.
- [27] F. Delachat, M. Carrada, G. Ferblantier, A. Slaoui, C. Bonafos, S. Schamm, and H. Rinnert. Structural and optical properties of Si nanocrystals embedded in  $\text{SiO}_2/\text{SiN}_x$  multilayers. *Physica E: Low-dimensional Systems and Nanostructures*, 41(6):994 – 997, 2009. ISSN 1386-9477. doi: <http://dx.doi.org/10.1016/j.physe.2008.08.006>. URL <http://www.sciencedirect.com/science/article/pii/S1386947708002889>. Proceedings of the E-MRS 2008 Symposium C: Frontiers in Silicon-Based Photonics.
- [28] F. Delachat, M. Carrada, G. Ferblantier, J.-J. Grob, and A. Slaoui. Properties of silicon nanoparticles embedded in  $\text{SiN}_x$  deposited by microwave-PECVD. *Nanotechnology*, 20(41):415608, 2009. URL <http://stacks.iop.org/0957-4484/20/i=41/a=415608>.
- [29] P. E. Batson and J. R. Heath. Electron energy loss spectroscopy of single silicon nanocrystals: The conduction band. *Physical Review Letters*, 71:911–914, Aug 1993. doi: 10.1103/PhysRevLett.71.911. URL <http://link.aps.org/doi/10.1103/PhysRevLett.71.911>.
- [30] Y. W. Wang, J. S. Kim, G. H. Kim, and Kwang S. Kim. Quantum size effects in the volume plasmon excitation of bismuth nanoparticles investigated by electron energy loss spectroscopy. *Applied Physics Letters*, 88(14):143106, 2006. doi: <http://dx.doi.org/10.1063/1.2192624>. URL <http://scitation.aip.org/content/aip/journal/apl/88/14/10.1063/1.2192624>.
- [31] V. A. Gritsenko, H. Wong, J. Xu, R. Kwok, I. Petrenko, B. Zaitsev, Y. Moroko, and Y. Novikov. Excess silicon at the silicon nitride/thermal oxide interface in oxide-nitride-oxide structures. *Journal of Applied Physics*, 86: 3234–3240, 1999.
- [32] L. Gu, V. Srot, W. Sigle, C. Koch, P. van Aken, F. Scholz, S. B. Thapa, C. Kirchner, M. Jetter, and M. Rühle. Band-gap measurements of direct and indirect semiconductors using monochromated electrons. *Physical Review B*, 75:195214, May 2007. doi: 10.1103/PhysRevB.75.195214. URL <http://link.aps.org/doi/10.1103/PhysRevB.75.195214>.
- [33] R. F. Egerton. *Electron Energy-Loss Spectroscopy in the Electron Microscope*. Springer US, 3rd edition, 2011.

- [34] F. J. García de Abajo. Optical excitations in electron microscopy. *Reviews on Modern Physics*, 82:209–275, Feb 2010. doi: 10.1103/RevModPhys.82.209. URL <http://link.aps.org/doi/10.1103/RevModPhys.82.209>.
- [35] J. Tauc, R. Grigorovici, and A. Vancu. Optical properties and electronic structure of amorphous germanium. *Physica Status Solidi (b)*, 15(2):627–637, 1966. ISSN 1521-3951. doi: 10.1002/pssb.19660150224. URL <http://dx.doi.org/10.1002/pssb.19660150224>.
- [36] Z. H. Zhang, M. He, and Q. Li. Obtaining the effective electron mass from valence electron energy-loss spectroscopy. *Solid State Communications*, 149(41–42):1856 – 1859, 2009. ISSN 0038-1098. doi: <http://dx.doi.org/10.1016/j.ssc.2009.06.031>. URL <http://www.sciencedirect.com/science/article/pii/S0038109809003925>.
- [37] H. Vach. Ultrastable silicon nanocrystals due to electron delocalization. *Nano Letters*, 11(12):5477–5481, 2011. doi: 10.1021/nl203275n.
- [38] M. H. Gass, A. J. Papworth, R. Beanland, T. J. Bullough, and P. R. Chalker. Mapping the effective mass of electrons in III-V semiconductor quantum confined structures. *Physical Review B*, 73(3):035312, 2006.
- [39] P. Yu and M. Cardona. *Fundamentals of Semiconductors: Physics and Materials Properties*. Graduate Texts in Physics. Springer, 2010. ISBN 9783642007101. URL [http://books.google.es/books?id=5aBuKYBT\\_hsC](http://books.google.es/books?id=5aBuKYBT_hsC).
- [40] P. D. Nguyen, D. M. Kepaptsoglou, R. Erni, Q. M. Ramasse, and A. Olsen. Quantum confinement of volume plasmons and interband transitions in germanium nanocrystals. *Physical Review B*, 86:245316, Dec 2012. doi: 10.1103/PhysRevB.86.245316. URL <http://link.aps.org/doi/10.1103/PhysRevB.86.245316>.





# Chapter 8

## Conclusions

The main goal of this thesis has been to develop quantitative methods for the analysis of materials from low-loss EELS data obtained at the highest spatial and energy resolution. In particular, it has been focused on theoretical and experimental works related to the low-loss EELS of group-III nitride and silicon-based structures. Theoretical work can be divided in two main branches. On one hand, a considerable amount of effort has been put into building a coherent synthesis of the existing formulation of inelastic scattering of electrons by material media. In this sense, the introductory sections of this thesis, Chapter 1 and also Chapter 2, will hopefully provide the reader with a useful review of the theoretical framework available for the analysis of low-loss EELS. On the other hand, original band structure simulations have been designed and performed using the Wien2k software package.

Experimental work has been devoted to the analysis of hyperspectral HAADF-EELS data-sets, acquired on a probe-corrected, monochromated STEM. Data has been analyzed using advanced computational methods, including, to name the most relevant: Model-based analysis of low-loss EELS data, typically through non-linear fitting routines; Kramers-Kronig analysis (KKA) to obtain the complex dielectric function (CDF), and energy-loss function (ELF); calculation of parameters either from raw EELS data, such as the relative thickness ( $t/\lambda$ ), or from the CDF, such as absolute thickness ( $t$ ); and application of advanced multivariate analysis (MVA) algorithms for the factorization of hyperspectral low-loss EELS datasets. Most of these methods have been designed or adapted from the literature to the considered problem. The developed methodologies have been made available through careful descriptions in published works (derived from this thesis), so that calculations can be reproduced, typically using resources in Hyperspy. Hyperspy is an open-source software repository, designed specifically

for EELS, to which a number of contributions have been made in the context of the present thesis. In the following lines, we summarize the most relevant results of simulations and data analysis of III-V and Si-based materials.

## 8.1 Simulation of group-III ternary compounds

DFT band-structure simulations of group-III nitride binary compounds and ternary alloys have been performed. Using them, the dielectric response (CDF and ELF) in a random phase approximation (RPA) framework has been studied. The results of these simulations, presented in Chapter 3, include the following:

- The lattice parameters for the binary nitrides (AlN, GaN and InN) have been optimized for DFT calculations, in an initial structural relaxation step. We have found that, for the wurtzite structures, the total energy strongly depends on the volume of the primitive cell when the ratio between the lattice parameters,  $c/a$ , is kept constant. We have observed a much weaker dependence on  $c/a$  ratio when constraining the volume to the optimized one. The optimization results are relevant, as these III-nitrides often grow epitaxially in the  $c$  direction on an hexagonal substrate with similar lattice parameters.
- Also in these simulations, an improvement has been found after implementation of the modified Becke-Johnson (mBJ) exchange-correlation (XC) potential, leading to more realistic band gap values than those obtained by generalized gradient approximation (GGA). Moreover, the GGA simulations wrongly predict a metallic behavior for InN ( $E_{gap}^{GGA} = 0$  eV), which is corrected in mBJ ( $E_{gap}^{mBJ} = 0.69$  eV).
- In the simulation of the ternary alloys,  $\text{Al}_x\text{Ga}_{1-x}\text{N}$ ,  $\text{In}_x\text{Ga}_{1-x}\text{N}$ ,  $\text{In}_x\text{Al}_{1-x}\text{N}$ , the application of a super-cell simulation strategy has allowed to account for variations in composition,  $x$ . Using these calculations, the evolution of relevant electronic parameters, such as band gap and plasmon energies, with  $x$ , is predicted.
- In this analysis, we have also shown that it is advantageous to monitor the plasmon energy in the CDF ( $\varepsilon = \varepsilon_1 + i\varepsilon_2$ ) using the  $E_{cut}$  parameter. This parameter indicates the collective mode energy threshold, related to plasmon energy, without the need to perform model-based fitting of the ELF, thus overcoming the detrimental influence that single electron transitions can have in model-based fit procedures.

- The results obtained from this analysis predict that the composition dependence of both band gap and plasmon energies in AlGaN alloys is well adjusted by a linear Vegard law.
- In indium-containing alloys, as InGaN and InAlN, these parameters are better adjusted by parabolic Vegard laws. Additionally, some higher-order deviations have been observed for low indium concentrations.

## 8.2 Group-III ternary compound-based structures

Three different group-III nitride heterostructures have been examined using a combination of HAADF and low-loss EELS. These structures are composed of a stacking of III-nitride layers, with characteristic sizes in the nanometer range. A chemical and structural characterization has been performed, obtaining an important insight on several issues that can affect the final device performance. In this sense, we have carried out a quantitative chemical characterization of three ternary alloys (InAlN, AlGaN and InGaN) based on the heuristic relationship between the measured shift of the plasmon energy ( $E_P$  or  $E_{max}$ ) and the local composition (Vegard law). This dependence is typically monitored by model-based fitting of the plasmon peak in the energy-loss spectrum, either using a simple Lorentzian peak shape or the more accurate Drude plasmon model.

In Chapter 4, two distributed Bragg reflector (DBR) structures have been characterized.

- In the first studied system, an AlN / GaN DBR structure, plasmon energy analysis reveals the presence of a repeating four-layer structure of AlGaN alloys, composed of  $\sim 10$ ,  $15$ ,  $50$  and  $15$  nm wide AlGaN1, GaN, AlGaN2 and AlN layers, respectively. These layers are spontaneously formed by phase separation: GaN and AlN layers show a nearly pure composition; the two AlGaN layers show an intermediate, graded composition.
- Furthermore, two dimensional mapping of plasmon energy reveals the formation of anomalous segregations and metallic Al inclusions in the heterostructure. The linear dependence of plasmon energy with composition in AlGaN alloys, predicted in the simulations, is confirmed. The experimental HAADF intensity profiles and maps have been successfully compared with HAADF simulations, built using atomistic models based on the local composition determined through plasmon energy.
- Additionally, using Drude model-based fits, the plasmon width parameter,  $\Gamma_P$ , related to plasmon lifetime in the context of this model, has also been

obtained. These measurements indicate a broadening of the plasmon in the abrupt interfaces between nearly pure AlN and GaN layers. Moreover, a broadening of the plasmon has also been detected in the  $\text{Al}_x\text{Ga}_{1-x}\text{N}$  regions surrounding metallic aluminum inclusions. In both cases, the structural differences between regions are likely to produce a strained state of the crystalline lattices.

- In the second studied system, an InAlN / GaN DBR structure, a general method is proposed to adjust the parabolic composition dependence on plasmon energy, given that the non-linear term (bowing) is unknown. The InAlN layers present an In-rich segregation region, located just above the GaN layers. Using our method, the local composition from these regions, under 5 nm in size, is obtained, and the value of the parabolic bowing parameter is measured ( $b = 3.1$  eV). The obtained results suggest that bowing in this system is not well defined by a parabolic law for low indium concentrations, and may be better described by a higher order law, as hinted in the DFT simulations.
- Using KKA of the experimental low-loss EELS data from this system, we have extracted the CDF and the ELF. Using this treatment, an insight into structural and electronic properties of the system is obtained. Moreover, additional properties have been then calculated from the obtained CDF; absolute thickness,  $t$ , and effective electron number,  $n_{eff}$ .
  - The CDF is used to detect characteristic transitions pertaining to both wurtzite and zinc-blende crystalline phases. This indicates the coexistence of both phases (polytypism), in good agreement with a previous TEM characterization. Hence, the calculation of the CDF extends the structural characterization capabilities of low-loss EELS.
  - Using the calculated ELFs, we have been able to measure band gap energy onsets from a model-based fit in the InAlN and GaN layers. Our measurements for the In-deficient regions are in relatively good agreement with the expected band gap energies. However, the characteristic delocalization length for this energy-loss region is large, almost 10 nm for an  $\sim 3$  eV loss, making it impossible to measure a change in the band gap energy related to the relatively small In-rich regions, under 5 nm in width.
  - Finally, it has been deemed necessary to perform full-relativistic calculations to assess the impact of radiative losses in the low energy-loss region. These calculations have been carried out using  $\varepsilon(E)$  data obtained after KKA. The results indicate that the impact of bulk Čerenkov losses is not negligible because of the high voltages involved

( $E_0 = 300$  keV). However, given the small thickness of the examined regions, always below 100 nm, it can be concluded that the shape and position of the band gap signal is not modified and can be safely measured.

In Chapter 5, an InGaN multiple quantum well (QW) heterostructure is examined, with In-rich QWs of very reduced nominal dimensions (1.5 nm). In this case, we have used geometrical phase analysis (GPA) measurements in high resolution HAADF images to complement our low-loss EELS analysis.

- The analysis of the high resolution HAADF images reveal chemical and structural inhomogeneities in the  $\text{In}_x\text{Ga}_{1-x}\text{N}$  QW multilayer. In this sense, strain mapping using geometric phase analysis (GPA) is applied to the images, and the results are related to local composition. A higher strain gradient is found in regions where the QW is thicker than the nominal dimensions, 1.5 nm. This result is associated with a local indium enrichment above the nominal composition,  $x = 0.2$ , but not above values indicating In-clustering,  $x > 0.5$ .
- Using the low-loss EELS data, we have been able to measure band gap energy onsets by directly examining the inflexion point in the raw signal. As for the InAlN / GaN DBRs in the preceding chapter, our measurements for the relatively In-poor barriers are in good agreement with the expected band gap energies; meanwhile, the characteristic delocalization length, around  $\sim 10$  nm, makes it unlikely to measure a change in the band gap energy related to the relatively small QWs, under 5 nm in width.
- As in the preceding chapter, plasmon energy and width in these low-loss data have been studied using Drude model-based fits. Plasmon energy shift and broadening for QW regions below 2 nm in width have been measured.
  - The obtained plasmon energy values are unexpectedly high ( $E_P \sim 19.4$  eV in the QWs), indicating, in principle, an incompatibility between Vegard law and nominal composition regardless of the applied bowing. However, given the small size of these layers, we have related the increase in plasmon energy to spatial delocalization and a quantum confinement effect.
  - In this case, the broadening of the plasmon in the QW has been directly related to strain through the analysis of the high resolution HAADF images. Notice that the presence of a QW represents both a chemical and a structural change in the structure, as the inclusion of more indium atoms in the epitaxial growth process induces a lattice deformation.

- Again, KKA of the experimental low-loss EELS data has been used to extract the CDF and the ELF, and a greater variety of properties have been then calculated from the obtained CDF:
  - We have monitored the zero-cut energy,  $E_{cut}$ , using the obtained CDF. For this purpose, we use a direct measurement method, similar to the one applied to the analysis of the theoretical CDFs obtained from DFT simulations. Comparison of the  $E_{cut}$  and  $E_P$  maps shows that  $E_{cut}$  presents significant variations between the QW and barrier regions ( $\Delta E_P \sim 0.3$  eV,  $\Delta E_{cut} \sim 1.0$  eV).
  - Thickness normalization, performed after KKA, has been crucial to obtain Ga 3d transition intensity maps. The intensity of the single electron transition from the Ga 3d band can be qualitatively related to gallium concentration. In our case, by mapping the Ga 3d intensity in the normalized SSD, we have obtained an insight into the compositional inhomogeneities in the InAlN QWs.
  - We have calculated electron effective mass,  $m^*$ , maps from the CDFs. They do not show a consistent contrast in the QW regions; yet, the obtained values are in good agreement with other low-loss EELS observations from similar systems ( $m^* \sim 0.15m_0$ ).
  - Finally, a full-relativistic calculation to assess the impact of radiative losses in the low energy-loss region has also been carried out, but, in this case, we use  $\varepsilon(E)$  data from optical measurements in the literature. The results are similar to the ones in the preceding chapter, and that the shape and position of the band gap signal is not modified and can be safely measured.

### 8.3 Silicon-based structures

Several different silicon-based structures, containing pure silicon particles with sizes in the nanometer range embedded in a silicon-based dielectric material matrix, have been examined using HAADF-EELS. In this sense, Chapter 6 presents the results of an Er-doped heterostructure, consisting of silicon nano-particles in a SiO<sub>2</sub> matrix; meanwhile, in Chapter 7, three systems are presented, that contain silicon nano-particles in different dielectric-based matrices (*i.e.* SiO<sub>2</sub>, Si<sub>3</sub>N<sub>4</sub> and SiC).

The examined structures have in common being composed of pure silicon regions surrounded by a dielectric matrix. For this reason, we expect low-loss EELS data to always contain mixed contributions from these regions. Additionally, the difference between pure silicon and silicon-based dielectric regions, in terms of

atomic number, is small. For these reasons, the interpretation of spectra, as well as HAADF images, is difficult. Indeed, energy-filtered TEM (EFTEM) is typically preferred for the examination of these kinds of layers. Nevertheless, energy-loss spectra potentially contain more information than EFTEM images. Because of this, we have proposed several approaches that improve our ability to obtain insight into the studied systems from HAADF-EELS data. Our most relevant findings can be summarized as follows:

- We have calculated the relative thickness parameter,  $t/\lambda$ , through the log-ratio formula, from the energy-loss spectra. This is a relatively fast calculation, that allows to assess thickness variations in the examined regions. This is very relevant to the quality of the sample for low-loss EELS and HAADF observation, as plural scattering and thickness variations can strongly affect both spectra and images.
  - In Chapter 6,  $t/\lambda$  has been used for sample quality assessment. As this specimen has been prepared by focused-ion beam (FIB), a small thickness gradient is expected. The  $t/\lambda$  maps show that the thickness of the examined region is nearly constant ( $t/\lambda \sim 0.9$ ). This allows to use the  $\lambda$  contrast in the  $t/\lambda$  maps and the Z-contrast in the HAADF images to characterize the Si-ncs regions.
  - In Chapter 7, the final goal has been to probe each Si nano-particle individually. However, in thick specimens we may measure several Si-nanocrystals (NCs) at once, making this task difficult. Therefore, mechanical preparation is used; in comparison to FIB preparation, it allows obtaining thinner specimens, even if with smaller observable regions and more inhomogeneous thickness profiles. Indeed, the  $t/\lambda$  maps calculated from all the acquired EELS-SI confirm the low thickness of the prepared specimens, with  $t/\lambda \leq 0.35$ .
- In order to study the plasmon energy and width in the low-loss EELS data, separately for each contribution, a signal un-mixing problem has to be tackled. Two different strategies are proposed to solve this problem. In both cases, preliminary model-based fitting of the plasmon peak has been used to identify the trace of pure silicon in our hyperspectral datasets: silicon has an expected plasmon energy of 16.9 eV; for dielectric compounds, this value is slightly higher, in the 21.5 – 24 eV range.
  - We have first demonstrated a double plasmon model-based fit, adjusting two different Drude plasmon models to the low-loss EELS data. In the Er-doped SRO case, a “high-energy” plasmon model is always used to fit the  $\text{SiO}_2$  peak (23.7 eV); conversely, a “low-energy” plasmon

model is used to differentiate the Si-ncs peak from the  $\text{SiO}_2$  interband transition. This strategy has allowed us to locate the Si-ncs in the whole active layer, in which they appear scattered with a relatively low concentration and have a subtle impact in the low-loss EELS data. Notice that this strategy relies on the possibility to adjust the conditions of the fit to a specific spectral shape. Thus, this method is not as useful when the dielectric matrix has a plasmon energy closer to that of pure Si.

- Thus, in Chapter 7, we have proposed a novel method based on MVA of the low-loss EELS data from particular regions, that is useful even when the spectral contributions are quite similar. Our method works in two steps. First, the hyperspectral data are segmented using plasmon energy thresholding to identify “Si-dominant” regions that exhibit a plasmon peak similar to that of crystalline silicon (but still mixed with a dielectric contribution). Second, MVA algorithms are applied to factorize the EELS-SI in terms of Si-NC and dielectric contribution. We have shown the successful application of this method in the  $\text{SiO}_2$  and  $\text{Si}_3\text{N}_4$  structures. However, the SiC structure is severely affected by composition inhomogeneities that produce a continuous shift of the plasmon peaks, leading to artifacts in the MVA factorization. In such cases, this method is not appropriate.
- Using the factorizations, we have measured plasmon energy and width in the components, which we can interpret as the contributions from the Si-NCs and their surrounding dielectric matrices. These values are then compared with spectra obtained in sample regions of known composition, namely the crystalline silicon substrate and the pure dielectric barriers:
  - For the Si-NCs, plasmon energies in the 17 – 18 eV range have been obtained, above the expected value for pure crystalline silicon. Additionally, a broadening of the plasmon is observed in the Si-NCs. Taking into account the small size of the silicon particles, these deviations have been interpreted as reflecting a quantum confinement effect.
  - For the  $\text{SiO}_2$  and  $\text{Si}_3\text{N}_4$  matrices surrounding the nano-particles, plasmon energies of 22.7 eV and 22.7 eV have been measured, respectively. In this case, the  $\text{SiO}_2$  plasmon in the matrix presents a broadening similar to the one in the barrier, but plasmon energy is 1 eV lower, indicating the formation of a sub-oxide ( $\text{SiO}_x$ ). Meanwhile, the  $\text{Si}_3\text{N}_4$  plasmon in the matrix matches the one measured in the barrier in both energy and broadening, indicating a pure dielectric matrix.

- Additionally, the MVA strategy allows to perform KKA using the spectral features obtained by factorization. The CDFs resulting from the KKA of the Si-NCs and dielectric contributions have been extracted in the  $\text{SiO}_2$  and  $\text{Si}_3\text{N}_4$  structures.
  - In order to test this procedure, we have compared these results with the CDFs extracted from the experimental EELS data in the crystalline silicon substrate and purely dielectric barrier regions, respectively. They have been found to be in excellent agreement, taking into account the observed plasmon shifts and broadenings.
  - From these CDFs, we have calculated  $m^*$  values using the Bethe-f sum rule. We obtain  $0.1m_0$  for the c-Si substrate and around  $0.13m_0$  for the Si-NCs, indicating a good agreement between both measurements.

In summary, the developed methods have revealed structural and chemical properties of the examined materials at a high spatial and analytical resolution, allowing to elucidate the intimate configuration of state-of-the-art optoelectronic devices.



## Appendix A

# Sample growth, preparation procedures and instrumentation

### Sample growth

All the group-III nitride samples were grown by the group of E. Calleja at the *Instituto de Sistemas Optoelectrónicos y Microtecnología* (ISOM), at *Universidad Politécnica de Madrid*, which also carried out previous macroscopic characterizations.

The electro-optical active slot waveguide, examined in Chapter 6, was developed by the group of B. Garrido, at the *Departament d'Electrònica* of the *Universitat de Barcelona*. The examined devices were grown by J.-M. Fedeli at *Laboratoire d'électronique des technologies de l'information* (CEA-LETI), in Grenoble, France.

The SiC samples, examined in Chapter 7, were grown by the group of C. Summonte at *Istituto per la Microelettronica e i Microsistemi* (CNR-IMM), in Bologna, Italy. The SiO<sub>2</sub> and Si<sub>3</sub>N<sub>4</sub> samples were grown by the group of M. Zacharias at the *Institut für Mikrosystemtechnik* (IMTEK), located in Freiburg, Germany.

### Sample preparation

All the devices and systems examined in this thesis were prepared for TEM observation in cross-section geometry using traditional mechanical preparation or FIB preparation, in the facilities of the Scientific and Technical Centers of

*Universitat de Barcelona* (CCiT-UB).

**Mechanical preparation** was carried out by parallel polishing down to 50 µm, followed by a dimpling down to 25 µm. Finally, an Ar<sup>+</sup> bombardment was performed at  $V = 5$  kV and  $I = 15$  µA with an incident angle of 7° using a PIPS-Gatan equipment. Preliminary observation was always carried out, in order to check that no significant amorphization occurred.

**FIB preparation** allows choosing the region of interest of a given device very selectively. For FIB preparation a FEI Strata Dual Beam instrument was used with a Ga<sup>+</sup> energy of 30 kV and with an intensity varying from 700 pA to 30 pA, depending on the process step. A copper grid was used as a support for the sample, using the gas-injection system with a platinum precursor for welding.

## Instrumentation

Preliminary STEM-HAADF experiments were carried out in a **JEOL J2010F (S)TEM** operated at 200 keV, also at CCiT-UB.

For the data acquisition at high spatial and energy resolution a probe-corrected **FEI Titan 60-300 (S)TEM** operated at 300 kV and equipped with a Wien filter monochromator and a Gatan Tridiem 866 ERS energy filter/spectrometer was used. This equipment is found at the Advanced Microscopy Laboratory at the *Instituto de Nanociencia de Aragón* (LMA-INA), in Zaragoza, Spain.





# Appendix B

## Resumen en Español

El objetivo marcado para esta tesis es el desarrollo de métodos cuantitativos para el análisis de materiales en el microscopio electrónico de transmisión (TEM), usando espectroscopía de pérdida de energía (EELS) en el régimen de bajas pérdidas (*low-loss*). En líneas generales, en la preparación de este trabajo se han realizado estudios teóricos y experimentales relacionados con *low-loss* EELS en estructuras basadas en nitruros del grupo III y silicio. Estos materiales se encuentran entre los más relevantes para el diseño e implementación de circuitos electrónicos, con especial interés en el campo de la optoelectrónica. De hecho, el pequeño tamaño de los componentes estructurales donde se implementan estos materiales hace del uso de técnicas de microscopía electrónica una exigencia. En particular, logramos una caracterización específica, adquiriendo espectros localizados en el espacio usando el modo de barrido (STEM). En este sentido, hemos analizado estructuras con dimensiones características en el rango de las decenas de nm o menos.

En el Capítulo 1, se ha sintetizado la formulación teórica de la dispersión (*scattering*) inelástica de electrones rápidos por medios materiales. Revisamos en profundidad un modelo de respuesta dieléctrica, que es el punto de partida que hemos considerado para la simulación y el análisis del *low-loss* EELS. Por un lado, la función clave en este marco teórico es la permitividad compleja (CDF),  $\varepsilon = \varepsilon_1 + i\varepsilon_2$ , relacionada con las propiedades cuánticas del material. Es importante señalar que es posible medir la CDF por diversas técnicas experimentales (*e.g.* espectroscopías electrónicas u ópticas) o calcularla a partir de simulaciones *ab initio*. Por otro lado, usando la función de pérdidas (ELF),  $\text{Im}(-1/\varepsilon)$ , podemos diseñar modelos fenomenológicos del *low-loss* EELS que incluyen las excitaciones elementales, plasmón y transiciones interbanda, que esperamos poder medir experimentalmente.

En el Capítulo 2, se han descrito en detalle las herramientas analíticas usadas para realizar los estudios, experimentales y teóricos, recogidos en los capítulos posteriores:

- Se presentan primero los métodos generales de procesado del espectro; calibración y deconvolución del espectro, los algoritmos Fourier-log y Richardson-Lucy. Además, se explica el análisis Kramers-Kronig (KKA) que sirve para obtener las ELF y CDF a partir de un espectro experimental y con ellas relacionar las medidas experimentales con propiedades electrónicas (*e.g.* regla de suma de Bethe). La explicación se ha visto complementada con dos ejemplos prácticos de análisis usando espectros experimentales de silicio y nitruro de galio (GaN).
- También se ha incluido un apartado sobre los modos de adquisición “hiper-spectrales” de STEM-EELS, el *spectrum-image*, en los que adquirimos una colección de espectros espacialmente localizados para analizar una región de interés en la muestra. Además de adaptar todas nuestras rutinas computacionales al procesado de estos “cubos de datos”, hemos propuesto la aplicación de algoritmos de análisis multivariante (MVA) en *low-loss* EELS. Estos algoritmos MVA se usan para identificar las diferentes contribuciones espectrales y, si es posible, factorizar en consecuencia los “cubos de datos”.
- Finalmente, hemos dedicado un apartado a los métodos de simulación *ab initio* por teoría del funcional de la densidad (DFT), que se han utilizado para el estudio teórico de *low-loss* EELS. Estas simulaciones permiten predecir la estructura de bandas de un material, y, a partir de ésta, calcular un gran número de propiedades. Entre otras propiedades interesantes, se logra una caracterización teórica de la respuesta dieléctrica, pudiendo obtener predicciones de las CDF y ELF, con el interés de comparar estas simulaciones con resultados experimentales.

En el Capítulo 3, se ha descrito el estudio teórico del *low-loss* EELS, centrado en nitruros del grupo III, en particular los compuestos binarios y ternarios de tipo (Al, Ga, In)N. Para este estudio, hemos incluído avanzadas herramientas como el potencial de intercambio y correlación Becke-Johnson modificado (mBJ) y la simulación con super-celdas. Hemos propuesto, además, una estrategia para el estudio de la evolución de la energía de la banda prohibida, o *band gap* ( $E_{gap}$ ), y de la energía del plasmón de volumen, basada en modelos fenomenológicos para la CDF (*e.g.* modelo de Drude) y la llamada ley de Vegard para tener en cuenta la variación con la composición en aleaciones ternarias.

- Por un lado, se demuestra que la introducción del mBJ mejora la formulación de la estructura de bandas, en el sentido de que las anchuras de la

banda prohibida en los materiales binarios (*i.e.* AlN, GaN e InN) se aproximan más ajustadamente a los valores esperados.

- Por otro lado, gracias al uso de las super-celdas es posible simular aleaciones ternarias (*i.e.*  $\text{Al}_x\text{Ga}_{1-x}\text{N}$ ,  $\text{In}_x\text{Ga}_{1-x}\text{N}$  e  $\text{In}_x\text{Al}_{1-x}\text{N}$ ) en todo su rango composicional  $0 < x < 1$ .
- En el análisis de los resultados de la energía del plasmón, se han considerado dos parámetros para medirla de forma distinta,  $E_P$  y  $E_{cut}$ . Se han demostrado las ventajas que ofrece examinar  $E_{cut}$  en la CDF detectando un punto de corte, frente a medir  $E_P$  en la ELF usando un ajuste al modelo de Drude. En este último caso, la posibilidad de ajustar el plasmón se ve afectada negativamente por la presencia de transiciones entre niveles profundos que modifican la forma del espectro.
- Los resultados obtenidos tras este análisis para AlGaN predicen que la dependencia en composición de las energías de *band gap* y plasmón se ven bien descritas por una ley lineal. Para InGaN e InAlN, estas mismas dependencias se ajustarían a una ley parabólica, teniendo en cuenta, además, ciertas desviaciones para bajas concentraciones de indio, que indican la necesidad de tener en cuenta términos de mayor orden.

En el Capítulo 4, se ha procedido a la caracterización de dos sistemas de reflectores distribuidos de Bragg (DBR), compuestos por aleaciones ternarias de nitruros del grupo III, a partir de medidas experimentales EELS-HAADF. En ambos casos, se usa la ley de Vegard para asociar el desplazamiento de la energía del plasmón con la composición de las aleaciones. Para determinar esta dependencia de manera precisa se usan ajustes del *low-loss* EELS basados en modelos fenomenológicos de la ELF presentados en el capítulo anterior.

- En el primer sistema, un DBR (AlN / GaN) $\times 20$ , este análisis revela una estructura periódica de cuatro capas de aleaciones AlGaN, dos de ellas capas de AlN y GaN casi puros, y dos capas de composición intermedia; una de ellas relativamente corta, la otra mas larga; formadas de manera espontánea por separación de fases. Además, es posible construir mapas de la energía del plasmón usando EELS-SI, para así revelar la composición en regiones localizadas que presentan segregaciones anómalas o inclusiones metálicas. Como indican las simulaciones DFT, se ha supuesto una ley de Vegard lineal para obtener estos resultados. Para reforzar la confianza en esta suposición se han llevado a cabo simulaciones de la intensidad HAADF a partir de los resultados obtenidos por EELS. La correspondencia de estas simulaciones con las imágenes HAADF experimentales es excelente, confirmando la hipótesis de partida.

- Adicionalmente, las EELS-SIs tomadas han servido para un estudio más detallado de las segregaciones anómalas e inclusiones metálicas. En este sentido, se ha medido la anchura del plasmón,  $\Gamma_P$  (en el contexto del modelo de Drude), y el espesor relativo,  $t/\lambda$ , comparando ambos con las imágenes HAADF. Estos análisis muestran el ensanchamiento del plasmón en las intercaras abruptas y alrededor de las inclusiones.
- En la segunda estructura estudiada, un DBR (InAlN / GaN)x10, se ha propuesto un método general para ajustar la dependencia de la composición con la energía del plasmón, en el supuesto de que esta sea parabólica, como se espera para este sistema. Por un lado, así logramos caracterizar la composición en las capas de InAlN. En las imágenes HAADF, estas capas presentan una zona con contraste brillante, que nuestro análisis determina que se trata de una segregación rica en indio con tamaño menor de 5 nm. Por otro lado, el método aplicado resulta en una medida del término no-lineal de la ley de Vegard parabólica (*bowing*). Esta medida indica que el comportamiento de este sistema no se predice de forma correcta usando simplemente un término parabólico, y que términos de más alto orden pueden ser necesarios a bajas concentraciones de indio, tal y como habían predicho las simulaciones DFT.
- También se ha realizado, sobre estos mismos datos, una caracterización exhaustiva de propiedades electrónicas y estructurales. La CDF del sistema, recuperada por KKA, evidencia el politipismo de las capas de GaN, en las que coexisten una estructura hexagonal (Wurtzita) y una estructura cúbica (Zinc-Blenda). Las energías de *band gap* de las capas, determinadas en la ELF, revelan valores muy próximos, de 3.2 y 3.4 eV, para capas de GaN e InAlN, respectivamente.

En el Capítulo 5, se ha caracterizado otro sistema basado en nitruros del grupo III, en este caso una heteroestructura de  $\text{In}_x\text{Ga}_{1-x}\text{N}$ , que presenta capas ricas en indio de dimensiones muy reducidas (1.5 nm) que pueden ser denominadas *quantum wells* (QWs). En este caso, además de haber utilizado herramientas de análisis basadas en *low-loss* EELS, se han estudiado imágenes HAADF de alta resolución.

- Dichas imágenes revelan que los QW presentan ciertas inhomogeneidades químicas y estructurales. Se ha utilizado el análisis de fase geométrica (GPA), una técnica para calcular mapas de deformación en la red cristalina, para obtener información cualitativa, a escala nanométrica, sobre estas inhomogeneidades. En las zonas donde se ensancha el QW se observa un mayor gradiente de deformación, que se puede asociar con una acumulación de indio en esas regiones. Esta acumulación estaría por encima del

valor nominal,  $x = 0.2$ , pero sin superar valores de  $x > 0.5$ , que indicarían un *clustering* de indio.

- En el análisis del *low-loss* EELS, se han medido valores de *band gap*, obteniendo una buena correspondencia con los valores esperados para las barreras, sin que su distribución espacial revele la existencia de un QW de distinta composición. Este resultado se explica por la delocalización espacial, que es grande ( $\sim 10$  nm) para pérdidas de energía tan bajas como las correspondientes al *band gap*.
- Sobre los datos de *low-loss* EELS se ha analizado, como en los casos anteriores, la energía y anchura del plasmón ( $E_P$  y  $\Gamma_P$ ) usando un modelo de Drude, registrando de forma consistente desplazamientos y ensanchamientos en las regiones de QW. Es relevante reseñar que no es posible relacionar cuantitativamente el desplazamiento de  $E_P$  con un contraste químico, como en los anteriores capítulos. Asociamos este efecto al impacto de la delocalización y el incremento de las energías del estado fundamental asociados al reducido tamaño de las estructuras QW.
- En cambio, el contraste en los mapas de  $\Gamma_P$  vuelve a aparecer relacionado con la inhomogeneidad química y estructural en las capas, por comparación directa con los mapas de deformación. Despues del KKA, medimos la intensidad de la transición Ga 3d y el parámetro  $E_{cut}$ . Estos dos parámetros mejoran la resolución espacial obtenida con  $E_P$  en las capas QW, proporcionando valiosa información acorde también con lo observado hasta ahora. De los resultado de KKA se obtienen valores de  $m^*$ , que, aunque no muestran un contraste consistente en la zona del QW, dan valores en buena correspondencia con otras observaciones de *low-loss* EELS en sistemas similares.

En los dos siguientes capítulos se examinan varias estructuras basadas en silicio. Las estructuras consideradas tienen en común que en ellas el silicio forma nanocristales rodeados de una matriz de material dieléctrico amorfo también basado en silicio. El objetivo aquí es la caracterización individual de estos cristales, siempre sirviéndonos de la combinación de *low-loss* EELS y HAADF. Por la configuración de las estructuras consideradas, la interpretación de estos espectros e imágenes se ve complicada por el solapamiento entre las contribuciones de nanopartículas y matriz. En cada capítulo se propone una estrategia distinta para resolver este problema y, así, aprovechar la resolución espacial y energética que proporciona el EELS-SI.

En el Capítulo 6, se ha examinado una heteroestructura de SiO<sub>2</sub> amorfo con capas ricas en silicio que contienen clústeres de tamaño nanométrico de silicio cristalino (Si-ncs) dopadas con erbio. Hemos caracterizado una muestra preparada

por haz de iones focalizado (FIB), técnica que permite conseguir un perfil de espesor muy homogéneo. Para el análisis del *low-loss* EELS, se ha utilizado un ajuste múltiple basado en el modelo de Drude del plasmón, y además se ha monitorizado el espesor a partir del parámetro  $t/\lambda$ . Un objetivo adicional ha sido buscar evidencias de clusterización del erbio, que no se había podido detectar para esta estructura por rayos X (EDX).

- Las imágenes HAADF y los mapas  $t/\lambda$  obtenidos confirman la homogeneidad del espesor de la muestra en la región examinada. Esto permite interpretar el contraste Z y el de  $\lambda$  para caracterizar las regiones con Si-ncs. En este sentido, observamos la presencia de capas ricas en silicio con algunas acumulaciones localizadas, de manera consistente con un cálculo del recorrido libre medio para la dispersión inelástica, aunque no es posible discernir la posible presencia de clústeres de erbio.
- Para la caracterización de estas estructuras, se ha utilizado un modelo que contiene dos picos con el objetivo de ajustar dos plasmones distintos. Uno de ellos ha de ajustarse al plasmón del material dieléctrico ( $E_P^{\text{SiO}_2} = 23.7$  eV), siempre presente, y el otro detecta la presencia de los Si-ncs por la aparición de un plasmón en  $\sim 17$  eV. Esta estrategia permite localizar la posición de los Si-ncs en las multicapas, aunque se encuentran bastante dispersos, con una concentración baja, y representan una contribución pequeña al *low-loss* EELS medido. En este sentido, adaptar las condiciones del ajuste a la forma del espectro es crucial para el funcionamiento de esta estrategia.
- En este análisis, se han obtenido energías de plasmón para los Si-ncs y el SiO<sub>2</sub> mayores de lo esperado, además de un incremento sensible en  $\lambda$  para el SiO<sub>2</sub>. Se pueden relacionar estas medidas con la presencia de erbio disperso a lo largo de toda la estructura examinada y, en el caso de los Si-ncs, con un efecto de confinamiento cuántico.

En el Capítulo 7, se han examinado tres sistemas que presentan nano-cristales de silicio (Si-NCs), con diámetros del orden de 5 nm, en distintas matrices dieléctricas amorfas (*i.e.* SiO<sub>2</sub>, Si<sub>3</sub>N<sub>4</sub> y SiC). Se ha propuesto una estrategia de análisis basada en la identificación y segmentación de las regiones de interés por la energía del plasmón, y, finalmente, la factorización del *low-loss* EELS usando algoritmos MVA.

- En este sentido, se ha demostrado el uso de MVA para separar las contribuciones espectrales de los Si-NCs y las matrices dieléctricas. Los algoritmos MVA funcionan de manera excelente en las muestras de SiO<sub>2</sub> y Si<sub>3</sub>N<sub>4</sub>, en las cuales se constata el correcto crecimiento de las muestras. El punto clave

para el uso de los algoritmos MVA es la identificación de regiones de composición homogénea, atendiendo a las medidas de energía de plasmón. En este sentido, en la muestra de SiC el crecimiento ha sido más complicado; el desplazamiento continuo del pico de plasmón indica que se produce una inhomogeneidad estructural y química. En estas circunstancias, el uso de los algoritmos MVA está desaconsejado por la aparición de artefactos en la factorización.

- Los algoritmos MVA utilizados (NMF y BLU) han sido adaptados usando la normalización de Poisson. Esta normalización permite tener en cuenta correctamente la distribución estadística de la intensidad registrada en *low-loss* EELS, lo cual es clave para el buen funcionamiento de los algoritmos.
- Además, se ha podido realizar un análisis detallado de las propiedades electrónicas a partir de los resultados que se derivan de la factorización por MVA, usando KKA. Este análisis permite extraer información separadamente de la respuesta dieléctrica de los Si-NCs y las matrices dieléctricas. En este sentido, se han comparado las CDFs de los Si-NCs con las del sustrato de silicio cristalino, obteniendo muy buena correspondencia si tenemos en cuenta que el confinamiento cuántico produce un aumento de la energía del estado fundamental en las nanopartículas, en el rango de 17 – 18 eV. Encontramos también una buena correspondencia si comparamos el material dieléctrico en las matrices con las barreras dieléctricas, especialmente en  $\text{Si}_3\text{N}_4$ . En  $\text{SiO}_2$ , observamos un decremento de la energía del plasmón en la matriz, de 1 eV, lo cual nos indica la formación de un sub-óxido ( $\text{SiO}_x$ ) alrededor de las nanopartículas.
- Finalmente, se han podido calcular valores de  $m^*$  a partir de las CDFs obtenidas con anterioridad. Es interesante señalar de nuevo la buena correspondencia que encontramos entre el sustrato de silicio cristalino y los Si-NCs, con valores ligeramente superiores en las nanopartículas.

En suma, los métodos desarrollados han revelado propiedades estructurales y mecánicas de los materiales examinados, a una alta resolución espacial y analítical, permitiendo así dilucidar la configuración de avanzados dispositivos optoelectrónicos.



# **Appendix C**

# **Scientific Curriculum**

## **Education**

2009 LICENCIATURA EN FÍSICA, Universidade de Santiago de Compostela.

2010 MSc IN BIOPHYSICS, Universitat de Barcelona.

## **Appointments held**

2010 RESEARCH ASSISTANT, LENS (Laboratory of electron nanoscopies), Departament d'Electrònica, Universitat de Barcelona.

2014 ASSISTANT PROFESSOR, 160 hour contract teaching freshman level informatics for scientists (Python), Universitat de Barcelona.

## **Research stages**

2011 FACULTAD DE QUÍMICA, Universidad Complutense de Madrid, Spain. November-December (1 month).

2012 DEPARTMENT OF METALLURGY, University of Cambridge, United Kingdom. December (10 days).

2013 ERNST RUSKA-CENTRE for Microscopy and Spectroscopy with Electrons (ER-C) in Forschungszentrum Jülich, Germany. June-September (3 months).

## Workshops & schools

- 2010 TEM-UCA SUMMER WORKSHOP, Transmission Electron Microscopy on Catalytic Materials and Nanoparticles. *Universidad de Cádiz*, Spain, 12th-16th July.
- 2011 1ST TEM SCHOOL, *Laboratorio de Microscopia Avanzada - Instituto de Nanociencia de Aragón (LMA-INA)*, *Universidad de Zaragoza*, Spain, 14th-16th December.
- 2012 EELS IN MATERIALS SCIENCE International workshop, Uppsala, Sweden, 18th-20th June.

## Grants, honors & awards

- 2011 EXCELLENT STUDENT PRESENTATION Award, International Conference on Microscopy of Semiconducting Materials XVII.
- 2013 GRANT 2012-BE1-00714 for a three month international research stage, Generalitat de Catalunya.

## MSc thesis supervision

- 2014 X. Sastre. Ab initio calculations of the EELS low-loss spectra in ternary III-nitride semiconductors. Master's thesis, Facultat de Física, Universitat de Barcelona, 2014. Supervisors: A. Eljarrat and S. Estradé

## Reviewer for the following journals

- CRYSTAL GROWTH AND DESIGN
- JOURNAL OF MICROSCOPY
- NANOSCALE

## Journal articles

First-author contributions are indicated using boldface numbers.

- 1** A. Eljarrat, Ž. Gačević, S. Fernández-Garrido, E. Calleja, C. Magén, S. Estradé, and F. Peiró. (V)EELS characterization of InAlN/GaN distributed Bragg reflectors. *Journal of Physics: Conference Series*, 326(1):012014, 2011.
- 2** A. Eljarrat, S. Estradé, Ž. Gačević, S. Fernández-Garrido, E. Calleja, C. Magén, and F. Peiró. Optoelectronic properties of InAlN/GaN distributed Bragg reflector heterostructure examined by valence electron energy loss spectroscopy. *Microscopy and Microanalysis*, 18:1143–1154, 10 2012.
- 3** L. Yedra, A. Eljarrat, R. Arenal, E. Pellicer, M. Cabo, A. Lopez-Ortega, M. Estrader, J. Sort, M. D. Baró, S. Estradé, and F. Peiró. EEL spectroscopic tomography: Towards a new dimension in nanomaterials analysis. *Ultramicroscopy*, 122:12–18, 2012.
- 4** A. Eljarrat, L. López-Conesa, C. Magén, Ž. Gačević, S. Fernández-Garrido, E. Calleja, S. Estradé, and F. Peiró. Insight into the compositional and structural nano features of AlN/GaN DBRs by EELS-HAADF. *Microscopy and Microanalysis*, 19(03):698–705, 2013.
- 5** A. Eljarrat, L. López-Conesa, J. M. Rebled, Y. Berencén, J. M. Ramírez, B. Garrido, C. Magén, S. Estradé, and F. Peiró. Structural and compositional properties of Er-doped silicon nanoclusters/oxides for multilayered photonic devices studied by STEM–EELS. *Nanoscale*, 5(20):9963–9970, 2013.
- 6** Ž. Gačević, A. Eljarrat, F. Peiró, and E. Calleja. Insight into high-reflectivity AlN/GaN Bragg reflectors with spontaneously formed (Al, Ga)N transient layers at the interfaces. *Journal of Applied Physics*, 113:183106–7, 2013.
- 7** J. M. Ramírez, Y. Berencén, L. López-Conesa, J. M. Rebled, A. Eljarrat, S. Estradé, F. Peiró, J. M. Fedeli, and B. Garrido. (invited) optimizing er-doped layer stacks for integrated light emitting devices. *ECS Transactions*, 53(4):81–84, 2013.
- 8** A. Eljarrat, L. López-Conesa, J. López-Vidrier, S. Hernández, B. Garrido, C. Magén, F. Peiró, and S. Estradé. Retrieving the electronic properties of silicon nanocrystals embedded in a dielectric matrix by low-loss EELS. *Nanoscale*, 6(24):14971–14983, 2014.

- 9 L. Yedra, A. Eljarrat, J. M. Rebled, L. López-Conesa, N. Dix, F. Sánchez, S. Estradé, and F. Peiró. EELS tomography in multiferroic nanocomposites: from spectrum images to the spectrum volume. *Nanoscale*, 6(12):6646–6650, 2014.
- 10 L. Yedra, P. Torruella, A. Eljarrat, A. D. Darbal, J. K. Weiss, F. Peiró, and S. Estradé. Precessed electron beam electron energy loss spectroscopy of graphene: Beyond channelling effects. *Applied Physics Letters*, 105(5):053117, 2014.
- 11 A. Eljarrat, L. López-Conesa, S. Estradé, and F. Peiró. Electron energy loss spectroscopy on semiconductor heterostructures for optoelectronics and photonics applications. *Journal of Microscopy*, 2015. *In Press*.
- 12 A. Eljarrat, X. Sastre, F. Peiró, and S. Estradé. DFT modeling of low-loss EELS in wurtzite III-nitride ternary alloys. *Physical Chemistry Chemical Physics*, 2015. Submitted.

## Selected conference contributions

- 1 A. Eljarrat, Ž. Gačević, S. Fernández-Garrido, E. Calleja, C. Magén, S. Estradé, and F. Peiró. Optical and structural properties of InAlN/GaN Bragg reflectors examined by transmission electron microscopy and electron energy loss spectroscopy. In *Microscopy at the Frontiers of Science (MFS): 2nd Joint Congress of the Portuguese and Spanish microscopy societies.*, 2011. **Oral**
- 2 A. Eljarrat, D. Hosseini, Ž. Gačević, S. Fernández-Garrido, E. Calleja, C. Magén, S. Estradé, and F. Peiró. VEELS characterization of InAlN/GaN distributed Bragg reflectors. In *Journées EELS 2011, 19-21 January, Les Diablerets*, 2011. **Oral**
- 3 A. Eljarrat, D. Hosseini, Ž. Gačević, S. Fernández-Garrido, E. Calleja, C. Magén, S. Estradé, and F. Peiró. VEELS characterization of InAlN/GaN distributed Bragg reflectors. In *Microscopy of Semiconducting Materials (MSM XVII), 4-7 Abril, Cambridge*, 2011. **Poster, Excellent Student Presentation Award**
- 4 A. Eljarrat, L. López-Conesa, Ž. Gačević, S. Fernández-Garrido, E. Calleja, C. Magén, S. Estradé, and F. Peiró. EELS-HAADF spectrum imaging for characterization of (AlGa)N multilayer heterostructures. In *The 13<sup>th</sup> edition of Trends in Nanotechnology International Conference (TNT), Madrid*, 2012. **Oral**

- 
- 5 L. Yedra, A. Eljarrat, R. Arenal, M. Cabo, A. López-Ortega, M. Estrader, E. Pellicer, J. Nogués, S. Estradé, and F. Peiró. EEL spectroscopic tomography: towards a new dimension in nanomaterials analysis. In *European Materials Research Society (EMRS) Spring Meeting, Strasbourg*, 2012. **Oral**
- 6 A. Eljarrat, L. López-Conesa, Ž. Gačević, S. Fernández-Garrido, E. Calleja, C. Magén, S. Estradé, and F. Peiró. EELS-HAADF combination for characterization of a new AlN/GaN DBRs growth method. In *15th European Microscopy Congress (EMC), 16-21 September, Manchester*, 2012. **Oral**
- 7 L. Yedra, A. Eljarrat, R. Arenal, M. Cabo, A. López-Ortega, M. Estrader, E. Pellicer, M.D. Baró, S. Estradé, and F. Peiró. Accessing new dimensions of nanomaterials: EEL spectroscopic tomography. In *Materials Research Society (MRS) Fall meeting, Boston*, 2012. **Oral**
- 8 S. Estradé, J.M. Rebled, L. Yedra, A. Eljarrat, L. López-Conesa, and F. Peiró. Advanced transmission electron microscopy solutions for nanoscience problems. In *36th International Conference and Exposition on Advanced Ceramics and Composites (ICACC)*, 2012. **Oral, Invited**
- 9 A. Eljarrat, L. López-Conesa, J.M. Ramirez, Y. Berencén, S. Harnández, J. López-Vidrier, S. Estradé, C. Magén, B. Garrido, and F. Peiró. Chemical and structural characterization of Si-based electroluminescent and photovoltaic devices through HAADF-EELS. In *Journées d'EELS, 23-25 October, Aix les Bains*, 2012. **Oral**
- 10 L. Yedra, A. Eljarrat, R. Arenal, M. Cabo, A. López-Ortega, M. Estrader, E. Pellicer, S. Nogués, J. Estradé, and F. Peiró. Accessing new dimensions of nanomaterials: EEL spectroscopic tomography. In *Journées EELS (JEELS), 23-25 October, Aix les Bains*, 2012. **Oral**
- 11 A. Eljarrat, L. López-Conesa, Ž. Gačević, S. Fernández-Garrido, E. Calleja, C. Magén, S. Estradé, and F. Peiró. AlN/GaN DBR layers low-loss EELS-HAADF compositional mapping. In *Workshop on EELS in Materials Science, 18th-20th June, Uppsala*, 2012. **Oral**
- 12 A. Eljarrat, L. López-Conesa, Ž. Gačević, S. Fernández-Garrido, E. Calleja, C. Magén, S. Estradé, and F. Peiró. Electron energy loss spectroscopy for the analysis of AlN/GaN interfaces in MBE grown distributed Bragg reflectors. In *17th European Molecular Beam Epitaxy Workshop, 10-13 Marzo, Levi, Finlandia*, 2013. **Oral**

- 13 A. Eljarrat, L. López-Conesa, Ž. Gačević, S. Fernández-Garrido, E. Calleja, C. Magén, S. Estradé, and F. Peiró. Plasmon mapping for the analysis of III-V nitride distributed Bragg reflectors. In *Microscopy at the Frontiers of Science (MFS): 3rd Joint Congress of the Portuguese and Spanish microscopy societies*, 2013. **Oral**
- 14 L. Yedra, A. Eljarrat, J. M. Rebled, N. Dix, F. Sánchez, J. Fontcuberta, S. Estradé, and F. Peiró. 3D chemical nanocharacterization: EELS tomography of BFO/CFO self assembled structures. In *EUROMAT 2013, Symposium: A2III, 7-12 Septiembre, Sevilla*, 2013. **Oral**
- 15 L. Yedra, A. Eljarrat, J. M. Rebled, L. López-Conesa, S. Estradé, and F. Peiró. Eels tomography: from spectrum images to spectrum volume. In *2nd Conference on Frontiers Of Aberration Corrected Electron Microscopy, Nederlands*, 2013. **Poster**
- 16 J.M. Ramírez, Y. Berencén, L. López-Conesa, J.M. Rebled, A. Eljarrat, S. Estradé, F. Peiró, J.M. Fedeli, and B. Garrido. Optimizing er-doped layer stacks for integrated light emitting devices. In *223rd Electrochemical Society 223rd ECS Meeting, 12-17 May*, 2013. **Oral, Invited**
- 17 A. Eljarrat, L. López-Conesa, J. M. Ramirez, Y. Berencén, J. López-Vidrier, S. Hernández, S. Estradé, C. Magén, B. Garrido, and F. Peiró. Using high resolution (V)EELS for imaging of novel silicon devices. In *International Electron Energy Loss Spectroscopy meeting on Enhanced Data Generated by Electrons (EDGE), 26-31 May, Sainte-Maxime*, 2013. **Poster**
- 18 L. Yedra, A. Eljarrat, J. M. Rebled, N. Dix, F. Sánchez, F. Fontcuberta, S. Estradé, and F. Peiró. Nanostructure tomography: an EELS approach to the 4th dimension. In *International Electron Energy Loss Spectroscopy meeting on Enhanced Data Generated by Electrons (EDGE), 26-31 May, Sainte-Maxime*, 2013. **Oral**
- 19 F. de la Peña, S. Mazzucco, M. Nord, A. Eljarrat, G. Donval, M. Walls, L.-F. Zagonel, and M. Sarahan. HyperSpy, an opensource solution for EELS analysis of multidimensional datasets. In *International Electron Energy Loss Spectroscopy meeting on Enhanced Data Generated by Electrons (EDGE), 26-31 May, Sainte-Maxime*, 2013. **Oral**
- 20 A. Eljarrat, L. López-Conesa, Ž. Gačević, S. Fernández-Garrido, E. Calleja, C. Magén, S. Estradé, and F. Peiró. Electron energy loss spectroscopy for the analysis of AlN/GaN distributed Bragg reflectors. In *Microscopy of Semiconducting Materials (MSM XVIII), 7-11 Abril, Oxford*, 2013. **Oral**

- 21 L. López-Conesa, A. Eljarrat, J.M. Ramírez, Y. Berencén, J. López-Vidrier, S. Hernández, S. Estradé, C. Magén, B. Garrido, and F. Peiró. Si-based electroluminescent and photovoltaic devices: EFTEM-HAADF-EELS characterization. In *Microscopy of Semiconducting Materials (MSM XVIII)*, 7-11 Abril, Oxford, 2013. **Oral**
- 22 A. Eljarrat, L. López-Conesa, C. Magén, S. Estradé, and F. Peiró. Plasmon and dielectric function mapping of multiple InGaN QW sample by HAADF-EELS. In *18th International Microscopy Congress, 7-12 September, Prague, 2014*. **Poster**
- 23 A. Eljarrat, L. López-Conesa, J. López-Vidrier, S. Harnández, S. Estradé, C. Magén, B. Garrido, and F. Peiró. EELS of Si-nanocrystals by hyperspectral segmentation and multivariate factorization. In *18th International Microscopy Congress, 7-12 September, Prague, 2014*. **Poster**
- 24 P. Torruella, R. Arenal, Z. Saghi, L. Yedra, A. Eljarrat, L. López-Conesa, F. de la Peña, M. Estrader, G. Salazar-Álvarez, A. López-Ortega, J. Nogués, P. A. Midgley, F. Peiró, and S. Estradé. 3D mapping of oxidation states in heterostructured nanomaterials. In *18th International Microscopy Congress, 7-12 September, Prague, 2014*. **Poster**
- 25 L. Yedra, A. Eljarrat, J. M. Rebled, L. López-Conesa, N. Dix, F. Sánchez, J. Fontcuberta, S. Estradé, and F. Peiró. EELS and tomography: from EELS spectrum images to spectrum volumes. In *18th International Microscopy Congress, 7-12 September, Prague, 2014*. **Oral**
- 26 P. Torruella, R. Arenal, Z. Saghi, L. Yedra, A. Eljarrat, F. de la Peña, P. Midgley, S. Estradé, and F. Peiró. Fe oxidation state 3D mapping of core-shell nanoparticles. In *Journées de l'EELS, 23-26 June, Roscoff, 2014*. **Oral**
- 27 A. Eljarrat, L. López-Conesa, J. López-Vidrier, S. Harnández, S. Estradé, C. Magén, B. Garrido, and F. Peiró. Optoelectronic properties of Si-NCs embedded in a dielectric matrix by low loss eels. In *Materials Research Society (MRS) Fall meeting, Boston, 2014*. **Oral**
- 28 L. López-Conesa, J.M. Rebled, A. Eljarrat, G. Dezanneau, S. Estradé, and F. Peiró. Structural causes of ferroelectricity in the uniaxial relaxor SBN. In *Materials Research Society (MRS) Fall meeting, Boston, 2014*. **Poster**
- 29 P. Torruella, R. Arenal, Z. Saghi, L. Yedra, A. Eljarrat, L. López-Conesa, F. de la Peña, M. Estrader, G. Salazar-Álvarez, A. López-Ortega, J. Nogués, P. A. Midgley, F. Peiró, and S. Estradé. 3D mapping of oxidation states in

heterostructured nanomaterials. In *Materials Research Society (MRS) Fall meeting, Boston*, 2014. **Oral**

- 30** A. Eljarrat, L. López-Conesa, J. López-Vidrier, S. Harnández, S. Estradé, C. Magén, B. Garrido, and F. Peiró. Optoelectronic properties of Si-nanocrystals embedded in a dielectric matrix by low-loss EELS. In *European Materials Research Society (EMRS) Spring Meeting, Lille*, 2015. **Oral**

## Languages

**Spanish and Galician** native level.

**English** spoken (well), read (well) and written (well). Exchange student in Ireland for 2 months. Proficient use of the language in a professional context.

**Portuguese and Catalan** spoken (well), read (well) and written (sufficient).

**French and Italian** spoken (sufficient), read (well) and written (basic). Courses taken at School and University level.

**German** spoken (basic), read (basic), read (basic) and written (basic). Course taken at University level.